Mitigation of motion sickness in automated vehicles

Original Citation:
Mitigation of motion sickness in automated vehicles / Rini, Gabriele. - ELETTRONICO. - (2025).

Availability:
This version is available at http://hdl.handle.net/11589/282040 since: 2025-01-13

Published version
DOI:

Publisher: Politecnico di Bari

Politecnico
di Bari

Department of Electrical and Information Engineering
ELECTRICAL AND INFORMATION ENGINEERING
Ph.D. Program
SSD: IIND-02/A – APPLIED MECHANICS

Final Dissertation

Mitigation of Motion Sickness in Automated Vehicles

---

by
Rini Gabriele

Supervisors:
Prof. Francesco Bottiglione
Prof. Nicola Menga
Prof. Aldo Sorniotti
Dr. Georgios Papaioannou

Coordinator of Ph.D. Program:
Prof.ssa Caterina Ciminelli

Course n°37, 01/11/2021-31/10/2024

La ricerca è stata realizzata con il cofinanziamento dell'Unione europea - **POC Puglia 2014-2020 – Asse X - Azione 10.4 "Interventi volti a promuovere la ricerca e per l'istruzione universitaria". Approvazione Avviso pubblico n. 1/POC/2021 "Dottorati di ricerca in Puglia XXXVII Ciclo".**

Department of Electrical and Information Engineering
ELECTRICAL AND INFORMATION ENGINEERING
Ph.D. Program
SSD: IIND-02/A – APPLIED MECHANICS

Final Dissertation

Mitigation of Motion Sickness in Automated Vehicles

by
Rini Gabriele

Referees:
Prof. Flavio Farroni
Prof. Barys Shyrokau

Supervisors:
Prof. Francesco Bottiglione
Prof. Nicola Menga
Prof. Aldo Sorniotti
Dr. Georgios Papaioannou

Coordinator of Ph.D. Program:
Prof.ssa Caterina Ciminelli

Course n°37, 01/11/2021-31/10/2024

MITIGATION OF MOTION SICKNESS IN AUTOMATED VEHICLES

Contents

SUMMARY

This dissertation addresses the pressing challenge of motion sickness in automated vehicles, emphasising the development of motion planning and control strategies to enhance passenger comfort. With the advent of autonomous driving, vehicles are no longer controlled by a driver who can intuitively adjust manoeuvres based on passenger comfort, making the issue of motion sickness more prominent. Automated driving offers numerous benefits and can lead to unpredictable vehicle dynamics from a passenger's perspective, resulting in a heightened incidence of discomfort and motion sickness. This dissertation investigates methods to mitigate these effects to improve user experience and support wider acceptance of autonomous vehicle technology. The research begins by exploring the phenomenon of motion sickness and examining its causes, symptoms, and physiological impacts on passengers. Various theories are reviewed to explain why motion sickness occurs, including sensory conflict, postural instability, and subjective vertical mismatch theories, each offering insight into how human perception and control systems respond to unpredictable or sustained vehicle motion. The dissertation delves into methods for evaluating motion sickness, discussing different models, questionnaires, and indexes that quantify the likelihood or severity of motion sickness in various driving scenarios. Furthermore, it examines existing mitigation methods, categorising them into three broad approaches: behavioural practices, medical and supplementary solutions, and technological interventions related to vehicle design and control. This comprehensive understanding of motion sickness forms the foundation for the control and planning strategies proposed later in the dissertation. A central focus of the research is motion planning for comfort, identifying the significance of designing trajectories that reduce abrupt changes in speed and direction. Motion planning is positioned as one of the most promising methods for mitigating motion sickness, as it allows for pre-emptive control of vehicle dynamics to maintain smooth and predictable motion. The dissertation evaluates several planning algorithms and methodologies, illustrating how strategic trajectory design can contribute to reducing the lateral and longitudinal forces that typically lead to discomfort. By emphasising smooth, predictable movements, motion planning significantly enhances passenger comfort, supporting the hypothesis that a tailored approach to trajectory design can minimise motion sickness. In addition to motion planning, the dissertation explores nonlinear model predictive control (NMPC) algorithms, which are particularly suited to handling the complex, nonlinear dynamics involved in automated driving. Several NMPC strategies are discussed, including traction control, torque vectoring, and active suspension systems. Through simulations and experiments, the NMPC strategies demonstrate their capacity for precisely modulating vehicle dynamics, paving the way for further investigation of their efficiency in counteracting the potential sources of motion sickness by keeping movements within comfortable bounds. This combination of motion planning and NMPC strategies could offer a holistic approach to enhancing passenger comfort in autonomous vehicles. The findings illustrate that by integrating smooth trajectory planning with advanced control algorithms, it is possible to create an automated driving experience that prioritises comfort and reduces the risk of motion sickness. Concluding the dissertation, the research points to future directions that could build on these results, such as refining motion sickness modelling, developing more adaptive control systems, and validating the methods in real-world driving scenarios. Through its in-depth investigation of motion sickness and its proposed mitigation methods, this dissertation contributes valuable insights to the field of autonomous vehicle design, aiming to make autonomous driving more comfortable and appealing for passengers.

1

INTRODUCTION

Once something is a passion, the motivation is there.

Michael Schumacher

1.1 MOTIVATION

The rapid advancement of automated vehicle technology has the potential to transform transportation, offering increased safety, efficiency, and convenience. However, despite the remarkable technical progress in autonomy and control, a crucial aspect has received less attention: passenger comfort, specifically motion sickness. For this reason, leading automakers and mobility companies, such as Tesla, Waymo and Zoox, are prioritising passenger comfort to ease the broad acceptance by the public of this technology. Moreover, with the rise of shared mobility services like Uber, Lyft and autonomous shuttles, ensuring passengers' comfort during multiple-stop journeys is a crucial aspect. Motion sickness (MS) is a phenomenon that can significantly impair the passenger experience, causing symptoms such as nausea, dizziness, and general discomfort. With the transition from driver-controlled to autonomous vehicles, the nature of vehicle dynamics and passenger roles has fundamentally shifted, leading to new challenges in understanding and mitigating motion sickness. In conventional, driver-controlled vehicles, passengers can anticipate motion by observing the driver's actions, which helps alleviate some symptoms of motion sickness. In autonomous vehicles, however, passengers lack this anticipatory control and are more likely to engage in activities such as reading or working on electronic devices – activities that are highly conducive to motion sickness. As a result, the prevalence of MS in automated vehicles is anticipated to increase, potentially posing a barrier to adopting these technologies. Therefore, finding effective strategies to predict, measure, and mitigate motion sickness has become essential for the success of autonomous vehicle deployment. Understanding the mechanisms behind motion sickness and developing methods to minimise its effects in automated vehicles represents a highly interdisciplinary challenge. Research must incorporate human physiology, psychology, vehicle dynamics, and control engineering insights. While motion sickness has been studied for decades, especially in contexts like maritime, aviation, and virtual reality, the unique conditions of automated road transport introduce additional complexities. For instance, in vehicles, low-frequency accelerations – particularly those within around 0.2 Hz – are known to provoke motion sickness most intensely. This frequency range often corresponds to typical vehicle accelerations and decelerations, making automated driving scenarios especially prone to induce discomfort. In the context of automated vehicles, new methodologies are needed to understand the root causes of motion sickness and develop effective strategies to counteract it through vehicle control. Many conventional mitigation strategies, such as behavioural practices and medical solutions, may offer limited relief and can be inconsistent with the autonomous driving experience. Consequently, there is a compelling need to explore technological solutions that are both robust and seamlessly integrable within the framework of automated vehicle control systems. Specifically, motion planning and control strategies that consider passenger comfort as a primary design objective hold promise as practical solutions to address motion sickness.

The goal of this research is motivated by the need to bridge gaps in current motion sickness mitigation strategies for automated vehicles. This research aims to reduce the incidence of motion sickness symptoms without compromising vehicle performance by optimising motion planning and vehicle control systems. Additionally, understanding the physiological impact of vehicle motion on passengers – such as the impact of accelerations at various frequencies on the human vestibular system – offers a pathway to design algorithms that account for human comfort at a granular level. This is particularly significant because conventional vehicle control systems are typically designed for objectives like stability, responsiveness, and efficiency, with limited regard for human comfort regarding motion sickness. The field requires new approaches incorporating motion sickness considerations as an integral part of vehicle dynamics control. This research also seeks to develop practical guidelines and frameworks for integrating motion sickness mitigation strategies within motion planning and nonlinear model predictive control (NMPC) systems in response to these challenges. NMPC techniques allow for a proactive approach to motion sickness mitigation, enabling real-time adjustments to vehicle dynamics that accommodate the comfort needs of passengers. By implementing torque-vectoring, traction control, and active suspension strategies, this research aims to deliver a holistic solution that addresses motion sickness from multiple angles, encompassing lateral and vertical dynamics control. These solutions not only optimise vehicle performance but may also enhance passenger comfort – a critical aspect that will play a decisive role in the widespread acceptance of autonomous vehicles. Additionally, by exploring and incorporating advanced control strategies and motion planning algorithms that leverage proper motion sickness metrics, this research seeks to lay the groundwork for future motion sickness assessment and mitigation solutions tailored for autonomous vehicles. The broader motivation for this research extends beyond individual comfort. The success of automated vehicles depends on user acceptance, and comfort is a primary factor in shaping public perception and willingness to adopt this technology. A vehicle that minimises discomfort will contribute positively to the image of autonomous technology, influencing market penetration and overall societal impact. For vulnerable groups, such as elderly or sensitive passengers, addressing motion sickness becomes even more crucial, ensuring that autonomous vehicles are accessible and comfortable for a wide range of users. Ultimately, achieving a comfortable, motion sickness-free experience in automated vehicles will be an essential milestone in the journey toward fully autonomous transportation systems that are technically capable and human-centred. In conclusion, this research addresses a critical challenge that autonomous vehicles face as they transition from technical concepts to widely used transportation options. By investigating motion sickness mechanisms, developing effective control and motion planning strategies, and creating a framework for continuous improvement, this work aims to contribute significantly to the emerging field of motion comfort in automated vehicles. This research aspires to push the boundaries of current vehicle dynamics control approaches, paving the way for a new generation of autonomous systems that prioritise passenger well-being, enhance user experience, and ensure sustainable adoption of this transformative technology.

1.2 OVERVIEW OF CHAPTERS

This dissertation is organised into five chapters designed to guide readers through the research and its context. The following overview highlights the focus of each chapter and illustrates their interconnections. Chapter 1 presents the research's motivation, technical background, and relevant literature. The subsequent three chapters provide in-depth analyses of the research conducted, including discussions on the interpretation of findings. The core objective of this dissertation is to identify the causes of motion sickness, as discussed in the literature, explore existing mitigation strategies, and lay the groundwork for advanced motion planning control through a study of multi-actuated vehicles. Chapter 2 reviews existing theories, metrics, and models used to quantify motion sickness and mitigation strategies suggested in the literature. Chapter 3 evaluates a motion planning algorithm to reduce motion sickness, with additional advanced formulations proposed for future research. Chapter 4 examines various vehicle actuation strategies –traction control, torque vectoring, and active suspension systems – to identify the optimal approach for future integration into advanced motion planning control algorithms. Finally, Chapter 5 presents the main conclusions drawn from Chapters 2–4, along with recommendations for future research in this area. For clarity, a summary of Chapters 2–4 is provided below.

1.3.1 Chapter 2

This chapter presents a comprehensive review of motion sickness (MS), covering foundational theories that explain its onset and underlying mechanisms. The chapter delves into a range of MS indices, scales, questionnaires, and models used to estimate and measure the severity of motion sickness. This detailed examination of assessment tools clarifies their theoretical basis and highlights their practical applications across various contexts. Following this, an extensive analysis of existing MS mitigation strategies is provided, organised into three main categories: (i) behavioural practices, consisting of recommendations passengers can follow to alleviate symptoms; (ii) medical and supplementary solutions, including wearable devices designed to counteract symptoms; and (iii) technological solutions, encompassing vehicle design considerations, the use of feedback devices, and advanced planning and control strategies. The chapter concludes with insights into emerging trends and offers recommendations on the most promising MS mitigation methods, laying a foundation for innovative approaches in this field.

1.3.2 Chapter 3

This chapter focuses on developing motion planning strategies to mitigate motion sickness (MS) in automated vehicles. It begins with an overview of the state-of-the-art research on the sources of MS in autonomous systems, highlighting how accelerations within specific frequency ranges are especially likely to induce discomfort. To assess MS effectively, the chapter emphasises the importance of applying particular weighting filters that translate seat accelerations into the accelerations experienced by the passenger's head, providing a more accurate measure of potential motion sickness triggers. Four motion planning algorithms are developed and presented in pursuit of optimised passenger comfort, each integrating these weighting filters into an optimal control framework. This approach ensures that passenger comfort considerations are embedded within the motion planning process, advancing autonomous vehicles' capacity to minimise motion sickness proactively.

1.3.3 Chapter 4

In this chapter, several nonlinear model predictive control (NMPC) strategies are developed and presented, focusing on advanced vehicle dynamics control. The chapter is structured into three main subchapters, each dedicated to a distinct NMPC approach. The first subchapter introduces torque-vectoring and traction control strategies, investigating optimal integration methods to achieve the best synergy between the two algorithms for enhanced vehicle stability and performance. The second subchapter focuses on a torque-vectoring approach explicitly designed to control trailer sway in a car-trailer system, aiming to identify the most effective technique to stabilise the trailer's lateral movement. The final subchapter builds upon this work by extending the torque-vectoring strategy to include active suspension control. This combined approach addresses vertical dynamics and handling behaviour, enhancing control over the car-trailer system. This focus on trailer control through torque vectoring and active suspension systems is justified by the dynamic similarities between car-trailer configurations and articulated buses, enabling the development of safety control strategies that can be extended to future automated articulated buses, with the potential to incorporate motion sickness metrics for enhanced passenger comfort. Each subchapter begins with a comprehensive state-of-the-art review and concludes with practical guidelines for implementing future NMPC algorithms, contributing valuable insights for further advancements in vehicle dynamics control.

1.3 CONTRIBUTIONS

This dissertation presents multiple advancements in enhancing motion comfort for automated vehicles, contributing to various aspects of the field, including:

- Comprehensive literature review on motion sickness: provided an extensive review of motion sickness theories, assessment tools (indices, scales, questionnaires, models), and mitigation strategies, categorising these into behavioural practices, medical solutions, and technological approaches. Recommendations for future trends and promising mitigation methods are also offered.
- Development of motion planning algorithms for MS mitigation: design and implement of four motion planning algorithms to reduce motion sickness in automated vehicles. These algorithms integrate weighting filters to translate seat accelerations into passenger head accelerations, allowing for more accurate MS assessments and proactive mitigation.
- Advancements in nonlinear model predictive control (NMPC) for vehicle dynamics:
    - Torque-Vectoring and Traction Control integration: developed and analysed strategies combining torque-vectoring with traction control, identifying the optimal integration for enhanced vehicle stability.
    - Control of trailer sway in car-trailer configurations: designed NMPC strategies using torque-vectoring to mitigate trailer swaying, enhancing stability in multi-actuated car-trailer systems.
    - Incorporation of active suspension for vertical and handling dynamics: extended the torque-vectoring strategies to include active suspension systems, addressing vertical dynamics and improving handling behaviour in car-trailer setups.
- Guidelines for future algorithm development: each technical chapter concludes with practical guidelines, offering implementation insights and recommendations for future NMPC and motion planning algorithms in the context of vehicle dynamics and motion sickness mitigation.

2

MOTION SICKNESS

Movement is tranquillity.

Stirling Moss

2.1 INTRODUCTION

In recent years, the amount of time people spend driving has steadily increased, reflecting growing trends in urban sprawl, commuting distances, and reliance on personal vehicles for transportation. According to the AAA Foundation for Traffic Safety, the time spent in cars in 2023 reached ~370 *hours* per year per person [1]. The primary inconvenience of driving a conventional car is the constant need for active involvement in driving tasks; meanwhile, the appealing idea of removing the driver from the equation by using fully autonomous vehicles (AVs) is gaining traction. AVs have the potential to relieve the driver from the driving tasks, prospecting increased productivity and leisure during AV travel [2], [3]. To achieve this, AVs are typically equipped with a wide range of sensors, enabling them to collect data from the environment even in the most challenging conditions and make the best driving decision to ensure passenger safety, avoid accidental collisions and enhance energy efficiency.

However, to succeed in the complete transition from conventional vehicles to AVs, the benefits mentioned above are not enough, as occupants' engagement in non-driving-related tasks has been proven to cause motion sickness (MS), thus discomfort due to increased conflicts between visual motion cues and vestibular stimuli. MS is identified as one of the comfort factors in AVs [4] and is still considered a cause of hesitation for the broad acceptance by the public of AVs.

In a survey conducted across several countries, including the US, China, India, Japan, the UK, and Australia, participants were asked if they would ride in an AV. In the US, 23 % of respondents said they would not, with similar figures in Australia (21 %) and the UK (23 %). Significantly lower percentages were observed in India (8 %) and China (3 %), while Japan had a notably higher percentage of 33 % [2], [3]. An interesting finding is the percentage of people who indicated what they would do while riding in an autonomous vehicle. On average, 46 % of passengers said they would watch the road,. In contrast,the remaining passengers would be engaged in other activities such as reading, texting, talking, sleeping, watching movies, working, or playing games. The same study provides data on the frequency and severity of MS experienced by occupants engaged in these activities. Watching a video is less likely to induce MS than reading; 15 % of people watching a video reported moderate to severe symptoms of MS, while this number more than doubled to 32 % when reading a book. Finally, it is noted that, on average, $5-12\,\%$ of occupants would experience moderate to severe MS at some point. In addition to this survey, other studies have shown that blind individuals are particularly susceptible to MS [5], [6]. Conversely, those who are hypothetically immune to MS under any condition are individuals with a total loss of labyrinthine function [7], [8]. However, individuals with a disordered vestibular system may be even more prone to MS in everyday environmental situations [9].

For this reason, the authors of [10], [11] analyse the causes of MS in AVs and offer guidelines on how these technologies should be designed and developed. As AVs and related technologies are attracting increasing attention, the issue of MS in AVs has yet to be fully addressed.

This chapter aims to provide a systematic review of MS theories found in the literature, along with MS indices, scales, and models used to estimate the feeling of sickness. It also examines existing techniques proposed to mitigate MS in AVs. Finally, the chapter discusses potential future research on mitigation methods and their implementation in AVs.

2.2 THEORIES

Reading in a moving vehicle, such as a car, is a luxury that not everyone can enjoy. Approximately one-third of the population experiences nausea when attempting to focus on a book while in motion, whether in a car, boat, train, or plane. MS, a common phenomenon, is still not fully understood by scientists, though several theories attempt to explain it. The most widely accepted theory is the conflict theory, suggesting that MS results from mismatched sensory signals. When travelling in a car, the body receives conflicting information: the eyes perceive the interior of a stationary vehicle, thus signal to the brain that the body is standing still; on the other hand, the vestibular system located in the inner ear is responsible for detecting movement, signals to the brain that the body is accelerating. The vestibular system consists of three semicircular canals, each sensitive to rotation in a different dimension of space, and two fluid-filled sacs lined with hair cells, see Figure 2.1.

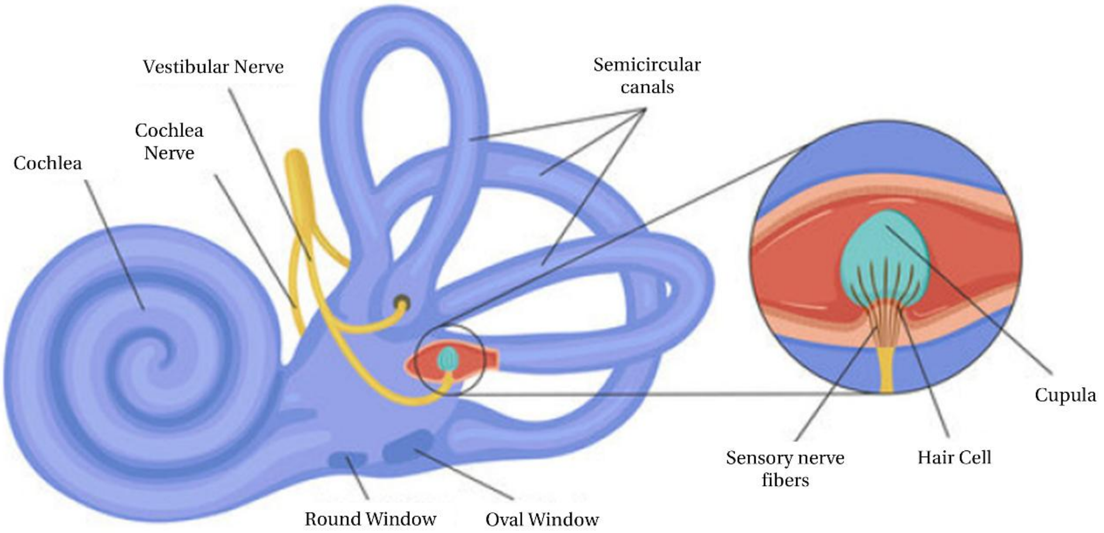

Figure 2.1: Overview of the vestibular system

As the body moves, the fluid within the sacs shifts, stimulating the hair cells and informing the brain about changes in horizontal or vertical movement. These combined sensory inputs allow the body to determine its direction, acceleration, and orientation. Thus, in a moving car, the vestibular system accurately senses motion, but the eyes – especially if focused on a book – do not. This sensory conflict can also happen in reverse, for example, while watching a movie with sweeping camera movements. In such cases, the eyes perceive motion, but the vestibular system knows the body is stationary. Early studies about these conflicting signals can be traced back to 1881 when Irwin [12] published an article in *The Lancet* titled "*The Pathology of Sea-Sickness,*" in which he was the first to attribute sea-sickness – essentially the same as MS – to a mismatch between information from the visual sensory system and the vestibular system. Subsequently, in 1924 Beadnell proposed a theory similar to Irwin's [13]. Then, Claremont in 1931, again proposed that MS is caused by a conflict between sensory cues, specifically when there is a discrepancy between motion cues perceived by the visual and vestibular systems [14]. Later, in 1936, Hill published a study on sea-sickness, in which he stated that *“immunity to sea-sickness consists in the development of appropriate conditioned reflex responses”* [15]. This implies that sea-sickness is not solely due to conflicting signals but also depends on how individuals adapt and respond to such situations. This claiming lay the groundwork for the development of two more theories, the sensory rearrangement theory and the postural instability theory. The former was proposed by Reason in 1975, hinting that MS is caused by a conflict between the motion we perceive by sense organs, and the motion our brain expects based on past experiences and thus how we react to the mismatch [16]. Whilst, the latter was proposed by Riccio in 1991 [17], who stated that the sick feeling comes out in situations in which the animals do not possess or do not have yet learned strategies that are effective for the maintenance of postural stability. Postural instability occurs when the central nervous system is not able to properly integrate sensory signals from visual, vestibular and proprioceptive systems, leading to a loss in maintaining muscle balance. Although the postural instability theory has been extensively discussed in the literature, the sensory conflict theory has shown more congruence with experimental results [18]. Later on, the conflict theory and the sensory rearrangement theory were further developed in [19]. The authors proposed the subjective-vertical conflict theory, redefining the mismatch as a conflict between the perceived vertical acceleration sensed by the vestibular system and the subjective vertical acceleration, i.e. the expected motion based on prior experience. However, the role of the visual system in the occurrence of MS remained unclear. An early study on visual-vestibular interaction was presented in [20], as well as in [21], [22], where the authors described the interactions that occur when viewing images that may induce MS. Further advancements in this area were proposed in [23], where the authors explored the role of sensory-induced self-motion, specifically vection. The subjective-vertical conflict theory was broadened in [24] where the authors identified as source of MS not solely the vertical mismatch but also the horizontal, i.e. lateral acceleration. Finally, in [25], the authors expanded the conflict to the longitudinal component as well. These extensions are supported by the findings presented in [26], where the authors conducted an analysis of frequency-weighted accelerations in multiple directions that passengers experience on different types of coaches. The study revealed that, regardless of the coach type, fore-and-aft, lateral, and vertical motions consistently exhibit greater magnitudes compared to rotational motions. These translational movements, therefore, play a significant role in the onset of MS. Another critical aspect in understanding the causes of MS is the frequency of these accelerations. In [27], [28], researchers examined the proportion of individuals reaching a specific illness rating when exposed to accelerations within the frequency range of 0.0315 Hz to 0.2 Hz. The study found that as the frequency approached 0.2 Hz, a larger proportion of participants reported higher illness ratings, indicating that lower frequency values provoke less MS. Similar conclusions were drawn in [29], where the authors explored the mean time to sickness rating, defined as the average duration it takes for subjects to experience initial symptoms, mild nausea, and moderate nausea, in relation to acceleration frequency. The shortest time to sickness was consistently observed around 0.2 Hz, further highlighting that this frequency range holds the greatest potential for inducing nausea. While many theories emphasise the conflicting information received from two different systems, this alone may not fully explain MS. For instance, as proposed in [30] the inter-sensory conflict can occur within the vestibular system itself, between the otoliths (which detect linear acceleration) and the semi-circular canals (which detect rotational velocity), as seen in phenomena caused by Coriolis acceleration. Aside from the several declinations of the sensory conflict theory, other paths were investigated over the years. Another theory claims that virtual environments (VE) can produce MS, and it is caused by eye movement conflict [31]. When moving the head in the real world, eyes naturally adjust to maintain a stable view of the surroundings, thanks to the vestibulo-ocular reflex (VOR), however in VE, head movements may not result in corresponding visual adjustment on the screen. This inconsistency forces the eyes to work harder, leading to discomfort and nausea. This phenomenon is often related to simulator sickness. In some VE, particularly those that simulate first-person movement, the visual flow of the motion could be strong enough to trigger a perception of motion in the brain, even though the body is not moving. This causes confusion between the systems responsible for spatial orientation, which can result in symptoms of MS like dizziness, nausea and disorientation. In this direction, Cohen et al. [32] propose that MS is mediated through the orientation properties of velocity storage in the vestibular system that tend to align eye velocity produced by the angular vestibular-ocular reflex (aVOR) with gravity-inertial acceleration (GIA); later on, in [33] the authors reviewed the source of the conflicts that cause the body to generate the autonomic signs and symptoms that constitute MS and provide a summary of the experimental data that has led to an understanding of how MS is generated and can be controlled. In summary, all theories in the literature are grounded in the interaction of three key factors: i) the visual sensory system, ii) the vestibular system, and iii) the physical environment. Despite the numerous theories proposed, none have been able to fully explain the phenomenon of MS. It remains one of those seemingly straightforward problems that, despite significant scientific advancements, is still not fully understood. For this reason, much of the research focuses on assessing MS through various metrics, scales, questionnaires and models, which will be addressed in the following chapter.

2.3 INDEXES AND MODELS

Understanding and quantifying MS has long been a subject of great interest across multiple disciplines, from transportation and aviation to virtual reality and human physiology. Despite its prevalence and the impact, it has on both comfort and performance, MS remains a complex and elusive phenomenon to measure. The challenge lies in the multifaceted nature of MS, which can manifest through various physical, psychological, and sensory factors. These factors interact in unpredictable ways, making it difficult to pinpoint the precise mechanisms that cause an individual to experience discomfort or nausea. To address this complexity, researchers have developed a range of methods to estimate and evaluate MS. These approaches vary widely in their focus, from objective measurements of physiological responses to subjective assessments of individual perception. Some methods aim to capture the onset of symptoms, while others strive to predict susceptibility before symptoms arise. The diversity of these approaches reflects both the complexity of MS itself and the need to account for its variable impact across individuals and contexts. In this chapter, the different methodologies that have been proposed to estimate MS are explored. Their underlying principles, their practical applications, and the insights they offer into the broader understanding of MS will be considered. The MS susceptibility questionnaires (MSSQs) designed by Reason and Brand were the first systematic tools developed to measure susceptibility to MS [16], [34]. It is a retrospective tool assessing an individual's likelihood of experiencing MS based on past experiences in various motion environemnts, such as land, air, and sea travel. It features a two-part structure evaluating childhood and adulthood experiences, uses a weighted scoring system for frequency and severity, and serves as a predictive measure for future susceptibility, making it a versatile and widely used instrument in motion sickness research. These questionnaires were later revised by Golding in 1998 [35], resulting in the MSSQ-Long Form (MSSQ-LF), which contained 54 items and took a significant amount of time to complete. To address this, Golding further revised the questionnaire in 2006 [36], creating the MSSQ-Short Form (MSSQ-SF), which reduced the number of items to 18. Since virtual reality (VR) technology at the time was not as advanced as it is today and exposure to such systems was relatively limited, VR-related questions were excluded from the MSSQ-SF. In fact, during the development process in 2006, references to visual devices like cinema, video games, and VR were intentionally omitted, as these technologies were not as prevalent or widespread as they are today. The MSSQ-SF is widely regarded as the standard tool for predicting traditional MS; however, it was not specifically developed to assess visually induced MS (VIMS) or cybersickness. To address these forms of MS, the literature offers a variety of measurement tools specifically designed to evaluate VIMS and cybersickness [37]–[40]. A different approach is used for the Nausea Profile (NP) [41], defined as a self-report questionnaire that focuses on the severity of nausea and related symptoms. It evaluates different dimensions of nausea, such as the urge to vomit, stomach awareness, and overall discomfort, making it useful in both traditional and visually induced MS. Equivalently, the authors in [42] propose the Motion Sickness Assessment Questionnaire (MSAQ), which is a comprehensive tool that evaluates MS across four symptom domains: gastrointestinal, central (such as dizziness and fatigue), peripheral (such as sweating), and sopite-related symptoms (such as drowsiness and disinterest). This questionnaire provides a detailed assessment of the different ways MS can affect individuals.

Despite the huge number of questionnaires available in the literature, over the years, researchers have developed various scales to measure the severity and impact of MS across different contexts, whether it occurs in traditional settings, such as vehicles and simulators, or in more modern environments, like virtual reality. These scales provide valuable insights into the onset, progression, and intensity of symptoms, helping to better understand and predict MS. Examples of scales used to estimate MS include: i) the Pensacola Diagnostic Index [43], one of the earliest tools used to diagnose and rate MS, providing a scoring system based on a range of physical symptoms, including nausea, vomiting, dizziness, and sweating, and still referenced in research despite being less commonly used today; ii) the MIsery SCale (MISC) rating symptoms on a scale where 0 indicates no issues, 1 represents mild discomfort without specific symptoms, 2-5 cover a range of symptoms from vague to severe, excluding nausea, 6-9 reflect increasing levels of nausea, and 10 corresponds to vomiting [44]; and iii) the Fast Motion Sickness Scale (FMS), which is a verbal rating scale that ranges from 0, indicating no MS, to 20, representing severe MS [45]. Both questionnaires and scales are valuable tools for evaluating MS. However, incorporating them into control strategies poses a challenge, as such strategies typically require a mathematical formulation. This is where mathematical indexes become essential, providing a more objective and quantitative approach to understanding MS. These indexes are usually derived from physiological measurements or motion data, allowing for a more precise assessment of MS. Through the use of mathematical models and formulas, these indexes quantify key factors like acceleration, head movement, and exposure frequency, all of which contribute to the onset and severity of MS. In this context, the ISO 2631-1 is an international standard that provides guidelines for evaluating human exposure to whole-body vibration [46]. It outlines methods for assessing the impact of mechanical vibrations and shocks on human comfort, health, and performance, with a particular focus on motion-induced discomfort or MS. The standard defines how to measure and assess whole-body vibration using weighted acceleration values across three axes (x, y, and z). It emphasises the importance of frequency weighting, as the human body is more sensitive to vibrations at specific frequencies. Lower frequencies, particularly between 0.1 Hz and 0.5 Hz, are strongly associated with MS. Additionally, ISO 2631-1 accounts for the duration of exposure, recognising that the length of time someone is subjected to vibration significantly affects its impact. Cumulative exposure is often considered in assessing health risks, while shorter exposures focus primarily on comfort. This standard is applied across various environments, including transportation (e.g., vehicles, boats, and aircraft), industrial settings, and workplaces where humans are exposed to whole-body vibrations. In addition to providing a comprehensive framework for evaluating vibrations in different contexts, ISO 2631-1 also defines the Motion Sickness Dose Value (MSDV). The MSDV quantifies MS by measuring cumulative exposure to motion over time, and it is defined as the root mean square (RMS) of vertical acceleration and the duration of exposure, see equation (2.1):

$$MSDV_z = \sqrt{\int_0^T [a_w(t)]^2 dt} \tag{2.1}$$

where $a_w(t)$ is the frequency-weighted acceleration in the z direction, T is the total period during which motion occurs. The MSDV, is widely used to predict the likelihood of MS in vehicles or environments with prolonged motion exposure. A further elaboration of the MSDV, is the Illness Rate (IR), defined as follows:

$$IR = K \cdot MSDV \tag{2.2}$$

where K is an empirically derived constant – usually set up to 0.02 – based on data from studies of MS in ships and road [47]–[49]. Having explored the various questionnaires, scales, and indexes used to assess MS, it is essential to now turn the attention to the more advanced approaches involving mathematical models. While indexes provide useful metrics and quantitative assessments, mathematical models offer deeper insights by simulating the underlying mechanisms that lead to MS. These models not only account for the relationship between physical stimuli and physiological responses but also allow for the prediction of MS across different scenarios and environments. Transitioning from purely descriptive measures to mathematical modelling represents a significant step towards a more dynamic and predictive understanding of MS, enabling to better capture its complexity. Between 1974 and 1976, O'Hanlon and McCauley conducted one of the most well-known and reliable studies aimed at understanding the phenomenon of MS [50], [51]. In these works, the authors were the first to propose a mathematical formulation for calculating the Motion Sickness Index (MSI) using the mean values and standard deviation of the logarithmic acceleration threshold:

$$MSI = \int_{-\infty}^{\log \overline{a}} \frac{100}{\sigma\sqrt{2\pi}} e^{-\{[x-\mu]^2/2\sigma^2\}} dx \tag{2.3}$$

where x is a variable of integration in unifs of $\log \overline{a}$, and σ and μ are parameters with values determined empirically. The first mathematical model of MS was introduced by Reason et al. in 1978 [34], with the proposal of the neural mismatch model, outlined in Figure 2.2. This model aimed to address fundamental questions surrounding MS, such as where and when it occurs. By focusing on the mismatch between sensory inputs from different systems – such as the visual, vestibular, and proprioceptive systems – the model sought to explain how conflicting information leads to the onset of MS symptoms.

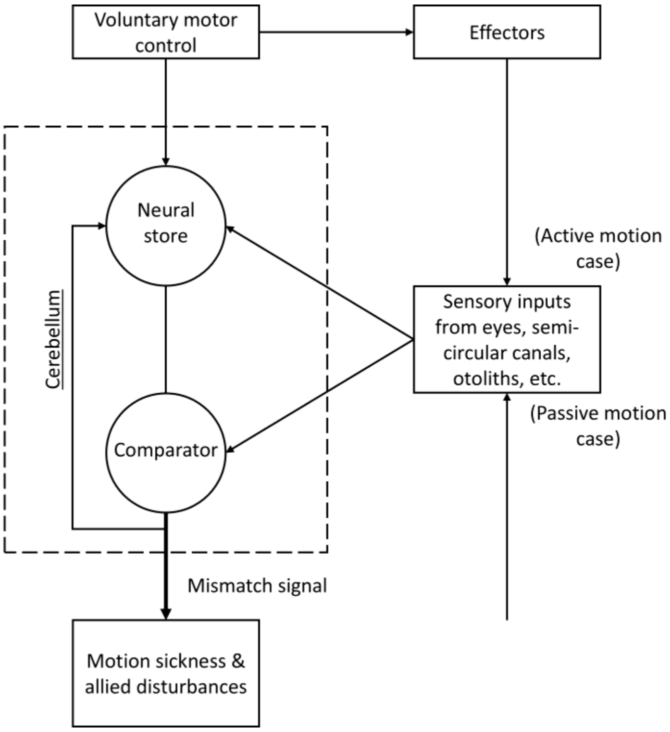

Figure 2.2: Neural Mismatch Model proposed in [34].

However, the proposed model offers a qualitative explanation of the phenomenon of MS without providing a formal mathematical framework. Progress in this direction was made by Oman in 1982 [52], who developed a mathematical model for conflict generation based on the Neural Mismatch Model. The model is depicted in Figure 2.3, where x is the body actual state vector, u is the forcing vector, m is the motor outflow vector from the Central Nervous System (CNS), a is the polysensory afference vector to CNS, n_e is the external disturbance vector, n_a is the sense organ output vector, A is the matrix describing the effect on x of $\dot{x}$, B is the matrix describing the effect of forcing vector on $\dot{x}$, C is the control matrix, S is the matrix of sense organ gain factors, T is the conflict sensitivity matrix, K_c is a gain factor, x_d represents the desired state vector, c is the sensory conflict and the notation $\widehat{\ }$ represents the respective estimated states and matrices within the internal model. This model also incorporates von Holst's "reafference principle" [53], findings from Held's experiments on adaptation to "sensory rearrangement" [54]–[57], and the control engineering perspective introduced by Young et al. [58], which describes the role of the CNS and its interaction with the visual and vestibular systems.

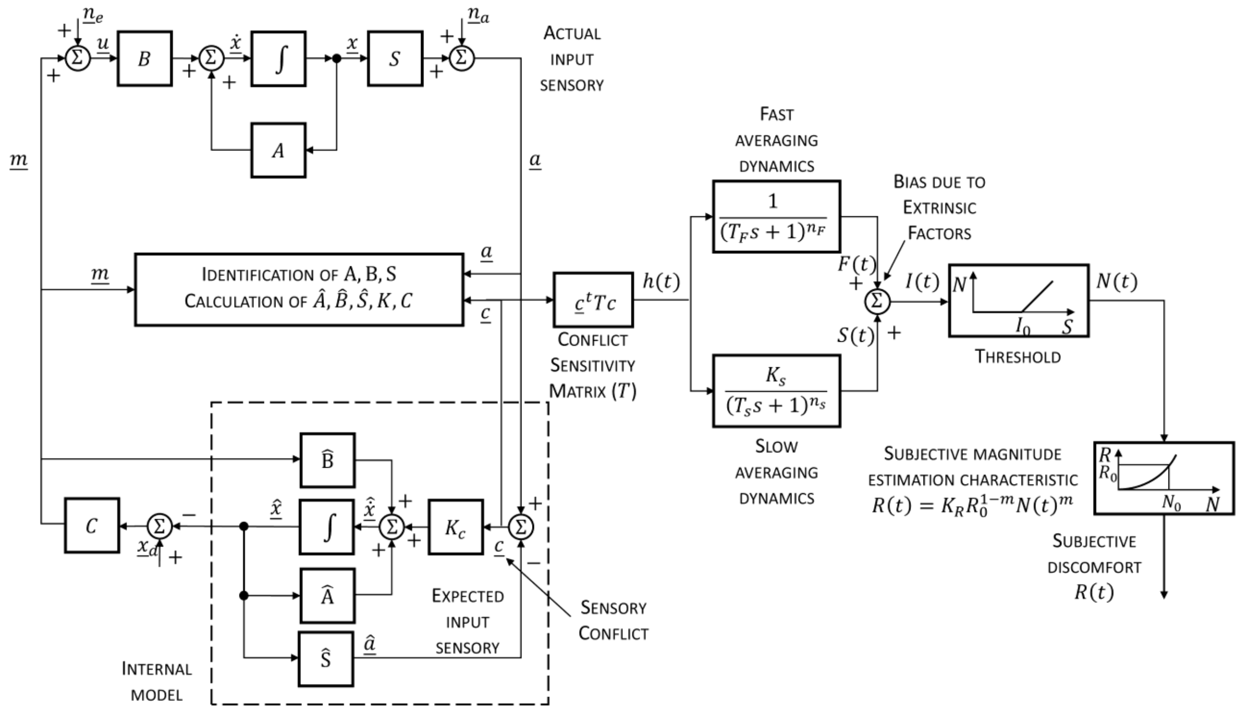

Figure 2.3: Heuristic Mathematical Model proposed in [52] for the calculation of subjective discomfort.

In [59], the author reviewed the stimuli causing MS, presenting a contemporary observer theory of the sensory conflict hypothesis and a revised model describing the dynamic relationship between conflict signals and the estimated intensity of nausea. Building on Oman's work, Bles and Bos later proposed the Subjective Vertical Conflict (SVC) theory in [60], [61]. They extended Oman's model by incorporating knowledge of the vestibular system and reaffirming the sensory rearrangement theory. The proposed model is shown in Figure 2.4a), where V is the module to compute the sensed vertical, F is the transfer module allowing compute the measured subjective vertical, d is the mismatch vector between the perceived vertical and the subjective vertical, i.e. the one computed within the internal model, K_d is a gain factor for the mismatch. In Figure 2.4b) the detailed module V is represented, where VIS, SOM, OTO, SCC are the transfer functions for the visual system, the somatosensory system, the otholiths and semi-circular canals respectively; LP is a low-pass filter, allowing to consider the frequencies around 0.2 Hz, t is the difference between the gravito-inertial force vector and the sensed vertical and r is the vector for the head tilt. In [61] the authors argued that "*All situations which provoke motion sickness are characterised by a condition in which the sensed vertical, as determined based on the integrated information from the eyes, the vestibular system and the non-vestibular proprioceptors is at variance with the subjective vertical as expected from previous experience*". This concept was further refined through optimal estimation theory, using an internal model (or observer) with transfer functions analogous to those of the otoliths (OTO) and semicircular canals (SCC) to predict the subjective vertical for a given stimulus [60].

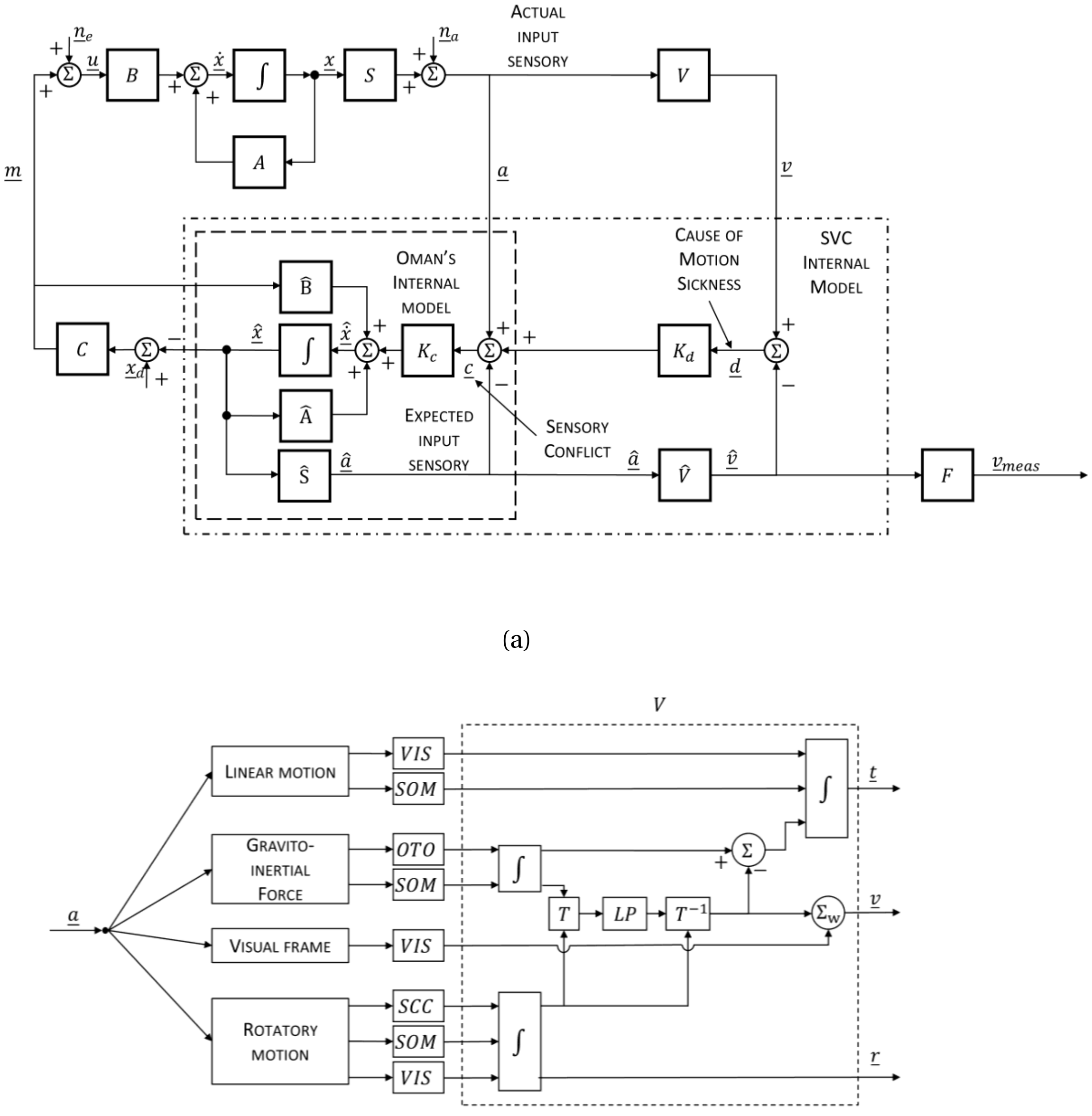

(a)

(b)

Figure 2.4: (a) SVC Model proposed in [60] and [61], (b) Detailed module V included in (a).

Always in [60], the authors propose a model to predict the amount of MS given any kind of motion stimulus, using a model based on the explicit knowledge of the vestibular system. In particular, the authors compute the cumulation of MS starting from the SVC model output, which is fed into a non-linear transfer function, i.e. Hill Function, which can be written as in equation (2.4):

$$h = \frac{[d/b]^{\,n}}{1 + [d/b]^{n}} \tag{2.4}$$

where b is the indifferent point, i.e. the point where $h(b) = 0.5$ and n defines the steepness of the function, see Figure 2.5.

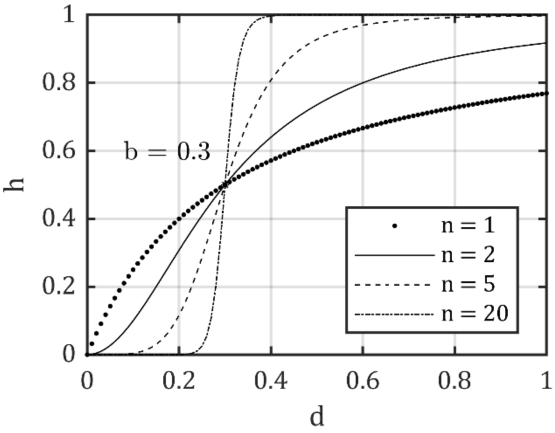

Figure 2.5: Hill Function with different steepness levels and fixed indifferent point b = 0.3.

Then the output h of the Hill Function is fed into a transfer function, see equation (2.5), to compute the MSI as follows:

$$MSI = \frac{P}{[\mu s + 1]^2} h \tag{2.5}$$

where P considers the maximum percentage of people suffering from MS under the given conditions and μ is a time constant. Finally, the authors present the predicted MSI after 2 hours of vertical sinusoidal motion, plotted as a function of frequency and acceleration:

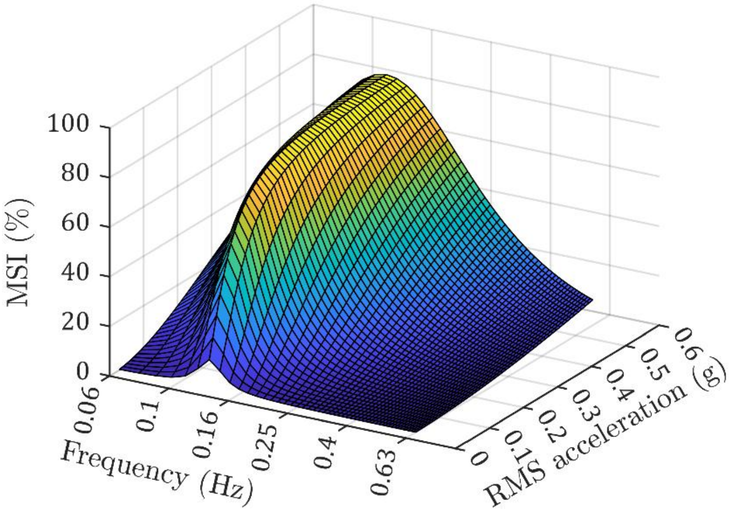

Figure 2.6: Motion Sickness Incidence as a function of frequency and RMS of the acceleration.

In 2001, Braccesi and Cianetti [62] proposed a two-dimensional extension of the model presented in [60], which accounts for both vertical and lateral accelerations. The authors also analysed the predicted outcomes for tilting trains, emphasising that the empirical approach outlined in [46] does not provide reliable predictions for MSI. In 2011, the authors further extended the model by proposing: i) a 3D version based solely on vestibular stimuli, using linear accelerations in the x, y, and z directions as inputs, and ii) a model that accounts for the contribution of the visual system to motion perception, as well as its role in generating inter-sensory conflict, which had not yet been formalised in MS prediction models [63]. However, they were not the only ones investigating the interactions between the vestibular and visual systems. Back in 2001, Telban and Cardullo developed a model of human motion perception that integrates mathematical models for both vestibular and visual motion sensations, incorporating non-linear interactions between these stimuli [64]. The model also accounts for visually induced self-motion, known as vection. Subsequent work focused on visual-vestibular interactions, as described in [65], where the authors explore this phenomenon and highlight key vestibular concepts fundamental to understanding MS. Building on Bos's SVC model, [66] developed a three-dimensional nerve system model, i.e. the 3D-SVC, to estimate MS. Further advancements are found in [24], [67], where the Subjective-Vertical-Horizontal-Conflict model accounts for horizontal conflict in a manner similar to vertical conflict. The authors claim that this model outperforms those based solely on the SVC. In 2013, Wada et al. [68] proposed a mathematical model to calculate MSI with 6 Degrees of Freedom (DoF), including head rotation, which can be seen as an extension of the 3D-SVC. This model is based on neurophysiological knowledge of the vestibular system but initially neglected the contribution of the visual system, which was later incorporated in [69]. The schematic of the model, which is nowadays one of the most prominent and used to predict MSI, is shown in Figure 2.7.

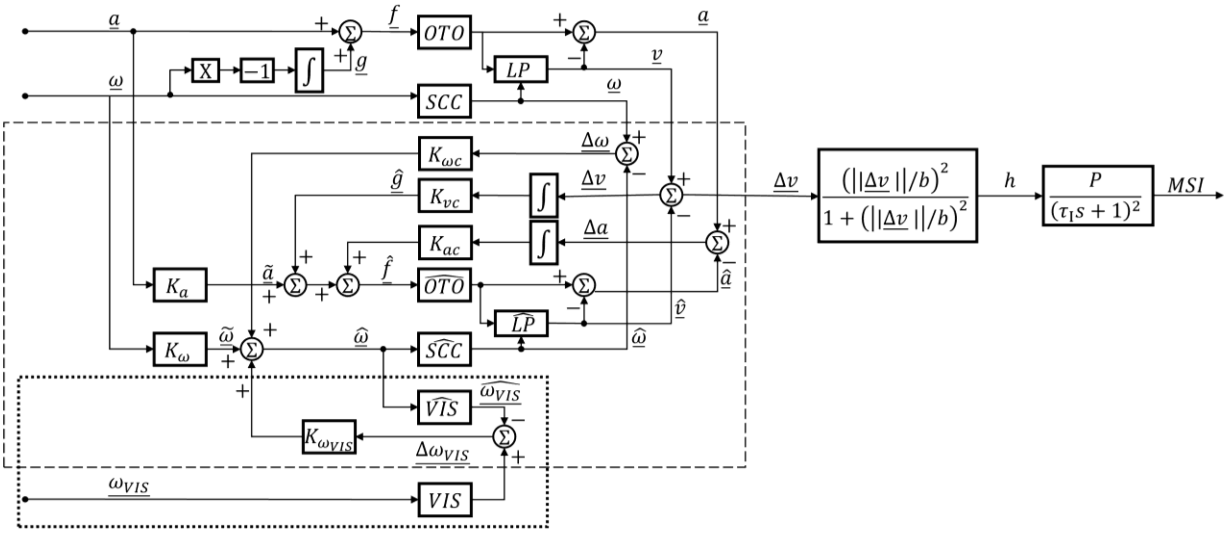

Figure 2.7: 6DoF-Model including visual system interaction proposed in [69].

where the dashed line identifies the internal model, the dotted line highlights the contribution of the visual system, and the terms with K are scaling factors. It is important to note that, according to the optimal estimation theory, the transfer function for the vestibular systems, i.e. the otholiths (OTO), the semi-circular canals (SCC), and the visual system (VIS), along with the low-pass filter (LP) defined in the sensory part, are identical for the internal model. A more recent model, the Visual-Vestibular Motion Sickness

(VVMS) model, is described in [70]. The VVMS model integrates vestibular sensory dynamics, visual motion perception, and visual-vestibular cue conflict to determine the discrepancy between the sensed and true vertical orientation of the passenger. With the aim of offering a comprehensive comparison to help identify gaps in existing models and guide future research, table X provides a summary of various MS models, categorised by the different theories found in the literature. It highlights the causes of MS identified by the respective authors, the sensory systems considered, the type of model used, as well as its inputs, outputs, and key assumptions. Additionally, the table outlines each model's novelties and limitations.

Table 2.1 – Overview of the main models presented in literature to understand the phenomenon of motion sickness

THEORY	FIRST AUTHOR	YEAR	MS CAUSE(S)	SENSORY SYSTEM(S)	TYPE OF MODEL	MODEL INPUT I AND OUTPUT O	ASSUMPTION(S) A, NOVELTY(IES) N AND LACK(S) L
I	O'Hanlon J.	1974	Sinusoidal motion	Vestibular	Mathematical Human Factor Research Model	I1. Mean values of the logarithmic acceleration threshold I2. Standard deviation of the logarithmic acceleration threshold O1. MSI	A1. Conditions of sinusoidal motion: frequency range from 0.083 Hz to 0.500 Hz and average acceleration over the cycle from about 0.03 g to 0.4 g N1. Experimental data of subjects exposed to vertical sinusoidal motion N2. Mathematical model to evaluate the MSI L1. The mathematical model does not consider the influence of the visual system on the generation of the sickness feeling L2. The mathematical model does not consider the influence of the rotational speeds on the generation of the sickness
	McCauley M.	1976	Sinusoidal motion	Vestibular	Mathematical Human Factor Research Model	I1. Mean values of the logarithmic acceleration threshold I2. Standard deviation of the logarithmic acceleration threshold O1. MSI	A1. Conditions of *Study III*: frequency range from 0.500 Hz to 0.700 Hz and average acceleration over the cycle of 0.44 g and 0.55 g N1. Investigation of frequencies of oscillation above 0.500 Hz confirms the MSI decreasing as a function of frequency for all frequencies greater than ~0.160 Hz L1. The mathematical model does not consider the influence of the visual system on the generation of the sickness feeling L2. The mathematical model does not consider the influence of the rotational speeds on the generation of the sickness feeling

THEORY	FIRST AUTHOR	YEAR	MS CAUSE(S)	SENSORY SYSTEM(S)	TYPE OF MODEL	MODEL INPUT (I) AND OUTPUT (O)	ASSUMPTION(S) A, NOVELTY(IES) N AND LACK(S) L
SENSORY REARRANGEMENT	Reason J. T.	1978	Neural Mismatch	Visual and Vestibular	Neural Mismatch Model	I1. Sensory inputs from eyes, semi-circular canals and otolith O1. Motion sickness feeling O2. Allied disturbances	A1. The mismatch signal increases as a function of the discrepancy present in any sensory channel A2. The mismatch signal increases with the number of discrepant sensory channels contributes to the sensory rearrangement A3. The mismatch signal is inversely proportional to the degree of consolidation of the reafferent trace combination N1. The model considers the visual and vestibular system's influence L1. No index used to assess the sickness feelingNo index used to assess the sickness feeling
SENSORY CONFLICT	Oman C. M.	1982	Sensory Conflict	Visual and Vestibular	Heuristic Mathematical Model	I1. Sensed motion by semi-circular canals and otolith O1. Subjective Discomfort	A1. Mathematical model based on the sensory conflict theory A2. Use of an "internal model" as an "observer" N1. First mathematical formulation for the sensory conflict theory L1. No index used to assess the sickness feeling
	Oman C. M.	1989	Sensory Conflict	Visual and Vestibular	Heuristic Mathematical Model	I1. Sensed motion by semi-circular canals and otolith O1. Subjective Discomfort	A1. Mathematical model based on the sensory conflict theory A2. Use of an "internal model" as an "observer" N1. Review of the stimuli that cause motion sickness N2. Synthetisation of a contemporary observer theory view of the Sensory Conflict hypothesis N3. Revised model for the dynamic coupling between the putative conflict signals and nausea magnitude estimation L1. No index used to assess the sickness feeling

THEORY	FIRST AUTHOR	YEAR	MS CAUSE(S)	SENSORY SYSTEM(S)	TYPE OF MODEL	MODEL INPUT (I) AND OUTPUT (O)	ASSUMPTION(S) A, NOVELTY(IES) N AND LACK(S) L
SUBJECTIVE VERTICAL CONFLICT	Bles W.	1998	Vertical Conflict	Visual and Vestibular	Sunjective Vertical Conflict Model	I1. Vertical acceleration sensed by the vestibular system I2. Angular velocity O1. Motion Sickness Conflict O2. Measured Subjective Vertical	A1. Explicit knowledge of the vestibular system N1. Restatement of the sensory rearrangement theory N2. Extension of the model proposed in [59] with the necessary modules to compute the subjective vertical N3. The motion sickness is now due to the conflict between the sensed vertical and the subjective vertical L1. Longitudinal and lateral accelerations are not considered
	Bos J. E.	1998	Vertical Conflict	Visual and Vestibular	Sunjective Vertical Conflict Model	I1. Actual head vertical acceleration O1. MSI	A1. Explicit knowledge of the vestibular system A2. Optimal estimation theory: the internal model has the same transfer functions as the real system N1. Introduction of the Hill Function and a cumulative function in the block diagram to transform the subjective vertical conflict into MSI L1. The rotations are not considered L2. Longitudinal and lateral accelerations are not considered L3. The influence of the visual system is not considered
	Bos J. E.	2001	Vertical Conflict	Visual and Vestibular	Sunjective Vertical Conflict Model	I1. Vertical acceleration sensed by the vestibular system I2. Angular velocity O1. Motion Sickness Conflict O2. Measured Subjective Vertical	A1. Explicit knowledge of the vestibular system N2. Description of visual-vestibular interactions regarding motion and attitude perception L1. Longitudinal and lateral accelerations are not considered

THEORY	FIRST AUTHOR	YEAR	MS CAUSE(S)	SENSORY SYSTEM(S)	TYPE OF MODEL	MODEL INPUT (I) AND OUTPUT (O)	ASSUMPTION(S) A, NOVELTY(IES) N AND LACK(S) L
SUBJECTIVE VERTICAL CONFLICT	Bos J. E.	2007	Vertical Conflict	Visual and Vestibular	Subjective Vertical Conflict Model	I1. Vertical acceleration sensed by the vestibular system I2. Angular velocity O1. Motion Sickness O2. Measured Subjective Vertical O3. Eye movement	A1. Explicit knowledge of the vestibular system N1. Description of visual-vestibular interactions as these occur when viewing images N2. Framework including visual-vestibular interactions L1. Longitudinal and lateral accelerations are not considered
	Wada T.	2020	Vertical Conflict	Visual and Vestibular	Subjective Vertical Conflict Model	I1. Acceleration and angular velocity of the head I2. Visual perception of the angular velocity O1. MSI	A1. Explicit knowledge of the vestibular system A2. Explicit knowledge of the visual system A3. Visual perception process is assumed to be a unit matrix N1. Visual system included in the internal model of the CNS L1. Longitudinal and lateral accelerations are not considered
	Jalgaonkar N.	2021	Vertical Conflict	Visual and Vestibular	Subjective Vertical Conflict Model	I1. Head acelerations and angular velocities along x, yand z as perceived by vestibular and visual systems O1. MSI	A1. Explicit knowledge of the vestibular system A2. The visual system can only estimate the angular velocities A3. The visual and vestibular reference frames are collocated and co-aligned at the midpoint of the line connecting the two ears N1. Sensitivity analysis on the tunable gain parameters L1. Longitudinal and lateral accelerations are not considered

Theory	First Author	Year	MS Cause(s)	Sensory System(s)	Type of Model	Model Input (I) and Output (O)	Assumption(s) A, Novelty(ies) N and Lack(s) L
Subjective Vertical – Horizontal Conflict	Braccesi C.	2001	Vertical-Horizontal Conflict	Vestibular	Subjective Vertical-Horizontal Conflict Model	I1. Vertical acceleration sensed by the vestibular system I2. Angular velocity O1. MSI	A1. Explicit knowledge of the vestibular system Parameters of the horizontal component based on [27], [35] N1. Horizontal acceleration is considered in the model L1. Visual system not considered
	Kamiji N.	2007	Vertical-Horizontal Conflict	Vestibular	Subjective Vertical-Horizontal Conflict Model	I1. Actual head accelerations (x, y, z) and angular velocities (x, y, z) as perceived by the vestibular system O1. MSI	A1. Otolith organ, and its respective in the internal model, are assumed as unit matrices from the otolith dynamic response characteristic Distinct transfer function for semi-circular canals in the internal model A2. Occupant's head is a three links straight-chain structure N1. Developed a 3D-SVC model capable to deal with the accelerations and angular velocity in all directions L1. Visual system not considered
	Khalid H.	2011	Vertical-Horizontal Conflict	Vestibular	Subjective Vertical-Horizontal Conflict Model	I1. Actual head accelerations (x, y, z) and angular velocities (x, y, z) as perceived by the vestibular system O1. $MSI_{tot} = \sqrt{MSI_v^2 + MSI_h^2}$	A1. Explicit knowledge of the vestibular system A2. CNS carries imprints of all human sensory systems and can predict their typical outputs N1. Horizontal acceleration is considered in the model L1. Visual system not considered

THEORY	FIRST AUTHOR	YEAR	MS CAUSE(S)	SENSORY SYSTEM(S)	TYPE OF MODEL	MODEL INPUT (I) AND OUTPUT (O)	ASSUMPTION(S) A, NOVELTY(IES) N AND LACK(S) L
SUBJECTIVE VERTICAL – HORIZONTAL CONFLICT	Khalid H.	2011	Vertical-Horizontal Conflict	Vestibular	Subjective Vertical-Horizontal Conflict Model	I1. Actual head accelerations (x, y, z) and angular velocities (x, y, z) as perceived by the vestibular system O1. $MSI_{tot} = \sqrt{MSI_v^2 + MSI_h^2}$	A1. Explicit knowledge of the vestibular system A2. CNS carries imprints of all human sensory systems and can predict their typical outputs N1. Horizontal acceleration is considered in the model L1. Visual system not considered
SUBJECTIVE VERTICAL – HORIZONTAL–LONGITUDINAL CONFLICT	Braccesi C.	2011	Vertical-Horizontal-Longitudinal Conflict	Visual and Vestibular	Subjective Vertical-Horizontal-Longitudinal Conflict Model	I1. Actual head accelerations (x, y, z) and angular velocities (x, y, z) as perceived by the vestibular system I2. Actual head accelerations (x, y, z) as perceived by the visual system O1. MSI	A1. Explicit knowledge of the vestibular system Interaction between vestibular and visual perceived accelerations assumed based on [Telban2001] and modified N1. All directions (x, y, z) are considered N2. Inclusion of the visual system into the prediction model

2.4 STATE-OF-THE-ART OF MITIGATION METHODS

So far, this chapter has introduced the phenomenon of MS, reviewed the prominent theories that explain its causes, and outlined various methods used to estimate its occurrence and severity. While understanding the underlying mechanisms and prediction methods is essential, it is equally important to explore strategies for mitigating MS, especially given its impact on comfort and performance in various environments, such as transportation, virtual reality, and autonomous systems. In the following section, the approaches developed to reduce or prevent MS are examined. In literature, several solutions are proposed to mitigate MS, which can be categorised into three main groups: i) behavioural practices, consisting of recommendations that passengers can follow; ii) medical and supplementary solutions, including wearable devices; iii) technological solutions, encompassing vehicle design considerations, use of feedback devices, as well as planning and control strategies. Behavioural practices are a simple yet effective approach to mitigating MS by minimising sensory conflicts and discomfort during travel. Passengers are advised to focus on stable visual references, such as the horizon, and to sit in areas with less motion, such as the front seat of a vehicle, to reduce the effects of conflicting sensory inputs. Activities that require close visual focus, like reading or using screens, should be avoided as they can intensify symptoms. Taking regular breaks, practising controlled breathing, and ensuring proper ventilation are also useful strategies. Additionally, maintaining light meals and avoiding alcohol before travel can help prevent nausea. These practices, although easy to implement, play a significant role in improving passenger comfort during motion exposure. While behavioural practices can be effective in mitigating MS for many individuals, they may not work for everyone. As a result, some people turn to medical and supplementary solutions or wearable devices to manage their symptoms more effectively. Medical and supplementary solutions include a range of remedies designed to prevent or alleviate the symptoms of MS. Common medications, such as antihistamines, are widely used to reduce nausea and dizziness by blocking signals from the vestibular system. In addition to medications, wearable devices like acupressure wristbands and specialised goggles with moving fluid are designed to help stabilise the sensory input and reduce the mismatch between visual and vestibular signals. These wristbands apply pressure to specific points on the wrist, believed to ease nausea, while the fluid-filled goggles create an artificial horizon, helping the brain process motion more accurately. Together, these medical and supplementary solutions offer an alternative for individuals who do not find relief through behavioural practices alone. Nevertheless, while many individuals rely on behavioural practices, medical solutions, including wearable devices, or a combination of these methods to find relief from MS, their effectiveness can vary significantly among users. This variability underscores the necessity for ongoing research and innovation in technological solutions aimed at enhancing overall comfort and reducing the incidence of MS. In this regard, in [4], the authors describe all the passenger side effects of riding an autonomous vehicle, with the associated research solutions proposed in the literature until 2015. The authors emphasise how MS can be mitigated by using device-vehicle interface (DVI) feedback systems, redesigning certain components of the vehicle, or by employing a smooth lateral control coupled with the generation of continuous curvature paths. These approaches aim to minimise abrupt changes in motion and enhance passenger comfort by reducing sensory conflicts during travel. DVI solutions aim at letting the passenger know what the next manoeuvre will be, thus reducing the sense of loss of controllability [71]. This approach involves the use of VR systems to align the visual path with the actual travel path, as drivers typically rely on specific visual references on the road to match its curvature. In this context, Cho et al. [72] conducted an experiment comparing sickness levels before and after implementing three different scenarios while riding in a car and using VR: i) the default scenario, where VR content is displayed without modification; ii) the transparent wall scenario where both the VR content and its background adjust in response to the car's motion; and iii) the particle flow scenario, in which the estimated motion flow of the car is visualised as moving particles that blend with the VR content. The results indicate that both scenarios ii) and iii) consistently reduce MS, although not to a negligible level. Regarding vehicle design considerations, several solutions have been proposed, such as those outlined in [73], where the authors suggest using Occipital Bone Support (OBS) to stabilise the head and minimise excessive low-frequency accelerations. Additionally, emerging research trends are exploring the development of pre-emptive active seats that can tilt passengers in response to vehicle manoeuvres, aiming to reduce the sensation of MS [74]. While others propose vibrating seats, cueing the passenger into the upcoming manoeuvre [75]. These innovations focus on directly mitigating the physical causes of sensory conflict during travel. Other mitigation strategies involve optimising trajectory planning to generate smoother paths, as proposed in [76], using continuous curvature path-planning methods, as explored in [77], [78], or including jerk minimisation within the path-planning problem as suggested in [79]. These approaches aim to reduce abrupt lateral accelerations and jerky motions, which can exacerbate MS, by ensuring smoother transitions and more predictable vehicle movements. However, based on the studies presented in [26]–[29], to effectively address MS, the solution must be sought somewhere else within the software architecture of AVs. This suggests that simply modifying vehicle design or applying control strategies may not be sufficient, and more advanced approaches, such as rethinking the interaction between vehicle dynamics and passenger comfort systems, may be required to significantly reduce MS in autonomous transport systems. Motion planning, among the various countermeasures, is the best candidate to mitigate MS with its capability to control the accelerations and their frequencies. In [80], the authors proposed a motion planning strategy aimed at optimising MS feeling by minimising the IR for both longitudinal and lateral accelerations, while also considering journey time. Building on this, in [81], the same authors further explored the fundamentals of motion planning to minimise MS. In the study, a Pareto front is introduced, illustrating the trade-off between travel time and MS, highlighting the conflicting relationship between the two: longer travel times result in lower MS, whereas shorter travel times lead to increased susceptibility to MS. Li et al. [82]

proposed a novel approach to addressing motion sickness (MS) by focusing on motion planning rather than motion control. Their strategy incorporates a frequency-shaping approach that targets the most provocative frequencies associated with MS. Similarly, in [83], the authors developed a motion planning strategy in which speed profiles are optimised by minimising accelerations, leading to a reduction in the MSDV. Another method is presented by [84], where trajectory and velocity planning are used to adjust AV paths, mitigating the negative effects of bumpy roads on passenger comfort by keeping the weighted RMS of acceleration below a predefined threshold of 0.315 m/s^2. In [85], a trajectory planning algorithm is proposed that calculates paths based on predefined waypoints describing a global map. Each candidate path is paired with a velocity profile and evaluated against several criteria, including passenger comfort—measured by the peak value of lateral acceleration – as well as obstacle avoidance and overall trajectory tracking. While these studies offer various ways to mitigate MS, none incorporate the most advanced MS models, such as those discussed in earlier sections, for predicting the MSI – one of the most reliable metrics for evaluating passenger discomfort. A small step in this direction is taken in [86], where the authors conducted two studies on real-world autonomous driving conditions and measured induced MS in passengers. They used the 6DoF-SVC model to predict MSI, but found that the model, in its current form, was not fully reliable. By optimising the parameters of the model, they improved its accuracy for the specific experiments conducted. A more recent and advanced approach is presented in [87], where the authors developed an optimisation-based motion planning strategy to mitigate MS by using frequency-weighted filtered accelerations within a receding horizon framework. Results demonstrated a reduction of frequency-weighted accelerations by 11.3 % compared to methods that did not consider frequency sensitivity. Additionally, experiments on human drivers in real-world conditions showed a 19 % improvement in overall acceleration comfort and a 32 % reduction in squared MSDV, highlighting the potential benefits of implementing this algorithm in real transportation systems. In conclusion, numerous strategies have been explored to mitigate MS, ranging from behavioural practices and medical solutions to vehicle design modifications and control strategies. Among these, motion planning has emerged as the most promising approach due to its ability to manage accelerations and their frequencies, directly addressing the core causes of MS. By optimising trajectory smoothness and minimising the most provocative motion frequencies, motion planning offers a targeted, proactive solution that holds great potential for enhancing passenger comfort, especially in AVs.

2.5 CONCLUDING REMARKS

Motion sickness (MS) remains a multifaceted issue, driven by an interplay of sensory, cognitive, and environmental factors. Theories such as the sensory conflict theory, postural instability theory, and subjective vertical mismatch theory have each contributed essential perspectives, though no single framework fully explains the wide range of symptoms or their varying intensity among individuals. This underscores the complexity of the phenomenon, suggesting that future advancements in understanding MS will likely depend on an integration of these theoretical models. Equally challenging is the task of measuring MS, as estimation methods range from subjective scales – such as self-reported questionnaires and symptom scales – to objective approaches like monitoring physiological responses, including heart rate variability and galvanic skin responses. Although these methods provide insight into the severity and onset of MS, variability in individual responses and experimental conditions can make it difficult to apply them universally, highlighting the need for more robust and comprehensive metrics. When it comes to mitigation, the state of the art reflects a broad spectrum of strategies. Behavioural practices, including habituation techniques and controlled exposure, remain valuable for certain contexts but are often limited by their reliance on long-term adaptation. On the medical front, pharmacological interventions such as antihistamines and anticholinergics offer immediate relief but may come with side effects that limit their use, especially in situations requiring cognitive alertness. Meanwhile, non-invasive wearable devices that use techniques such as galvanic vestibular stimulation are gaining traction as supplementary solutions with minimal side effects. However, the most promising area of development lies in technological interventions. Advances in vehicle design, particularly the optimisation of motion cues and the reduction of sensory conflicts through intelligent motion planning and control strategies present an innovative approach to mitigating MS. These technological innovations not only address the root causes of sensory conflict but also pave the way for more comfortable and efficient transportation systems, especially in the era of automated vehicles. In summary, while significant strides have been made in understanding and addressing MS, it remains a field ripe for further research and innovation. The growing intersection of behavioural science, medicine, and technology holds promise for future solutions that could one day make MS outdated. Through continued interdisciplinary collaboration and technological advancements, it is conceivable that MS, once seen as an inevitable consequence of motion, will become a manageable and, in many cases, preventable issue.

BIBLIOGRAPHY

[1]Zhang, X. & Steinbach, R. (2024). American Driving Survey: 2023 (Research Brief). Washington, D.C.: AAA Foundation for Traffic Safety.

[2]M. Sivak, M. and B. Schoettle, “Motion Sickness in Self-Driving Vehicles,” University of Michigan, Ann Arbor, *Transportation Research Institute*, Tech. Rep. 2015.

[3]M. Sivak, M. and B. Schoettle, “Would Self-driving Vehicles Increase Occupant Productivity?,” p. 11, 2016.

[4]M. Elbanhawi, M. Simic, and R. Jazar, “In the passenger seat: Investigating ride comfort measures in autonomous cars,” *IEEE Intell. Transp. Syst. Mag.,* vol. 7, no. 3, pp. 4-17, 2015.

[5]J. R. Lackner, “Motion Sickness: More than Nausea and Vomiting,” Exp. Brain Res. 232(8):2493-2510, 2014.

[6]A. Graybiel, “Susceptibility to Acute Motion Sickness in Blind Persons,” *Aerosp. Med.* vol. 41, no 6, pp. 650-653, 1970.

[7]W. H. Johnson, F.A. Sunahara, and J.P. Landolt, “Importance of the Vestibular System in Visually Induced Nausea and Self-Vection,” *J. Vestib. Res. Equilib. Orientat.* Vol. 9, no. 2, pp. 83-87, 1999

[8]M. Dai, T. Raphan, B. and Cohen, “Labyrinthine Lesions and Motion Sickness Susceptibility,” *Exp. Brain Res.* vol 178, no. 4, pp. 477-487, 2007

[9]M. Bronstein, J. F. Golding, and M. A. Gresty, "Vertigo and Dizziness from Environmental Motion: Visual Vertigo, Motion Sickness, and Drivers' Disorientation," *Semin. Neurol.*, vol. 33, pp. 219–230, 2013.

[10]C. Diels “Will autonomous vehicles make us sick?,” in *Contemporary Ergonomics and Human Factors 2014*, pp. 301-307, 2014.

[11]C. Diels and J.E. Bos, “Self-Driving Carsickness,” *Appl. Ergon.*, vol 53, pp: 374-382, 2016.

[12]J. A. Irwin, “The Pathology of Sea-Sickness,” *The Lancet*, vol. 118, no. 3039, pp.907-909, 1881.

[13]C. M. Beadnell, “The Psychology of Sea-Sickness,” *The Lancet*, vol. 203, no. 5260, p.1289, 1924.

[14]C. A. Claremont, “The Psychology of Sea-Sickness,” Psyche (Stuttg.) 11:86-90, 1931.

[15]J. Hill, “The Care of The Sea-Sick,” *Br Med. J.*, vol. 2, no. 3955, pp. 802-807, 1936.

[16]J. T. Reason and J.J. Brand, “Motion Sickness,” *Academic* Press, Oxford, England 1975.

[17]G. E. Riccio and T. A. Stoffregen, “An ecological theory of motion sickness and postural instability,” Ecological psychology, vol. 3, no. 3, pp. 195–240, 1991.

[18]L. A Warwick-Evans, N. Symons, T. Fitch, L. and Burrows, “Evaluating Sensory Conflict and Postural Instability. Theories of Motion Sickness,” *Brain Res. Bull.* vol. 47, no. 5, pp. 465–469, 1998.

[19]J. E. Bos and W. Bles, “Modelling motion sickness and subjective vertical mismatch detailed for vertical motions,” *Brain Res. Bull.,* vol. 47, no. 5, pp. 537-542, 1998.

[20]A. Berthoz, B. Pavard and L.R. Young, “Perception of Linear Horizontal Self-Motion Induced by Peripheral Vision (Linear vection) Basic Characteristics and Visual-Vestibular Interactions,” *Exp. Brain Res.* vol. 23, no. 5, 1975.

[21]J. E. Bos and W. Bles, “Modeling human spatial orientation and motion perception,” *AIAA Modeling and Simulation Technologies Conference and Exhibit,* 2001.

[22]J. E. Bos, W. Bles, E.L. and Groen, “A Theory on Visually Induced Motion Sickness,” *Displays* vol. 29, no. 2, pp. 47-57, 2007.

[23]S. A. E. Nooij, P. Pretto, D. Oberfeld, H. Hecht and H.H. Bülthoff, “Vection Is the Main Contributor to Motion Sickness Induced by Visual Yaw Rotation: Implications for Conflict and Eye Movement Theories,” *PLOS ONE*, vol.12, no. 4 pp. e0175305, 2017.

[24]H. Khalid, O. Turan and J. E. Bos, “Theory of a subjective vertical-horizontal conflict physiological motion sickness model for contemporary ships,” *Journal of Marine Sci. and Tech.*, vol. 16, 2011.

[25]C. Braccesi and F. Cianetti, “Motion Sickness. Part I: development of a model for predicting motion sickness incidence,” *International Journal of Human Factors Modelling and Simulation*, vol. 2, no. 3, pp. 163-187, 2011.

[26]M. Turner and M. J. Griffin, "Motion sickness in public road transport: the effect of driver, route and vehicle," *Ergonomics*, vol. 42, pp. 1646-1664, 1999.

[27]J. F. Golding, M.I. Finch and J.R. Stott, “Frequency effect of 0.35-1.0 Hz horizontal translational oscillation on motion sickness and the somatogravic illusion,” *Aviation Space & Environmental Medicine*, vol.68, no. 5, pp:396-402, 1997.

[28]J. F. Golding, A. Mueller, and M. A. Gresty, “A motion sickness maximum around the 0.2 hz frequency range of horizontal translational oscillation,” *Aviation, space, and environmental medicine*, vol. 72, no. 3, pp. 188–192, 2001.

[29]B. E. Donohew and M. J. Griffin, “Motion sickness: effect of the frequency of lateral oscillation,” *Aviation, space, and environmental medicine*, vol. 75, no. 8, pp. 649–656, 2004.

[30]J. E. Bos, and W. Bles, “Theoretical Considerations on Canal-Otolith Interaction and an Observer Model,” *Biol. Cybern.* vol. 86, no. 3, pp. 191-207, 2002.

[31]S. M. Ebenholtz, “Motion Sickness and Oculomotor Systems in Virtual Environments,” *Presence Teleoperators Virtual Environ.* vol. 1, no. 3, pp. 302-305, 1992.

[32]B. Cohen, M. Dai, and T. Raphan, “The Critical Role of Velocity Storage in Production of Motion Sickness,” *Ann. N. Y. Acad. Sci.* vol. 1004, no. 1, pp. 359-376, 2003.

[33]B. Cohen, M. Dai, S.B. Yakushin, and C. Cho, “The Neural Basis of Motion Sickness,” *J.* Neurophysiol. vol. 121, no. 3, pp. 973-982, 2019.

[34]J. T. Reason, “Motion Sickness Adaptation: A Neural Mismatch Model,” *J. R. Soc. Med.* vol. 71, no. 11, pp. 819-829, 1978.

[35]J. F. Golding, “Motion sickness susceptibility questionnaire revised and its relationship to others form of sickness,” *Brain. Res. Bull.*, vol. 47, no. 5, pp: 507-516, 1998.

[36]J. F. Golding, “Predicting individual differences in motion sickness susceptibility by questionnaire,” *Personality and Individual Differences*, vol 41, no. 2, pp. 237-248, 2006.

[37]R. S. Kennedy, N. E. Lane, K. S. Berbaum and M. G. Lilienthal, “Simulator sickness questionnaire: an enhanced method for quantifying simulator sickness,” *International Journal of Aviation and Psychology*, vol. 3, pp. 203-220, 1993.

[38]H. K. Kim, J. Park, Y. Choi and M. Choe, “Virtual reality sickness questionnaire (VRSQ): motion sickness measurement index in a virtual reality environment,” *Applied Ergonomics*, vol 69, pp. 66-73, 2018.

[39] B. Keshavarz and H. Hecht, “Validating an Efficient Method to Quantify Motion Sickness,” *Human Factors*, vol. 53, no. 4, pp. 415-426, 2011.

[40]E. Ugur, B.O. Konukseven, M. Topdag, M. E. Cakmakci and D. O. Topdag, “Expansion to the Motion Sickness Susceptibility Questionnaire-Short Form: A Cross-Sectional Study,” *J Audiol Otol.*, vol. 26, no. 2, pp. 76-82, 2022.

[41]E. R. Muth, R. M. Stern, J. F. Thayer and K. L. Koch, “Assessment of the multiple dimensions of nausea: The Nausea Profile (NP),” *Journal of Psychosomatic Research*, vol. 40, no. 5, pp. 511–520, 1996.

[42]P. Gianaros, E. Muth, J. Mordkoff, M. Levine and R. Stern, “A Questionnaire for the Assessment of the Multiple Dimensions of Motion Sickness,” *Aviation, space, and environmental medicine*, vol. 72, pp. 115-119, (2001).

[43]E. F. Miller and A. Graybiel, “A provocative test for grading susceptibility to motion sickness yielding a single numerical score,” *Acta Otolaryngol Suppl.*, vol. 274, pp. 1-20, 1970.

[44]B. Correia Grácio, M. Wentink, J. Bos, M. Van Paassen and M. Mulder, “An Application of the Canal-Otolith Interaction Model for Tilt-Coordination During a Braking Maneuver,” *AIAA Modeling and Simulation Technologies Conference 2012,* 2012.

[45]B. Keshavarz, B. Murovec, N. Mohanathas and J. F. Golding, “The Visually Induced Motion Sickness Susceptibility Questionnaire (VIMSSQ): Estimating Individual Susceptibility to Motion Sickness-Like Symptoms When Using Visual Devices,” *Human Factors: The Journal of the Human Factors and Ergonomics Society*, (2021).

[46]*Mechanical Vibration and Shock – Evaluation of Human Exposure to Whole-Body Vibration – Part 1: General Requirements*, ISO 2631-1, International Organisation for Standardisation, Geneve, 1997.

[47]A. Lawther and M.J. Griffin, “The motion of a ship at sea and the consequent motion sickness amongst passengers,” *Ergonomics*, vol. 29, no. 4, pp.535-552, 1986.

[48]A. Lawther and M.J. Griffin, “Prediction of the incidence of motion sickness from the magnitude frequency, and duration of vertical oscillation,” *Journal of Acoustical Society of America*, vol. 82, pp. 957-966, 1987.

[49]A. Lawther and M.J. Griffin, “Motion sickness and motion characteristics of vessels at sea,” *Ergonomics*, vol. 31, no.10, pp.1373-1394, 1988.

[50]J. F. O’Hanlon, and M.E. McCauley, “Motion Sickness Incidence as a Function of the Frequency and Acceleration of Vertical Sinusoidal Motion,” *Aerosp. MED*, vol. 45, no. 4, pp. 366-369, 1974.

[51]M. E. McCauley, J. W. Royal, C. D. Wylie, J. F. O’Hanlon, and R.R. Mackie, “Motion Sickness Incidence: Exploratory Studies of Habituation, Pitch and Roll, and the Refinement of a Mathematical Model,” *Fort Belvoir, VA: Defense Technical Information Center*, 1976.

[52]C. M. Oman, “A Heuristic Mathematical Model for the Dynamics of Sensory Conflict and Motion Sickness Hearing in Classical Musicians,” in *Acta Oto-Laryngologica*, vol. 94. pp. 4-44, 1982.

[53]E. von Holst, “Relations between the central Nervous System and the peripheral organs,” *The British Journal of Animal Behaviour*, vol. 2, no. 3, pp. 89-94, 1954.

[54]R. Held, "Exposure-history as a factor in maintaining stability of perception and coordination," T*he Journal of nervous and mental disease*, vol. 132, no. 1, pp. 26-32, 1961.

[55]R. Held and J. Bossom, "Neonatal deprivation and adult rearrangement: complementary techniques for analyzing plastic sensory-motor coordinations," *Journal of comparative and physiological Psychology*, vol. 54, no. 1, p. 33, 1961.

[56]A. Hein and R. Held, "A neural model for labile sensorimotor coordinations," *Proceedings of the Second Annual Bionics Symposium*, pp. 71-74, 1961.

[57]R. Held and J. Rekosh, "Motor-sensory feedback and the geometry of visual space," *Science*, vol. 141, no. 3582, pp. 722-723, 1963.

[58]L. R.Young, “On visual vestibular interaction,” *Proc. Fifth Symposium on the Role of Vestibular Organs in Space Exploration*, NASA SP-314, p. 205-210, 1970.

[59]C. M. Oman, “Sensory conflict in motion sickness: an observer theory approach,” *Pictorial communication in virtual and real environments*, 1989.

[60]J. E. Bos and W. Bles, “Modelling Motion Sickness and Subjective Vertical Mismatch Detailed for Vertical Motions,” in *Brain Res. Bull.*, vol. 47, pp. 537-542, 1998.

[61]W. Bles, J. E. Bos, B. de Graaf, E. Groen and A. H. Wertheim, “Motion sickness: only one provocative conflict?,” in *Brain Res. Bull.*, vol. 47, pp. 481-487, 1998.

[62]C. Braccesi and F. Cianetti, “Implementazione di un modello di valutazione della cinetosi in treni ad assetto variabile,” XXX Convegno Nazionale AIAS, 2001.

[63]C. Braccesi and F. Cianetti, “Motion sickness. Part II: experimental verification on the railways of a model for predicting motion sickness incidence,” *Int. J. Human Factors Modelling and Simulation*, vol. 2, no. 3, pp. 188-203, 2011.

[64]R. Telban and F. Cardullo, “An Integrated Model of Human Motion Perception with Visual-Vestibular Interaction,” *Proc. of the AIAA Modelling and Simulation Technologies Conference and Exhibit*, Montreal, Canada, 2001.

[65]J. E. Bos, W. Bles and R. Hosman, “Modelling human spatial orientation and motion perception,” *Proc. of the AIAA Modelling and Simulation Technologies Conference and Exhibit*, Montreal, Canada, 2001.

[66]N. Kamiji, Y. Kurata, T. Wada and S. Doi, “Modelling and validation of carsickness mechanism,” in *SICE Annual Conference 2007*, pp. 1138-1143, 2007.

[67]H. Khalid, O. Turan, J. E. Bos and A. Incecik, “Application of the subjective vertical-horizontal-conflict physiological motion sickness model to the fields trials of contemporary vessels,” *Elsevier - Ocean Engineering*, vol. 38, pp. 22-33, 2011.

[68]T. Wada, N. Kamiji and S. Doi, “A mathematical model of motion sickness in 6DOF motion and its application to vehicle passengers,” in *Int. Digital Human Modeling Symp.*, 2013.

[69]T. Wada, J. Kawano, Y. Okafuji, A. Takamatsu and M. Mitsuhiro, “A computational model of motion sickness considering visual and vestibular information,” in *2020 IEEE Int. Conf. on Syst., Man, and Cybern. (SMC)*, pp. 1758-1763, 2020.

[70]N. Jalgaonkar, D. S. Schulman, S. Ojha and S. Awtar, “A visual-vestibular model to predict motion sickness response in passengers of autonomous vehicles,” in *SAE Int. J. Adv. & Curr. Prac. in Mobility*, vol.3, pp. 2421-2432, 2021.

[71]M. Bloch, “Alleviating Motion Sickness through Presentations on Interior Panels of Autonomous Vehicles,” *Master Thesis Universiteit Twente, Enschede, The Netherlands*, 2018.

[72]H.-J. Cho and G. J. Kim, “RideVR: Reducing Sickness for In-Car Virtual Reality by Mixed-in Presentation of Motion Flow Information,” in *IEEE Access*, vol. 10, pp. 34003-34011, 2022.

[73]K. Kato, K. Suzuki and C. Honda, “Reduction of Carsickness using a Headrest with Support to Suppress Head Motion,” *in Proceedings of Comfort Congress 2021*, 2021.

[74]“Motion Sickness Mitigation in Autonomous Vehicles using Preemptive Control of Active Systems,” https://psdl.engin.umich.edu/preact.php

[75]D. Li and L. Chen L, “Mitigating motion sickness in automated vehicles with vibration cue system,” *Ergonomics*, vol. 65, no. 10, pp. 1313-1325, 2022.

[76]L. Labakhua, U. Nunes, R. Rodrigues and F. S. Leite, “Smooth trajectory planning for fully automated passengers vehicles: spline and clothoid based methods and its simulation,” in *Int. Conf. on Inform. in Control, Automat. And Robot.*, 2006.

[77]Y. Kwangjin and S. Sukkarieh, "An Analytical Continuous-Curvature Path-Smoothing Algorithm," *IEEE Trans. on Robot.*, vol. 26, pp. 561-568, 2010.

[78]M. Elbanhawi, M. Simic, and R. Jazar, "Continuous Path Smoothing for Car-Like Robots Using B-Spline Curves," *J. of Intell & Robotic Syst.*, pp. 1-34, 2015.

[79]F. Mohseni, J. Aslund, E. Frisk and L. Nielsen, “Fuel and Comfort Efficient Cooperative Control for Autonomous Vehicles,” *IEEE Intelligent Vehicles Symposium (IV)*, 2017.

[80]Z. Htike, G. Papaioannou, E. Velenis and S. Longo, “Motion planning of self-driving vehicles for motion sickness minimisation,” *2020 European Control Conference (ECC)*, pp. 1719-1724, 2020.

[81]Z. Htike, G. Papaioannou, E. Siampis, E. Velenis and S. Longo, “Fundamentals of motion planning for mitigating motion sickness in automated vehicles,” in *IEEE Transactions on Vehicular Technology*, vol. 71, no. 3, pp. 2375-2384, Mar. 2022

[82]D. Li and J. Hu, “Mitigating motion sickness in automated vehicles with frequency-shaping approach to motion planning,” in *IEEE Robotics and Automation Letters*, vol. 6, no. 4, pp. 7714-7720, Oct. 2021.

[83]N. A. Vroom, “Jerk based motion planning,” M.S. thesis, Dept. Mechanical, Maritime and Materials Engineering, Delft Univ. of Tech., Delft, NL, 2021. [Online]. Available: http://resolver.tudelft.nl/uuid:c167a041-b1be-493f-b389-d8dad0141a3b.

[84]S. Yan, C. Liu and J. Cao, “Comfort-based trajectory and velocity planning for automated vehicles considering road conditions,” in *Int. J. Automot. Technol.*, vol. 22, pp. 883-893, 2021.

[85]A. Said, R. Talj, C. Francis and H. Shraim, "Local trajectory planning for autonomous vehicle with static and dynamic obstacles avoidance," *2021 IEEE Int. Intell. Transp. Syst. Conf. (ITSC)*, pp. 410-416, 2021.

[86]B. Buccheit, E. N. Schneider, M. Alayan, F. Dauth and D. J. Strauss, “Motion Sickness Prediction in Self-Driving CarsUsing the 6DOF-SVC Model,” *IEEE Transactions on Intelligent Transportation Systems*, vol. 23, no. 8, pp. 13582-13591, 2022.

[87]Y. Zheng, B. Shyrokau and T. Keviczky, “Mitigating Motion Sickness with Optimization-based Motion Planning,” *arXiv :2301.07977v1,* 2023.

3

MOTION PLANNING

If you no longer go for a gap that exists, you are no longer a racing driver.

Ayrton Senna

3.1 STATE-OF-THE-ART

The rise of automated vehicles (AVs) signifies a new era in transportation, promising a transformative impact on how people travel. To achieve the complete transition from conventional vehicles to AVs, the focus on occupants' comfort becomes a pivotal area of exploration. The prospect of increased productivity and leisure during AV travel [1] is considered as one of the main reasons for the adoption of AVs by consumers [2]. However, occupants' engagement in non-driving-related tasks has proven to increase motion sickness (MS) due to increased conflicts between visual motion cues and vestibular stimuli. Meanwhile, AVs driving style is expected to be more aggressive increasing postural instability and head motion. Hence, an urgent need has risen to mitigate MS and enhance comfort in AVs to secure their acceptance, and their great potential. Current research efforts focus on understanding MS and developing countermeasures for its mitigation while being driven in AVs. MS has been attributed to multiple theories, yet none of them has been claimed to be definitive. Most of the studies relate MS to sensory conflict [3]–[5]; others associate it with postural instability [6]. The majority of the experimental research about sickness originates from sea studies highlighting vertical accelerations as the most provocative, which is also adopted by ISO-2631 [7] the international about evaluating human body vibrations. The standard considers the assessment of MS incidence levels as a function of the frequency-weighted vertical accelerations only. However, as far as the vehicle dynamics, longitudinal and lateral accelerations have proven to be the most provocative for MS [8]–[10], particularly in the range between 0.03 and 0.20 Hz [11], [12]. To that end, motion planning has been considered one of the main countermeasures for mitigating MS in AVs by minimising the low-frequency horizontal accelerations.

The motion planner layer in AVs determines the optimal trajectory and behaviour based on surroundings, being able to ensure a more comfortable ride experience. Previous research has proposed a method to produce smooth trajectories [13] or continuous curvature paths [14]. The former relies on the use of clothoid curves, which increase the computational effort required, whilst the latter is restricted to wheelchairs. Other works proposed to mitigate MS through motion planning by minimising jerk [15]. However, no MS metric was used neither as an objective for optimising the trajectory, nor for assessing the optimal trajectories. More recently, Htike et al. [16], [17] proposed a motion planning strategy that minimises the Illness Rating [9], [10] for longitudinal and lateral accelerations without compromising the journey time. As a drawback, these works relied on an oversimplified vehicle model, and the algorithm was developed in an offline optimisation software (GPOPs-II [18]) not providing real-time configurations. Later, a similar algorithm was implemented in real-time and tested with human-in-the-loop experiments, mitigating MS by even 40 % [19]. A more recent study focused on enhancing the accuracy of MS assessment within the control modules by proposing a frequency-shaping-based motion planning algorithm [20]. Nevertheless, the weighting was conducted using the corresponding filter for vertical accelerations proposed by ISO-2631:1991 [7], which has proven incompatible with the longitudinal and lateral accelerations [21], [22]. A further step in this direction is presented in [23], where a receding-horizon formulation is proposed for optimisation-based motion planning. In the same fashion as [20], a band-pass filter was designed to filter the accelerations. The effectiveness of the motion planning algorithm proved to surpass human driving, saving up to 70 % frequency-weighted acceleration energy. Despite the efforts to enhance the performance of the algorithms either by improving the MS assessment within the control modules or the performance of the motion planner, limited studies have considered body dynamics. Head motion significantly differs from vehicle motion and is proven to be a key determinant for the accumulation of MS. According to simulation studies [24], [25], neglecting a human body model leads to an overall underestimation of MS of ~65%. A more accurate model would be needed for a better prediction; as a drawback, it might increase the computational burden if all the degrees of motion are considered [26]. In this direction, [27] proposed a trajectory planning algorithm incorporating passive head tilting and the subjective vertical conflict (SVC) model. However, the vehicle model is a simple kinematic model and the human body model is oversimplified.

To this end, the contributions of this work are the following:

- Consideration of proper seat-to-head transfer functions within the optimal control problem [24];
- Use of appropriate frequency weightings [7], [21], [22] together with the seat-to-head weighting filters to account only for head longitudinal, lateral and rotational accelerations;
- Development of a real-time motion planning algorithms with non-linear model predictive control (NMPC) to mitigate MS and enhance postural stability.

The rest of the chapter is organised as follows. Section 3.2 introduces the simulation models in detail, including the formulation of the seat-to-head transfer function and the frequency weighting. Section 3.3 describes the motion planning algorithms, the optimal control problem and the testing scenarios chosen for assessing the algorithms. Section 3.4 shows the results with a detailed discussion of the achievement. Finally, Section 3.5 concludes the chapter by summarising this study’s findings and limitations and suggesting potential future research directions.

3.2 SIMULATION MODELS

3.2.1 VEHICLE MODEL

The NMPC prediction model is based on a nonlinear 3-degree-of-freedom (3DoF) front-wheel steering double-track formulation, neglecting wheel dynamics. The sign conventions of the main variables are in Figure 3.2.1, and its main parameters are reported in Table 3.2.1.

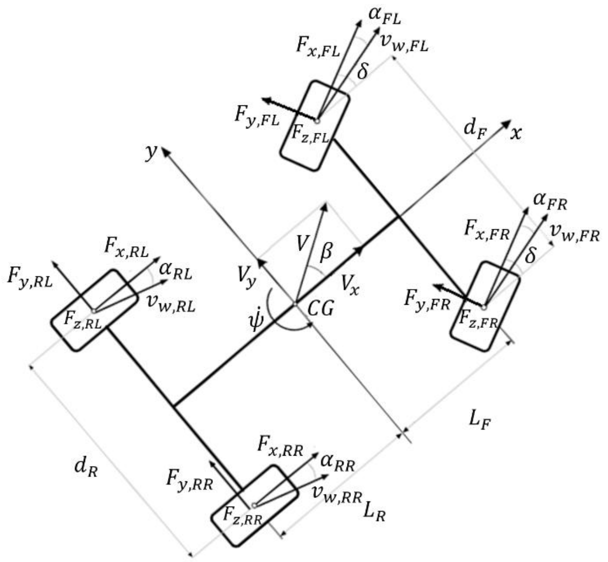

Figure 3.2.1: Top view of the vehicle, with indication of the main variables and their sign conventions.

Table 3.2.1 – Main vehicle parameters.

Symbol	Name and unit	Value
m	Mass [kg]	6800
J_z	Yaw mass moment of inertia [kgm^2]	12994.917
L_{TOT}	Wheelbase [m]	3.57
L_F	Front semi-wheelbase [m]	1.05
d_F	Front track width [m]	1.625
d_R	Rear track width [m]	1.625
H_{CG}	Height of the vehicle centre of mass [m]	0.55
$C_{y,F}$	Front axle cornering stiffness [kN/rad)	252.1
$C_{y,R}$	Rear axle cornering stiffness [kN/rad]	236.0
$F_{x,tot}^{TR,max}$	Maximum rear axle longitudinal traction force [kN]	10
$F_{x,tot}^{BR,max}$	Maximum rear axle longitudinal braking force [kN)	30

The model is described by the following differential equations:

- Longitudinal force balance

$$m\dot{V}_x = \left\{ \left[F_{x,FL} + F_{x,FR}\right]\cos(\delta) - \left[F_{y,FL} + F_{y,FR}\right]\sin(\delta) + \left[F_{x,RL} + F_{x,RR}\right] - \frac{1}{2}\rho V^2 S C_{drag} \right\} + mV_y\dot{\psi} \qquad (3.2.1)$$

where m is the vehicle mass; V_x and V_y are the longitudinal and lateral components of vehicle velocity; $\dot{\psi}$ is the yaw rate; $F_{x,ij}$ and $F_{y,ij}$ are the longitudinal and lateral tire forces;

ρ is air density in [kg/m^3]; S is the vehicle frontal area in [m^2]; and C_{drag} is the aerodynamic drag coefficient.

- Lateral force balance

$$m\dot{V}_y = \{[F_{x,FL} + F_{x,FR}]\sin(\delta) + [F_{y,FL} + F_{y,FR}]\cos(\delta) + [F_{y,RL} + F_{y,RR}]\} - mV_x\dot{\psi} \tag{3.2.2}$$

- Yaw moment balance

$$\begin{aligned} J_z\ddot{\psi} = {} & L_F\{[F_{y,FL} + F_{y,FR}]\cos(\delta) + [F_{x,FL} + F_{x,FR}]\sin(\delta)\} - L_R[F_{y,RL} + F_{y,RR}] \\ & + \frac{d_F}{2}\{[F_{y,FL} - F_{y,FR}]\sin(\delta) + [F_{x,FR} - F_{x,FL}]\cos(\delta)\} \\ & + \frac{d_R}{2}[F_{x,RR} + F_{x,RL}] \end{aligned} \tag{3.2.3}$$

where J_z is the vehicle yaw mass moment of inertia; L_F and L_R are the front and rear semi-wheelbases; and d_F and d_R are the front and rear track widths. The lateral tyre forces are modelled with the linear model through equations (3.2.1)–(3.2.3):

$$\mathrm{F}_{y,ij} = -C_{y,i}\alpha_{ij} \tag{3.2.4}$$

where C_{ij} is the tyre cornering stiffness on each corner; and α_{ij} is the tyre slip angle on each corner computed as follows:

$$\alpha_{ij} = \tan^{-1}\left(\frac{V_y + k_2\dot{\psi}L_i}{V_x + k_1\dot{\psi}\frac{d_i}{2}}\right) - k_3\delta \tag{3.2.5}$$

where k_1, k_2 and k_3 are defined based on the subscripts i and j:

$$\begin{aligned} j = L,R \quad & \begin{cases} k_1 = -1 & \text{if} \quad j = L \\ k_1 = 1 & \text{if} \quad j = R \end{cases} \\ i = F,R \quad & \begin{cases} k_2 = 1 & \text{if} \quad i = F \\ k_2 = -1 & \text{if} \quad i = R \end{cases} \\ i = F,L \quad & \begin{cases} k_3 = 1 & if \quad i = F \\ k_3 = 0 & if \quad i = R \end{cases} \end{aligned} \tag{3.2.6}$$

3.2.2 ROAD MODEL

A common approach in motion planning involves adding three more equations on top of (3.2.1)–(3.2.3), to account for the road's curvilinear coordinates:

$$\dot{S} = \frac{\dot{V}_x\cos(\alpha_s) - V_y\sin(\alpha_s)}{1 - S_n\kappa} \tag{3.2.7}$$

$$\dot{S}_n = V_x\sin(\alpha_s) + V_y\cos(\alpha_s) \tag{3.2.8}$$

$$\dot{\alpha}_s = \dot{\psi} - \dot{S}\kappa(S) \tag{3.2.9}$$

$$\alpha_s = \psi - \theta_R \tag{3.2.10}$$

where S is the travelled distance by the vehicle; S_n is the lateral deviation of the vehicle from the centre lane of the road; α_s is the deviation of the vehicle heading angle, i.e. ψ, from the road angle θ_R, see equation (3.2.10); $\kappa(S)$ is the road curvature as a function of the travelled distance S.

3.2.3 MOTION COMFORT ASSESSMENT

Given that the primary goal of motion planning is to mitigate MS, it is essential to incorporate MS metrics directly into the internal model. This integration can be achieved by introducing additional differential equations that represent the dynamic factors contributing to MS. In this direction, the ISO-2631-1 [7], provides objective guidelines for measuring and evaluating human exposure to whole-body mechanical vibration and repeated shock. According to the guidelines, two comfort metrics are derived: i) Ride Comfort (RC) emphasising the higher frequencies (mainly above 1 Hz); ii) MS emphasising the lower frequencies (mainly below 1 Hz), as suggested in [11], [12]. According to the standard, comfort is assessed by combining the root-mean-square (RMS) values of weighted accelerations ($MS_{i,W}$), along all translational and rotational directions, measured at the vehicle's centre of gravity, whilst the total MS is computed as the sum of the squared $MS_{i,W}$:

$$MS_{i,W} = \left[\frac{1}{t}\int_0^t \left[a_{i,W}\right]^2 dt\right]^{1/2} \tag{3.2.11}$$

$$MS_{tot} = \sum_i \left[MS_{i,W}\right]^2 \tag{3.2.12}$$

3.2.4 WEIGHTING FILTER DESIGN

In this work, two sets of weighting filters are designed: i) the seat-to-head weighing filters to transfer the vehicle-based accelerations to the head [24], and ii) the frequency-weighting filters to weight the head accelerations based on MS susceptibility [7], [21], [22].

The filtered accelerations in the most complex formulation, i.e. including both set of filters, are fed at first into the seat-to-head weighting filters, and then the resulting filtered accelerations are fed into the frequency-weighting filters

3.2.4.1 Seat-to-head weighting filters

These filters are available as experimental data in the literature [24]; however, they can also be implemented within the internal model by expressing them as transfer functions. To achieve this, equations describing the filter dynamics are derived by fitting the data using the *iirlpnorm Matlab Function* [28]. The *iirlpnorm* function generates a filter with a numerator of order n and denominator of order d, providing the best approximation to the desired frequency response (defined by input frequency and amplitude), in the least pth-sense.

The algorithm to get the transfer functions consists of three steps:

- Map the weighting curves in continuous-time frequency onto the unit circle via the bilinear transformation:

$$\Omega_i = \frac{2}{T} tan^{-1}\left(\frac{T\omega_i}{2}\right) = \frac{2}{T} tan^{-1}(T\pi f_i)\,,\ with\, T = 0.5 \tag{3.2.13}$$

- Design the optimal least-pth digital filter $W_D(z)$ to be nimised:

$$\sum_{i=1}^{N} \left| |W_D(z_i)| - W_i \right|^p, with\, p = 2 \tag{3.2.14}$$

$$z_i = e^{j\Omega_i} \tag{3.2.15}$$

$$W_D(z_i) = \frac{\bar{b}_n z^{-n} + \cdots \bar{b}_1 z^{-1} + \bar{b}_0}{z^{-n} + \cdots \bar{a}_1 z^{-1} + \bar{a}_0} \tag{3.2.16}$$

where, W_i are the empirical frequency weightings, $W_D(z_i)$ are the frequency-weighting obtained by the transfer function, and p defines the order of the filter, which for the test case is set up to 2;

- Obtain the filter in the s-domain via the bilinear transformation:

$$W(s) = W_D(z)|_{z=(1+Ts/2)/(1-Ts/2)} \tag{3.2.17}$$

For the test case, the considered transfer functions account for: i) head's longitudinal and pitch acceleration due to seat longitudinal acceleration; ii) head's lateral and yaw acceleration due to seat lateral acceleration; and iii) head's yaw acceleration due to vehicle yaw acceleration. Leading to a total of five transfer functions ($W_{s,h}$), where the subscript s identifies the vehicle's acceleration influencig the head's acceleration identified with the subscript h. The general formulation of the filters is the following:

$$W_{s,h}(s) = \frac{a_{s,h,BPF}(s)}{a_s(s)} = \frac{As + B}{s^2 + Cs + D} \tag{3.2.18}$$

where $a_{s,h,BPF}(s)$ is the band-pass seat-to-head filtered acceleration; $a_s(s)$ is the seat acceleration, in the specific implementation approximated to vehicle's acceleration a_i; and A, B, C, D are the generic coefficients of the band-pass filters

The fitted transfer functions are defined through equations (3.2.19)–(3.2.23), and the fitted curves are shown in Figure 3.2.2:

$$W_{x,x}(s) = \frac{6.0465s + 135.0036}{s^2 + 12.4489s + 126.6507} \tag{3.2.19}$$

$$W_{x,\theta}(s) = \frac{[1.4679s + 1.6974] \cdot 10^4}{s^2 + 10.4703s + 553.0141} \tag{3.2.20}$$

$$W_{y,y}(s) = \frac{-1.1201s + 112.2811}{s^2 + 8.6734s + 90.3275} \tag{3.2.21}$$

$$W_{y,\psi}(s) = \frac{[1.5365s + 2.2522] \cdot 10^3}{s^2 + 5.7160s + 119.2104} \tag{3.2.22}$$

$$W_{\psi,\psi}(s) = \frac{5.8346s - 381.9114}{s^2 + 5.3268s + 348.8255} \tag{3.2.23}$$

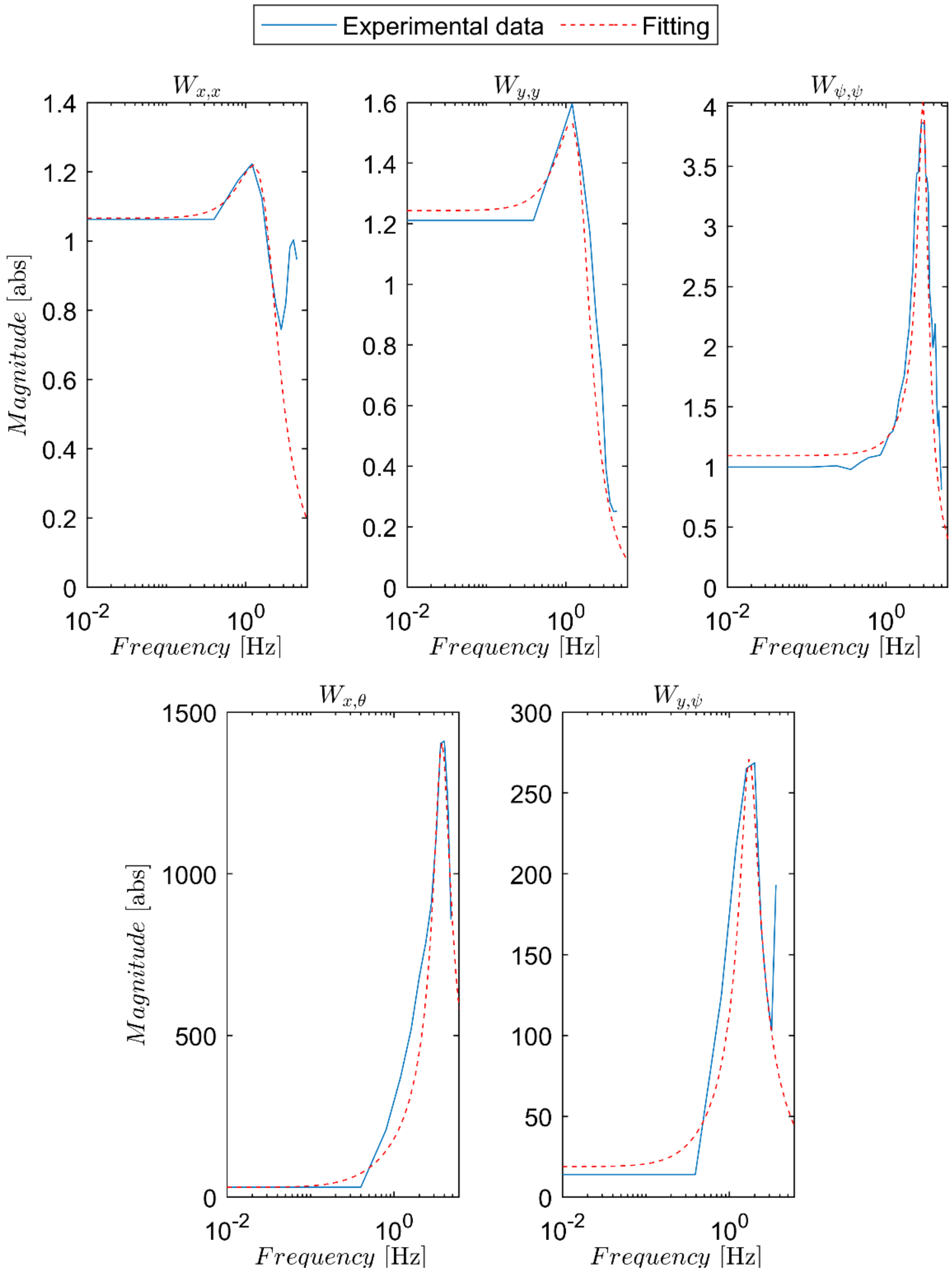

Figure 3.2.2: Fitted seat-to-head weighting filters.

3.2.4.2 Frequency weighting filters

The frequency weighting filters are designed to cut-off the acceleration components which are not involved in causing MS. These are defined for translational acceleration along the z-axis and rotational accelerations [7], translational acceleration along the x-axis [21], and y-axis [22], see Figure 3.2.3:

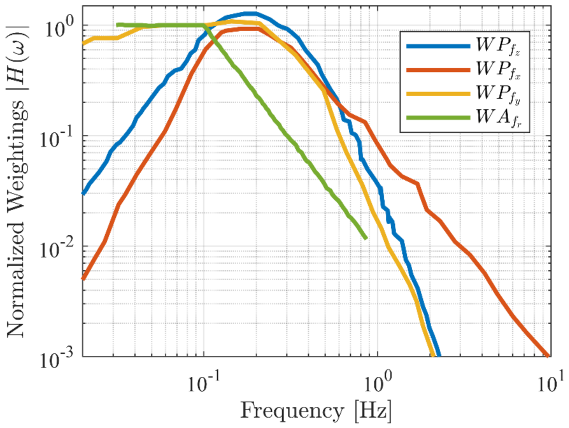

Figure 3.2.3: Frequency weighting filters for translational and rotational accelerations.

As for the seat-to-head filters, the same procedure described in Section 3.2.4.1, using equations (3.2.13)–(3.2.17) is applied for the frequency-weighting filters.

The general formulation of the filters is the following:

$$WP_{fs}(s) = \frac{a_{BPF}^{FS}(s)}{a_{s,h,BPF}(s)} = \frac{As + B}{s^2 + Cs + D} \tag{3.2.24}$$

where $a_{BPF}^{FS}(s)$ is the band-pass frequency-weighted filtered acceleration.

The fitted transfer functions are defined through equations (3.2.25)–(3.2.28), and the fitted curves are shown in Figure 3.2.4:

$$WP_{fx}(s) = \frac{0.6316s + 1.1 \cdot 10^{-3}}{s^2 + 0.5764s + 1.1542} \tag{3.2.25}$$

$$WP_{fy}(s) = \frac{0.6771s + 1.6313 \cdot 10^{-4}}{s^2 + 0.6s + 0.09} \tag{3.2.26}$$

$$WP_{fz}(s) = \frac{0.7531s + 1.18 \cdot 10^{-2}}{s^2 + 0.5277 + 1.0323} \tag{3.2.27}$$

$$WA_{fr}(s) = \frac{0.0861s + 1.3004}{s^2 + 1.5375s + 1.3045} \tag{3.2.28}$$

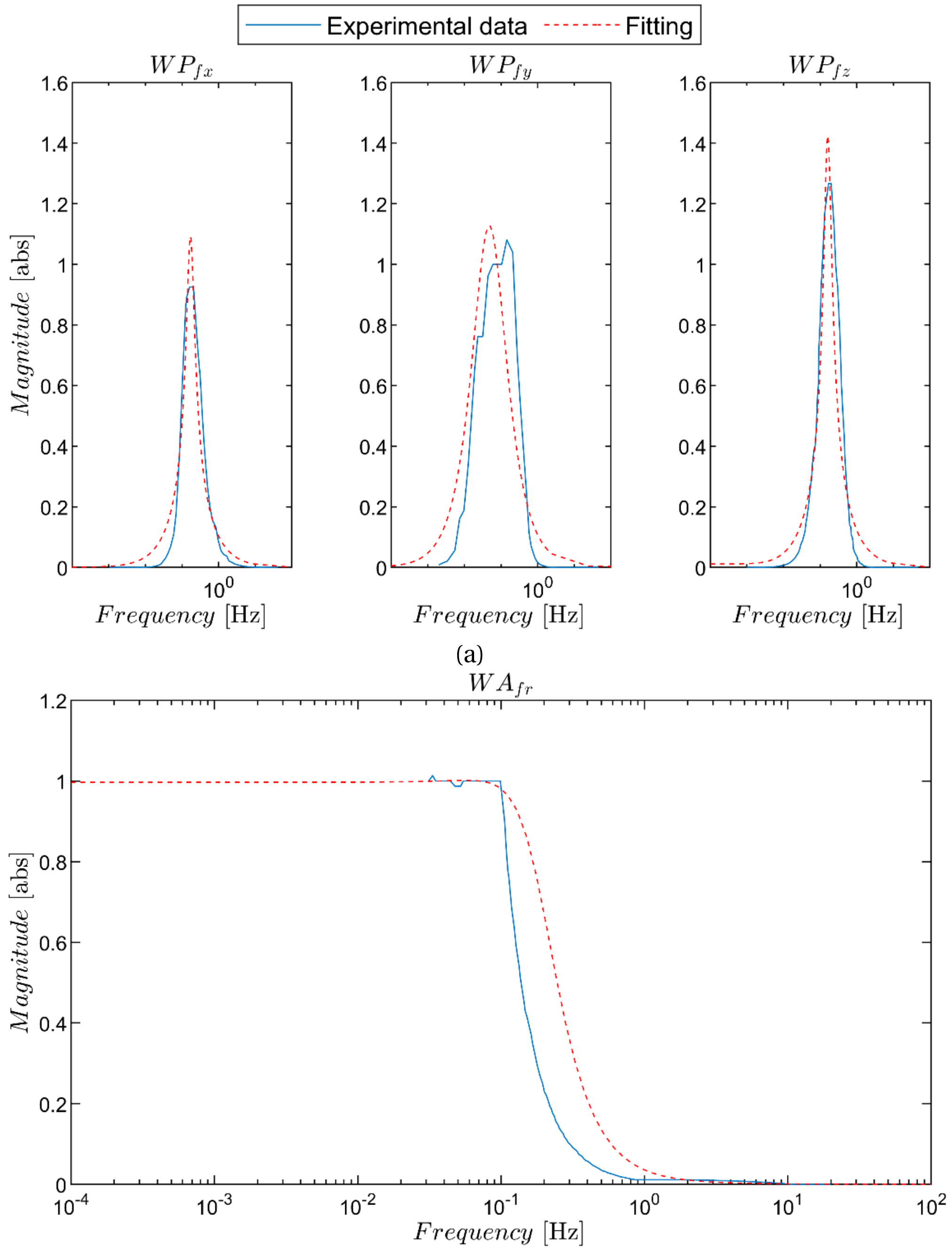

(a)

(b)

Figure 3.2.4: Fitted frequency weighting filters for (a) longitudinal, lateral and vertical accelerations; and (b) rotational accelerations.

3.2.4.3 Filters implementation

Both set of filters described in Sections 3.2.4.1–3.2.4.2 need to be rearranged as ordinary differential equation in order to be implemented within the internal model formulation. To this end, it should be noted that the seat-to-head filters are essentially band-pass filters and consequently, equations (3.2.19)–(3.2.23) can be factorised at the denominator to simplify their implementation as a series of an high-pass filter and a low-pass filter. However, the factorisation cannot be achieved without using complex numbers. To sidestep the issue of factorisation, a dummy low-pass filter, i.e. with a small time constant, is added to each filter:

$$W_{s,h}(s) = \frac{a_{s,h,BPF}(s)}{a_i(s)} = \frac{1}{10^{-5}s+1}\frac{As+B}{s^2+Cs+D} \tag{3.2.29}$$

The vehicle's acceleration $a_i(s)$ can be treated as input to the dummy low-pass filter, with the resulting filtered acceleration then used as input to the band-pass filter.

These mathematical operations can be expressed as follows:

$$\frac{a_{s,h,D-LPF}(s)}{a_i(s)} = \frac{1}{10^{-5}s+1} \tag{3.2.30}$$

$$\dot{a}_{s,h,D-LPF}(s) = \frac{a_i(s) - a_{s,h,D-LPF}(s)}{10^{-5}} \tag{3.2.31}$$

where $a_{s,h,D-LPF}(\mathrm{s})$ is the filtered signal through the dummy low-pass filter, and $\dot{a}_{s,h,D-LPF}(\mathrm{s})$ is the time derivative of $a_{s,h,D-LPF}(\mathrm{s})$, which is used in the band-pass filter's equations:

$$\frac{a_{s,h,BPF}(s)}{a_{s,h,D-LPF}(s)} = \frac{As+B}{s^2+Cs+D} \tag{3.2.32}$$

$$\ddot{a}_{s,h,BPF}(s) = A\dot{a}_{s,h,D-LPF}(s) + Ba_{s,h,D-LPF}(s) - C\dot{a}_{s,h,BPF}(s) - Da_{s,h,BPF}(s) \tag{3.2.33}$$

$$\dot{a}_{s,h,BPF}(s) = \frac{d}{dt}\left(a_{s,h,BPF}(s)\right) \tag{3.2.34}$$

where $\dot{a}_{s,h,BPF}(s)$ and $\ddot{a}_{s,h,BPF}(s)$ are respectively the first time and second time derivative of the band-pass filtered acceleration $a_{s,h,BPF}(s)$.

As for the frequency-weighting filters, they do not require any further manipulation, thus equation (3.2.18) can be rearranged as:

$$\ddot{a}^{FS}(s) = A\dot{a}_{s,h,BPF}(s) + Ba_{s,h,BPF}(s) - C\dot{a}^{FS}(s) - Da^{FS}(s) \tag{3.2.35}$$

$$\dot{a}^{FS}(s) = \frac{d}{dt}\left(a^{FS}(s)\right) \tag{3.2.36}$$

In summary, the seat-to-head weighting filters can be incorporated into the internal model by adding three differential equations per filter, while the frequency-weighting filters require the addition of two differential equations each.

3.3 MOTION PLANNING ALGORITHM

3.3.1 PROBLEM FORMULATION

The motion planning algorithms are formulated as optimal control problems (OCPs) applied to driving on a path known a priori, neglecting interactions with other road users. As the aim of the work is to investigate the compromise of motion planner between journey time and MS mitigation, the whole state space is converted from time domain to space domain using the following relation:

$$\frac{dX}{dS} = X' = \frac{X}{dt}\frac{dt}{dS} = \dot{X}t' \tag{3.3.1}$$

where X' represents the differential variable X in the space domain, while t' is an additional differential state useful to incorporate the journey time as a state variable in the OCP. The state array of each formulation depends on the considered filters within the internal model. In particular the set of states can be written as:

$$X_1 = \left[V_x, V_y, \dot{\psi}, S, S_n, \alpha_s, t\right] \tag{3.3.2}$$

$$X_2 = \left[a_{s,h,D-LPF}, a_{s,h,BPF}, a'_{s,h,BPF}\right] \tag{3.3.3}$$

$$X_3 = [a_{BPF}^{FS}, a_{BPF}'^{FS}] \tag{3.3.4}$$

$$X_4 = \left[MS_{i,W}\right] \tag{3.3.5}$$

$$X_5\left[\delta, F_{x,tot}\right] \tag{3.3.6}$$

Where, X_1 includes the vehicle and road states as well as the journey time, derived from equations (3.2.1)–(3.2.3), (3.2.7)–(3.2.9) and (3.3.1); X_2 includes the seat-to-head weighting filters' states, derived from equations (3.2.32)–(3.2.34); X_3 includes the frequency-weighting filter's states, derived from equations (3.2.35)–(3.2.36); X_4 includes the MS metrics along each considered direction, see equations (3.2.11); and X_5 includes the integral of the control actions. All states vector in equations (3.3.2)–(3.3.6) are defined in space domain according to (3.3.1). All states are obtained from the differential states of the systems, and are defined in the space domain according to (3.3.1).

Finally, the control actions vector U is defined as:

$$U = \left[\delta', F'_{x,tot}\right] \tag{3.3.7}$$

Where δ' and $F'_{x,tot}$ are the steering rate of the front wheels and the longitudinal force rate on the rear axle of the car, defined in space domain.

In particular, four motion planning algorithms are developed and are: i) the motion planner based vehicle accelerations to compute the MS metric, is described by X_1, X_4 and X_5 without any consideretion of the filters; ii) the motion planner that considers the seat-to-head weighting filters described by X_1, X_2, X_4 and X_5; iii) the motion planner that considers the frequency weighting filters described by X_1, X_3, X_4 and X_5; and iv) the most advanced formulation of motion planner, accounting for both set of filters and described by X_1, X_2, X_3, X_4 and X_5.

3.3.2 OBJECTIVES

The OCP is implemented through nonlinear model predictive control (NMPC) with the receding horizon approach [29] in ACADO [30]. The NMPC minimises a cost function J, subjected to equality and inequality constraints, and the discrete form of the nonlinear optimal control problem is defined as:

$$
\begin{gathered}
\min_{U} J\left(Z(0), U(\cdot)\right) \coloneqq \frac{1}{2} \sum_{k=0}^{N-1} \left(\left\| Z^k - Z^k_{ref} \right\|_Q + \| U^k \|_R \right)^2 + \left\| Z^N - Z^N_{ref} \right\|^2_{Q_N} \\
\text{s.t.} \\
X^{k+1} = f_d\,(X^k, U^k) \\
Z^k = h_d\,(X^k, U^k) \\
\underline{Z} \leq Z^k \leq \overline{Z} \\
\underline{Z} \leq Z^N \leq \overline{Z} \\
\underline{U} \leq U^k \leq \overline{U} \\
U(\cdot) : [0, N-1]
\end{gathered}
\tag{3.3.8}
$$

where the index k refers to the step number along the prediction horizon, including N steps in total; Z is the output vector; Z_{ref} is the reference value of Z; the symbols ‘ _ ’ and ‘ ¯ ’ indicates the lower and upper limits respectively of the array; f_d and h_d are the discretised nonlinear functions; and R, Q, and Q_N are positive semi-definite weight matrices. The length of the prediction horizon H_p is given by:

$$
H_p = N \cdot D_s \tag{3.3.9}
$$

where D_s is the size of each step, expressed in meters. In the specific implementation $N = [25, 25, 25]$ and $D_s = [0.1, 0.5, 1.0]$, leading to a total length of H_p of 40 m. The choice of the prediction horizon, defined in terms of step size, is calibrated to balance an appropriate level of accuracy in representing vehicle dynamics within the internal model, while simultaneously extending the horizon sufficiently to capture the accumulation of MS to an appreciable degree, thereby enabling effective mitigation; this setup is also chosen with consideration for the real-time implementation of the algorithm.

Given the objective of the motion planner, the terms in Z are the increment of time Δt and the increment of ΔMS along the prediction horizon:

$$
\Delta t = t^k - t_{init} \tag{3.3.10}
$$

$$
\Delta MS = MS^k_{i,w} - MS_{init} \tag{3.3.11}
$$

where t^k and $MS^k_{i,w}$ are the predicted time and MS along the prediction horizon, whilst t_{init} and MS_{init} are the values at the beginning of the prediction horizon, provided as feedback data from the previous simulation step. Given the terms in Z, the respective reference vector $Z_{ref} = [0,0]$.

The hard constraints in (3.3.8) are defined for: the longitudinal and lateral vehicle speed V_x and V_y; the vehicle yaw rate $\dot{\psi}$ and yaw acceleration $\ddot{\psi}$; the lateral shift from the centerline of the road S_n; the longitudinal and lateral acceleration of the vehicle a_x and a_y;

the steering angle and steering rate δ and $\dot{\delta}$; and the longitudinal axle force and longitudinal axle force rate $F_{x,tot}$ and $\dot{F}_{x,tot}$.

In particular, the longitudinal and lateral accelerations are bounded with the friction circle equation:

$$\sqrt{k_a a_x^2 + [1 - k_a] a_y^2} \leq \mu g k_d \tag{3.3.12}$$

Here, k_a and k_d are additional tuning parameters designed to keep total acceleration within comfort limits [31]. These parameters also allow for shifting the emphasis within the friction circle between a_x and a_y, thus adjusting the relative importance of these components depending on whether the vehicle is in traction or braking conditions, see equations (3.3.13)–(3.3.16).

$$k_a^{TR} = \frac{\overline{a_x}^2}{\overline{a_x}^2 + \overline{a_y}^2} \tag{3.3.13}$$

$$k_a^{BR} = \frac{\underline{a_x}^2}{\underline{a_x}^2 + \underline{a_y}^2} \tag{3.3.14}$$

$$k_d^{TR} = \frac{\left[\overline{a_x}^2 + \overline{a_y}^2\right]^{1/2}}{g} \tag{3.3.15}$$

$$k_d^{BR} = \frac{\left[\underline{a_x}^2 + \underline{a_y}^2\right]^{1/2}}{g} \tag{3.3.16}$$

where the superscript 'TR' and 'BR' indicates the traction and braking mode, which are selected based on the actual value of the longitudinal acceleration:

$$k_a = \begin{cases} k_a^{TR} & if \quad a_x \geq 0 \\ k_a^{BR} & if \quad a_x < 0 \end{cases} \tag{3.3.17}$$

$$k_d = \begin{cases} k_d^{TR} & if \quad a_x \geq 0 \\ k_d^{BR} & if \quad a_x < 0 \end{cases} \tag{3.3.18}$$

Table 3.3.1 summarises the values for the lower and upper limits of each constraint:

Table 3.3.1 – Lower and upper limits of each constraint

Limits	Units
$5 \leq V_x \leq 25$	m/s
$-1.5 \leq V_y \leq 1.5$	m/s
$-0.7 \leq \dot{\psi} \leq 0.7$	rad/s
$-2 \leq \ddot{\psi} \leq 2$	rad/ s^2
$-1.5 \leq S_n \leq 1.5$	m
$-2.94 \leq a_x \leq 1.47$	m/s^2
$-3.92 \leq a_y \leq 3.92$	m/s^2
$-0.45 \leq \delta \leq 0.45$	rad
$-0.5 \leq \dot{\delta} \leq 0.5$	rad/s
$-30 \leq F_{x,tot} \leq 10$	kN
$-10 \leq \dot{F}_{x,tot} \leq 10$	kN/s

3.3.3 COST FUNCTION NORMALISATION

Given the various nature of the terms in the cost function, i.e. increment of time, increment of MS metric, steering rate and force rate, a common approach in these cases is to normalise each term with respect to a parameter so that the magnitude of each term is ~ 1. Consequently, easing the choice of weighting matrices Q, R and Q_N in equation (3.3.8), and facilitating the interpretation of the controllers' objective function. To this end, the choice of the normalisation factor is crucial to ensure a fair influence of each term.

A brute force algorithm is developed with Matlab *fmincon* [33], seeking for the best combination of weights to achieve: i) the minimum journey time; and ii) the minimum MS alongh the path. The initial guesses for the optimisation algorithm are derived from a set of manually tuned weights, carefully selected to ensure the successful completion of the simulation. The two limit cases, i) and ii), are useful to define the range of the weights in Q and R:

$$\begin{gathered} J_{KPI}^{*} = \min_{Q_{opt}, R_{opt}} J_{KPI}\Big|_{S_i}^{S_f} \\ \text{s.t.} \\ \underline{Q} \leq Q_{opt} \leq \bar{Q} \\ \underline{R} \leq R_{opt} \leq \bar{R} \end{gathered} \tag{3.3.19}$$

where $\underline{Q}, \bar{Q}, \underline{R}$ and $\bar{R}$ are the vector of the lower and upper bounds of the tuning weights in (3.3.8); Q_{opt} and R_{opt} are the optimal values of the weight vectors; S_i and S_f are the initial and final spaces of the relevant portion of the test; and J_{KPI}^{*} is the optimal value of J_{KPI}, which can be either the journey time or the total cumulated MS alongh the path shown in Figure 3.4.1.

As an outcome of the optimisation, in both limit cases, the weight related to the steering rate resulted higher in magnitude with respect to the others, whilst the weight related to the force rate is zero. The higher weight on the steering rate is justified by the tool used for the NMPC implementation [30]. Specifically, the algorithm implemented in ACADO is exported as a Real-Time Iteration Scheme (RTI), which does not fully converge to the solution of the nonlinear optimisation at each time step. Instead, it performs only one iteration of a sequential quadratic programming algorithm, based on the estimation of the previous solution. This approach prioritises quick control feedback to the system, and a higher sampling frequency to improve the closed-loop system's stability. Consequently, it is not possible to set the KKT tolerance as a convergence criterion for the algorithm [32]. Therefore, high weight values are necessary to ensure that the optimisation algorithm adheres to a sufficiently small tolerance.

To ensure a balanced influence of the terms in the cost function, the weights are configured so that the controller's focus is equally distributed between the steering rate and either Δt or ΔMS, aiming for either minimal journey time or reduced MS, respectively.

The normalisation factors are determined through an optimisation process as defined in equation (3.3.20):

$$\begin{gathered} J_{KPI}^{*} = \min_{N_{opt}} J_{KPI}\Big|_{S_i}^{S_f} \\ \text{s.t.} \\ \underline{N} \leq N_{opt} \leq \overline{N} \end{gathered} \tag{3.3.20}$$

where $\underline{N}$ and $\overline{N}$ are the vector of the lower and upper bounds of the normalisation factors; and N_{opt} is the optimal values of the normalisation factors vector.

Once $N_{\Delta \mathrm{t}}, N_{\Delta \mathrm{t}}$ and $N_{\dot{\delta}}$ have been defined, i.e. the normalisation factor for $\Delta t, \Delta MS$ and $\dot{\delta}$, it is possible to rewrite the NMPC cost function in equation (3.3.8) as:

$$\begin{gathered} \min_{U} J\left(Z(0), U(\cdot)\right) \coloneqq \frac{1}{2}\sum_{k=0}^{N-1}\left(\left\|\frac{Z^k - Z_{ref}^k}{N_Z}\right\|_Q + \left\|\frac{U^k}{N_U}\right\|_R\right)^2 + \left\|\frac{Z^N - Z_{ref}^N}{N_Z}\right\|_{Q_N}^2 \\ \text{s.t.} \\ X^{k+1} = f_d\left(X^k, U^k\right) \\ Z^k = h_d\left(X^k, U^k\right) \\ \underline{Z} \leq Z^k \leq \overline{Z} \\ \underline{Z} \leq Z^N \leq \overline{Z} \\ \underline{U} \leq U^k \leq \overline{U} \\ U(\cdot) : [0, N-1] \end{gathered} \tag{3.3.21}$$

where N_Z and N_U are the normalisation vectors for the output vector and control actions vector, respectively.

3.4 RESULTS

The test path was designed to replicate typical driving conditions that challenge both vehicle stability and passenger comfort. The path begins with an initial straight segment measuring 31 meters in length, providing a controlled start to the testing scenario. Following this straight section, the path transitions into a left turn with a radius of curvature of approximately 7.5 meters, covered over a distance of 7.75 meters. Immediately after, the path reverses direction into a right turn, again with a radius of curvature of roughly 7.5 meters, spanning another 7.75 meters to bring the vehicle back to a straight trajectory. This sequence is followed by a second straight segment of 31 meters, leading into another set of turns that mirrors the first turning sequence: left-right and left-right curves, each with similar curvatures and distances. This repeated sequence of turns adds complexity, requiring the vehicle's control system to continuously adapt to changes in path curvature. The test concludes with a final straight segment of 31 meters., see Figure 3.4.1.

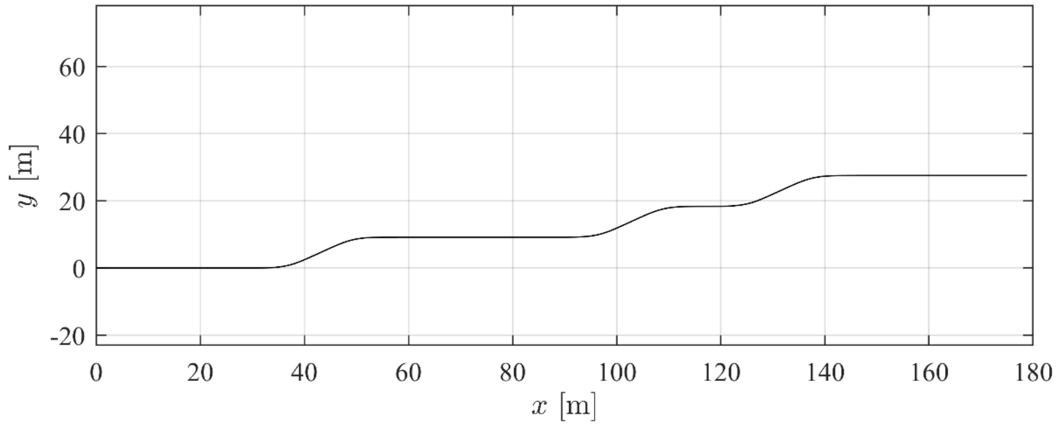

Figure 3.4.1: Path used for the test case.

This structured pattern of straight lines and alternating curves was selected to capture a comprehensive range of manoeuvres, allowing for effective assessment of the control system's response in both steady-state and transitional dynamics. The frequent changes in curvature create conditions conducive to evaluating both vehicle stability and passenger comfort, as well as the control system's ability to mitigate MS.

3.4.1 MOTION PLANNER BASED ON VEHICLE ACCELERATIONS – COST FUNCTION NOT NORMALISED

The motion planner that computes the MS metric based on vehicle acceleration, described in Section 3.3.1, has been tested on the path shown in Figure 3.4.1. The minimum time and minimum MS scenarios for this algorithm are computed based on equation (3.3.19). The space profiles of the main variables are shown in Figure 3.4.2:

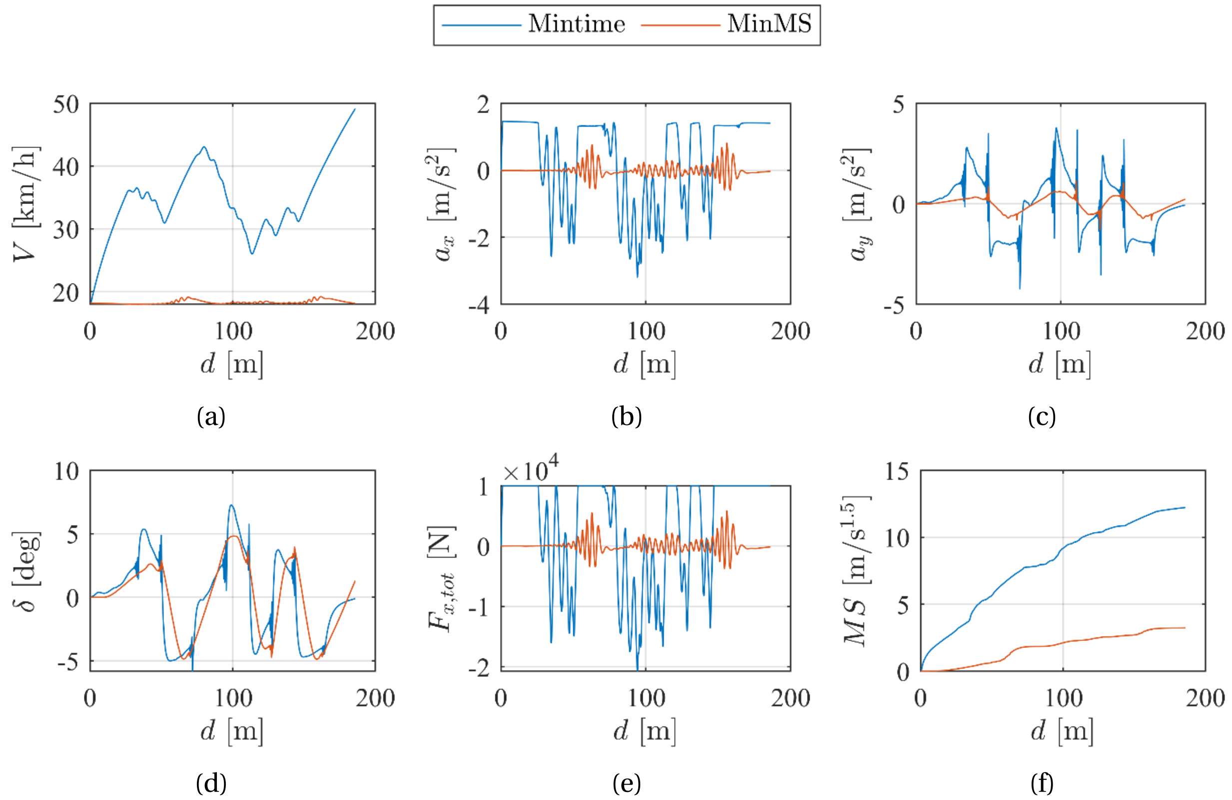

Figure 3.4.2: Space profiles of the main variables of the motion planner based on vehicle accelerations to compute the MS metric with cost function not normalised for the minimum time and minimum MS scenarios: (a) speed profile; (b) longitudinal acceleration; (c) lateral acceleration; (d) steering angle profile; (e) longitudinal force on the rear axle; and (f) MS accumulation.

Following the theoretical findings outlined in Chapter 2, the minimum MS scenario yields to an almost constant speed profile, shown in Figure 3.4.1 (a), reflecting the reduction in the accelerations, see Figure 3.4.1 (b)–(c). Nevertheless, the longitudinal acceleration profiles are affected by high-frequency oscillations that may be attributed to the not normalised cost function since the algorith might prioritise certain objective excessively at the expenses of smoothness. Thus, this imbalance can result in chattering behaviour, where the planner produces overly aggressive control actions to achieve its goal, leading to high-frequency noise in the longitudinal acceleration profiles to avoid exceeding the constraint on $\mathrm{S_n}$. The speed profile for the minimum time case decreases only in the cornering sections. Figure 3.4.1 (d) depicts the steering angle δ, highlighting a smoother behaviour for the minium MS case with respect to the minimum time case, reflecting a smaller lateral acceleration in Figure 3.4.1 (c). The total longitudinal force on the rear axle $F_{x,tot}$ in Figure 3.4.1 (e) highlights a more aggressive behaviour for the minimum time case, with frequent slope variations, leading to a similar behaviour in the longitudinal acceleration depicted in Figure 3.4.1 (b). Finally, as expected, the minimum time case leads to an overall higher MS of 12.22 $\mathrm{m/s^{1.5}}$ against the 3.22 $\mathrm{m/s^{1.5}}$ for the minimum MS case, whilst the journey times are ~19.52 s and ~36.45 s respectively. For the specific test case, a reduction of ~73.65 % in the MS metrics, corresponds to an increase of ~86.73 % in journey time.

3.4.2 MOTION PLANNER BASED ON VEHICLE ACCELERATIONS – NORMALISED COST FUNCTION

As detailed in Section 3.3.3, the terms in the cost function need normalisation factors to ensure a fair influence of the terms in equation (3.3.8).

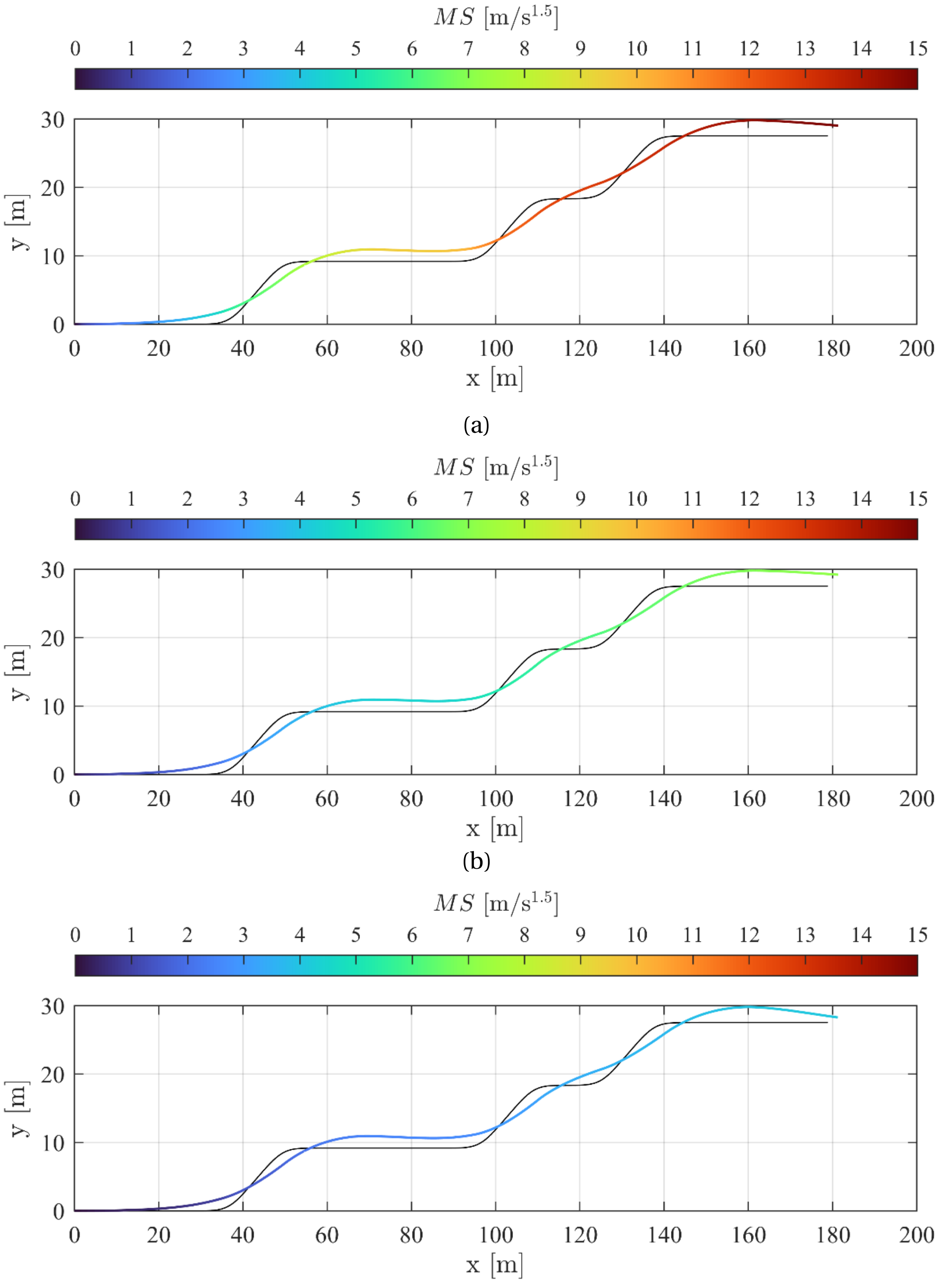

(a)

(b)

(c)

Figure 3.4.3: MS cumulation along the path in the case of: (a) minimum time; (b) trade-off; and (c) minimum MS.

For this purpose, using the cost function defined in equation (3.3.21). Figure 3.4.3 compares the MS cumulation along the path in three scenarios: i) minimum time; ii) the minimum MS; and iii) trade-off, with 70 % focus on minimising Δt and 30 % on minimising ΔMS. From Figure 3.4.3 (a)–(b) it is possible to observe that the minimum time scenario reaches comparable levels of MS cumulation with respect to the trade-off scenario at $x = 60$ m, whilst from Figure 3.4.3 (a)–(c), it is possible to observe a comparable level of cumulated MS already in the first portion of the manoeuvre, i.e. before $x = 40$ m. The second portion of the manoeuvre, $x = 100$ m up to $x = 140$, is more provocative for MS as it is possible to observe a sudden increment, i.e. color shift from blue to red, in the minimum time and trade-off scenarios, whilst the transition is quite smooth for the minimum MS case. As for the journey time and the MS cumulation are of the same magnitude of the one presented in 3.4.1, while the trade-off scenario completes the path in ~25 s, with a MS of ~6.14 m/s$^{1.5}$.

The advantage of using a normalised cost function relies upon the capability to gradually shift the weight from Δt to ΔMS, generating all the intermediate trade-off scenarios, without compromising the steering rate required to face the cornering portions of the path. The trade-off scenarios highlight the relationship between the journey time and the accumulation of MS along the path:

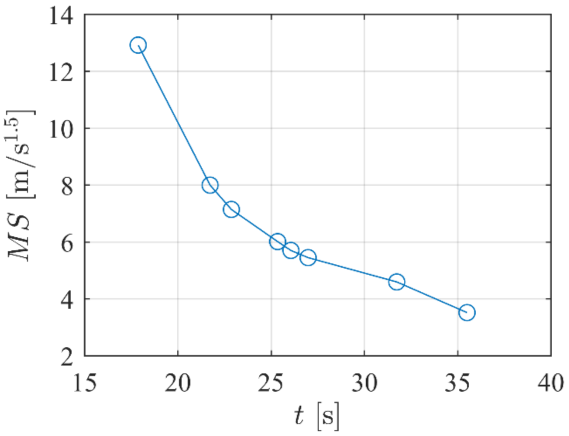

Figure 3.4.4: Pareto front for journey time and MS cumulation

The Pareto front in Figure 3.4.4 illustrates the trade-off between minimising MS cumulation and journey time. Points along the front, highlight that as the journey time increases, there is a corresponding decrease of MS cumulation, reflecting the balance between passenger comfort and travel efficiency. The points closer to the left of the plot represent scenarios with quicker journeys, whilst the points toward the right represent scenario favouring passenger's comfort with lower cumulated MS.

For a further understanding of the relationship between journey time and MS cumulation, Table 3.4.1 shows the reduction of MS in % due to the increase of time in %, with respect to the minimum time scenario:

Table 3.4.1 – Time increment vs MS reduction

t_Δ [%]	MS_Δ [%]
21.57	-38.10
27.96	-44.72
39.91	-52.51
41.81	-53.45
45.80	-55.88
50.95	-57.82
77.54	-64.43
98.61	-72.77

In Table 3.4.1 t_Δ and MS_Δ are computed as follows:

$$t_\Delta = \frac{t_{end,i} - t_{end,mintime}}{t_{end,mintime}} \cdot 100 \tag{3.4.1}$$

$$MS_\Delta = \frac{MS_{end,i} - MS_{end,mintime}}{MS_{end,mintime}} \cdot 100 \tag{3.4.2}$$

where $t_{end,i}$ and $MS_{end,i}$ are the time and MS of each point on the Pareto front, whilst $t_{end,mintime}$ and $MS_{end,mintime}$ are the time and MS of the minimum time scenario.

The results suggest that it may not be needed to fully sacrifice the journey time to effectively reduce the cumulative MS, as an increase in journey time of only 39.91 % achieves a reduction in MS of 52.51 %.

These initial results highlight the promising potential of using motion planning to mitigate MS. Future work will focus on implementing more advanced motion planning strategies that incorporate frequency-weighting filters and seat-to-head transfer functions, as outlined in Sections 3.2.4.1–3.2.4.2, to further enhance passenger comfort. Additionally, exploring alternative actuation strategies, such as traction control, torque-vectoring, and active suspension control, alongside refined MS metrics, will broaden the vehicle's capabilities, ensuring safety while providing smoother, more comfortable journeys.

3.5 CONCLUDING REMARKS

This study presented a comparison among four implementable NMPC strategies for motion planning for MS mitigation through consideration of appropriate MS metrics. The first algorithm computes the MS based on the vehicle's acceleration; the second one considers seat-to-head weighting filters as suggested by the literature; the third applies frequency-weighting filters accounting for the most provocative frequencies for MS insurgence; and the fourth based on both set of filters. All four motion planner are based on a 3DoF vehicle model neglecting wheel dynamic, and the road curvilinear coordinates, while the OCP is shifted into space domain through t'. For a fair assessment of the relationship between journey time and MS cumulation, the terms within the OCP cost function are normalised with appropriate factors, defined through an optimisation routine for the case of fixed weights on the increment of time, or increment of MS cumulation along the prediction horizon, and steering rate. The motion planner has been assessed on a path designed to replicate typical driving conditions challenging both vehicle stability and passengers' comfort, and the simulation analysis brought the following main conclusions:

- The motion planner with the terms not normalised in the cost function is capable to mitigate MS or minimise the journey time, at the cost of higher complexity in defining the weights for the terms in the cost function.
- The minimum time and minimum MS scenario obtained using the algorithm which employs a cost function with unnormalised terms, do not share consistent weights on the control actions, i.e. the steering rate. This disparity in weights suggest that deriving a Pareto front to balance these objectives would be complex.
- Conversely, using a motion planner with a normalised cost function simplifies the definition of weights and enhances the clarity of the controller's focus.
- However, due to the diverse nature of the terms within the cost function and limitations imposed by the NMPC implementation tool, determining the normalisation factors requires an optimisation routine that establishes these factors for given fixed weights assigned to the cost function terms.
- Nonetheless, the motion planner using the normalised cost function demonstrates more consistent behaviour, particularly in the steering angle produced by the steering rate, whose percentage importance remains constant across different scenarios.
- Furthermore, the algorithm with the normalised cost function simplifies the process of generating a Pareto front, allowing for trade-off scenarios that illustrate the relationship between journey time and cumulative MS.
- The results demonstrate the overall effectiveness of the proposed algorithm in mitigating motion sickness. Future developments in this area include refining the alternative motion planner, which is based on frequency-weighted filters or/and the seat-to-head transfer function, with the aim of comparing the planners'

performance while addressing the challenges of real-time implementation posed by the increased number of states.

BIBLIOGRAPHY

[1] M. Sivak and B. Schoettle, “Motion sickness in self-driving vehicles,” University of Michigan, Ann Arbor, *Transportation Research Institute*, Tech. Rep., 2015.

[2] E. Lehtonen, F. Malin, T. Louw, Y. M. Lee, T. Itkonen, and S. Innamaa, “Why would people want to travel more with automated cars?,” *Transportation research part F: traffic psychology and behaviour*, vol. 89, pp. 143–154, 2022.

[3] J.T. Reason, “Motion Sickness Adaptation: A Neural Mismatch Model,” *J. R. Soc. Med.* vol. 71, no. 11, pp. 819–829, 1978.

[4] C. M. Oman, “Sensory conflict in motion sickness: an observer theory approach,” *Pictorial communication in virtual and real environments*, 1989.

[5] J. E. Bos and W. Bles, “Modelling Motion Sickness and Subjective Vertical Mismatch Detailed for Vertical Motions,” in *Brain Res. Bull.*, vol. 47, pp. 537-542, 1998.

[6] G. E. Riccio and T. A. Stoffregen, “An ecological theory of motion sickness and postural instability,” Ecological psychology, vol. 3, no. 3, pp. 195–240, 1991.

[7] *Mechanical Vibration and Shock – Evaluation of Human Exposure to Whole-Body Vibration – Part 1: General Requirements*, ISO 2631-1, International Organisation for Standardisation, Geneve, 1997.

[8] M. Turner and M. J. Griffin, “Motion sickness in public road transport: the relative importance of motion, vision and individual differences,” British Journal of Psychology, vol. 90, no. 4, pp. 519–530, 1999.

[9] M. Turner, “Motion sickness in public road transport: passenger behaviour and susceptibility,” Ergonomics, vol. 42, no. 3, pp. 444–461, 1999.

[10] M. Turner and M. J. Griffin, "Motion sickness in public road transport: the effect of driver, route and vehicle," *Ergonomics*, vol. 42, pp. 1646-1664, 1999.

[11] J. F. Golding, A. Mueller, and M. A. Gresty, “A motion sickness maximum around the 0.2 hz frequency range of horizontal translational oscillation,” *Aviation, space, and environmental medicine*, vol. 72, no. 3, pp. 188–192, 2001.

[12] B. E. Donohew and M. J. Griffin, “Motion sickness: effect of the frequency of lateral oscillation,” *Aviation, space, and environmental medicine*, vol. 75, no. 8, pp. 649–656, 2004.

[13] L. Labakhua, U. Nunes, R. Rodrigues and F. S. Leite, “Smooth trajectory planning for fully automated passengers vehicles: spline and clothoid based methods and its simulation,” in *Int. Conf. on Inform. in Control, Automat. And Robot.*, 2006.

[14] S. Gulati and B. Kuipers, “High performance control for graceful motion of an intelligent wheelchair,” in 2008 IEEE International Conference on Robotics and Automation. IEEE, 2008, pp. 3932–3938.

[15] F. Mohseni, J. Aslund, E. Frisk and L. Nielsen, “Fuel and Comfort Efficient Cooperative Control for Autonomous Vehicles,” *IEEE Intelligent Vehicles Symposium (IV)*, 2017.

[16] Z. Htike, G. Papaioannou, E. Velenis and S. Longo, “Motion planning of self-driving vehicles for motion sickness minimisation,” *2020 European Control Conference (ECC)*, pp. 1719-1724, 2020.

[17]Z. Htike, G. Papaioannou, E. Siampis, E. Velenis and S. Longo, "Fundamentals of motion planning for mitigating motion sickness in automated vehicles," in *IEEE Transactions on Vehicular Technology*, vol. 71, no. 3, pp. 2375-2384, Mar. 2022

[18] M. A. Patterson and A. V. Rao, "Gpops-ii: A matlab software for solving multiple-phase optimal control problems using hp-adaptive gaussian quadrature collocation methods and sparse nonlinear programming," ACM Transactions on Mathematical Software (TOMS), vol. 41, no. 1, pp. 1–37, 2014.

[19]V. Jain, S. S. Kumar, G. Papaioannou, R. Happee, and B. Shyrokau, "Optimal trajectory planning for mitigated motion sickness: Simulator study assessment," IEEE Transactions on Intelligent Transportation Systems, 2023.

[20]D. Li and J. Hu, "Mitigating motion sickness in automated vehicles with frequency-shaping approach to motion planning," in *IEEE Robotics and Automation Letters*, vol. 6, no. 4, pp. 7714-7720, Oct. 2021.

[21]M. J. Griffin and K. L. Mills, "Effect of frequency and direction of horizontal oscillation on motion sickness." Aviation, space, and environmental medicine, vol. 73, no. 6, pp. 537–543, 2002.

[22]M. J. Griffin and M. M. Newman, "Visual field effects on motion sickness in cars," Aviation, space, and environmental medicine, vol. 75, no. 9, pp. 739–748, 2004.

[23]Y. Zheng, B. Shyrokau and T. Keviczky, "Mitigating Motion Sickness with Optimization-based Motion Planning," *arXiv: 2301.07977v1,* 2023.

[24]G. Papaioannou, R. Desai, and R. Happee, "The impact of body and head dynamics on motion comfort assessment," arXiv preprint arXiv:2307.03608, 2023.

[25]G. Papaioannou, J. Jerrelind, L. Drugge, and B. Shyrokau, "Assessment of optimal passive suspensions regarding motion sickness mitigation in different road profiles and sitting conditions," in 2021 IEEE International Intelligent Transportation Systems Conference (ITSC). IEEE, 2021, pp. 3896–3902.

[26]M. Mirakhorlo, N. Kluft, B. Shyrokau, and R. Happee, "Effects of seat back height and posture on 3d vibration transmission to pelvis, trunk and head," International Journal of Industrial Ergonomics, vol. 91, p. 103327, 2022.

[27]A. Steinke and U. Konigorski, "Trajectory planning considering motion sickness and head movements," IFAC-PapersOnLine, vol. 55, no. 14, pp. 113–119, 2022.

[28]"Least p-norm optimal iir filter - matlab iirlpnorm." [Online]. Available: https://mathworks.com/help/dsp/ref/iirlpnorm.html

[29]M. H. Moradi, "Predictive control with constraints, jm maciejowski; pearson education limited, prentice hall, london, 2002, pp. ix+ 331, 2003.

[30]B. Houska, H. J. Ferreau, and M. Diehl, "Acado toolkit—an open-source framework for automatic control and dynamic optimization," Optimal Control Applications and Methods, vol. 32, no. 3, pp. 298–312, 2011.

[31]I. Bae, J. Moon, J. Jhung, H. Suk, T. Kim, H. Park, J. Cha, J. Kim, D. Kim and S. Kim, "Self-Driving like a Human driver instead of a Robocar: Personalized comfortable driving experience for autonomous vehicles," *arXiv: 2001.03908*, 2020.

[32]"KKT Tolerance– Toolkit for Automatic Control and Dynamic Optimization." [Online]. Available: https://sourceforge.net/p/acado/discussion/general/thread/6e412636/

[33] "Find minimum of constrained nonlinear multivariable function - matlab fmincon." [Online]. Available: https://mathworks.com/help/optim/ug/fmincon.html

4

NONLINEAR MODEL PREDICTIVE CONTROL

Control is not just about steering and braking.
It's about managing your mind, emotions, and your fear at 200 mph.

Jenson Button

4.1 INTRODUCTION

In this chapter, advanced strategies using nonlinear model predictive control (NMPC) will be explored, focusing on: traction control (TC), torque-vectoring (TV) and active suspension system (AS). TC is fundamental in ensuring vehicle stability, enhancing handling, and optimising passenger comfort under varying driving conditions, making it a key aspect in mitigating motion sickness (MS). NMPC, with its ability to predict future vehicle behaviour and optimise control inputs in real time, provides a powerful framework for managing the complex dynamics involved in traction control, offering opportunities to minimise vehicle oscillations, abrupt movements, and other dynamics that often trigger MS. TC focuses on maintaining the appropriate level of grip between the tires and the road, ensuring the vehicle does not experience wheel slip or lose traction in challenging conditions, such as during rapid acceleration or on slippery surfaces. By regulating torque distribution to the wheels, TC systems prevent sudden changes in vehicle velocity or direction, which are common contributors to MS. Maintaining consistent grip and stability helps reduce jerks, unwanted accelerations, and sudden shifts in body posture, all of which are triggers for MS. Furthermore, by providing smoother acceleration and deceleration profiles, traction control plays a key role in creating a more predictable and comfortable ride, which is critical for passengers who are prone to MS. TV, which – in the specific test case – dynamically adjusts the distribution of driving torque between the left and right wheels of an axle, adds an additional layer of control to traction systems. It is particularly useful in enhancing the vehicle's cornering capabilities and maintaining optimal yaw control. By selectively distributing torque, TV can reduce understeer or oversteer, keeping the vehicle more aligned with the intended path and reducing abrupt lateral accelerations or oscillations that can exacerbate MS. From the perspective of MS mitigation, TV is significant because it can fine-tune the vehicle's lateral dynamics, minimising the unpredictable, swaying motions that often lead to discomfort in passengers. It enables smoother cornering transitions and better control over the vehicle's rotational behaviour, reducing the forces acting on the passengers' vestibular systems, which is often a key contributor to the onset of MS. However, TV alone may not address all aspects of vehicle dynamics that contribute to MS, particularly those related to vertical and lateral body movements over uneven terrain. To mitigate MS more comprehensively, it is important to consider its integration with AS. This system provides the capability to modify the suspension forces in real time, adjusting to road conditions to control body roll, pitch, and vertical accelerations. These vertical dynamics are critical for MS, as excessive or sudden changes in pitch (nose diving or lifting) and roll (side-to-side body tilt) can trigger vestibular disturbances. By actively counteracting these motions, AS can reduce the perception of abrupt or excessive movements that might provoke MS symptoms. In addition, AS systems help in maintaining optimal tire contact with the road, which not only improves traction and handling but also ensures smoother ride quality, further minimising the high-frequency vibrations and bumps that can lead to discomfort. When TV and AS systems are integrated into a unified control strategy, they offer a more comprehensive approach to addressing the various aspects of vehicle dynamics that contribute to MS. Torque vectoring's precise control over yaw and lateral dynamics, combined with active suspension's ability to manage vertical dynamics and body roll, can create a much smoother, more controlled driving experience. This synergy helps in reducing the lateral, longitudinal, and vertical forces that act on the passengers, significantly mitigating the triggers of motion sickness. By leveraging NMPC to predict and optimise these control strategies in real time, this integrated approach presents an effective solution for motion sickness mitigation, particularly in vehicles that navigate complex terrains or engage in dynamic manoeuvres.

4.2 TRACTION CONTROLLERS

4.2.1 STATE-OF-THE-ART

Passenger cars can experience lateral stability and agility issues in several situations, e.g., while traveling on slippery roads, or, in general, during emergency steering conditions, such as those of obstacle avoidance manoeuvres. Critical vehicle behaviour is caused by the saturation of the lateral tire forces when they reach the friction limit [1], which usually does not concurrently occur on the front and rear axles.

During the last three decades, vehicle dynamics control systems based on direct yaw moment control (DYC) have been widely implemented in production cars, to improve their active safety performance. While these systems traditionally rely on the actuation of the friction brakes only in emergency conditions [2], a broad literature has also dealt with the benefits of continuously active torque-vectoring (TV), especially for electric vehicle architectures with two powertrains per axle [3].

The main targets of DYC systems [4] are: i) at the vehicle level, lateral and yaw dynamics control, via the attenuation of the yaw rate and sideslip angle peaks during limit handling operation, and, in case of TV, generation of desirable levels of vehicle understeer throughout the lateral acceleration range, e.g., to increase cornering agility; and ii) at the individual corner level, wheel slip control in traction and braking, which also contributes to i). With respect to (w.r.t.) ii), the higher control bandwidth and accuracy in torque generation of individually controlled electric motors enable continuous wheel torque modulation, which brings enhanced tire slip control, and thus the reduction of the vehicle stopping distances and acceleration times, see the experimental results in [5] and [6].

In parallel, thanks to the rapidly increasing performance of the available computing hardware and numerical optimisation algorithms, model predictive control (MPC) has become a popular technique for vehicle dynamics applications at the research level. MPC is based on the solution of an optimisation problem minimising a cost function evaluated by a model along a finite prediction horizon, subject to a set of constraints [7]. Several MPC formulations for vehicle dynamics control have been demonstrated in real-time, e.g., see [8]–[14], which makes MPC potentially attractive also for future production vehicles. In the active safety context, MPC implementations mainly address: 1) path tracking for automated or semi-automated vehicles, e.g., see the nonlinear model predictive controllers (NMPCs) in [15] and [16], and the comparison between an NMPC and two linear time-varying (LTV) MPCs in [9]; 2) active safety control systems, e.g., see [17], including DYC, which is the focus of this study; and 3) the combination of 1) and 2) [10].

W.r.t. DYC, targets i) (i.e., vehicle yaw/sideslip control), and ii) (i.e., wheel slip control) can be achieved through different MPC-based architectures, depending on:

- The nature of the selected MPC algorithm, i.e., the optimal control problem: 1) can be linear (e.g., see the LTV MPCs in [18], and [11]), nonlinear [13], [14], [19]–[21], or hybrid [17]; and 2) can be solved online ([11], [13], [21]), in the framework of the so-called implicit MPC, which implies significant computational load in the control unit, or offline [17], [19], [20], in which case the optimal (explicit) solution is stored in the control unit, which only needs to carry out a computationally light function evaluation, at the expense of much more demanding memory requirements.
- The mechanical degrees of freedom of the vehicle prediction model embedded in the MPC algorithm, and in particular on whether this: 1) considers [12], [13], [21], [22] or neglects [18], [19] the longitudinal vehicle dynamics; and 2) includes ([13], [23], [22]) or excludes [12], [14], [18], [19], [21] the rotational wheel dynamics.
- The DYC control input, which can be in the form of: 1) a reference direct yaw moment [17], to be converted into reference wheel torque levels by the bottom layers of the control architecture; 2) reference longitudinal slip ratios for the four vehicle corners, which requires the presence – outside the DYC algorithm – of external continuously active wheel slip controllers [21], [22]. Although 2) brings some numerical benefits in the solution of the DYC optimisation problem [24], from a practical viewpoint this arrangement is difficult to implement in TV systems, because it requires accurate and smooth wheel slip control also in normal driving conditions; or 3) reference wheel torque levels for the four vehicle corners [11], [13], [22], [23].
- The inclusion of the wheel slip control function in the DYC algorithm [23], according to a centralised architecture, or in an external control layer [21], [22] within a multi-layer architecture. In the first case, the longitudinal slip limitation can be implemented in the form of a constraint on the individual slip ratios, wheel torque levels, or longitudinal tire forces. In some studies, such constraint is based on the imposed or estimated tire-road friction factor [11], which, however, on its own would not be practically effective on real vehicles, given the significant level of uncertainty of currently available estimators. Alternatively, similarly to production vehicles, the wheel slip control function can be achieved through feedback control structures in a separate control layer w.r.t. the DYC, see the architecture in [21], [22], which uses sliding mode control (SMC) for traction control (TC). Further examples of independent wheel slip controllers that are applicable to multi-layer control layouts are the proportional integral (PI) controller in [25], the SMC in [26], the maximum transmissible torque estimation strategy in [27], and the MPCs in [25], [28]–[30].

The literature includes extremely limited comparative analyses of MPC-based DYCs, from the viewpoint of their integration and interaction with the wheel slip control function. More specifically, [22] compares: a model predictive DYC including the wheel slip dynamics in the prediction model, and using the individually controllable rear wheel torque levels as control inputs; with: 2) an MPC-based DYC neglecting the wheel dynamics, and adopting the rear longitudinal slips as control inputs, which are continuously tracked by an SMC. The authors state that the inclusion of the wheel dynamics results only in a more complex optimisation problem and does not provide any appreciable performance benefit. However, the comparison is conducted for typical pure cornering manoeuvres, with zero torque demand at the vehicle level, in which high wheel slip events are marginal. The detailed comparisons among multiple implicit and explicit MPC-based DYC configurations in [20] and [21] only involve prediction models without wheel dynamics, and – again – focus the assessment on the lateral vehicle dynamics.

In summary, for operating conditions with significant longitudinal acceleration during extreme cornering, the available MPC-based DYC literature lacks analyses and performance comparisons of: 1) prediction model implementations excluding and including wheel dynamics; and 2) centralised and multi-layer architectures for vehicle stability and wheel slip control, and the interaction between the two functions.

To address the gap, during cornering-while-accelerating manoeuvres at the limit of handling, this study proposes and compares: 1) a novel multi-layer TV and TC architecture, consisting of an NMPC algorithm for DYC, using prediction models with and without wheel dynamics, and coupled with external feedback wheel slip controllers, which communicate their control inputs to the powertrains, as well as back to the DYC for imposing realistic direct yaw moment constraints; and 2) a centralised NMPC architecture ('Centralised NMPC' in the remainder), similar to the one in [13], which includes a soft constraint on the longitudinal slips, in addition to the terms for the control of the yaw and sideslip dynamics. The simulation analysis, based on a high-fidelity vehicle model, considers the computational performance and aspects associated with the prediction horizon length and its discretisation. The chapter is organised as follows: Section 4.2.2 discusses the simulation and control framework; Section 4.2.3 describes the controllers; Section 4.2.4 deals with the controller calibration routine and key performance indicators (KPIs); Section 4.2.5 analyses the simulation results; finally, the main conclusions are summarised in Section 4.2.6.

4.2.2 SIMULATION AND CONTROL FRAMEWORK

The simulation and control framework, integrated in the Matlab/Simulink environment, consists of (Figure 4.2.1):

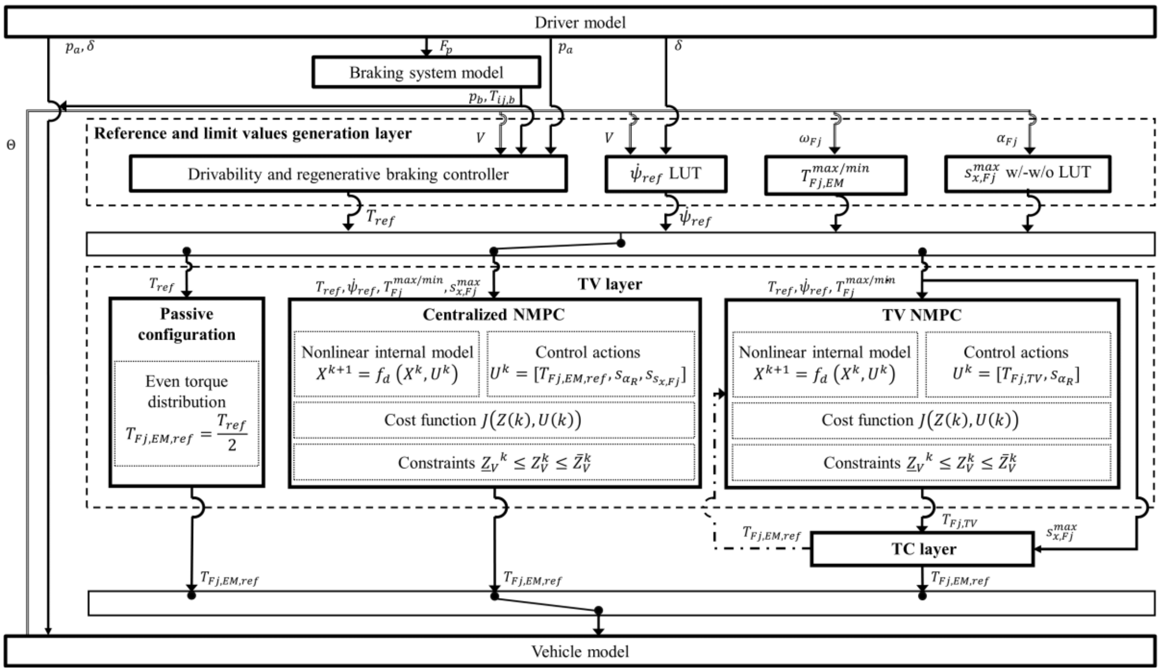

Figure 4.2.1: Simplified schematic of the implemented simulation and control framework.

- The driver model, which outputs the accelerator pedal position, p_a; the brake pedal force, F_p; and the steering angle, δ.
- The braking system model, which converts F_p into a tandem master cylinder pressure, pb, and friction braking torque values, $T_{ij,b}$, where the subscript i = F, R indicates the front or rear axles, and the subscript j = L, R refers to the left or right sides.
- The reference and limit values generation layer, including: 1) the drivability and regenerative braking controller, which computes the total torque demand,T_{ref}, for the electric powertrains; 2) the reference yaw rate $\dot{\psi}_{ref}$ generator; 3) the generator of the limit values of the longitudinal slip ratios, $s_{x,Fj}^{max}$, for traction control operation; and 4) the generator of the motor torque limits, $T_{Fj}^{max/min}$, which vary with speed and temperature.
- The TV layer, which outputs the individual front reference powertrain torque values, referred to as $T_{Fj,EM,ref}$ or $T_{Fj,TV}$, depending on the controller configuration. This layer includes: 1) the NMPCs that implement the optimal control problems described in Section 3, where 'Centralised NMPC' operates as an integrated DYC and TC system, while 'TV NMPC' operates only as a DYC; and 2) alternatively to 1), the benchmarking 'Passive' configuration, which provides even front motor torque distribution on the left and right machines. Appropriate switches are implemented

in the simulation environment to select the control configuration for the specific test.

- The TC layer, which is active only with 'TV NMPC', and contains proportional integral (PI) TCs, which output the modified motor torque demands, $T_{Fj,PI}$, to prevent excessive wheel slip. The $T_{Fj,PI}$ values are sent only to the plant in the so-called 'TV NMPC w/o FB' configurations, i.e., the TV block is not aware of the TC interventions. On the contrary, in the 'TV NMPC w/ FB' configurations, the $T_{Fj,PI}$ values are also communicated back to the TV controller, which considers them within the constraints, see Section 4.2.3.
- The high-fidelity nonlinear simulation model for control system assessment, implemented in CarMaker, including the degrees of freedom of the sprung and unsprung masses, suspension elasto-kinematics, and a nonlinear tire model (the magic formula 5.2) with relaxation. The model formulation is completely independent from the one of the prediction models in Section 3, which enables a realistic assessment of controller robustness. The model generates the set of vehicle variables, Θ, required for the operation of the other simulation and control layers. As it is discussed by a broad literature, e.g., see [31], the state estimation layer, e.g., to estimate the sideslip angle (β) and vehicle speed (V) values for the operation TV controllers, is not included in the implementation. The case study application is the front-wheel-drive commercial electric vehicle with direct drive in-wheel motors of the European SYS2WHEEL project. Its main parameters, provided by the involved industrial participants, are reported in Table 4.2.2.

Table 4.2.2 – Main vehicle parameters.

Symbol	Name and unit	Value
m	Mass (kg)	2252
J_z	Yaw mass moment of inertia (kgm^2)	4825
L_{TOT}	Wheelbase (m)	3.1
L_F	Front semi-wheelbase (m)	1.6
R_w	Laden wheel radius (m)	0.31
d_F	Front track width (m)	1.51
d_R	Rear track width (m)	1.53
H_{CG}	Height of the vehicle centre of mass (m)	0.62
$T_{mot,Fj}^{max}$	Peak value of the in-wheel motor torque (Nm)	700
$P_{mot,Fj}^{max}$	Maximum in-wheel motor power (kW)	75
$\omega_{mot,Fj}^{max}$	Maximum in-wheel motor speed (rpm)	1500

4.2.3 CONTROLLER FORMULATIONS

4.2.3.1 Reference yaw rate and longitudinal slip ratios

In accordance with the requirements provided by the manufacturer of the considered light commercial vehicle, the objective of the specific TV controller is to bring a cornering response that is as close as possible to the one of the 'Passive' configuration in steady-state cornering in high tire-road friction conditions, for given steering input and vehicle speed. Hence, the TV system compensates the effects of the steering transients and traction/braking torque levels, thus enhancing active safety, but – given the vehicle category – is not used to shape the understeer characteristic in nominal conditions. As a consequence, the steady-state reference yaw rate, $\dot{\psi}_{ref,SS}$, is expressed as a nonlinear map, see Figure 4.2.2, that is a function of δ and V, and was generated by simulating the 'Passive' vehicle during ramp steer manoeuvres at different constant speed values, for high tire-road friction conditions. In the online algorithm, $\dot{\psi}_{ref,SS}$ is saturated based on the available tire-road friction level:

$$\begin{gathered}\dot{\psi}_{ref,SS,\mu} = sat_{-\dot{\psi}_{sat,\mu}}^{\dot{\psi}_{sat,\mu}}\left(\dot{\psi}_{ref,SS}\right), \\ \text{with:}\, \dot{\psi}_{sat,\mu} = \frac{\mu g}{V}\end{gathered} \tag{4.2.1}$$

where μ is the estimated tire-road friction coefficient, and g is the gravitational acceleration. Then $\dot{\psi}_{ref,SS,\mu}$ is filtered through a first order transfer function, which provides the reference dynamic behaviour in cornering, and outputs $\dot{\psi}_{ref}$. The selected steady-state reference yaw rate formulation tends to compensate for the variation of the understeer characteristic associated with the tire-road friction level, and thus enhances the predictability of the cornering response. Future analyses for different demonstrator vehicles will include reference yaw rate set-ups that modify also the steady-state cornering response, see [3]. Nevertheless, during the activity it was verified that the reference yaw rate formulation does not have any significant impact on the results of the comparison between centralised and multi-layer MPC implementations, which is the objective of this study.

Two options were considered w.r.t. the slip ratio (s_x) threshold used by the TCs, to ensure that the conclusions of the comparison are not misled by a specific threshold selection: 1) constant threshold set to 0.1. $s_{x,Fj}^{max} = 0.1$ is a rather conservative selection for the specific tire characteristics, see the very limited reduction of F_y, and thus vehicle cornering capability, w.r.t. F_{y0}, for any tire slip angle value, α, in the plot in Figure 4.2.3 of the nondimensional lateral tire force, F_y/F_{y0}, as a function of s_x, where F_y is the lateral tire force at the considered s_x value, and F_{y0} is the lateral tire force at zero slip ratio; and 2) variable slip ratio threshold as a function of α, to achieve the condition $F_y/F_{y0} = 0.45$ for any α, according to the horizontal line in Figure 4.2.3. Setting 2) implies less invasive TC interventions at significantly larger s_x levels than 1).

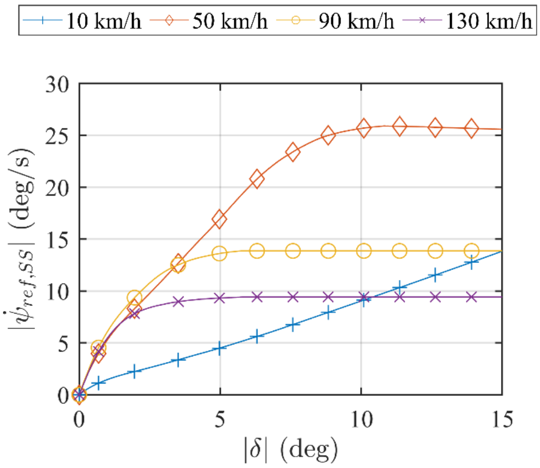

Figure 4.2.2: Extract of the nonlinear reference yaw rate map.

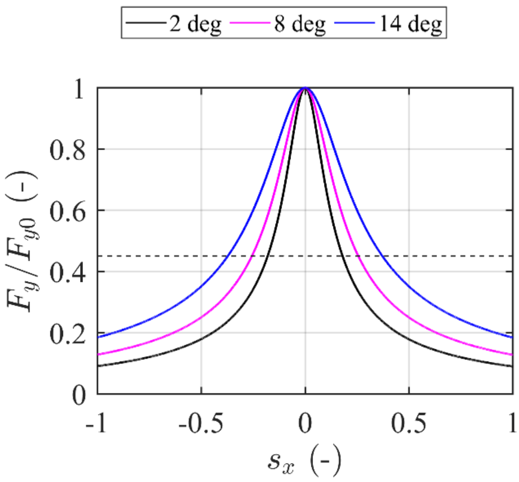

Figure 4.2.3: Normalised lateral tire forces as functions of the slip ratio for different slip angles, at a constant vertical load (4 kN).

4.2.3.2 Prediction models

In the most advanced NMPC set-ups of this study, the prediction model is based on a nonlinear 7-degree-of-freedom (7-DoF) double track formulation, including wheel dynamics. The sign conventions of the main variables are in Figure 4.2.4.

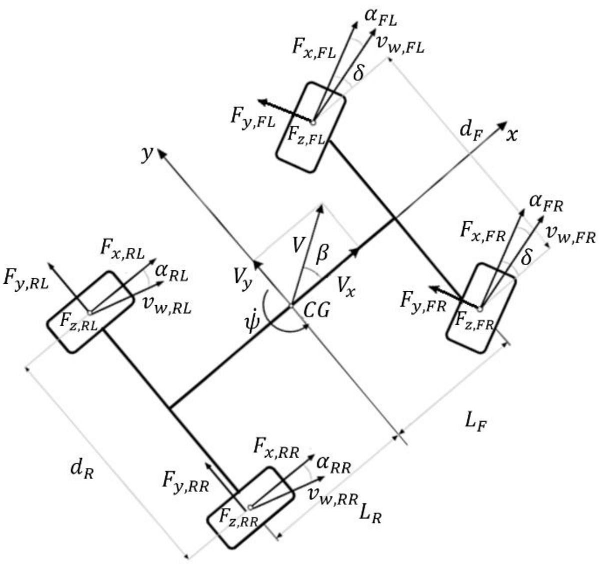

Figure 4.2.4: Top view of the vehicle, with indication of the main variables and their sign conventions.

The model is described by the following differential equations:

- Longitudinal force balance

$$m\dot{V}_x = \Big\{\big[F_{x,FL} + F_{x,FR}\big]\cos(\delta) - \big[F_{y,FL} + F_{y,FR}\big]\sin(\delta) + \big[F_{x,RL} + F_{x,RR}\big] - \frac{1}{2}\rho V^2 S C_{drag}\Big\} + mV_y\dot{\psi} \tag{4.2.2}$$

where m is the vehicle mass; V_x and V_y are the longitudinal and lateral components of vehicle velocity; $\dot{\psi}$ is the yaw rate; $F_{x,ij}$ and $F_{y,ij}$ are the longitudinal and lateral tire forces; ρ is air density; S is the vehicle frontal area; and C_{drag} is the aerodynamic drag coefficient.

- Lateral force balance

$$m\dot{V}_y = \{[F_{x,FL} + F_{x,FR}]\sin(\delta) + [F_{y,FL} + F_{y,FR}]\cos(\delta) + [F_{y,RL} + F_{y,RR}]\} - mV_x\dot{\psi} \tag{4.2.3}$$

- Yaw moment balance

$$\begin{aligned} J_z\ddot{\psi} = {} & L_F\{[F_{y,FL} + F_{y,FR}]\cos(\delta) + [F_{x,FL} + F_{x,FR}]\sin(\delta)\} - L_R[F_{y,RL} + F_{y,RR}] \\ & + \frac{d_F}{2}\{[F_{y,FL} - F_{y,FR}]\sin(\delta) + [F_{x,FR} - F_{x,FL}]\cos(\delta)\} \\ & + \frac{d_R}{2}[F_{x,RR} + F_{x,RL}] \end{aligned} \tag{4.2.4}$$

where J_z is the vehicle yaw mass moment of inertia; L_F and L_R are the front and rear semi-wheelbases; and d_F and d_R are the front and rear track widths.

- Wheel moment balance

$$I_{w,i}\dot{\omega}_{ij} = T_{ij} - F_{x,ij}R_w - f_{roll}F_{z,ij}R_w \tag{4.2.5}$$

where $I_{w,i}$ is the wheel moment of inertia, which – given the presence of front in-wheel motors – is larger on the front axle; $\dot{\omega}_{ij}$ is the angular wheel acceleration; T_{ij} is the individual wheel torque, caused by the front electric powertrains ($T_{Fj,EM}$ contribution) and/or friction brakes ($T_{ij,b}$ contribution), i.e., $T_{Fj} = T_{Fj,EM} - T_{Fj,b}$ and $T_{Rj} = -T_{Rj,b}$; f_{roll} is the rolling resistance coefficient; and $F_{z,ij}$ is the vertical tire load.

- Electric motor and inverter dynamics

$$\dot{T}_{Fj,EM} = \frac{T_{Fj,EM,ref} - T_{Fj,EM}}{\tau_s} \tag{4.2.6}$$

where $T_{Fj,EM}$ is the simulated actual electromagnetic torque of the in-wheel machine; $T_{Fj,EM,ref}$ is the reference torque for the individual front motor, i.e., the control input; and τ_s is the time constant approximating the powertrain dynamics. The tire forces are modelled through a simplified version of the Pacejka magic formula [32], which determines the total tire force coefficient, μ_{ij}, as:

$$\mu_{ij}(s_{ij}) = D_{ij}\sin(C\tan^{-1}(B_{ij}s_{ij})) \tag{4.2.7}$$

where s_{ij} is the total tire slip; and D_{ij}, C and B_{ij} are the peak, shape, and stiffness factors. Equation (4.2.7) is a simple yet realistic formulation, which is easy to tune and independent from the complete set of magic formula coefficients of the high-fidelity vehicle model. While C is constant, D_{ij} and B_{ij} are expressed as:

$$D_{ij} = a_1F_{z,ij}^2 + a_2F_{z,ij} \tag{4.2.8}$$

$$B_{ij} = \frac{a_3\sin(a_4\tan^{-1}(a_5F_{z,ij}))}{CD_{ij}} \tag{4.2.9}$$

where a_1 ,.., a_5 are constant coefficients. s_{ij} results from the composition of the longitudinal and lateral slip components, $s_{x,ij}$ and $s_{y,ij}$:

$$s_{ij} = \sqrt{s_{x,ij}^2 + s_{y,ij}^2} \tag{4.2.10}$$

with $s_{x,ij}$ and $s_{y,ij}$ being defined as:

$$s_{x,ij} = \frac{\omega_{ij} R_{w,roll} - v_{w,ij}\cos(\alpha_{ij})}{v_{w,ij}\cos(\alpha_{ij})} \tag{4.2.11}$$

$$s_{y,ij} = -\tan(\alpha_{ij}) \tag{4.2.12}$$

where $R_{w,roll}$ is the wheel rolling radius; and $v_{w,ij}$ is the linear wheel speed at the ground contact point, which is expressed as:

$$\begin{gathered} v_{w,ij} = V + k_1\dot{\psi}\left[\frac{d_i}{2}\cos(\beta) + k_1 k_2 L_i \sin(\beta)\right] \\ j = L, R \quad \begin{cases} k_1 = -1 & \text{if} \quad j = L \\ k_1 = 1 & \text{if} \quad j = R \end{cases} \\ i = F, R \quad \begin{cases} k_2 = 1 & \text{if} \quad i = F \\ k_2 = -1 & \text{if} \quad i = R \end{cases} \end{gathered} \tag{4.2.13}$$

where β is the sideslip angle at the vehicle center of gravity. α_{ij} is computed as in [33]:

$$\begin{gathered} \alpha_{ij} = \tan^{-1}\left(\frac{V_y + k_2\dot{\psi}L_i}{V_x + k_1\dot{\psi}\frac{d_i}{2}}\right) - k_3\delta \\ i = F, L \quad \begin{cases} k_3 = 1 & if \quad i = F \\ k_3 = 0 & if \quad i = R \end{cases} \end{gathered} \tag{4.2.14}$$

The longitudinal and lateral tire force coefficients, $\mu_{x,ij}$ and $\mu_{y,ij}$, are functions of the relative magnitude of the slip components:

$$\mu_{x,ij} = \frac{s_{x,ij}}{s_{ij}}\mu_{ij}(s_{ij}) \tag{4.2.15}$$

$$\mu_{y,ij} = \frac{s_{y,ij}}{s_{ij}}\mu_{ij}(s_{ij}) \tag{4.2.16}$$

and are used for the computation of $F_{x,ij}$ and $F_{y,ij}$:

$$F_{x,ij} = \mu_{x,ij} F_{z,ij} \tag{4.2.17}$$

$$F_{y,ij} = \mu_{y,ij} F_{z,ij} \tag{4.2.18}$$

The NMPC prediction model equations are re-arranged to be expressed through the following nonlinear continuous time (t) formulation:

$$\begin{gathered} \dot{X} = f(X(t), U(t)) \\ Z = h(X(t), U(t)) \end{gathered} \tag{4.2.19}$$

where X, U and Z are the state, control input and output vectors; and f and h are nonlinear functions. X, U, Y, Z and f and h differ among the controller configurations discussed in the following subsections.

4.2.3.3 Nonlinear optimal control problem

NMPC is based on the solution of an optimisation problem, in which the discretised dynamic prediction model of the system is solved over a finite prediction horizon, consisting of N steps. The sequence of optimal control inputs, $U(\cdot)$, targets the minimisation of the cost function J, subject to appropriate equality and inequality constraints, which depend on the considered controller formulation. Only the first element of the control input sequence, $U(0)$, is applied to the system. Once a new set of measured or estimated states is available at the next time step, the whole process is repeated, according to the receding horizon approach [7] and [28].

The discrete form of the nonlinear optimal control problem is:

$$\begin{gathered}
\min_{U} J\left(Z(0), U(\cdot)\right) := \frac{1}{2}\sum_{k=0}^{N-1}\left(\left\|Z^k - Z_{ref}^k\right\|_Q + \|U^k\|_R\right)^2 + \left\|Z^N - Z_{ref}^N\right\|_{Q_N}^2 \\
\text{s.t.} \\
X^{k+1} = f_d\left(X^k, U^k\right) \\
Z^k = h_d\left(X^k, U^k\right) \\
\underline{Z} \leq Z^k \leq \overline{Z} \\
\underline{Z} \leq Z^N \leq \overline{Z} \\
\underline{U} \leq U^k \leq \overline{U} \\
U(\cdot) : [0, N-1]
\end{gathered} \tag{4.2.20}$$

where the index k refers to the step number along the prediction horizon, including N steps in total; Z_{ref} is the reference value of the output vector; $\underline{Z}$ and $\overline{Z}$ are the lower and upper limits for Z; $\underline{U}$ and $\overline{U}$ are the lower and upper limits for U; f_d and h_d are the discretised versions of f and h; and R, Q, and Q_N are positive semi-definite weight matrices.

4.2.3.4 Centralised NMPC

The prediction model of 'Centralised NMPC' uses equations (4.2.1)–(4.2.18). The state, control input and output vectors are:

$$X = [V_x, V_y, \dot{\psi}, \omega_{FL}, \omega_{FR}, \omega_{RL}, \omega_{RR}, T_{FL,EM}, T_{FR,EM}]^T \tag{4.2.21}$$

$$U = [T_{FL,EM,ref}, T_{FR,EM,ref}, s_\alpha, s_{s_{x,FL}}, s_{s_{x,FR}}]^T \tag{4.2.22}$$

$$Z = [\dot{\psi}, T_{tot,EM,ref}, s_\alpha, s_{s_{x,FR}}, s_{s_{x,FR}}]^T \tag{4.2.23}$$

where $T_{tot,EM,ref}$ is the sum of the reference torque values for the front motors, which must track T_{ref}; s_α is the slack variable (i.e., an auxiliary variable to impose a soft constraint) on the rear axle sideslip angle; and $s_{s_{x,FL}}$ and $s_{s_{x,FR}}$ are the slack variables constraining the longitudinal slip ratios of the respective tires. The optimal control problem is formulated as (4.2.20), with hard constraints on $T_{Fj,EM,ref}$ (4.2.24) and the battery power P_{batt} (4.2.25), based on the respective component characteristics, and soft constraints on the rear axle sideslip angle (4.2.26)–(4.2.27) as well as on the longitudinal tire slip (4.2.28)–(4.2.29):

$$T_{Fj,EM}^{min} \leq T_{Fj,EM,ref}^k \leq T_{Fj,EM}^{max} \tag{4.2.24}$$

$$P_{batt}^{min} \leq P_{batt}^k \leq P_{batt}^{max} \tag{4.2.25}$$

$$s_\alpha \geq 0 \tag{4.2.26}$$

$$-\alpha_{rear}^{peak}(1 + s_\alpha) \leq \alpha_{rear}^k \leq \alpha_{rear}^{peak}(1 + s_\alpha) \tag{4.2.27}$$

$$s_{s_{x,Fj}} \geq \tag{4.2.28}$$

$$s_{x,Fj}^{min}\left[1 + s_{s_{x,Fj}}\right] \leq s_{x,Fj}^k \leq s_{x,Fj}^{max}\left[1 + s_{s_{x,Fj}}\right] \tag{4.2.29}$$

4.2.3.5 TV NMPC+PI with or without torque feedback

The notation ‘TV NMPC+PI’ indicates the controller architectures in which the TV function is carried out by the NMPC algorithm, while the TC function is implemented through a PI controller, see Figure 1 and the benchmarking TC in [25]. Given the presence of a bottom layer modifying the wheel torque, the prediction model of ‘NMPC TV+PI’ does not include the in-wheel motor dynamics expressed through (5), while the other internal model equations are identical to those of ‘Centralised NMPC’. Hence, X, U and Z are defined as:

$$X = [V_x, V_y, \dot{\psi}, \omega_{FL}, \omega_{FR}, \omega_{RL}, \omega_{RR}]^T \tag{4.2.30}$$

$$U = [T_{FL,TV}, T_{FR,TV}, s_\alpha]^T \tag{4.2.31}$$

$$Z = [\dot{\psi}, T_{tot,EM,ref}, s_\alpha]^T \tag{4.2.32}$$

The optimal control problem is formulated as (4.2.20), with constraints on the motor torque, battery power, and rear axle sideslip angle, see (4.2.24)–(4.2.27).

In the configuration ‘TV NMPC+PI w/ FB’, including feedback from the PI-based TC, the upper boundary of the electric motor torque, $T_{Fj,EM}^{max}$, accounts for the torque limitation applied by the TC layer in critical longitudinal slip conditions, on top of the torque limit, $T_{Fj,PWT}^{max}$, associated with the powertrain components (electric machine and inverter):

$$T_{Fj,EM}^{max} = \min\left(T_{Fj,PWT}^{max}, k_T T_{Fj,EM,ref}\right) \tag{4.2.33}$$

where k_T is a tunable relaxation factor, which is set to 1.1 in this study, to ensure that the TV layer does not over-constrain the reference torque w.r.t. the available tire-road friction level.

4.2.3.6 TV NMPC+PI with or without torque feedback and neglecting wheel dynamics

The prediction model formulation of the TV NMPC cases without wheel dynamics, indicated through the notation ‘w/o WD’ in the remainder (in the remainder, the absence of this notation implies that the wheel dynamics are considered), neglects the wheel moment balance (4.2.5) and the motor torque dynamics (4.2.6), i.e.:

$$F_{x,Fj} = \frac{T_{Fj,EM,ref} - T_{Fj,b}}{R_w} \tag{4.2.34}$$

while the longitudinal tire slips are considered constant along the prediction horizon. Therefore, X and Z are (see (4.2.31) for U):

$$X = [V_x, V_y, \dot{\psi}]^T \tag{4.2.35}$$

$$Z = [\dot{\psi}, F_{x,ref}, s_\alpha]^T \tag{4.2.36}$$

The optimal control problem is formulated as (4.2.20), with constraints on the motor torque, battery power, and rear axle sideslip angle, see (4.2.24)–(4.2.27), with the same distinction as in Section 4.2.3.5 between the upper boundary of the electric motor torque for the cases with and without TC torque feedback.

4.2.4 CONTROLLERS IMPLEMENTATION AND TUNING

4.2.4.1 Controller implementation

The NMPC formulations in Sections 4.2.3.4–4.2.3.6 were set up through the ACADO toolkit, which is a software environment and algorithm collection in C++ for automatic control and dynamic optimisation [34]. ACADO was used to solve the proposed constrained nonlinear optimisation problems (implicit NMPC). The toolkit generates a C-code, which is then usable in the Matlab/Simulink environment, see Figure 4.2.1, including the TC as well as the driver and CarMaker vehicle models. The selected solver parameters are: multiple shooting discretisation method, fourth order Runge Kutta integrator, and qpOASES QP optimisation algorithm.

4.2.4.2 Controller calibration routine

Given the significant variability of controller performance depending on the values of the calibration parameters, e.g., the cost function weights, a brute force optimisation routine of the proposed NMPCs was implemented, for a fair comparison of the architectures. The routine considers the following KPIs, where the notation '$\overline{}$' indicates that the index is normalised:

- The root mean square value of the yaw rate error, $\overline{RMSE_{\Delta\dot{\psi}}}$:

$$\overline{RMSE_{\Delta\dot{\psi}}} = \frac{\sqrt{\frac{1}{t_f - t_i}\int_{t_i}^{t_f}\left[\dot{\psi}_{ref}(t) - \dot{\psi}(t)\right]^2 dt}}{M_{\Delta\dot{\psi}}} \tag{4.2.37}$$

  where t_i and t_f are the initial and final times of the relevant part of the manoeuvre; and $M_{\Delta\dot{\psi}}$ is the normalisation factor.

- The maximum value of the yaw rate error magnitude along the manoeuvre, i.e., $\overline{\Delta\dot{\psi}^{max}}$, which penalises the yaw rate error peaks:

$$\overline{\Delta\dot{\psi}^{max}} = \frac{\max\left(\left|\dot{\psi}_{ref}(t) - \dot{\psi}(t)\right|\right)}{M_{\Delta\dot{\psi}^{max}}} \tag{4.2.38}$$

  with $M_{\Delta\dot{\psi}^{max}}$ being the normalisation factor.

- The peak value of the rear axle sideslip angle, $\overline{\alpha_{rear}^{max}}$, which assesses the stabilisation performance of the controller:

$$\overline{\alpha_{rear}^{max}} = \frac{\max|\alpha_{rear}|}{M_{\alpha_{rear}^{max}}} \tag{4.2.39}$$

  with $M_{\alpha_{rear}^{max}}$ being the respective normalisation factor.

- The normalised – through the factor $M_{V_{end}}$ – and re-arranged vehicle speed at the end of the manoeuvre, $\overline{V_{end}}$, which evaluates the longitudinal acceleration performance of the vehicle, and ensures that good performance corresponds to a low value of the indicator:

$$\overline{V_{end}} = 1 - \frac{V_{end}}{M_{V_{end}}} \tag{4.2.40}$$

- The root mean square value of the longitudinal slip error on the individual front tire, $\overline{RMSE_{\Delta s_{x,Fj}}}$, which assesses the TC performance:

$$\overline{RMSE_{\Delta s_{x,Fj}}} = \frac{\sqrt{\frac{1}{t_f - t_i}\int_{t_i}^{t_f}\left[\mathrm{DB}_{-\infty}^{s_{x,Fj,ref}}\left(s_{x,Fj,ref}(t) - s_{x,Fj}(t)\right)\right]^2 dt}}{M_{\Delta s_{x,Fj}}} \tag{4.2.41}$$

where $s_{x,Fj,ref} = s_{x,Fj}^{max}$ is the desired longitudinal slip; DB indicates the deadband function, which outputs a nonzero error only when $s_{x,Fj}$ exceeds $s_{x,Fj,ref}$; and $M_{\Delta s_{x,Fj}}$ is the normalisation factor.

- The integral of the absolute value of the direct yaw moment control action, $\overline{IACA_{M_z}}$, which evaluates the control effort:

$$\overline{IACA_{M_z}} = \frac{\frac{1}{t_f - t_i}\int_{t_i}^{t_f}|M_z|dt}{M_{IACA}} \tag{4.2.42}$$

where M_{IACA} is the normalisation factor; and M_z is the direct yaw moment, which is approximated as:

$$M_z = \frac{[T_{FL}(t) - T_{FR}(t)]d_F}{2R_w} \tag{4.2.43}$$

The normalisation factors ($M_{\Delta\dot{\psi}}$ = 20 deg/s; $M_{\Delta\dot{\psi}^{max}}$ = 60 deg/s; $M_{\alpha_{rear}^{max}}$ = 16 deg; $M_{V_{end}}$ = 125 km/h; $M_{\Delta s_{x,Fj}}$ = 0.12; and M_{IACA} = 3896 Nm) are considered as the values of the respective indicator in its dimensional form for the ‘Passive’ case, with the exception of M_{IACA}, which, being zero for the ‘Passive’ vehicle, is set as the maximum $IACA_{M_z}$ obtained through the controller configurations along the simulation set.

The automated brute force optimisation algorithm and the following analyses (see 4.2.5) focus on the multiple-step steer manoeuvre (i.e., a sequence of swift positive and negative steering inputs), carried out from an initial speed of 100 km/h, with T_{ref} = 600 Nm, and a maximum steering angle amplitude at the wheels of 14 deg, in high tire-road friction conditions. In the ‘Passive’ configuration, this test brings significant yaw rate and sideslip angle peaks, as well as evident wheel spinning. Therefore, this manoeuvre is selected as a representative example of extreme acceleration-while-turning conditions, requiring extensive and concurrent interventions of the TV and TC functions.

The optimisation routine runs simulations of the selected test – by using the high fidelity simulation model – for a dense grid of calibration parameter values, i.e., the elements of Q in (4.2.20), with the exception on the weight on the driver torque demand tracking, which is considered to be the same for all configurations. The brute force algorithm minimises the cost function J_{KPI}:

$$\begin{aligned} J_{KPI}^{*} &= \min_{Q} J_{KPI}\big|_{t_i}^{t_f} \\ &= \min_{Q}\Big[W_1 \overline{RMSE_{\Delta\dot{\psi}}} + W_2 \overline{\Delta\dot{\psi}^{max}} + W_3 \overline{\alpha_{rear}^{max}} + W_4 \overline{V_{end}} \\ &+ W_5 \sum_{j=L,R} \overline{RMSE_{\Delta s_{x,Fj}}} + W_6 \overline{IACA_{M_Z}}\ \Big] \\ &\text{s.t.}\ Q_{LB} \leq Q_{opt} \leq Q_{UB} \end{aligned} \tag{4.2.44}$$

where J_{KPI}^{*} is the optimal cost function value; $Q_{pq,LB}$ and $Q_{pq,UB}$ are the lower and upper bounds for the pq element of Q_{opt}; and W_1,…, W_6 are weights, which were selected (W_1 = 0.4; W_2 = 0.15; W_3 = 0.1; W_4 = 0.15; W_5 = 0.05; and W_6 = 0.1) to prioritise the yaw rate and sideslip angle performance, w.r.t. to the tracking of the individual tire slip ratios. For all configurations, α_{rear}^{peak} in (4.2.27) is set to 3 deg.

4.2.5 SIMULATION RESULTS

4.2.5.1 Sensitivity on prediction horizon and time step

For the ‘Centralised NMPC’ and ‘TV NMPC+PI w/ FB’ configurations, a sensitivity analysis was carried out with the simulation and control framework in Figure 1 along the considered multiple step steer, to investigate the effect of: 1) the controller sampling time, T_s, i.e., the time step at which the controller generates its control actions; and 2) the NMPC prediction horizon, $H_p = NT_s$, i.e., the time horizon covered by the NMPC prediction. For all configurations, the internal model discretisation time, T_d, i.e., the integration time step of the prediction model, was set to be $T_d = T_s/k_i$, with $k_i = 40$. The controller calibration was optimised according to (4.2.44) for the ‘TV NMPC+PI w/ FB’ configuration with $T_s =$ 30 ms and H_p = 90 ms, and – unless otherwise specified – was kept constant for the other configurations.

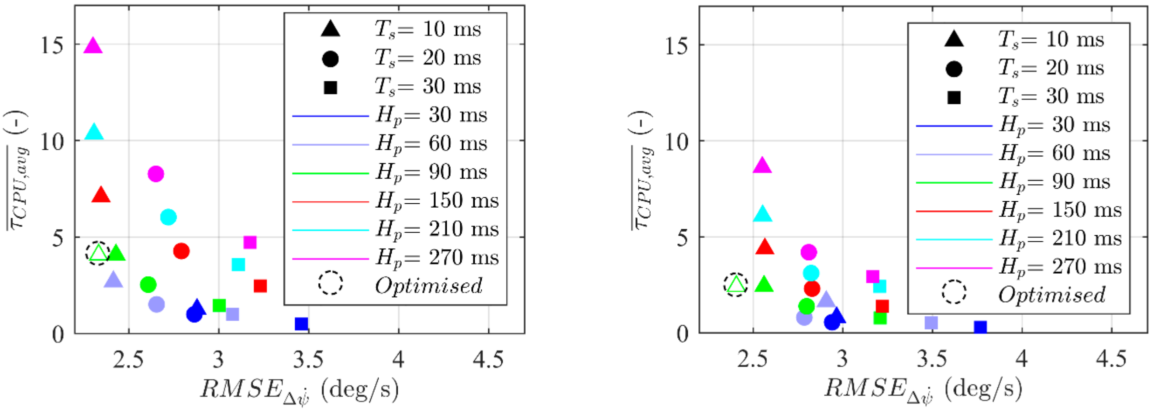

(a)

(b)

Figure 4.2.5: $\overline{\tau_{CPU,avg}}$ as a function of $RMSE_{\Delta\dot{\psi}}$, for different values of H_p and T_s: (a) ‘Centralised NMPC’; and (b) ‘TV NMPC+PI w/ FB’.

Figure 5 reports the NMPC execution time index, $\overline{\tau_{CPU,avg}}$, as a function of $RMSE_{\Delta\dot{\psi}}$, for ‘Centralised NMPC’ (subplot (a)) and ‘TV NMPC+PI w/ FB’ (subplot (b)). $\overline{\tau_{CPU,avg}}$ is a dimensionless value, defined as:

$$\overline{\tau_{CPU,avg}} = \frac{\tau_{CPU,avg}^{C,T_s-H_p}}{\tau_{norm}} \tag{4.2.45}$$

where $\tau_{CPU,avg}^{C,T_s-H_p}$ is the average central processing unit (CPU) time along the selected manoeuvre, for the controller operating at a given sample time T_s and prediction horizon H_p; and τ_{norm} is a normalisation time, which is the same in the two subplots, and corresponds to the CPU time of one of the real-time configurations in Section 4.2.5.2. For ‘Centralised NMPC’, $RMSE_{\Delta\dot{\psi}}$ improves, i.e., it is subject to a reduction, for decreasing values of T_s – and thus T_d – for a given H_p. For example, with H_p = 90 ms, $RMSE_{\Delta\dot{\psi}}$ goes from ~3 deg/s with T_s = 30 ms down to ~2.4 deg/s for T_s = 10 ms. At the same time, $\overline{\tau_{CPU,avg}}$ increases, e.g., from ~2 to ~4, respectively for T_s = 30 ms and 10 ms. For a fixed T_s, the increase of H_p tends to bring a smaller performance benefit than the decrease of T_s, at the price of a much more substantial increase in computational load. For example, for $T_s = 10$ ms, $RMSE_{\Delta\dot{\psi}}$ and $\overline{\tau_{CPU,avg}}$ are ~2.8 deg/s and ~1 at $H_p = 30$ ms, ~2.3 deg/s and ~7 at $H_p =$ 150 ms, and ~2.3 deg/s and ~15 at $H_p = 270$ ms.

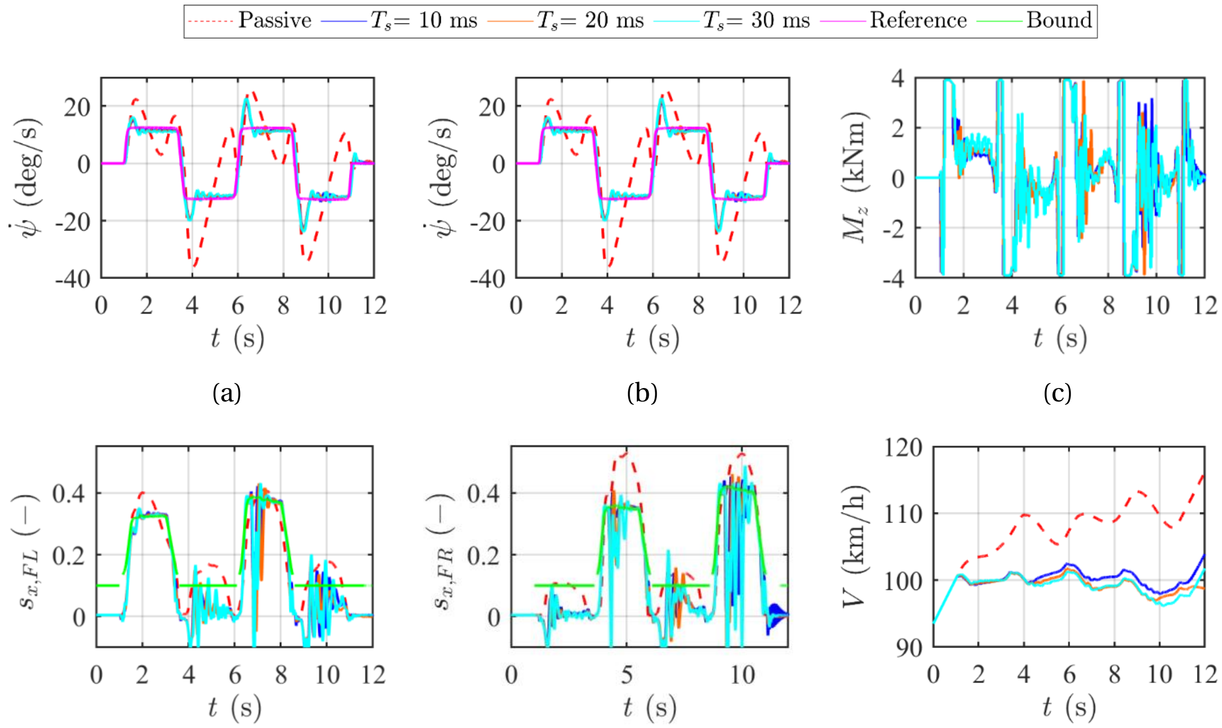

(a) (b) (c)

(d) (e) (f)

Figure 4.2.6: Time profiles of the main variables for 'TV NMPC+PI w/ FB', for $H_p = 90$ ms and different T_s values: (a) yaw rate tracking performance; (b) rear axle sideslip angle and its soft constraint bounds; (c) direct yaw moment; (d) front left and (e) front right longitudinal tire slips and their limit values; and (f) vehicle speed.

Figure 4.2.6 shows the time profiles of the main variables for 'Passive' and 'TV NMPC+PI w/ FB' with $H_p = 90$ ms and $T_s = 10$, 20, and 30 ms. Figure 6 highlights the major vehicle dynamics benefits in terms of yaw rate overshoot and rear axle sideslip angle peak reduction brought by 'TV NMPC+PI w/ FB' w.r.t. 'Passive'. The yaw rate and sideslip angle profiles are safe and comparable for all controller settings, although the increase of sampling time implies a rather marginal performance deterioration, e.g., see the slight yaw rate oscillations for $T_s = 30$ ms. As the wheel dynamics are faster than the vehicle yaw and sideslip response, the effect of T_s is much more evident on the longitudinal slip dynamics in Figure 4.2.6(d–e), which are significantly more oscillatory for $T_s = 30$ ms.

W.r.t. 'Centralised NMPC', 'TV NMPC+PI w/ FB' is characterised by a generalised reduction – by a factor exceeding 1.5 – of $\overline{\tau_{CPU,avg}}$. In parallel, w.r.t. the corresponding 'Centralised NMPC' configuration, i.e., with the same T_s and H_p values, 'TV NMPC+PI w/ FB' shows a slight deterioration – amounting to an average of ~0.3 deg/s – of the yaw rate tracking performance.

For both architectures, a good compromise between vehicle dynamics performance and computational effort is represented by H_p = 90 ms and T_s = 10 ms. Therefore, the automated calibration routine was run also for this setting, which corresponds to the results highlighted by the dashed circles in Figure 4.2.5. The optimised versions of 'Centralised NMPC' and 'TV NMPC+PI w/ FB' achieve $RMSE_{\Delta\dot{\psi}}$ of 2.3 and 2.4 deg/s (also J_{KPI}^{*} is marginally lower – i.e., better – for the centralised architecture), whilst their $\overline{\tau_{CPU,avg}}$ values are ~4 and ~2.5.

The important conclusions are that: 1) for enhancing control system performance without significantly penalising the computational effort, it is more convenient to reduce T_s rather than extending H_p; and 2) the vehicle dynamics results of the two architectures are almost comparable, but the average execution time is significantly lower for the multi-layer architecture, thanks to the reduced complexity of its prediction model, and the lower number of control inputs and states.

4.2.5.2 Real-time implementations

The proposed 'Centralised NMPC' and 'TV NMPC+PI' architectures were implemented in real-time on a rapid control prototyping unit, i.e., a dSPACE MicroAutoBox II 1401/1513 with an IBM 900 MHz processor, see Figure 4.2.7.

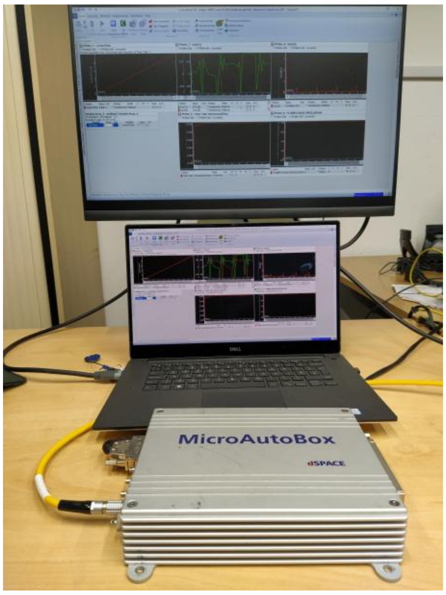

Figure 4.2.7: Real-time implementation set-up for the proposed NMPC configurations.

Table 4.2.2 lists the real-time capable controller configurations that were verified on the specific control hardware, and their settings in terms of T_s and respective N^{max}, i.e., the maximum value of N.

Table 4.2.2 – Settings of the considered real-time capable NMPC architectures

Controller configurations	T_s (ms)	N^{max} (-)
Centralised NMPC	27	2
TV NMPC+PI w/ or w/o FB	11	2
	16	3
	21	4
	26	5
TV NMPC+PI w/ or w/o FB, w/o WD	8	2
	12	3
	16	4
	20	5

The observation of the real-time options highlights that the wheel dynamics have an impact on the computational load of 'TV NMPC+PI', which, for example, can operate with $N^{max} = 3$ or 4 for $T_s = 16$ ms, respectively when including or excluding the wheel dynamics (WD). Because of its additional states and control inputs, 'Centralised NMPC' is by far computationally heavier than its multi-layer counterparts and could run in real-time only with $N^{max} = 2$ at $T_s = 27$ ms. Despite this, given the progressive availability of more performing control hardware, e.g., dSPACE MicroAutoBox III, 'Centralised NMPC' should not be excluded from future consideration for real-time implementation.

All controllers in Table 4.2.2 were analysed through the simulation framework in Section 4.2.2, along the following test cases:

- Test case 1: the same calibration weights for all controllers, according to the tuning used for Figure 4.2.5, and adoption of variable $s_{x,Fj,ref}$, see the discussion of Figure 4.2.3 in 0.
- Test case 2: optimised calibration weights for each controller configuration, and variable $s_{x,Fj,ref}$.
- Test case 3: the same as test case 1, but with $s_{x,Fj,ref} = 0.1$.

The resulting KPIs for the T_s and N settings providing the lowest J_{KPI} values for each controller configuration in each test case, together with those of 'Passive', are summarised in Table 4.2.3, see also their normalised values in the polar plots in Figure 4.2.8.

Table 4.2.3 – KPI values for a selection of real-time capable controllers

Controller	$RMSE_{\Delta\dot{\psi}}$ (deg/s)	$RMSE_{\Delta s_{x,FL}}$ (-)	$RMSE_{\Delta s_{x,FR}}$ (-)	$IACA_{M_z}$ (Nm)	$\lvert\Delta\dot{\psi}^{max}\rvert$ (deg/s)	$\lvert\alpha_{rear}^{max}\rvert$ (deg)	V_{end} (km/h)	J_{KPI} (-)
Test case 1: same calibration weights for all configurations and variable $s_{x,Fj,ref}$								
Centralised NMPC; T_s= 27 ms; N=2	3.35	0.01	0.01	1416	12.10	5.49	104.01	0.21
TV NMPC+PI w/ FB; T_s=21 ms; N=4	2.90	0.01	0.01	1680	9.63	4.72	98.12	0.20
TV NMPC+PI w/o FB; T_s=21 ms; N=4	2.88	0.01	0.01	1705	9.80	4.78	102.28	0.20
TV NMPC+PI w/ FB w/o WD; T_s=20 ms; N=5	3.95	0.01	0.01	1057	13.29	6.18	112.47	0.22
TV NMPC+PI w/o FB w/o WD; T_s=20 ms; N=5	3.93	0.01	0.01	1101	14.24	6.24	112.64	0.21
Test case 2: optimised weights for each configuration and variable $s_{x,Fj,ref}$								

Centralised NMPC; T_s= 27 ms; N=2	2.79	0.00	0.00	1847	8.61	4.60	97.94	0.19
TV NMPC+PI w/ FB; T_s=16 ms; N=3	2.74	0.01	0.01	1497	10.76	5.02	104.61	0.19
TV NMPC+PI w/o FB; T_s=26 ms; N=5	2.76	0.00	0.00	2031	7.54	4.14	98.57	0.19
TV NMPC+PI w/ FB w/o WD; T_s=12 ms; N=3	3.67	0.01	0.01	1140	12.94	5.69	110.71	0.21
TV NMPC+PI w/o FB w/o WD; T_s=8 ms; N=2	3.42	0.00	0.01	1189	12.16	5.51	107.32	0.20
Test case 3: same calibration weights for all configurations and $s_{x,Fj,ref}$ = 0.1								
Centralised NMPC T_s= 27 ms N=2	2.89	0.03	0.04	1870	8.83	5.01	69.12	0.25
TV NMPC+PI w/ FB T_s=21 ms N=4	2.62	0.01	0.02	2064	10.09	4.46	70.04	0.23
TV NMPC+PI w/o FB T_s=26 ms N=5	2.82	0.05	0.06	1882	8.53	4.67	85.65	0.25
TV NMPC+PI w/ FB w/o WD T_s=20 ms N=5	6.89	0.02	0.03	1509	21.73	10.79	74.26	0.39
TV NMPC+PI w/o FB w/o WD T_s=16 ms N=4	5.07	0.06	0.06	1266	16.17	8.06	99.93	0.32
Passive								
/	11.81	0.03	0.01	-	24.83	16.71	116.13	0.4794

The resulting KPIs for the T_s and N settings providing the lowest J_{KPI} values for each controller configuration in each test case, together with those of 'Passive', are summarised in Table 4.2.3, see also their normalised values in the polar plots in Figure 4.2.8. The normalisation is obtained by dividing the dimensional form of the KPI by its maximum value among the controlled configurations in the table.

The analysis of the results brings the following main conclusions:

- All proposed real-time implementations enable a major
- Vehicle response enhancement w.r.t. the 'Passive' configuration.
- For test case 2, i.e., among the configurations with optimised weights, 'Centralised NMPC' is at the top of the ranking, as it has the lowest J_{KPI}, followed by: 'TV NMPC+PI w/ FB', whose cost function value differs from the one of the centralised case by only ~0.001, and corresponds to the lowest $RMSE_{\Delta\dot{\psi}}$ value, see also Figure 4.2.9; 'TV NMPC+PI w/o FB'; 'TV NMPC+PI w/o FB w/o WD'; and 'TV NMPC+PI w/ FB w/o WD'.
- Given the specific tuning of J_{KPI}, focused on the cornering response, see Section 4, the best configurations bring very desirable yaw rate tracking and sideslip angle limitation performances, but tend to be characterised by the highest values of $IACA_{M_Z}$ and limited longitudinal acceleration, the latter caused by more aggressive torque reductions
- Although limiting the slip ratio peaks very effectively, 'Centralised NMPC' generates longitudinal slip oscillations, which are absent in 'TV NMPC+PI w/ FB' because of its lower T_s, see also Figure 4.2.9 and the TC results in [25]. Furthermore, 'TV NMPC+PI w/ FB', in addition to a better control of the longitudinal slip, manages to obtain a higher final speed than 'Centralised NMPC'.
- For test cases 1 and 3, i.e., without optimised weights, the best lateral vehicle control performance and the minimum J_{KPI} value are obtained by 'TV NMPC+PI w/

FB', which tends to have more robust performance than the specific 'Centralised NMPC' setting. The other rankings remain unaltered w.r.t. test case 2.

- In both configurations neglecting the wheel dynamics, $IACA_{M_Z}$ is significantly reduced (e.g., from 1680 Nm for 'TV NMPC+PI w/ FB' down to 1057 Nm for 'TV NMPC+PI w/ FB w/o WD' in test case 1), at the price of larger $RMSE_{\Delta\dot{\psi}}$ and $|\Delta\dot{\psi}^{max}|$ (e.g., 2.90 deg/s and 9.63 deg/s for 'TV NMPC+PI w/ FB', and 3.95 deg/s and 13.29 deg/s for 'TV NMPC+PI w/ FB w/o WD').
- For the 'TV NMPC+PI' configurations, the wheel slip control performance is significantly enhanced by the inclusion of torque feedback from the TC to the NMPC (e.g., with $RMSE_{\Delta s_{x,FL}}$ and $RMSE_{\Delta s_{x,FR}}$ values of 0.01 and 0.02 for 'TV NMPC w/ FB', and 0.05 and 0.06 for 'TV NMPC+PI w/o FB' in test case 3).

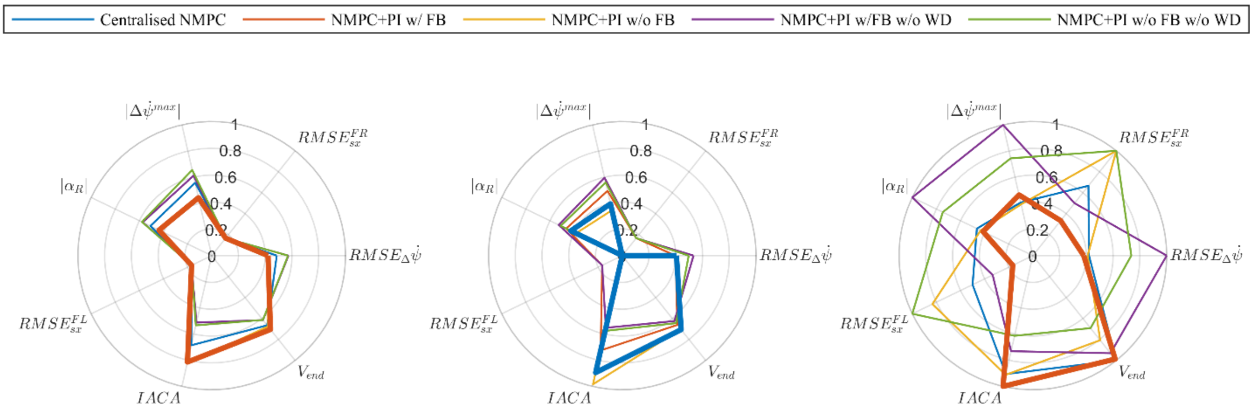

Figure 4.2.8: Polar plots of the normalised KPIs for the real-time implemented controller settings, for test cases 1–3. The bold line refers to the controller achieving the best performance, i.e., the lowest J_{KPI} value.

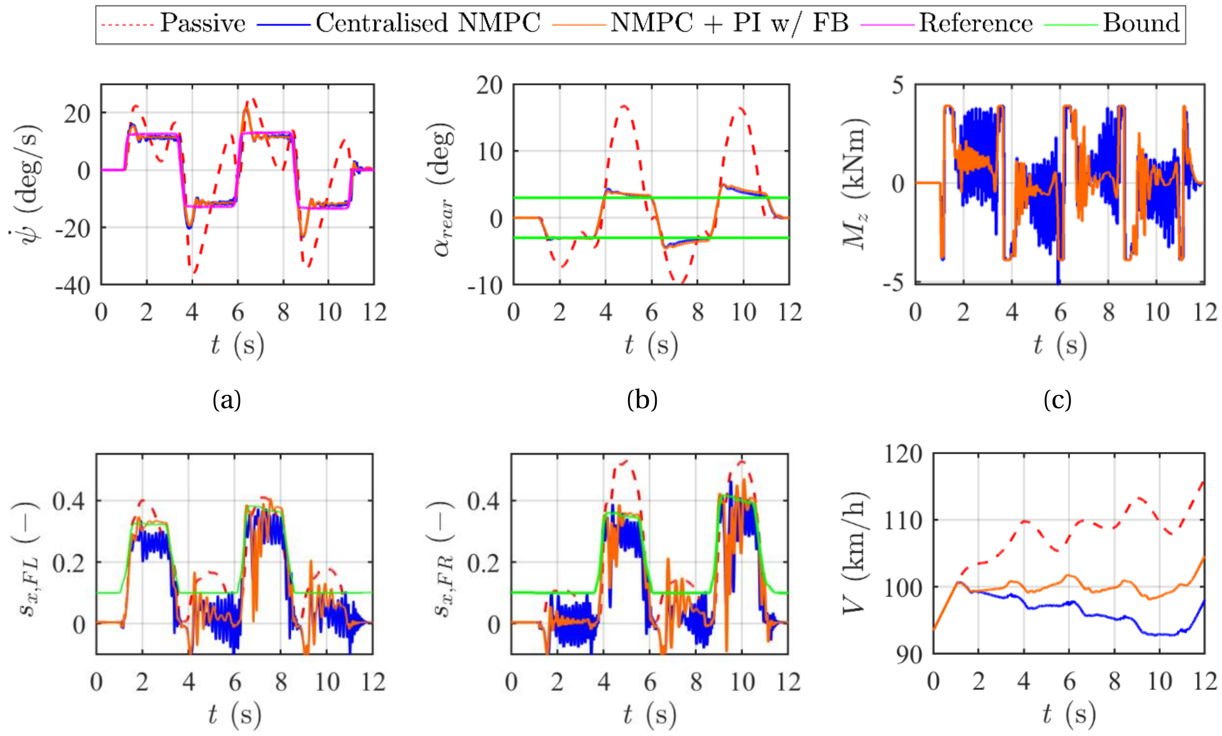

(a) (b) (c)

(d) (e) (f)

Figure 4.2.9: Time profiles of the main variables for 'Centralised NMPC' and 'TV NMPC+PI w/ FB' in test case 2, i.e., the best two real-time implementable configurations: (a) yaw rate tracking performance; (b) rear axle sideslip angle and its soft constraint bounds; (c) direct yaw moment; (d) front left and (e) front right longitudinal tire slips and their bounds; and (f) vehicle speed.

4.2.5.3 Effect of torque-feedback from the traction controller

To assess the effect of the torque feedback from the TC to the TV NMPC module, see Figure 4.2.1 and equation (4.2.33), the following additional KPI is considered:

$$RMSE_{\Delta M_z} = \sqrt{\frac{1}{t_f - t_i}\int_{t_i}^{t_f}[M_z^{Post-TC}(t) - M_z^{Pre-TC}(t)]^2 dt} \qquad (4.2.46)$$

where M_z^{Pre-TC} and $M_z^{Post-TC}$ are the direct yaw moments before (i.e., at the output of the TV NMPC algorithm) and after (i.e., at the output of the TC module, which intervenes when $s_{x,Fj}$ exceeds $s_{x,Fj,ref}$) the PI-based TC. M_z^{Pre-TC} and $M_z^{Post-TC}$ are calculated as:

$$\begin{gathered} M_z^{Pre-TC} = \frac{[T_{FL,EM,ref} - T_{FR,EM,ref}]d_F}{2R_w} \\ M_z^{Post-TC} = \frac{[T_{FL,PI} - T_{FR,PI}]d_F}{2R_w} \end{gathered} \qquad (4.2.47)$$

Figure 4.2.10: Test case 3 results: (a) time profiles of $|\Delta M_z|$ for 'TV NMPC+PI w/ FB' ($T_s = 11$; $N = 2$) and 'TV NMPC+PI w/o FB' ($T_s = 11$; $N = 2$); and (b) $RMSE_{\Delta M_z}$values for different T_s and N , for 'TV NMPC+PI w/ FB' and 'TV NMPC+PI w/o FB'.(a) reports the time profiles of $|\Delta M_z| = |M_z^{Pre-TC} - M_z^{Post-TC}|$, which show that the torque feedback significantly reduces the amplitude and extension of the peaks of direct yaw moment actuation error during the manoeuvre. This is reflected in the $RMSE_{\Delta M_z}$ histograms of Figure 4.2.10(b) for

multiple T_s and N settings, in which – on average – $RMSE_{\Delta M_z}$ is halved for the configurations with torque feedback. The conclusion is that the torque feedback function permits to tailor the intervention of the NMPC on the lateral dynamics to the longitudinal tire slip condition and the actually available tire-road friction level.

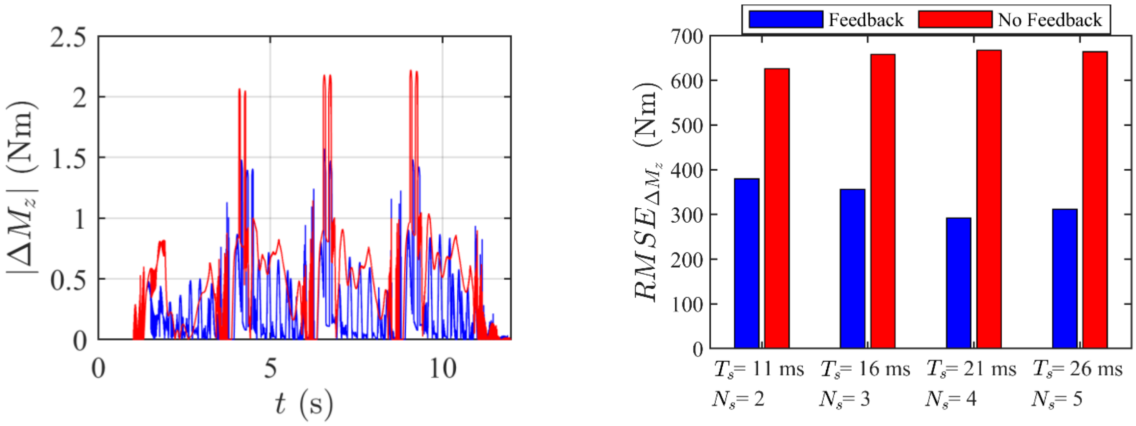

(a) (b)

Figure 4.2.10: Test case 3 results: (a) time profiles of $|\Delta M_z|$ for 'TV NMPC+PI w/ FB' ($T_s = 11$; $N = 2$) and 'TV NMPC+PI w/o FB' ($T_s = 11$; $N = 2$); and (b) $RMSE_{\Delta M_z}$values for different T_s and N , for 'TV NMPC+PI w/ FB' and 'TV NMPC+PI w/o FB'.

4.2.5.4 Robustness analysis

A controller robustness analysis was run for the multi-layer architecture, in which the CarMaker model parameters were significantly varied, while the NMPC prediction model parameters were kept equal to their nominal value in Table 3.2.1. This is a rather conservative assumption, as in modern vehicles the payload can be approximately estimated through dedicated observers and/or on-board sensors, e.g., those required for the operation of rear self-levelling suspension actuators. In particular, the performance has been evaluated for: i) nominal vehicle parameters; ii) increased vehicle mass by 750 kg; iii) increased yaw mass moment of inertia by 1607 kgm^2; and iv) concurrently increased m and J_z, by the same amounts specified under ii) and iii). The sensitivity analysis has been carried out during a multiple step steer test (with a steering angle magnitude of 12 deg for the first two steps, and 14 deg for the last two applications) in high tire-road friction conditions, from an initial speed of ~80 km/h, at a constant wheel torque demand of 1000 Nm. Table 4.2.4 reports the results for 'Passive' and 'TV NMPC + PI w/FB', where the latter is implemented with T_s = 16 ms, N = 3, and optimised cost function weights, see Table 4.2.2.

Table 4.2.4 – Analysis of controller performance sensitivity to vehicle mass and yaw mass moment of inertia.

Configuration	KPI	TV NMPC+PI w/ FB	Passive	I (%)
$m = 2252$ kg	$RMSE_{\Delta\dot{\psi}}$ (deg/s)	2.87	16.59	82.70
$J_z = 4825$ kgm^2	α_{rear}^{max} (deg)	4.76	22.49	78.84
$m = 3002$ kg	$RMSE_{\Delta\dot{\psi}}$ (deg/s)	3.50	36.32*	90.36
$J_z = 4825$ kgm^2	α_{rear}^{max} (deg)	5.23	79.71*	93.44
$m = 2252$ kg	$RMSE_{\Delta\dot{\psi}}$ (deg/s)	3.55	10.15	65.02
$J_z = 6432$ kgm^2	α_{rear}^{max} (deg)	5.04	13.09	61.50
$m = 3002$ kg	$RMSE_{\Delta\dot{\psi}}$ (deg/s)	4.02	38.36*	89.52
$J_z = 6432$ kgm^2	α_{rear}^{max} (deg)	5.42	82.33*	93.42

*: The vehicle does not complete the manoeuvre as it spins.

Table 4.2.4 includes $RMSE_{\Delta\dot{\psi}}$, α_{rear}^{max}, and I, i.e., the percentage reduction of the considered indicator brought by the controller:

$$I = \frac{KPI^C - KPI^P}{KPI^P} \cdot 100 \tag{4.2.48}$$

where KPI^C is the KPI for the controlled configuration, whilst KPI^P is the KPI for the passive configuration with the same inertial parameters. The main observations are: i) w.r.t. the corresponding passive configuration, 'TV NMPC+PI w/FB' significantly reduces $RMSE_{\Delta\dot{\psi}}$ and α_{rear}^{max} across the parametrisations, i.e., by at least by 65% and 61%; ii) 'TV NMPC+PI w/FB' shows a consistently safe vehicle response, with magnitude of the rear axle sideslip angle peaks below 5.5 deg; and iii) 'Passive' cannot complete the manoeuvre in the second and fourth test, because of vehicle spinning, which highlights the crucial stabilising function of the direct yaw moment controller. Comparable results were observed for the other controller configurations.

4.2.6 CONCLUDING REMARKS

This study presented a comparison among five real-time implementable nonlinear model predictive control (NMPC) strategies for torque-vectoring and traction control, one of them based on a centralised architecture, and the other four using a multi-layer approach, in which the top layer is responsible for the vehicle-level control aspects in terms of yaw rate tracking and sideslip angle limitation through torque-vectoring, and the bottom layer deals with the longitudinal slip control of the individual tires. For the multi-layer implementations, the analysis considered NMPC prediction models with and without wheel dynamics, as well as the presence or absence of torque feedback from the proportional integral (PI) wheel slip controllers to the NMPC torque-vectoring algorithm. For fairness of comparison, all strategies were assessed with the same NMPC weights, and also with optimised weights obtained through an automated calibration routine.

The simulation analysis, focused on extreme accelerating-while-turning manoeuvres in transient steering conditions, brought the following main conclusions:

- All proposed real-time implementations enable a major vehicle response enhancement w.r.t. the vehicle configuration without controllers, also in case of significant parameter variations.
- For the same controller implementation step (T_s) and prediction horizon (H_p), the vehicle dynamics results of the centralised and multi-layer architectures are almost comparable, but the average execution time is significantly lower for the multi-layer one, thanks to the reduced complexity of its optimisation problem, and the lower number of control inputs and states.
- For enhancing performance without significantly penalising the computational effort, in all considered strategies it is more convenient to reduce T_s than to extend H_p.
- Among the real-time configurations with optimised weights, the centralised architecture is at the top of the ranking, followed by the multi-layer one including wheel dynamics as well as torque feedback. Nevertheless, the calibration cost function value (J_{KPI}) of the latter is substantially aligned with that of the centralised one.
- Although limiting the peaks of slip ratio very effectively, the real-time implementation of the centralised architecture generates longitudinal slip oscillations that are absent in the multi-layer architectures, because of their lower T_s values (e.g., $T_s = 27$ and 16 ms, respectively for the real-time centralised and best multi-layer configurations).
- For the test cases using the same NMPC cost function weights in all controller configurations, the best lateral vehicle control performance and the minimum value of J_{KPI} are obtained by the multi-layer architecture with wheel dynamics and torque feedback, which overtakes the centralised one. In general, in comparison

with the centralised architecture, the real-time implemented multi-layer set-ups provide more robust performance w.r.t. their calibration parameters.

- In the specific tests implying concurrent interventions of the torque-vectoring and wheel slip control functions, it is more beneficial for the multi-layer architectures to include the wheel dynamics, rather than the torque feedback from the wheel slip control layer, although the latter approximately halves the root mean square value of the direct yaw moment generation error.

BIBLIOGRAPHY

[1] C. Beal and J. Gerdes, “Model Predictive Control for Vehicle Stabilization at the Limits of Handling,” *IEEE Transactions on Control Systems Technology*, vol. 21, no. 4, pp. 1258–1269, 2013.

[2] A. T. van Zanten, R. Erhardt and G. Pfaff, “VDC, the vehicle dynamics control system of Bosch,” SAE Technical Paper 950759, 1995.

[3] L. De Novellis, A. Sorniotti and P. Gruber, “Driving modes for designing the cornering response of fully electric vehicles with multiple motors,” *Mechanical Systems and Signal Processing*, vol. 64–65, pp. 1–15, 2015.

[4] A. T. van Zanten, “Bosch ESP Systems: 5 Years of Experience,” *SAE Transactions*, vol. 109, no. 7, pp. 428-436, 2000.

[5] S. Murata, “Innovation by in-wheel-motor drive unit,” *Vehicle System Dynamics*, vol. 50, no.6, pp. 807–830, 2012.

[6] V. Ivanov, D. Savitski, K. Augsburg and P. Barber, “Electric vehicles with individually controlled on-board motors: Revisiting the ABS design,” *IEEE International Conference on Mechatronics*, pp. 323-328, 2015.

[7] L. Grüne and J.Pannek, Nonlinear Model Predictive Control – Theory and Algorithms, Springer-Verlag, London, 2017.

[8] M. Dalboni, D. Tavernini, U. Montanaro, A. Soldati, C. Concari, M. Dhaens and A. Sorniotti, “Nonlinear Model Predictive Control for Integrated Energy-Efficient Torque-Vectoring and Anti-Roll Moment Distribution,” *IEEE/ASME Trans. Mechatr.*, vol. 26, no. 3, 2021.

[9] P. Falcone, F. Borrelli, J. Asgari, H. E. Tseng and D. Hrovat, “Predictive active steering control for autonomous vehicle systems,” *IEEE Transactions on Control Systems Technology*, vol. 15, no. 3, pp. 556–580, 2007.

[10] P. Falcone, H. E. Tseng, F. Borrelli, J. Asgari and D. Hrovat, “MPC-based yaw and lateral stabilisation via active front steering and braking,” *Vehicle System Dynamics*, vol. 46, pp. 611–628, 2008.

[11] M. Jalali, A. Khajepour, S. Chen and B. Litkouhi, “Integrated stability and traction control for electric vehicles using model predictive control,” *Control Engineering Practice*, vol. 54, 256–266, 2016.

[12] A. Nahidi, A. Kasaiezadeh, S. Khosravani, A. Khajepour, S. Chen and B. Litkouhi, “Modular integrated longitudinal and lateral vehicle stability control for electric vehicles,” *Mechatronics*, vol. 44, pp. 60–70, 2017.

[13] A. Parra, D. Tavernini, P. Gruber, A. Sorniotti, A. Zubizarreta, and J. Perez, “On nonlinear model predictive control for energy-efficient torque-vectoring,” *IEEE Trans. Veh. Technol.*, vol. 70, no. 1, pp. 173–188, 2020.

[14] Y. Zheng and B. Shyrokau, “A Real-Time Nonlinear MPC for Extreme Lateral Stabilization of Passenger Vehicles,” *IEEE International Conference on Mechatronics*, pp. 519-524, 2019.

[15] F. Borrelli, P. Falcone, T. Keviczky, J. Asgari and D. Hrovat, “MPC-based approach to active steering for autonomous vehicle systems,” *International Journal of Vehicle Autonomous Systems*, vol. 3, 265–291, 2005.

[16] T. Keviczky, P. Falcone, F. Borrelli, J. Asgari and D. Hrovat, “Predictive control approach to autonomous vehicle steering,” *Proceedings of the American Control*

Conference 6, 2006.

[17]S. Di Cairano, H.E. Tseng, D. Bernardini and A. Bemporad, “Vehicle yaw stability control by coordinated active front steering and differential braking in the tire sideslip angles domain,” *IEEE Transactions on Control Systems Technology*, vol. 21, no. 4, pp. 1236–1248, 2013.

[18]O. Barbarisi, G. Palmieri, S. Scala and L. Glielmo, “LTV-MPC for yaw rate control and side slip control with dynamically constrained differential braking,” *European Journal of Control*, vol. 15, pp. 468–479, 2009.

[19]M. Canale and L. Fagiano, “Vehicle yaw control using a fast NMPC approach,” *Proceedings of the 47th IEEE Conference on Decision and Control*, pp. 5360–5365, 2008.

[20]M. Metzler, D. Tavernini, P. Gruber and A. Sorniotti, “On Prediction Model Fidelity in Explicit Nonlinear Model Predictive Vehicle Stability Control,” *IEEE Transactions on Control Systems Technology*, vol. 29, no. 5, pp. 1964–1980, 2020.

[21]E. Siampis, E. Velenis, S. Gariuolo and S. Longo, “A Real-Time Nonlinear Model Predictive Control Strategy for Stabilization of an Electric Vehicle at the Limits of Handling,” *IEEE Transactions on Control Systems Technology*, vol. 26, no. 6, pp. 1982–1994, 2018.

[22]E. Siampis, E. Velenis and S. Longo, “Rear wheel torque vectoring model predictive control with velocity regulation for electric vehicles,” *Vehicle System Dynamics*, vol. 53, no. 11, 1555–1579, 2015.

[23]M. Ataei, A. Khajepour and S. Jeon, “Model Predictive Control for integrated lateral stability, traction/braking control, and rollover prevention of electric vehicles,” *Vehicle System Dynamics*, vol. 58, no. 1, 49-73, 2020.

[24]J. Wang and R. G. Longoria, “Coordinated and Reconfigurable Vehicle Dynamics Control,” *IEEE Transactions on Control Systems Technology*, vol. 17, no. 3, pp. 723–732, 2009.

[25]D. Tavernini, M. Metzler, P. Gruber and Sorniotti A., “Explicit Nonlinear Model Predictive Control for Electric Vehicle Traction Control,” *IEEE Transactions on Control Systems and Technology*, vol. 27, no. 4, pp. 1438–1451 2018.

[26]M. Amodeo, A. Ferrara, R. Terzaghi, C. Vecchio, “Wheel slip control via second order sliding modes generation,” *IEEE Conference on Decision and Control*, pp. 3889-3894, 2007.

[27]D. Yin, S. Oh and Y. Hori, “A Novel Traction Control for EV Based on Maximum Transmissible Torque Estimation,” *IEEE Transactions on Industrial Electronics*, vol. 56, no. 6, pp. 2086–2094, 2009.

[28]M. S. Basrah, E. Siampis, E. Velenis, D. Cao and S. Longo, “Integration of torque blending and slip control using nonlinear model predictive control,” *International Symposium on Advanced Vehicle Control*, pp. 585-592, 2016.

[29]M. S. Basrah, E. Siampis, E. Velenis, D. Cao and S. Longo, “Wheel slip control with torque blending using linear and nonlinear model predictive control,” *Vehicle System Dynamics*, vol. 55, no. 11, pp. 1665–1685, 2017.

[30]C. Satzger and R. de Castro, “Combined wheel-slip control and torque blending using MPC,” *International Conference on Connected Vehicles and Expo*, pp. 618-624, 2014.

[31]V. Mazzilli, D. Ivone, V. Vidal Munoz, S. De Pinto, P. Camocardi, L. Pascali, A. Doria Cerezo, P. Gruber, G. Tarquinio and A. Sorniotti, “On the vehicle state estimation benefits of smart tires,” *Pfeffer, P.E. (eds) 11th International Munich Chassis Symposium 2020. Proceedings*, Springer Vieweg, Berlin, Heidelberg, 2021.

[32] E. Bakker, L. Nyborg, H. B. Pacejka, “Tyre Modelling for Use in Vehicle Dynamics Studies,” *SAE Technical Paper* 870421, 1987.
[33] G. Genta, L. Morello,The automotive chassis., Volume 2: System Design, Springer-Link, Dordrecht, 2020.
[34] D. Ariens, B. Houska, J. Ferreau and F. Logist, ACADO for Matlab – User's Manual, 2010.

4.3 TORQUE-VECTORING

4.3.1 STATE-OF-THE-ART

The response of car-trailer systems in high-speed conditions can be affected by significant oscillations and stability issues, which are very difficult to control also for experienced drivers, and cause safety-critical scenarios. For example, depending on the vehicle parameters and operating conditions, car–trailer systems can become prone to jack-knifing and snaking. The insurgence of the hitch angle dynamics is facilitated by specific sets of trailer parameters, which vary with the payload. The dominant factors affecting lateral stability are the trailer yaw mass moment of inertia, the longitudinal position of the trailer centre of gravity, the location of the hitch joint, and the position of the trailer axle/s, while the trailer mass alone does not significantly affect high-speed stability [1]. Trailer oscillations can be mitigated through appropriate controllers. Several studies from the literature apply the control action only to the towing vehicle. For example, in Gerum et al. [2] braking torques are generated on the rear wheels of the tractor, to produce the direct yaw moment computed by an adaptive controller supported by an adaptive observer for hitch angle and hitch rate estimation. In [3] Mokhiamar and Abe propose two sliding mode formulations for direct yaw moment control, one based on the sideslip angle and the other one on the yaw rate of the towing vehicle. In [4] Deng and Kang compare multiple feedback controllers, which, starting from the hitch angle and hitch rate of the trailer, or on the yaw rate and lateral velocity of the towing vehicle, or the combination of the previous variables, generate a reference steering angle for the rear wheels of the car. Other authors only consider actuators located on the trailer. In this respect, in [5] Fernández and Sharp use the measured hitch angle and its time derivative to calculate asymmetric braking pressure demands for a caravan, to limit its sway. In [6] Plöchl et al. propose a sliding mode controller that calculates a corrective direct yaw moment actuated by the trailer brakes, starting from the yaw rates of the trailer and tractor. In [7] Sun et al. investigate an active trailer differential braking controller based on a linear quadratic regulator (LQR) and highlight that its integration with an active car differential braking controller would further improve the lateral stability of the car–trailer combination. In [8] Shamim et al. compare three stability control methods for car–trailer systems, namely active trailer braking, active trailer steering, and a variable geometry approach based on the active control of the lateral displacement of the car–trailer hitch joint. The results show that active trailer braking control has the best capability of rejecting external disturbances and maintaining stable operation of the car–trailer combination at high speeds. In [9] MacAdam et al. discuss a simple brake control algorithm to reduce the rearward amplification (RWA) in doubles and triples combination trucks, with a modular layout that can be implemented on a trailer-by-trailer basis. In [10] Milani et al. propose three LQR formulations to improve articulated heavy vehicle (AHV) manoeuvrability and stability through active semitrailer steering and anti-roll control, where the state feedback is based on the roll angle, roll rates, yaw rates and sideslip angles of the vehicle units. In [11]

Tabatabaei Oreh et al. discuss an active steering system for the trailer, based on fuzzy logic control, to track a reference hitch angle based on a novel formulation. References [12] and [13] deal with active trailer steering controllers for AHVs, based on LQRs including hitch angle feedback. In [14] the LQR approach, in this case based on state feedback using the yaw rate and lateral slip speed of each vehicle unit, is robustified through the implementation of a linear-matrix-inequality-based method. Islam et al. [15] present a parallel design optimisation method for AHVs with active safety systems, which simultaneously optimises the active design variables of the controllers and passive design variables of the trailers in a single loop. A few studies compare actuation solutions located on the towing vehicle, the trailer, or both. One of the main conclusions is that if the dynamic coupling between the towing vehicle and trailer is weak, then a leading unit based controller may not be effective to suppress violent trailer oscillations in critical conditions [16]. However, this does not have general validity. For example, Abroshan et al. [17] present a model predictive controller (MPC) for the yaw stabilisation of an articulated vehicle capable of differential braking actuated either on the trailer or the tractor, where the latter – for the specific vehicle – is the more effective solution. This outcome is confirmed by Zhang et al. [18], who propose a reconfigurable MPC architecture for articulated vehicle stabilisation, which is tested on an electrified car–trailer combination capable of multiple direct yaw moment generation options. In [19] Wang et al. highlight the benefits of the concurrent control of tractor and trailer, with respect to the control of the individual units, by applying a proportional integral derivative (PID) direct yaw moment controller to a single-track articulated vehicle model. The current industrial solution adopted in the stability controllers of passenger cars is to include trailer sway mitigation algorithms without any dedicated system to measure or estimate the hitch angle or yaw rate of the trailer [20], [21]. According to this approach, the yaw rate error of the car is subjected to band-pass filtering to obtain a signal in the typical frequency range of the trailer resonance. When this variable exceeds a threshold, critical trailer behaviour can be inferred, and appropriate control action is applied through the braking system of the car [22]. While the method can be effective in addressing the persistent oscillations of snaking at high speed, its benefits are very limited in the compensation of trailer sway caused by extreme transient steering applications, e.g. typical of obstacle avoidance or emergency manoeuvring. A simple yet effective commercially available solution is represented by the ATC system by AL-KO [23], which provides emergency braking functionality to the trailer, and is activated automatically if the vehicle combination experiences stability issues, i.e. if the swinging of the trailer reaches a critical level. The simulation and experimental analysis in [24] compares a conventional yaw rate based commercial trailer sway mitigation algorithm with a feedback control formulation correcting the yaw rate error with a hitch angle error contribution in case of major trailer oscillations in car–trailer combinations. The results show the potentially significant active safety benefits of direct hitch angle control, with respect to the production yaw rate focused strategies. Moreover, as the recent literature discusses several methods for hitch angle estimation or measurement, e.g. through model-based techniques or ultra-sonic sensors or vision systems located on the rear end of the towing vehicle [25]–[31], the additional complexity related to the on-board acquisition of the hitch angle information could soon become industrially viable. While in production passenger cars the trailer sway control function is actuated through the friction brakes, in next generation electric vehicles with multiple motors, the corrective direct yaw moment could be implemented through individual motor control, i.e. through torque-vectoring (TV) [24], thus providing enhanced tracking performance and progressivity as well as reduced power losses. MPC is gaining increasing attention for advanced vehicle dynamics control. For example, the path tracking controller of the automated articulated agricultural vehicle in [32] uses a nonlinear kinematic model, and, although providing excellent results for the specific application, neglects the axle slip angles, which are of the essence in road vehicles for capturing the hitch angle dynamics in emergency conditions. In the context of trailer sway control, the available pioneering implementations in [17], [18] and [33] are based on linear time-varying MPC, i.e. the internal vehicle model, and in particular its tyre model, is linearised at each time step, and its parametrisation is kept constant along the prediction horizon. This simplified prediction model is an extension of the well-known two-degree-of-freedom linear bicycle model for rigid vehicles. The benefit is a reduction of the computational effort for the solution of the optimal control problem, while still providing good vehicle stabilisation capability. The drawbacks are: (a) the potentially reduced performance, as the control input is expressed in terms of reference yaw moment, and therefore the prediction model does not account for the interaction between longitudinal and lateral tyre forces, see also the analysis in [34] on the significance of the internal model features on stability control performance in rigid vehicles; (b) the exclusion of the wheel dynamics from the internal model formulation, which does not allow the implementation of integrated wheel slip control; (c) the need for the continuous and precise information on the current value of the axle cornering stiffness, which implies additional estimation complexity, with respect to the estimation of the tangential tyre forces and slip angles; and (d) limitations with respect to the future development of MPC formulations considering longer prediction horizons, within which the linearisation approximation would not be reliable any longer. In fact, in the next generation of pre-emptive stability controllers for connected vehicles, see [35], the future steering inputs and reference state profiles, e.g. the reference yaw rate, could be approximately known a priori, and thus the extension of the prediction horizon would bring evident vehicle stabilisation improvements, provided that the internal model can accurately predict the vehicle system dynamics for the range of conditions within the selected horizon. In summary, to the best of our knowledge, none of the previous studies proposes hitch angle controllers based on nonlinear model predictive control (NMPC) technology, which is becoming real-time implementable, see the examples in [36]–[38], thanks to the development of dedicated computationally efficient solvers [39], and the progressive improvement of automotive control hardware. This chapter targets the identified gap, through the following contributions:

- Four NMPC formulations for an electric car with front individually controlled powertrains and towing a passive single-axle trailer, including continuous control of the yaw rate of the car as well as sideslip angle and hitch angle limitation in emergency conditions.
- The objective comparison of the performance of the proposed trailer sway mitigation algorithms with that of a benchmarking TV formulation designed for the control of the car on its own. All configurations are tuned through an optimisation routine and assessed through an experimentally validated vehicle model.
- The assessment of the sensitivity of controller performance to the variation of the trailer parameters, without varying the controller or prediction model parameters.

The chapter is organised as follows: Section 4.3.2 discusses the controller formulations; Section 4.3.3 describes the simulation environment, and the controller implementation and tuning details; Section 4.3.4 presents the controller comparison results; finally, Section 4.3.5 summarises the main conclusions.

4.3.2 CONTROLLER FORMULATIONS

4.3.2.1 Reference yaw rate and hitch angle

In the specific implementation of this study, for the control of the car yaw rate and hitch angle dynamics, in accordance with the common practices of vehicle stability control [40], [41], the reference variables correspond to the steady-state cornering condition of the vehicle, for the given driver inputs. The dynamic instability of the car–trailer combination is identified when the actual response significantly differs from the steady-state conditions. The nonlinear map of the steady-state reference yaw rate of the towing car, $\dot{\psi}_{d,SS}$, is designed to match the steady-state cornering response of the passive (i.e. without TV) rigid vehicle, and is expressed as a function of steering angle, SW, vehicle speed, V, and tyre-road friction coefficient, μ, see the extract in Figure 4.3.1. In the online implementation of the controller, $\dot{\psi}_{d,SS}$ is filtered through a first-order transfer function to obtain the car reference yaw rate, $\dot{\psi}_d$. It was verified that the controller can successfully operate even if the reference yaw rate for the car is not accounting for the interaction between trailer and car, which is, however, considered in the internal model described in the remainder for three of the proposed NMPC formulations, and through the hitch angle feedback. Figure 1 compares the steady-state yaw rate generated with the rigid vehicle, used as reference yaw rate for the car–trailer combination, and the actual steady-state yaw rate of the car–trailer combination, in case of trailer A (see Table 4.3.1 in Section 4.3.3.2). The presence of the trailer increases the vertical tyre load on the rear axle of the car and transmits lateral and longitudinal forces to the towing vehicle through the hitch joint. The result is an increase of the corresponding rear axle slip angles, and thus a reduction of the level of vehicle understeer, with increased yaw rate values of the car for given SW and V. However, the car yaw rate for the car–trailer combination is not significantly different from the yaw rate of the rigid vehicle, which means that the results presented in the remainder are acceptable. Moreover, it was verified through specific simulations that the inclusion of the reference yaw rate of the car–trailer combination would bring worse results in terms of hitch angle stability, given the marginally larger magnitude of the yaw rate of the combination vehicle. The conclusion is that the considered approximation is not only acceptable, but also safe and conservative. In the proposed formulations, the reference yaw rate mainly targets the control of the cornering behaviour of the car when the hitch angle dynamics are not critical, similarly to the operation of typical stability controllers or TV controllers for rigid vehicles, while the trailer sway mitigation function is mainly achieved through hitch angle feedback. Similarly to [24], the reference hitch angle, θ_d, is obtained from the differential equation describing the hitch dynamics at constant V, under the assumption of kinematic steering conditions, i.e. with zero axle slip angles:

$$\dot{\theta} = \frac{V}{L_{TOT}}\left\{\frac{L_{TOT}}{L_{TOT,T}}\sin(\theta) + \left[\frac{c - L_R}{L_{TOT}}\cos(\theta) + 1\right]\tan\left(S_W\right)\right\} \tag{4.3.1}$$

where $\dot{\theta}$ is the time derivative of the hitch angle θ , defined as the angle between the longitudinal axes of the towing vehicle and trailer, see the schematic and nomenclature in

Figure 4.3.2; L_{TOT} is the wheelbase of the towing car, while L_R is its rear semi-wheelbase; c is the longitudinal distance between the centre of gravity of the car (CG) and the hitch joint; and $L_{TOT,T}$ is the distance between the hinge and the rear axle of the trailer. By imposing $\dot{\theta} = 0$ in (4.3.1), θ_d is obtained as:

$$\theta_d = \tan^{-1}\left(\frac{\tan(S_W)\left[L_{TOT}^2 L_{TOT,T} + [c - L_R]\sqrt{\tan^2(S_W)\, L_{TOT}^2[c-L_R]^2 - \tan^2(S_W) L_{TOT}^2 L_{TOT,T}^2 + L_{TOT}^4}\right]}{L_{TOT}\left[-\tan^2(S_W) L_{TOT,T}[c-L_R] + \sqrt{\tan^2(S_W)\, L_{TOT}^2[c-L_R]^2 - \tan^2(S_W) L_{TOT}^2 L_{TOT,T}^2 + L_{TOT}^4}\right]}\right) \tag{4.3.2}$$

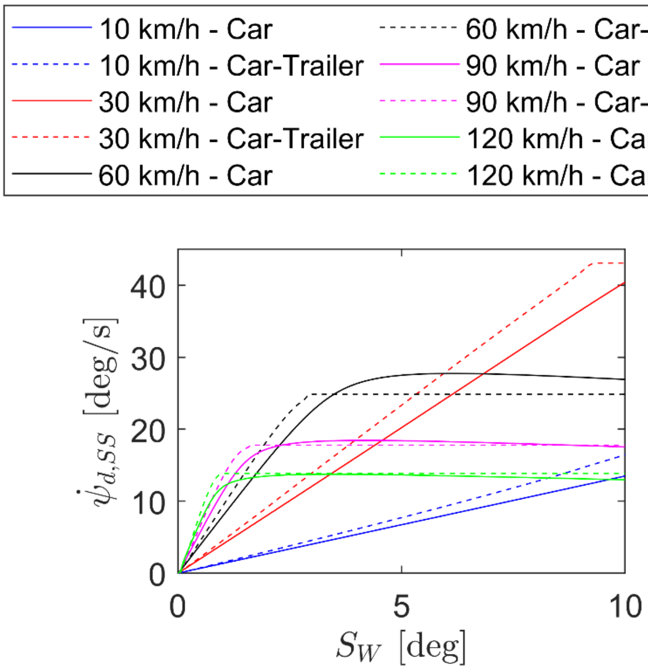

Figure 4.3.1: Steady-state yaw rate as a function of steering angle and vehicle speed, for high tyre-road friction conditions, obtained during ramp steer tests with the car (these profiles were used for the steady-state reference yaw rate map in the controller implementations of this study) and the car-trailer combination

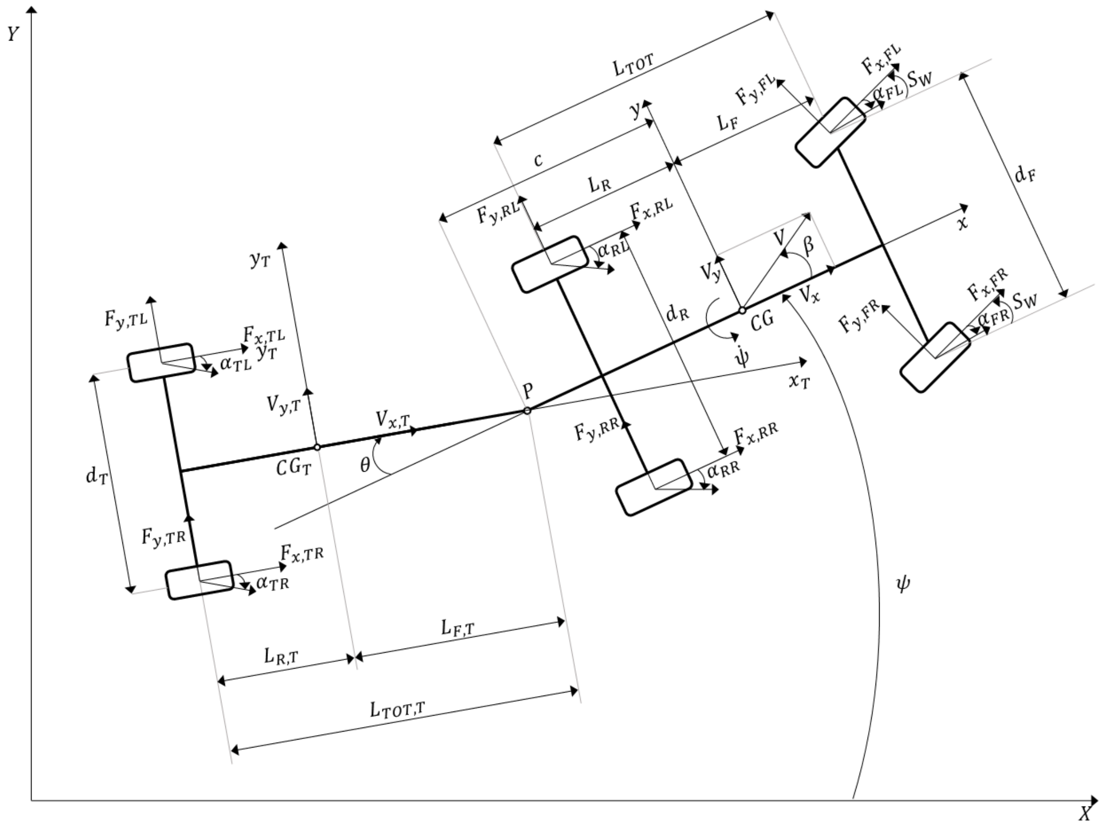

Figure 4.3.2: Simplified top view of the car-trailer system with the adopted nomenclature

4.3.2.2 Internal model formulation

The equations of the car–trailer body dynamics of the NMPC internal model – also called prediction model – were obtained through the Lagrange method, which, in the specific case, is expressed through the formulation in [42], to obtain the system dynamics in the reference frame of the towing car (xy):

$$\frac{\partial}{\partial t}\left(\frac{\partial T}{\partial w}\right) + A^T\left\{\dot{A} - \left[w^T A^T \frac{\partial A}{\partial q_l}\right]\right\}\frac{\partial T}{\partial w} - A^T\frac{\partial T}{\partial q_l} + \frac{\partial F}{\partial w} = A^T Q_l \qquad (4.3.3)$$

where t is time; T is the kinetic energy of the system; $w = \left[V_x, V_y, \dot{\psi}, \dot{\theta}\right]^T$ is the vector of generalised velocities, in which V_x and V_y are the longitudinal and lateral components of the vehicle velocity V, and $\dot{\psi}$ is the car yaw rate; $F = 0.5\Gamma\dot{\theta}^2$ is the Rayleigh dissipation function, which is used to approximate viscous or friction effects in the hitch joint, with Γ being the damping coefficient of the hinge; q_l, with $l = 1,\ldots,4$, indicates the individual generalised coordinates of the Lagrange formulation, which form the vector $q = [X_{CG}, Y_{CG}, \psi, \theta]^T$, with X_{CG} and Y_{CG} being the coordinates of the centre of gravity of the towing vehicle (i.e. the car) in the inertial reference frame; Q_l indicates the corresponding generalised forces, F_X and F_Y, in the inertial reference frame, and the moments related to the rotations ψ and θ; and A is the rotation matrix from the towing vehicle reference frame (xy) to the inertial reference frame (XY), such that $w = A^T\dot{q}$. According to this approach, the kinetic energy of the system can be expressed as a function of w:

$$T = \frac{1}{2}M\left[V_x^2 + V_y^2\right] + \frac{1}{2}J_1(\theta)\dot{\psi}^2 + \frac{1}{2}J_3\dot{\theta}^2 - J_2(\theta)\dot{\psi}\dot{\theta} \\ - m_T V_y\{c\dot{\psi}L_{F,T}\left[\dot{\psi} - \dot{\theta}\right]\cos(\theta) - m_T V_x L_{F.T}\left[\dot{\psi} - \dot{\theta}\right]\sin(\theta)\} \tag{4.3.4}$$

where $M = m + m_T$ is the total mass of the vehicle-trailer combination; m_T is the mass of the trailer; $L_{F,T}$ is the distance between the hinge and the centre of gravity of the trailer; and $J_1(\theta)$, $J_2(\theta)$ and J_3 are equivalent mass moments of inertia, defined as:

$$J_1(\theta) = J_Z + J_T + m_T\left[L_{F,T}^2 + c^2 + 2L_{F,T}c\,cos(\theta)\right] \tag{4.3.5}$$

$$J_2(\theta) = J_T + m_T\left[L_{F,T}^2 + L_{F,T}c\,cos(\theta)\right] \tag{4.3.6}$$

$$J_3 = J_T + m_T L_{F,T}^2 \tag{4.3.7}$$

where J_Z and J_T are the yaw mass moments of inertia of the car and trailer. The generalised forces and moments in the car reference frame, $A^T Q_l$, are obtained through D'Alembert's principle, according to which the total virtual work, δL, is defined as:

$$\delta L = \sum_n F_n \delta_{lin,n} + \sum_n M_n \delta_{ang,n} \tag{4.3.8}$$

where F_n and M_n indicate the virtual forces and moments; and $\delta_{lin,n}$ and $\delta_{ang,n}$ are the relevant components of the linear and angular displacements. The main sources of virtual work are the longitudinal and lateral tyre forces of the car and the trailer, which, in the remainder, are referred to as $F_{x,ij}$ and $F_{y,ij}$, where the subscript $i = F, R, T$ indicates the front or rear axles of the car, or the trailer axle, and $j = L, R$ indicates the left or right vehicle sides. For the derivation of the virtual work, $F_{x,Fj}$ and $F_{y,Fj}$ are projected along the axes of the xy reference system of the car, according to the steering angle SW, while, under the assumption of zero toe angle, $F_{x,Rj}$, $F_{y,Rj}$, $F_{x,Tj}$ and $F_{y,Tj}$, are already aligned with the axes of the coordinate systems of the respective vehicle, and therefore do not need any manipulation. The resulting forces are multiplied by the longitudinal and lateral virtual displacements of the car corners, $\delta_{x_{ij}}$ and $\delta_{y_{ij}}$, and trailer corners, $\delta_{x_{Tj}}$ and $\delta_{y_{Tj}}$, expressed in the respective vehicle unit reference frames:

$$\begin{cases} \delta_{x_{ij}} = \delta x - y_{ij}\delta\psi, i = F, R \\ \delta_{y_{ij}} = \delta y - x_{ij}\delta\psi, i = F, R \\ \delta_{x_{Tj}} = \delta x\cos(\theta) - \delta y\sin(\theta) + c\delta\psi\sin(\theta) - y_{Tj}[\delta\psi - \delta\theta] \\ \delta_{y_{Tj}} = \delta x\sin(\theta) - \delta y\cos(\theta) - c\delta\psi\cos(\theta) - L_{TOT,t}[\delta\psi - \delta\theta] \end{cases} \tag{4.3.9}$$

where the notation δ refers to a generic virtual displacement; x_{ij} and y_{ij} ($i = F, R$) are the longitudinal and lateral coordinates of the ij wheel of the car, in the xy system; and y_{Tj} is the lateral coordinate of the j wheel of the trailer, in the $x_T y_T$ reference system. The tyre self alignment moments are neglected in the prediction model formulations. The terms $A^T Q_l$ are obtained by differentiating the virtual work with respect to the virtual displacements $\delta x, \delta y, \delta\psi$ and $\delta\theta$:

$$A^T Q_l = \frac{\partial \delta L}{\partial \delta q_l} \tag{4.3.10}$$

The resulting equations of motion are:

- Longitudinal vehicle dynamics equation

$$\begin{aligned} M\big[\dot{V}_x - \dot{\psi}V_y\big] - m_T L_{F,t}\big[\ddot{\psi} - \ddot{\theta}\big]\sin(\theta) - 2m_T L_{F,T}\dot{\psi}\dot{\theta}\cos(\theta) + m_T L_{F,T}\dot{\theta}^2\cos(\theta) \\ + m_T\dot{\psi}^2\big[c + L_{F,T}\cos(\theta)\big] \\ = \big[F_{x,FL} + F_{x,FR}\big]\cos(S_W) - \big[F_{y,FL} + F_{y,FR}\big]\sin(S_W) + F_{x,RL} + F_{x,RR} \\ + \sum_{j=L,R}\big[F_{x,Tj}\cos(\theta) + F_{y,Tj}\sin(\theta)\big] - F_{drag} \end{aligned} \tag{4.3.11}$$

  where F_{drag} is the equivalend aerodynamic drag force of the vehicle comination, for simplicity considered along the longitudinal axis of the car.
- Lateral vehicle dynamics equation

$$\begin{aligned} M\big[\dot{V}_y + \dot{\psi}V_x\big] - m_T\ddot{\psi}\big[c + L_{F,T}\cos(\theta)\big] + m_T l_{F,T}\ddot{\theta}\cos(\theta) - m_T L_{F,T}\sin(\theta)\big[\dot{\psi} - \dot{\theta}\big]^2 \\ = \big[F_{x,FL} + F_{x,FR}\big]\sin(S_W) + \big[F_{y,FL} + F_{y,FR}\big]\cos(S_W) + \big[F_{y,RL} + F_{y,RR}\big] \\ + \sum_{j=L,R}\big[-F_{x,Tj}\sin(\theta) + F_{y,Tj}\cos(\theta)\big] \end{aligned} \tag{4.3.12}$$

- Yaw dynamics equation

$$\begin{aligned} J_1(\theta)\ddot{\psi} - J_2(\theta)\ddot{\theta} + m_T L_{F,T}C\sin(\theta)\big[\dot{\theta}^2 - 2\dot{\theta}\dot{\psi}\big] - m_T L_{F,T}\sin(\theta)\big[\dot{V}_x - V_y\dot{\psi}\big] \\ - m_T\big[\dot{V}_y + V_x\dot{\psi}\big]\big[C + L_{F,T}\cos(\theta)\big] \\ = L_F\big\{\big[F_{y,FL} + F_{y,FR}\big]\cos(S_W) + \big[F_{x,FL} + F_{x,FR}\big]\sin(S_W)\big\} \\ - L_R\big[F_{y,RL} + F_{y,RR}\big] \\ + \frac{d_F}{2}\big\{\big[F_{y,FL} - F_{y,FR}\big]\sin(S_W) + \big[F_{x,FR} - F_{x,FL}\big]\cos(S_W)\big\} \\ + \frac{d_R}{2}\big[F_{x,RR} - F_{x,RL}\big] \\ + \sum_{j=L,R}\big\{F_{x,Tj}\big[c\sin(\theta) - y_{Tj}\big] + F_{y,Tj}\big[-c\cos(\theta) - L_{TOT,t}\big]\big\} \end{aligned} \tag{4.3.13}$$

  where L_F is the front semi-wheelbase of the car; and d_F and d_R are its front and rear track widths.
- Hitch dynamics equation

$$\begin{aligned} J_3\ddot{\theta} - J_2(\theta)\ddot{\psi} + m_T L_{F,T}\cos(\theta)\big[\dot{V}_y + V_x\dot{\psi}\big] + m_T L_{F,T}\sin(\theta)\big\{\dot{V}_x - \dot{\psi}\big[V_y - c\dot{\psi}\big]\big\} \\ = \sum_{j=L,R}\big[F_{x,Tj}y_{Tj} + F_{y,Tj}L_{TOT,T}\big] - \Gamma\dot{\theta} \end{aligned} \tag{4.3.14}$$

The wheel moment balance equations, which were obtained outside the Lagrange formulation because of their simplicity are:

$$\begin{aligned} I_{w,F}\dot{\omega}_{Fj} &= \tau_{m,Fj} - \tau_{b,Fj} - F_{x,Fj}R - fF_{z,Fj}R \\ I_{w,R}\dot{\omega}_{Rj} &= -\tau_{b,Rj} - F_{x,Rj}R - fF_{z,Rj}R \\ I_{w,T}\dot{\omega}_{Tj} &= -\tau_{b,Tj} - F_{x,Tj}R - fF_{z,Tj}R \end{aligned} \tag{4.3.15}$$

Where $I_{w,F}$, $I_{w,R}$ and $I_{w,T}$ are the wheel mass moments of inertia on the front and rear axles of the car, and the trailer axle; τ_{m,F_j} is the electric powertrain torque at the wheel, which is present only on the front axle of the car given the front-wheel-drive architecture of the vehicle; $\tau_{b,ij}$is the braking torque, which, in this study focused on traction conditions, is considered as an external input; $F_{z,ij}$ is the vertical tyre load; R is the laden wheel radius;

and f is the rolling resistance coefficient. In (4.3.11)–(4.3.15), the longitudinal and lateral tyre forces are calculated with the Pacejka Magic Formula version in [43], starting from the tyre slip ratio, slip angle and vertical load, and including consideration of combined slip effects. The slip angles of the car (α_{ij}, with $i = F, R$)and the trailer (α_{Tj}) are given by:

$$\alpha_{ij} = \tan^{-1}\left(\frac{V_y + x_{ij}\dot{\psi}}{Vx - y_{ij}\dot{\psi}}\right) - k_1 S_W \text{, for } i\text{) } F, R, \text{where } \mathrm{k}_1 = \begin{cases} 1 & if \quad i = F \\ 0 & if \quad i = R \end{cases}$$
$$\alpha_{Tj} = \tan^{-1}\left(\frac{V_x\sin(\theta) + V_y\cos(\theta) - c\dot{\psi}\cos(\theta) - L_{TOT,T}[\dot{\psi} - \dot{\theta}]}{V_x\cos - V_y\sin(\theta) + c\dot{\psi}\sin(\theta) - y_{Tj}[\dot{\psi} - \dot{\theta}]}\right) \tag{4.3.16}$$

The vertical tyre loads, $F_{z,ij}$, are obtained as the sum of the static loads, $F_{z,s,ij}$, the longitudinal load transfers, $\Delta F_{z,long,i}$, and the lateral load transfers, $\Delta F_{z,lat,i}$:

$$F_{z,ij} = F_{z,s,ij} + \Delta F_{z,long,i} + k_2\,\Delta F_{z,lat,i}, \text{where } k_2 = \begin{cases} 1 & if \quad j = L \\ -1 & if \quad j = R \end{cases} \tag{4.3.17}$$

$\Delta F_{z,long,i}$ and $\Delta F_{z,lat,i}$ are computed through steady-state equations based on the system geometry and roll stiffness distribution, and are considered to be directly proportional to the measured longitudinal and lateral accelerations of the towing car, a_x and a_y, and the estimated longitudinal and lateral accelerations of the centre of gravity of the trailer, $a_{x,T}$ and $a_{y,T}$, which are assumed constant to the purpose of the NMPC prediction. Hence, also the resulting $\Delta F_{z,long,i}$ and $\Delta F_{z,lat,i}$ remain constant along the prediction horizon. In particular, the terms $\Delta F_{z,lat,i}$, which are especially relevant in the considered manoeuvres, are computed as:

$$\begin{aligned} &\Delta F_{z,lat,F} \\ &= -\left\{\frac{m a_y L_R}{L_{TOT}} - \left[m_T a_{x,T}\sin(\theta) + \frac{m_T a_{y,T} L_{R,T}}{L_{TOT,T}}\cos(\theta)\right]\frac{c - L_R}{L_{TOT}}\right\}\frac{RCH}{d_F} \\ &- \frac{K_{roll,F}\left\{m a_y H_{roll} + \left[m_T a_{x,T}\sin(\theta) + \dfrac{m_T a_{y,T} L_{R,T}}{L_{TOT,T}}\cos(\theta)\right][H_{hitch} - RCH]\right\}}{d_F[K_{roll,F} + K_{roll,R}]} \end{aligned} \tag{4.3.18}$$

$$\begin{aligned} &\Delta F_{z,lat,R} \\ &= -\left\{\frac{m a_y L_F}{L_{TOT}} + \left[m_T a_{x,T}\sin(\theta) + \frac{m_T a_{y,T} L_{R,T}}{L_{TOT,T}}\cos(\theta)\right]\frac{c + L_F}{L_{TOT}}\right\}\frac{RCH}{d_R} \\ &- \frac{K_{roll,R}\left\{m a_y H_{roll} + \left[m_T a_{x,T}\sin(\theta) + \dfrac{m_T a_{y,T} L_{R,T}}{L_{TOT,T}}\cos(\theta)\right][H_{hitch} - RCH]\right\}}{d_R[K_{roll,F} + K_{roll,R}]} \end{aligned} \tag{4.3.19}$$

$$\Delta F_{z,lat,T} = \frac{m_T a_{y,T} L_{R,T}}{d_T L_{TOT,T}} H_{hitch} - \frac{m_T a_{y,T} H_{CG,T}}{d_T} \tag{4.3.20}$$

where RCH is the roll centre height of the suspensions of the car, for which the roll axis is approximated as horizontal; H_{roll} is the distance between the centre of gravity and roll axis of the car; $H_{CG,T}$ is the centre of gravity height of the trailer; H_{hitch} is the height of the hitch joint from the ground; and $K_{roll,F}$ and $K_{roll,R}$ are the front and rear roll stiffness of the suspensions of the car. Equations (4.3.11)–(4.3.20), together with the definitions of the slip ratios, the tyre model, and the load transfer formulations, were re-arranged through symbolic computation software (MAPLE) into a nonlinear state-space formulation:

$$\dot{X}_S = f(X_S(t), U_C(t)) \tag{4.3.21}$$

where X_S is the state vector:

$$X_S = [V_x, V_y, \dot{\psi}, \dot{\theta}, \theta, \omega_{FL}, \omega_{FR}, \omega_{RL}, \omega_{RR}, \omega_{TL}, \omega_{TR}]^T \tag{4.3.22}$$

and U_C is the control action vector:

$$U_C = [\tau_{m,FL}, \tau_{m,FR}]^T \tag{4.3.23}$$

4.3.2.3 Nonlinear optimal control problem formulation

Nonlinear model predictive control is based on the solution of an optimisation problem, in which the discretised internal model is used to predict the future behaviour of the system over a finite prediction horizon, along which the control actions are obtained to minimise an optimality criterion, i.e., a cost function, while satisfying an assigned set of constraints. Only the control actions computed for the first step of the prediction horizon are applied to the plant, whilst the following control inputs are discarded. Once a new set of states at the next time step is obtained, the whole process is repeated, and new control actions are determined, according to the so-called receding horizon approach [44]. The discrete-time formulation of the nonlinear optimal control problem is:

$$\begin{gathered}
\min_{U} J\big(Z(0), U(\cdot)\big) := \frac{1}{2}\sum_{k=0}^{N-1}\left[\left\|Z^k - Z_d^k\right\|^2_Q + \|U^k\|^2_R\right] + \|Z^N - Z_d^N\|^2_{Q_N} \\
\text{s.t.} \\
Z^{k+1} = f_d\,(X^k, U^k) \\
\underline{Z} \le Z^k \le \overline{Z} \\
\underline{Z} \le Z^N \le \overline{Z} \\
\underline{U} \le U^k \le \overline{U} \\
U(\cdot) : [0, N-1]
\end{gathered} \tag{4.3.24}$$

where J is the cost function; Z is the output vector; U is the control input vector, which includes U_C and the slack variables (defined in the remainder); N is the number of steps of the prediction horizon, which is equal to the control horizon in the considered implementations; the superscript k indicates the discretisation step; Z_d is the vector of desired outputs, which are considered constant along the prediction horizon; $\underline{Z}$ and $\overline{Z}$ are the lower and upper limits for Z; $\underline{U}$ and $\overline{U}$ are the lower and upper limits for U; and Q, Q_N and R are positive semi-definite weight matrices. The following subsections 4.3.2.4–4.3.2.8 provide the details of the considered TV controller formulations based on the general nonlinear optimal control problem in (24).

4.3.2.4 Benchmarking TV controller for rigid vehicles (YR_{rig})

This controller, referred to as YR_{rig}, uses the internal model of the rigid vehicle configuration, i.e., it excludes the trailer terms of (4.3.11)–(4.3.22), and does not consider the presence of the trailer in any aspect of the formulation (hence, it excludes hitch angle feedback). Therefore, in the remainder it is considered as the benchmarking controller. The objective of the formulation is to simultaneously track the desired total powertrain torque demand, $\tau_{m,tot,d}$, set by a dedicated drivability module, and the reference yaw rate, $\dot{\psi}_d$, while limiting the rear axle sideslip angle, α_R, for stability reasons.

The output and reference vectors are defined as:

$$\begin{aligned} Z &= [\tau_{m,tot}\,, \dot{\psi}\,, s_\alpha]^T \\ Z_d &= [\tau_{m,tot,d}\,, \dot{\psi}_d\,, 0]^T \end{aligned} \tag{4.3.25}$$

where $\tau_{m,tot} = \tau_{m,FL} + \tau_{m,FR}$ is the total motor torque demand at the wheels; and s_α, which has zero as reference value, is the slack variable used for imposing the soft constraint on α_R. (4.3.26)–(4.3.29) are the constraint formulations:

$$\tau_{m,Fj}^{min} \le \tau_{m,Fj}^{k} \le \tau_{m,Fj}^{max} \tag{4.3.26}$$

$$s_\alpha^k \ge 0 \tag{4.3.27}$$

$$-\alpha_R^{max}(1 + s_\alpha^k) \le \alpha_R^k \le \alpha_R^{max}(1 + s_\alpha^k) \tag{4.3.28}$$

$$P_{Batt}^{min} \le P_{Batt}^{k} \le P_{Batt}^{max} \tag{4.3.29}$$

In particular, (4.3.26) expresses the constraint in terms of upper and lower bounds on the motor torque demand, defined from the limits of the electric machines and the possible output of an external traction controller; (4.3.27) and (4.3.28) express the soft constraint on α_R; and (4.3.29) deals with the battery power limits, defined by P_{Batt}^{min} and P_{Batt}^{max}. The constraints in (4.3.26)–(4.3.29) are used also in the other NMPC formulations in Sections 4.3.2.5–4.3.2.8, in which they are omitted for conciseness.

4.3.2.5 TV controller for car-trailer combinations, based on a modified reference yaw rate formulation ($MYR_{d,rig}$)

This formulation, referred to as $MYR_{d,rig}$, is very similar to YR_{rig}, as it uses the internal model of the rigid vehicle. However, when the car tows a trailer, $\dot{\psi}_d$ in (4.3.25) is replaced with a modified reference yaw rate, $\dot{\psi}_{dm}$, which is a weighted linear combination of $\dot{\psi}_d$, and the hitch angle error $\Delta\theta = \theta_d - \theta$, with θ_d being kept constant along the prediction horizon:

$$\dot{\psi}_{dm} = \dot{\psi}_d - W_\theta(1 - K_\theta)\Delta\theta \tag{4.3.30}$$

$\Delta\theta$ has an influence only when it exceeds pre-determined critical thresholds, according to the weighting factor K_θ that modulates the hitch angle correction:

$$K_{\theta} = \begin{cases} 1 & \text{if} \quad \Delta\theta \in [-\Delta\theta_{th}; \Delta\theta_{th}] \\ 1 + \dfrac{K_{\theta,min} - 1}{\Delta\theta_{th} - \Delta\theta_{lim}} [\Delta\theta_{th} - |\Delta\theta|] & \text{if} \quad \Delta\theta \in [-\Delta\theta_{lim}; -\Delta\theta_{th}] \cup [\Delta\theta_{th}; \Delta\theta_{lim}] \\ K_{\theta,min} & \text{if} \quad \Delta\theta \notin [-\Delta\theta_{lim}; \Delta\theta_{lim}] \end{cases} \tag{4.3.31}$$

where $\Delta\theta_{th}$, $\Delta\theta_{lim}$ (with $\Delta\theta_{lim} > \Delta\theta_{th}$) and $K_{\theta,min}$ are tuning parameters. In the first case in (4.3.31), the controller tracks only the reference yaw rate of the car, as the hitch angle dynamics are not deemed critical. In the second condition in (4.3.31), the controller progressively blends the car yaw rate and hitch angle error contributions, i.e., the reference yaw rate magnitude is increased if the trailer tends to sway toward the external side of the curve with respect to the reference, while the opposite occurs, i.e., $|\dot{\psi}_{dm}| < |\dot{\psi}_d|$, if the trailer tends to rotate to rotate toward the inner side of the turn. In extremely critical conditions, the blending uses $K_{\theta,min}$, which is a small strictly positive value that gives priority to hitch angle tracking, but still allows the TV controller to consider the steering input by the driver or the automated driving controller also during extreme oscillations of the trailer. Finally, W_{θ} is a constant gain that provides an extra degree of tuning and addresses the different dimensions of $\dot{\psi}_d$ and $\Delta\theta$.

4.3.2.6 TV controller based on the car-trailer model and a hitch angle error constraint ($YR + SC_{HAE}$)

The $YR + SC_{HAE}$ approach uses the car-trailer model in Section 4.3.2.2 for the NMPC prediction, and considers a soft constraint on $\Delta\theta$, which is activated only above the specified threshold $\Delta\theta_{lim}$, through a slack variable s_{θ}, included in the cost function. Therefore, Z and Z_d are:

$$Z = [\tau_{m,tot}, \dot{\psi}, s_{\alpha}, s_{\theta}]^T$$
$$Z_d = [\tau_{m,tot,d}, \dot{\psi}_d, 0, 0]^T \tag{4.3.32}$$

In addition to those in (4.3.26)–(4.3.29), the control problem includes the constraints related to s_{θ}:

$$s_{\theta}^k \geq 0 \tag{4.3.33}$$

$$-\Delta\theta_{lim}(1 + s_{\theta}^k) \leq \Delta\theta^k \leq \Delta\theta_{lim}(1 + s_{\theta}^k) \tag{4.3.34}$$

where the dynamics of $\Delta\theta$ along the prediction horizon are generated by the prediction model, starting from the measured hitch angle at the current time.

4.3.2.7 TV controller based on the car-trailer model and a hitch angle error function ($YR + HAE_{fun}$)

The $YR + HAE_{fun}$ formulation uses the car-trailer model, and includes the hitch angle error in J, through a continuous deadband-like function, according to which the effect of $\Delta\theta$ is progressively taken in account only if the predicted hitch angle error exceeds a pre-determined threshold. Z and Z_d are defined as:

$$Z = [\tau_{tot}, \dot{\psi}, \Delta\theta_c, s_{\alpha}]^T \tag{4.3.35}$$

$$Z_d = \left[\tau_{tot,d}\,, \dot{\psi}_d\,, 0, 0\,\right]^T$$

in which $\Delta\theta_c$ is the modified hitch angle error, shown in Figure 3 as a function of $\Delta\theta$, and formulated as:

$$\Delta\theta_c = \Delta\theta - \Delta\theta_{th}\tanh\left(\frac{\Delta\theta}{\Delta\theta_{th}}\right) \tag{4.3.36}$$

where $\Delta\theta_{th}$ is the hitch angle error threshold, which is constant along the prediction horizon, while $\Delta\theta_c$ and $\Delta\theta$ vary according to the prediction model dynamics.

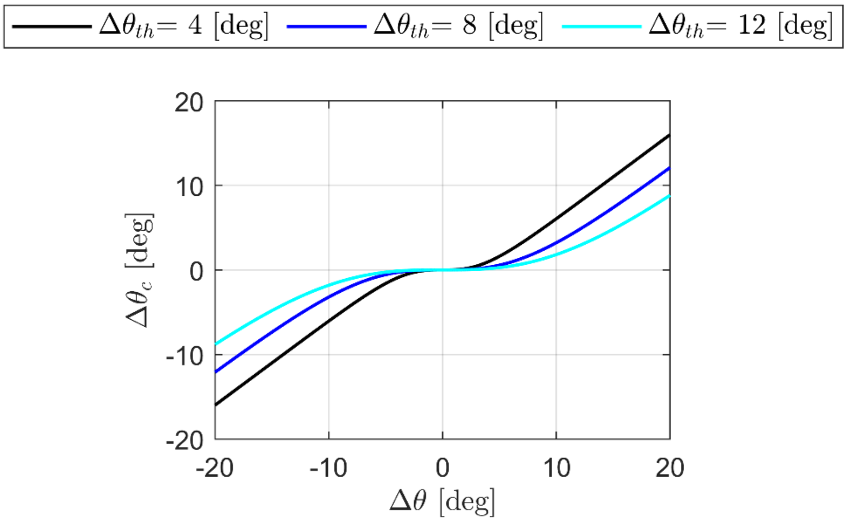

Figure 4.3.3: $\Delta\theta_c$ as a function of $\Delta\theta$, for different values of $\Delta\theta_{th}$

4.3.2.8 TV controller based on the car-trailer model and modified yaw rate error ($MYRE$)

The $MYRE$ approach modifies the yaw rate error $\Delta\dot{\psi} = \dot{\psi}_d - \dot{\psi}$, by substituting it with a weighted linear combination ($\Delta\dot{\psi}_m$) of the yaw rate error and hitch angle error, where the latter has an influence only when it exceeds pre-determined thresholds, as shown in [24]. Z and Z_d are defined as:

$$\begin{aligned} Z &= [\tau_{m,tot}, \Delta\dot{\psi}_m, s_\alpha]^T \\ Z_d &= \left[\tau_{m,tot,d}\,, 0\,,\ 0\right]^T \end{aligned} \tag{4.3.37}$$

where $\Delta\dot{\psi}_m$ is given by:

$$\Delta\dot{\psi}_m = K_\theta \Delta\dot{\psi} - W_\theta(1 - K_\theta)\Delta\theta \tag{4.3.38}$$

with K_θ having been defined in (4.3.31).

4.3.3 SIMULATION ENVIRONMENT AND CONTROLLER IMPLEMENTATION

4.3.3.1 Simulation environment

The simulation environment for control system performance assessment consists of the following functional blocks, see Figure 4.3.4:

- The driver model, which generates the steering and accelerator pedal inputs, S_W and p_a, according to the considered set of manoeuvres.
- The drivability controller, which outputs the total powertrain torque demand at the vehicle level, $\tau_{m,tot}$, starting mainly from V and p_a.
- The implicit (i.e., online) implementations of the NMPC formulations in 4.3.2.
- The traction controller, regulating the output torques of the TV controller through a proportional integral (PI) controller, to prevent significant levels of wheel slip in traction. This control function is not described in detail, as it is never active in the selected manoeuvres.
- The high-fidelity nonlinear vehicle simulation model for control system assessment, developed independently from the internal model of the controllers, and characterised by a significantly higher level of accuracy.

The estimators of the relevant vehicle states were not included, as they are covered by a rather extensive literature, e.g., see [25]–[31].

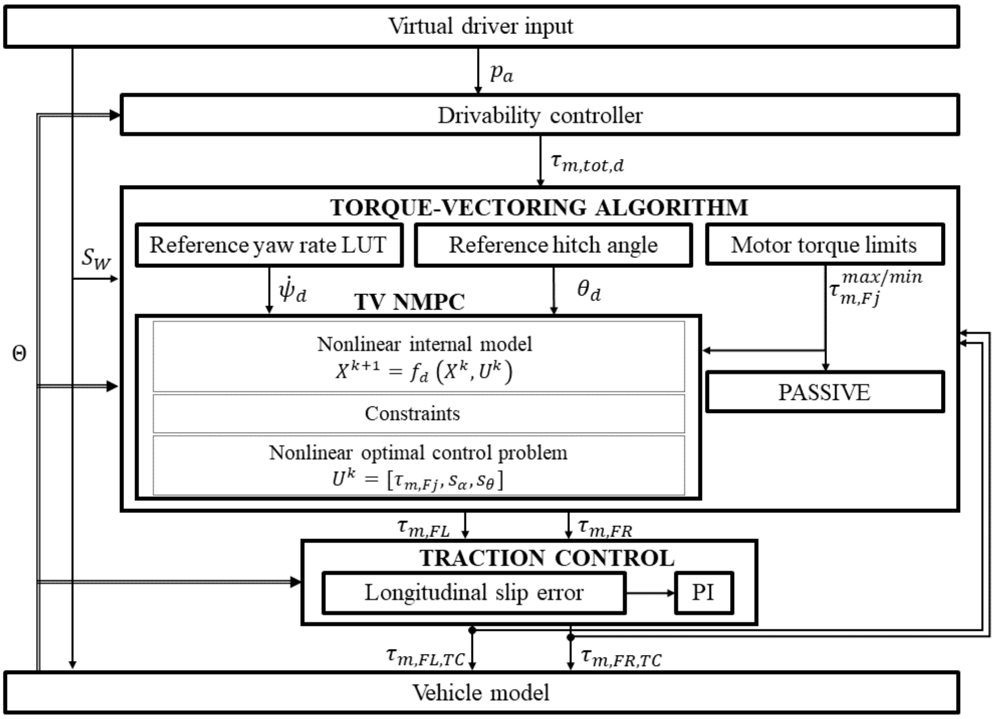

Figure 4.3.4: Functional blocks of the simulation environment

4.3.3.2 Case study vehicle and simulation model validation

The case study car is the front-wheel-drive version of the electric sport utility vehicle prototype with individually controlled powertrains, developed in the European projects E-VECTOORC and iCOMPOSE [24], see its main parameters in Table 4.3.1. The simulation model for control system assessment evaluates the combination of this car with three production trailers, referred to as trailers A–C in the remainder, with different geometric and inertial properties (the values in the table include the considered payload), to analyse the sensitivity of controller performance to the trailer parameters. The model was implemented in MATLAB-Simulink and includes the relevant degrees of freedom of the sprung masses and wheels, nonlinear suspension elasto-kinematics, as well as tyre nonlinearities (modelled through the magic formula, version 5.2) with relaxation.

Table 4.3.1 – Main car-trailer system parameters.

Symbol	Name and unit	Value		
m	Mass [kg]	2290		
J_z	Yaw mass moment of inertia [kgm^2]	2761		
L_{TOT}	Wheelbase [m]	2.660		
R	Wheel radius [m]	0.3706		
L_F	Front semi-wheelbase [m]	1.399		
c	Longitudinal distance from CG to hitch joint [m]	2.111		
d_F, d_R	Track width [m]	1.625		
H_{CG}	Centre of gravity height [m]	0.550		
RCH	Roll axis height at the longitudinal coordinate of CG [m]	0.150		
		Trailer A	Trailer B	Trailer C
m_T	Mass [kg]	1400	1000	500
I_T	Yaw mass moment of inertia [kgm^2]	778	646	481
$L_{F,T}$	Hitch joint to trailer centre of gravity distance [m]	2.666	1.961	2.863
$L_{TOT,T}$	Hitch joint to trailer axle distance [m]	2.800	2.300	2.940

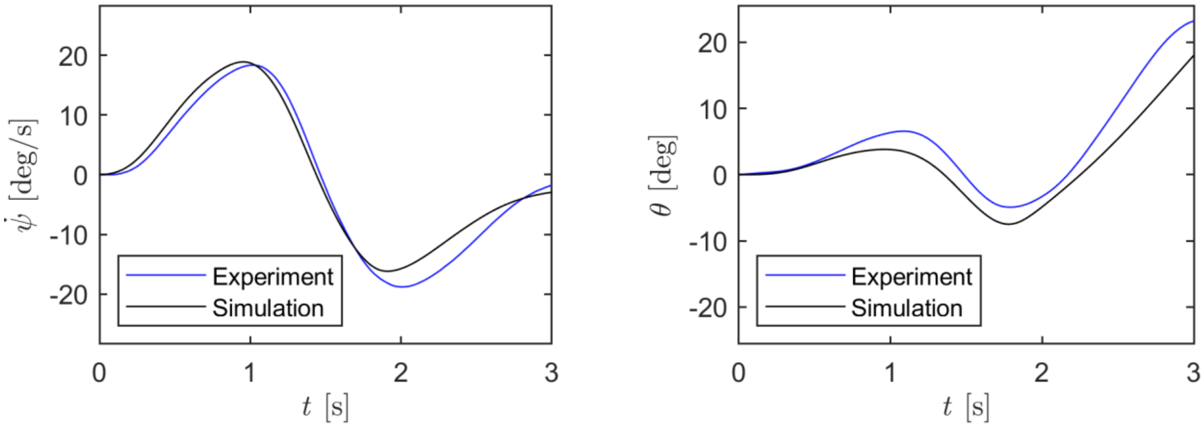

(a) (b)

Figure 4.3.5: Example of model validation results with trailer A: sinusoidal steering test at ~70 km/h. (a) car yaw rate; and (b) hitch angle

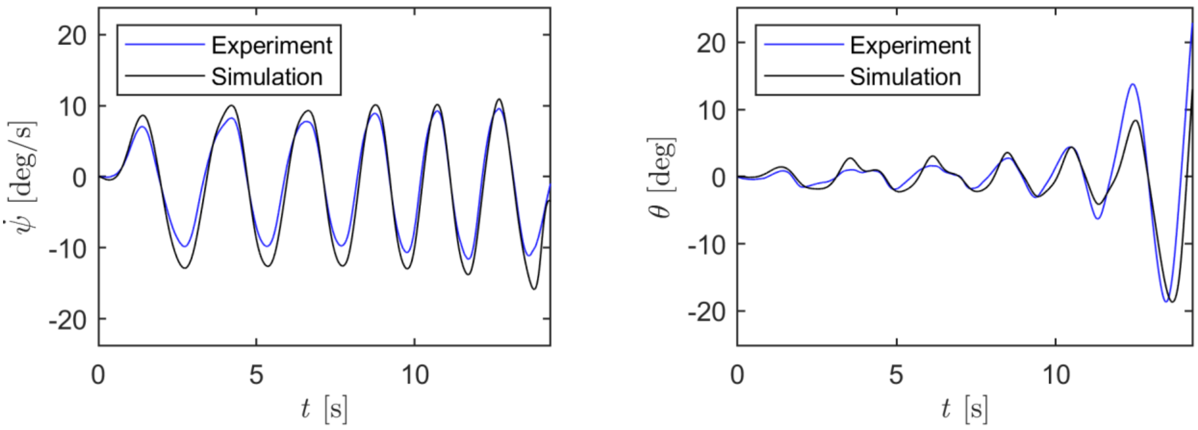

(a) (b)

Figure 4.3.6: Example of model validation results with trailer A: sweep steering test at ~90 km/h. (a) car yaw rate; and (b) hitch angle

The accuracy of the model was verified by providing experimental data from real-world tests as input to the model and comparing the resulting model outputs to the dynamic quantities measured during the tests, conducted at the Lommel proving ground (Belgium) at the Vehicle Dynamics Area, on the electric car prototype towing trailer A, without activation of the TV controller. For example, Figure 4.3.5 and Figure 4.3.6 report the comparison of the experimental and simulation time profiles of the car yaw rate and trailer hitch angle, along: i) a single sinusoidal steering test at constant torque demand, with a 40 deg steering wheel angle amplitude and 3 s duration, at an approximately constant speed of 70 km/h; and ii) a sweep steering test at constant torque demand, with a 25 deg sinusoidal steering wheel input at progressively increasing frequency, at ~90 km/h. The very good match between simulations and experiments, in particular in terms of hitch angle oscillations, confirms that the simulation model can be considered a valid tool for control system assessment.

4.3.3.3 Real-time implementation of the controllers

The controllers in Sections 4.3.2.4–4.3.2.8 were implemented in Simulink through the ACADO Toolkit [39], including Gauss-Newton iteration algorithms for fast NMPC with constraints. The selected solver parameters are: multiple shooting discretisation method, second order Runge Kutta integrator, and qpOASES solver.

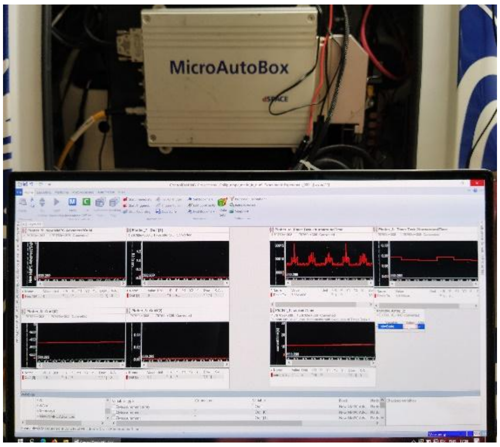

Figure 4.3.7: Real-time implementation set-up for the proposed NMPC configurations

Moreover, to demonstrate their real-time capability, all proposed controllers were run in real-time on a rapid control prototyping unit, i.e., a dSPACE MicroAutoBox II 1401/1513, with an IBM 900 MHz processor and 16 Mb flash memory, see Figure 7. Given the reduced number of prediction steps to achieve computationally efficient NMPC implementations, the specific dynamic system cannot be considered to be operating in steady-state conditions at the end of the prediction horizon [45], and therefore the controllers were set to have the same number of steps for the prediction and control horizons. For real-time implementation, the controller sampling time T_s , which is coincident with the implementation time, was set to 20 ms, with 2 optimisation steps, which corresponds to a 40 ms prediction horizon. The discretisation time of the internal model was set to 4 ms, which ensures numerical stability without significantly affecting the computational time. Unless otherwise specified, the results of the following sections are obtained with this controller parametrisation.

4.3.3.4 Controller tuning routine

The weights related to common cost function terms among all considered controllers (i.e., the weights related to $\tau_{m,tot}$, ψ, $\tau_{m,FL}$, $\tau_{m,FR}$, and s_{α}) were selected to be the same across all controllers, and to provide good performance in case of rigid vehicle operation, or articulated vehicle operation along manoeuvres with limited hitch angle dynamics. The cost function weights and calibration parameters that are specific to each controller (see Table 4.3.2) were optimised through the automated routine described in this section, to achieve a fair assessment.

Table 4.3.2 – Features of the implemented controllers and respective tuning parameters

Controller	Internal model	Description	$P_{LB} \leq P_{opt} \leq P_{UB}$
YR_{rig}	Rigid vehicle	Yaw rate tracking for the rigid vehicle	-
$MYR_{d,rig}$	Rigid vehicle	Reference yaw rate given by the weighted linear combination of the car yaw rate and hitch angle error	-100 $\text{s}^{-1} \leq W_\theta \leq$ -0.9 s^{-1} $0.1 \leq K_{\theta,min} \leq 0.9$ 3 deg $\leq \Delta\theta_{lim} \leq$ 10 deg
$YR + SC_{HAE}$	Car-trailer	Yaw rate tracking and soft constraint on hitch angle error	$2 \leq W_{s_\theta} \leq 1000$ 3 deg $\leq \Delta\theta_{lim} \leq$ 10 deg
$YR + HAE_{fun}$	Car-trailer	Yaw rate tracking and hitch angle error control through continuous function	$200 \leq W_{\Delta\theta_c} \leq 4000$
$MYRE$	Car-trailer	Control error given by the weighted linear combination of the yaw rate error and hitch angle error	-100 $\text{s}^{-1} \leq W_\theta \leq$ -1 s^{-1} $0.1 \leq K_{\theta,min} \leq 1$ 3 deg $\leq \Delta\theta_{lim} \leq$ 10 deg

The routine runs the simulation model for control system assessment, including the controllers, along a typical critical test (indicated as manoeuvre I in the remainder) for trailer dynamics evaluation, namely a single sinusoidal steering manoeuvre with a 50 deg steering wheel angle amplitude and 3 s duration, from an initial speed of 70 km/h, at a constant 200 Nm wheel torque demand, carried out with trailer A. The main features and tuning parameters of each controller are summarised in Table 2, where W_{s_θ} and $W_{\Delta\theta_c}$ are the weights associated with the hitch angle slack variable (4.3.33) and hitch angle error function (4.3.36) within the controller cost function (4.3.24). Given the rather limited number of tuning parameters of each controller, a brute force algorithm was used to cover the whole parameter space in Table 4.3.2, according to the following optimisation problem:

$$\begin{gathered} J_{KPI}^{*} = \min_{P_{opt}} J_{KPI}\big|_{t_i}^{t_f} \\ \text{s.t.}\, P_{LB} \leq P_{opt} \leq P_{UB} \end{gathered} \tag{4.3.39}$$

where P_{LB} and P_{UB} include the lower and upper bounds of the tuning parameters; P_{opt} is the optimal value of the parameter vector; t_i and t_f are the initial and the final times of the relevant part of the test; and J_{KPI}^{*} is the optimal value of the cost function J_{KPI}, which is given by the weighted sum of multiple non-dimensional key performance indicators (KPIs):

$$J_{KPI} = W_1\, RMSE_{\Delta\dot{\psi}} + W_2\, RMSE_{\Delta\theta^*} + W_3\, \alpha_R^{max} + W_4\, \theta^{max} + W_5\, IACA \tag{4.3.40}$$

where W_{1-5} are the weights for the individual indicators ($W_1 = 0.3$, $W_2 = 0.35$, $W_3 = 0.10$, $W_4 = 0.20$, and $W_5 = 0.05$ in the specific implementation).

The terms in (4.3.40) are:

- The root-mean-square value of the yaw rate error:

$$RMSE_{\Delta\dot{\psi}} = \frac{\sqrt{\frac{1}{t_f - t_i}\int_{t_i}^{t_f}\left[\dot{\psi}_d(t) - \dot{\psi}(t)\right]^2 dt}}{M_{\Delta\dot{\psi}}} \tag{4.3.41}$$

where $M_{\Delta\dot{\psi}}$ is a normalisation factor, expressed as the maximum expected value of the performance indicator, i.e., $RMSE_{\Delta\dot{\psi}}$. The same criterion was used for the selection of the normalisation factors of the other indicators, i.e., $M_{\Delta\theta^*}$, $M_{\alpha_R^{max}}$, and $M_{\theta^{max}}$, and M_{IACA}.

- The root-mean-square value of the hitch angle error, to assess the level of trailer sway:

$$RMSE_{\Delta\theta^*} = \frac{\sqrt{\frac{1}{t_f - t_i}\int_{t_i}^{t_f}[\Delta\theta^*]^2 dt}}{M_{\Delta\theta^*}} \tag{4.3.42}$$

$$\Delta\theta^* = \begin{cases} |\theta_d(t) - \theta(t)| - \Delta\theta_{bound} & \text{if} \quad |\theta_d(t) - \theta(t)| > \Delta\theta_{bound} \\ 0 & \text{if} \quad |\theta_d(t) - \theta(t)| \leq \Delta\theta_{bound} \end{cases} \tag{4.3.43}$$

where $\Delta\theta_{bound}$ = 7 deg is the hitch angle error bound of the deadband function in (4.3.43).

- The maximum rear axle sideslip angle (in absolute value), to assess the car's stability:

$$\alpha_R^{max} = \frac{\max|\alpha_R|}{M_{\alpha_R^{max}}} \tag{4.3.44}$$

- The maximum hitch angle (in absolute value), which shows the most critical condition of the vehicle combination:

$$\theta^{max} = \frac{\max|\theta|}{M_{\theta^{max}}} \tag{4.3.45}$$

- The integral of the absolute value of the control action, $IACA$, given by the front powertrain torque difference, which evaluates the control effort:

$$IACA = \frac{\frac{1}{t_f - t_i}\int_{t_i}^{t_f}\left|\tau_{m.FL}(t) - \tau_{m,FR}(t)\right| dt}{M_{IACA}} \tag{4.3.46}$$

To analyse the performance of the controllers in a wider range of conditions, in the remainder J_{KPI} and the respective individual performance indicators have been calculated also for a second test, referred to as manoeuvre II, i.e., a prolonged sinusoidal steering manoeuvre at a constant steering input frequency of 0.67 Hz, a 65 deg steering wheel angle amplitude, and a ~25 s duration, from an initial speed of 70 km/h, with a constant 200 Nm wheel torque demand. The simulations are stopped if the hitch angle reaches a critical value of 45 deg.

4.3.4 RESULTS

For the vehicle combination with trailer A and manoeuvres I and II, Figure 4.3.8 and Figure 4.3.9 show the time histories of the car yaw rate, hitch angle error, rear axle sideslip angle, and direct yaw moment control action, the latter calculated as:

$$M_z = \frac{[\tau_{m,FL} - \tau_{m,FR}]d_F}{2R} \tag{4.3.47}$$

In addition to the considered controlled configurations, the figures include the response of the Passive configuration, i.e., without TV control, which becomes unstable in both tests, i.e., the simulation is stopped as θ reaches the critical level of 45 deg. In these extreme manoeuvres, the baseline TV configuration, YR_{rig}, which neglects the hitch angle aspects, although behaving better than the passive vehicle, cannot manage to restrain $\Delta\theta$ within safe limits, i.e., the hitch angle error has a ~25 deg peak amplitude in manoeuvre I, while in manoeuvre II the simulation has to be stopped because of the unstable hitch angle dynamics. Interestingly, all formulations including the hitch angle error contribution show desirable hitch dynamics, with performance differences that are visible only in the zoomed plots in Figure 4.3.8(b) and Figure 4.3.9(b). For the single sinusoidal test, Figure 4.3.8(a) highlights that in the configurations with hitch angle feedback the car maintains a negative car yaw rate for > 0.5 s after the steering angle is brought back to zero at the end of the manoeuvre, because of the direct yaw moment required to correct trailer sway. In general, direct hitch angle control implies an increase of the M_z control action, see the profiles in Figure 4.3.8(d), in which $YR + SC_{HAE}$ and $YR + HAE_{fun}$ reach the yaw moment saturation value imposed by the specific electric motors. In the prolonged sinusoidal steering test, $YR + SC_{HAE}$ and $YR + HAE_{fun}$ show the best results in terms of hitch angle error limitation, see Figure 4.3.9(b). Among the configurations based on feedback hitch angle control, the highest hitch angle error peaks are associated with $MYR_{d,rig}$, as a consequence of its simpler internal model, see the comparison with the $MYRE$ formulation, which, although also using a hitch angle based yaw rate correction, considers the vehicle combination dynamics. The control action profile in Figure 4.3.9(d) is rather similar for all the hitch angle control configurations, and, given the rather extreme nature of the manoeuvre, M_z reaches its saturation value during each trailer oscillation cycle until ~17.5 s. Afterwards, the marginal vehicle speed reduction caused by the lateral tyre slip power losses makes the manoeuvre less critical, and thus requires less intense direct yaw moments. In the specific test, the M_z peaks tend to limit the magnitude of the yaw rate of the car, and thus to reduce the trailer sway toward the inner side of the vehicle trajectory. For each controller, Table 4.3.3 reports the values of the performance indicators and cost function defined in Section 4.3.3.4 along the two considered manoeuvres, performed with the car towing trailers A–C. To evaluate the controller robustness with respect to the variation of trailer parameters, for trailers B and C all controller tunings, including the internal model parameters, are kept constant and equal to those for trailer A. Interestingly, because of its higher mass and yaw moment of inertia, trailer A tends to originate the most critical results, and the NMPCs tuned for trailer A provide desirable performance also with trailers B and C, despite the significant difference in trailer parameters (e.g., the mass of trailer C is approximately one third of the mass of trailer A).

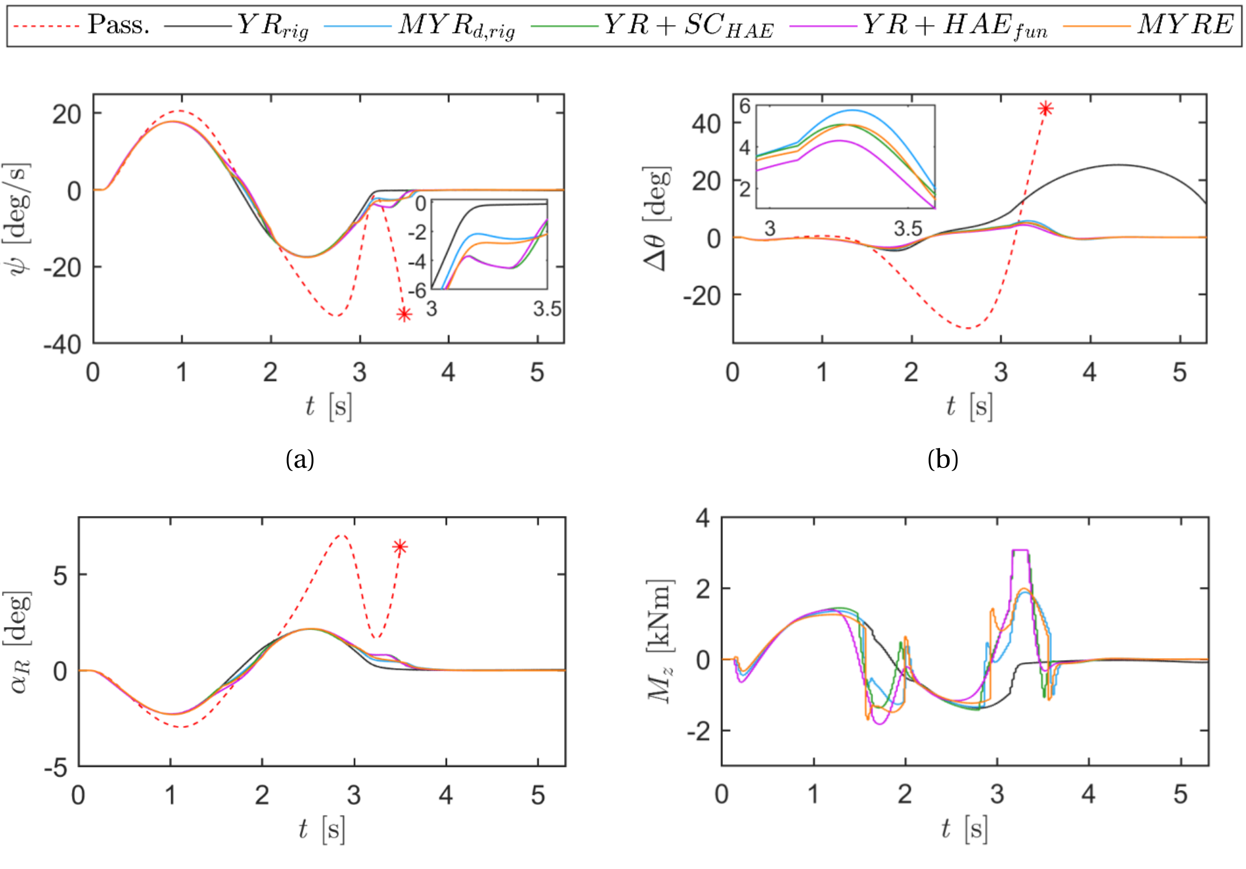

(a) (b)

(c) (d)

Figure 4.3.8: Single sinusoidal steering test (manoeuvre I) with trailer A: (a) car yaw rate; (b) hitch angle error; (c) rear axle sideslip angle; and (d) direct yaw moment control action.

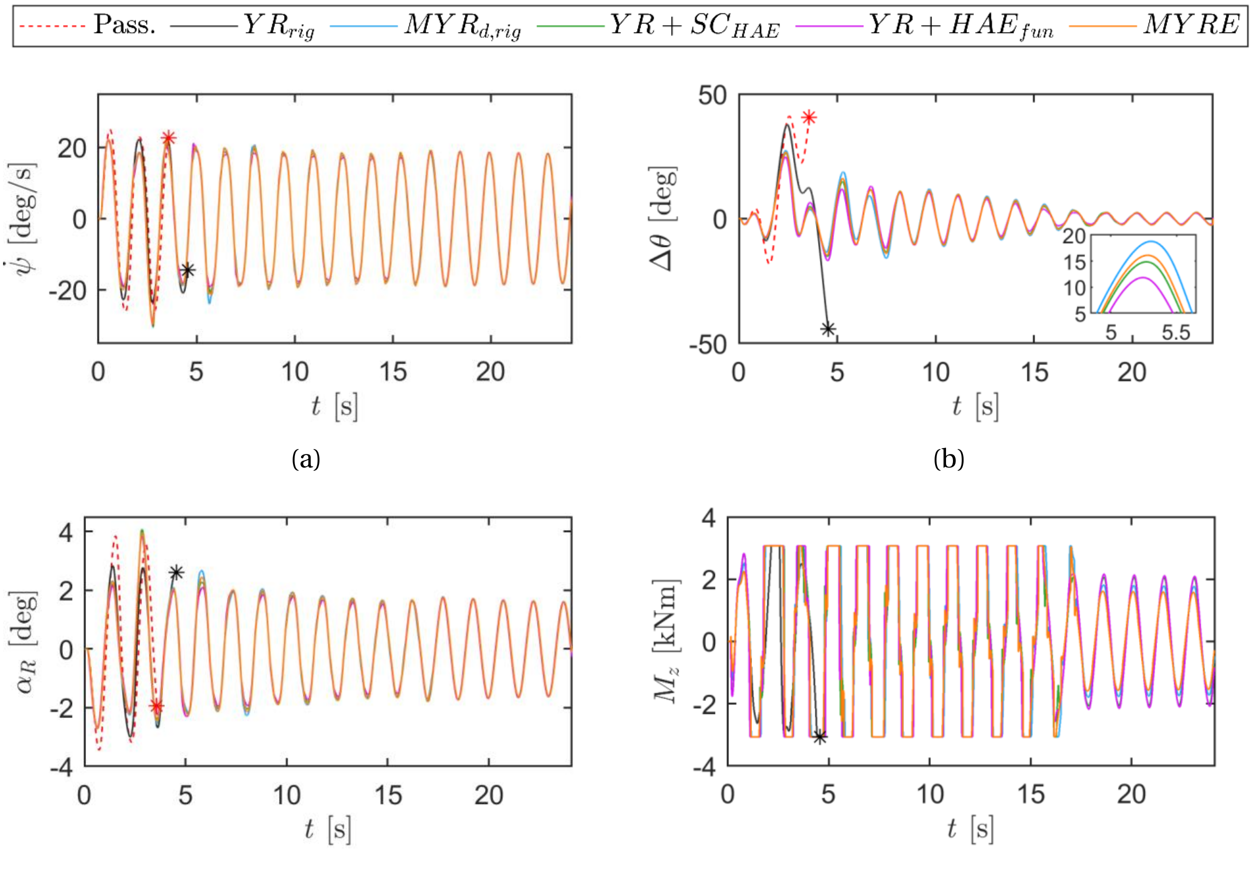

(a) (b) (c) (d)

Figure 4.3.9: Prolonged sinusoidal steering test (manoeuvre II) with trailer A: (a) car yaw rate; (b) hitch angle error; (c) rear axle sideslip angle; and (d) direct yaw moment control action

The important conclusion is that the model-based hitch angle controllers should be tuned for the most critical trailer parametrisation, and then the resulting controller performance will be acceptable for a very wide range of trailer parameters. The J_{KPI} values across all trailer configurations, as well as the other performance indicators, and in particular $RMSE_{\Delta\theta^*}$ and $|\theta^{max}|$, highlight the good performance of $YR+SC_{HAE}$ and $YR+HAE_{fun}$, i.e., the feedback hitch angle controller formulation should directly consider the hitch angle error, and use a prediction model with trailer dynamics. While in absence of significant hitch angle dynamics excitation, the controllers using the prediction model for the car-trailer tend to enhance the car yaw rate tracking performance in comparison with the benchmarking YR_{rig}, see manoeuvre I with trailer B, in presence of significant hitch angle dynamics, the hitch control stabilisation effort can marginally increase $RMSE_{\Delta\dot{\psi}}$, see manoeuvre I with trailer A, even if in most cases the hitch angle and yaw rate tracking performances concurrently improve.

Table 4.3.3 – Key performance indicators associated with the passive vehicle and the vehicle with the real-time (RT) implementations of the proposed NMPCs, with trailers A-C, and with the NMPCs with longer prediction horizon (LPH), applied to trailer A

		Manoeuvre	Pass.	YR_{rig}	$MYR_{d,rig}$	$YR + SC_{HAE}$	$YR + HAE_{fun}$	$MYRE$
Trailer A (RT)								
$RMSE_{\Delta\dot{\psi}}$	[deg/s]	I	9.90^{*}	1.11	1.61	1.82	2.03	1.82
		II	9.87^{*}	4.49^{*}	2.31	2.22	2.13	2.41
$RMSE_{\Delta\theta^{*}}$	[deg]	I	13.00^{*}	9.27	0.00	0.00	0.00	0.00
		II	16.70	13.37^{*}	3.44	3.08	2.83	3.18
$\|\alpha_R^{max}\|$	[deg]	I	7.06^{*}	2.29	2.29	2.27	2.27	2.29
		II	3.86^{*}	3.00^{*}	3.88	4.08	3.85	3.96
$\|\theta^{max}\|$	[deg]	I	45.00^{*}	25.25	5.89	5.44	5.13	5.65
		II	45.00^{*}	45.00^{*}	27.22	26.30	25.03	26.58
$IACA$	[Nm]	I	-	251	295	318	305	324
		II	-	825^{*}	900	920	962	843
J_{KPI}	[-]	I	/	0.56	0.15	0.15	0.15	0.15
		II	/	/	0.57	0.55	0.53	0.56
Trailer B (RT)								
$RMSE_{\Delta\dot{\psi}}$	[deg/s]	I	5.29^{*}	1.28	1.28	1.16	1.23	1.38
		II	5.97	2.91	2.12	2.22	2.33	2.37
$RMSE_{\Delta\theta^{*}}$	[deg]	I	8.63^{*}	0.00	0.00	0.00	0.00	0.00
		II	6.44	5.02	3.15	2.82	2.66	2.98
$\|\alpha_R^{max}\|$	[deg]	I	3.04^{*}	2.36	2.36	2.34	2.34	2.37
		II	3.76	2.97	2.71	2.68	2.69	2.70
$\|\theta^{max}\|$	[deg]	I	45.00^{*}	3.22	3.22	3.21	3.21	3.22
		II	40.33	31.88	23.70	22.18	21.88	22.92
$IACA$	[Nm]	I	-	262	262	280	269	248
		II	-	622	917	966	984	851
J_{KPI}	[-]	I	/	0.11	0.11	0.11	0.11	0.11
		II	-	0.64	0.51	0.48	0.48	0.49
Trailer C (RT)								
$RMSE_{\Delta\dot{\psi}}$	[deg/s]	I	2.71	0.98	0.98	0.88	0.88	1.07
		II	8.96^{*}	2.82	1.86	1.73	1.70	2.03
$RMSE_{\Delta\theta^{*}}$	[deg]	I	0.00	0.00	0.00	0.00	0.00	0.00
		II	17.58^{*}	4.39	2.21	1.84	1.79	2.12
$\|\alpha_R^{max}\|$	[deg]	I	2.84	2.24	2.24	2.23	2.23	2.25
		II	3.98^{*}	2.80	3.14	2.82	2.93	3.17
$\|\theta^{max}\|$	[deg]	I	5.03	3.94	3.94	3.92	3.92	3.93
		II	45.00^{*}	26.30	21.19	19.72	20.23	21.07
$IACA$	[Nm]	I	-	262	262	280	269	248
		II	-	622	917	966	984	851
J_{KPI}	[-]	I	-	0.11	0.11	0.11	0.11	0.11
		II	/	0.55	0.46	0.42	0.43	0.45
Trailer A (LPH)								
$RMSE_{\Delta\dot{\psi}}$	[deg/s]	I	9.90^{*}	1.31^{*}	1.26	2.17	2.10	1.37
		II	9.87^{*}	8.08^{*}	5.98	3.30	3.21	4.24
$RMSE_{\Delta\theta^{*}}$	[deg]	I	13.00^{*}	15.70^{*}	0.00	0.00	0.00	0.00
		II	16.70	19.85^{*}	6.74	1.49	1.57	4.10
$\|\alpha_R^{max}\|$	[deg]	I	7.06^{*}	2.31^{*}	2.31	2.29	2.29	2.29
		II	3.86^{*}	3.57^{*}	5.28	2.90	3.00	5.75
$\|\theta^{max}\|$	[deg]	I	45.00^{*}	45.00^{*}	6.51	5.03	5.18	6.19
		II	45.00^{*}	45.00^{*}	35.96	19.44	19.89	29.57
$IACA$	[Nm]	I	-	/	275	299	252	261
		II	-	/	699	746	756	793
J_{KPI}	[-]	I	/	/	0.15	0.15	0.14	0.15

	II	/	/	0.80	0.43	0.43	0.65

*: the hitch angle reaches the critical threshold at which the simulation is automatically interrupted
-: value not calculated
/: simulation interrupted; value not calculated

To appreciate the trade-off between yaw rate tracking and hitch angle stabilisation, Figure 4.3.10(a) plots the trailer sway mitigation improvement with respect to YR_{rig}, expressed through $I_{RMSE,\Delta\theta^*}$, as a function of the yaw rate tracking improvement, measured by $I_{RMSE,\Delta\dot{\psi}}$. For each controller, manoeuvre and trailer, $I_{RMSE,\Delta\theta^*}$ and $I_{RMSE,\Delta\dot{\psi}}$ are defined as:

$$I_{RMSE,\Delta\theta^*} = \begin{cases} 100\,\dfrac{RMSE_{\Delta\theta^*}^{YR_{rig}} - RMSE_{\Delta\theta^*}^{CC}}{RMSE_{\Delta\theta^*}^{Pass}} & \text{if} \quad RMSE_{\Delta\theta^*}^{Pass} > 0 \\ 0 & \text{if} \quad RMSE_{\Delta\theta^*}^{Pass} = 0 \end{cases} \tag{4.3.48}$$

$$I_{RMSE,\Delta\dot{\psi}} = 100\,\frac{RMSE_{\Delta\dot{\psi}}^{YR_{rig}} - RMSE_{\Delta\dot{\psi}}^{CC}}{RMSE_{\Delta\dot{\psi}}^{Pass}} \tag{4.3.49}$$

where the superscript 'YR_{rig}' highlights that the indicator is computed for the benchmarking YR_{rig} set-up; the superscript 'CC' indicates the considered controller, i.e., the one that is compared with YR_{rig}; and the superscript '$Pass$' refers to the passive configuration. Positive values of $I_{RMSE,\Delta\theta^*}$ and $I_{RMSE,\Delta\dot{\psi}}$ mean enhanced performance with respect to YR_{rig}, while negative values correspond to a performance decrease. The performance of the passive vehicle combination is used as normalisation factor in the denominators in (4.3.48)–(4.3.49), to provide a meaningful order of magnitude of the baseline performance (in some cases the root mean square values of all controlled configurations are so low, that the percentage variations would appear significant even in case of negligible variations of the actual system response). Along manoeuvre I the average $I_{RMSE,\Delta\dot{\psi}}$ values across the three trailers are -1.7%, -0.4%, -1.6% and -4.1%, respectively for $MYR_{d,rig}$, $YR + SC_{HAE}$, $YR + HAE_{fun}$, and $MYRE$, i.e., the yaw rate tracking performance tends to be very marginally reduced than for the benchmarking YR_{rig}, yet it is significantly better than for the passive configuration. However, very importantly, during the same manoeuvre all hitch angle controllers manage to keep $\Delta\theta$ within the defined deadband for the three trailers, while YR_{rig} cannot for trailer A, which causes vehicle instability, and corresponds to $I_{RMSE,\Delta\theta^*} = 71.3\%$. In manoeuvre II, the proposed hitch angle controllers bring concurrent benefits in terms of trailer sway stabilisation and yaw rate tracking for all trailers, with average values of $I_{RMSE,\Delta\theta^*}$ and $I_{RMSE,\Delta\dot{\psi}}$ equal to 33.6% and 15.3% for $MYR_{d,rig}$, 36.8% and 15.6% for $YR + SC_{HAE}$, 38.2% and 15.4% for $YR + HAE_{fun}$, and 35.2% and 13.0% for $MYRE$. These results, together with the generalised reduction of the J_{KPI} values in the table, indicate a major active safety enhancement, which would justify the additional complexity of the hitch angle measurement/estimation for the next generation of stability controllers for car-trailer systems. To evaluate whether these trends are significantly affected by the NMPC settings, for trailer A Table 4.3.3 and Figure 4.3.10(b) also include the performance indicators for configurations of the same controllers operating with a longer prediction horizon, i.e., 500 ms, obtained by setting $N = 50$ and 10 ms as update time of the control input. Such configurations are not real time implementable with the hardware in Figure 4.3.7, but could become so with the next generations of automotive micro-controllers, and the related results provide generality to the comparison. Interestingly, while with the baseline set-up the benchmarking YR_{rig} configuration manages to complete manoeuvre I, with $N = 50$ it fails to complete both manoeuvres, while all proposed hitch angle feedback control configurations are always successful. Among them, the best approaches are $YR + HAE_{fun}$ and $YR + SC_{HAE}$, which outperform $MYR_{d,rig}$ and $MYRE$. In general, the extension of the prediction horizon does not automatically ensure a performance improvement, as the driver inputs, i.e., the total wheel torque demand and steering angle, are considered constant along the prediction horizon, which is the typical assumption of model predictive control for vehicle dynamics control, in absence of integration of the predictive controller with the localisation and navigation systems, see the discussion on pre-emptive vehicle stability control in [35]. This is confirmed by Figure 4.3.10(b), which plots the percentage variation of J_{KPI}, i.e., ΔJ_{KPI}, for each configuration with the longer prediction horizon, with respect to the corresponding real-time case (a negative value of ΔJ_{KPI} indicates an improvement with the longer prediction horizon). The number of cases with positive and negative ΔJ_{KPI}, and the respective magnitudes, are approximately equivalent, which confirms the effectiveness of the proposed real-time implementations with short prediction horizon.

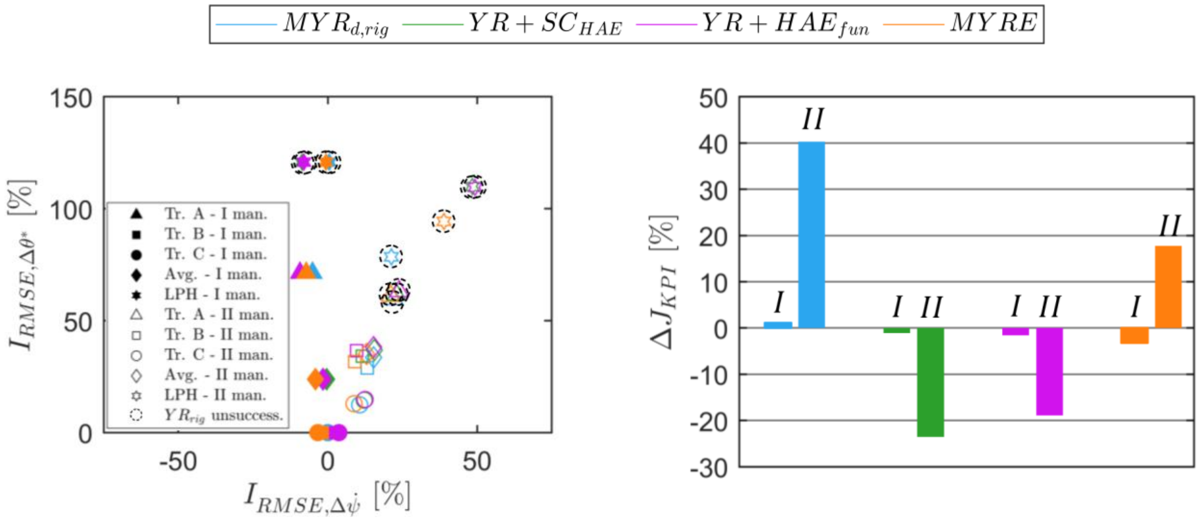

(a) (b)

Figure 4.3.10: Hitch angle stabilisation improvement of the real-time controller configurations, evaluated through $I_{RMSE,\Delta\theta^*}$, as a function of the car yaw rate tracking improvement, evaluated through $I_{RMSE,\Delta\dot{\psi}}$, with respect to YR_{rig} (the marker associated with 'YR_{rig} unsuccess.' highlights the cases in which YR_{rig} cannot complete the test because of trailer instability); and (b) Percentage variation of J_{KPI} for the controller implementations for trailer A with 500 ms prediction horizon, with respect to the corresponding ones with 40 ms prediction horizon

Similar simulation results, not included in the manuscript, were obtained also along lane change manoeuvres from 100 km/h [46], in which the proposed control strategies provide safe behaviour of the car-trailer combination, while the passive vehicle cannot complete the test because of the trailer sway with unstable hitch angle dynamics. The benefits, evident across the range of considered performance indicators, include the reduction the rearward amplification factor (RWA) of the lateral acceleration, defined as the ratio between the maximum value of the lateral acceleration of the centre of gravity of the trailer to that of the car during the test.

4.3.5 CONCLUDING REMARKS

This study presented four nonlinear model predictive control formulations for the torque-vectoring control of a car towing a single-axle trailer, under the assumption of the availability of measured or estimated hitch angle information. The proposed controllers target continuous yaw rate control and sideslip angle limitation for the towing car, while limiting the hitch angle dynamics in critical conditions of the vehicle combination. The four novel formulations were implemented in real-time on typical automotive rapid control prototyping hardware, tuned through an optimisation routine using an experimentally validated simulation model, and compared with a benchmarking nonlinear model predictive torque-vectoring controller, along two manoeuvres, conducted with three trailers covering a wide range of parameters. The analysis brought the following conclusions:

- The benchmarking TV controller, YR_{rig}, which tracks only the yaw rate of the car and uses a rigid vehicle model as internal model, does not manage to complete the manoeuvres when it is associated with the heaviest considered trailer. This confirms that dedicated controllers are highly beneficial to the active safety enhancement of vehicle combinations.
- The $MYR_{d,rig}$ controller, which uses the hitch angle error to correct the reference yaw rate of the towing car and only includes the towing car in its internal model, is able to stabilise trailer sway in all considered conditions and shows desirable yaw rate tracking performance in most cases. Nevertheless, the hitch angle indicators are generally not as good as for the formulations including the car-trailer dynamics in the internal model. $MYR_{d,rig}$ can represent a viable compromise between simplicity of implementation and effectiveness.
- The best performance was obtained with the $YR + HAE_{fun}$ and $YR + SC_{HAE}$ formulations, which include the car-trailer dynamics in their prediction models and use the hitch angle error either in the cost function or in the constraints.
- The least effective configuration among those including the trailer dynamics in the internal model is $MYRE$, which modifies the yaw rate error as a function of the hitch angle error. Nevertheless, the resulting performance is better than for $MYR_{d,rig}$ and especially YR_{rig}.
- The formulations using an internal model of the car-trailer show high level of robustness to the variation of the real trailer parameters with respect to their nominal values used within the prediction model, e.g., the controllers with fixed values of the inertial parameters provided safe performance in emergency conditions for trailer mass values ranging from 500 kg to 1400 kg.
- All proposed controllers are real-time implementable, provided that appropriate parameters, e.g., number of prediction steps and implementation time, are selected. Short prediction horizons do not represent a performance limitation for

the specific controllers, as the driver inputs are considered to remain constant along the prediction horizon.

- The next steps of this research will focus on the implementation and experimental assessment of the proposed algorithms on real demonstrator vehicles.

BIBLIOGRAPHY

[1]J. Darling, D. Tilley, and B. Gao, “An experimental investigation of car-trailer high-speed stability,” *Proc. Inst. Mech. Eng., Part D: J. Autom. Eng.*, vol. 223, no. 4, pp. 471–484, 2009.

[2]E. Gerum, P. Laszlo, A. Semsey, and G. Barta, “Method for drive stability enhancement of multi-unit vehicles,” U.S. 005,747,683, 1998.

[3]O. Mokhiamar and M. Abe, “Examination of different models following types of yaw moment control strategy for improving handling safety of a car–caravan combination,” *Proc. Inst. Mech. Eng., Part D: J. Autom. Eng.*, vol. 217, no. 7, pp. 561–572, 2003.

[4]W. K. Deng and X. Kang, “Parametric study on vehicle-trailer dynamics for stability control,” *SAE Technical Paper*, pp. 1411–1419, 2003.

[5]M. A. Fernández and R. S. Sharp, “Caravan active braking system-Effective stabilisation of snaking of combination vehicles,” *SAE Technical Paper* 2001-01-3188, 2001.

[6]M. Plöchl, P. Lugner and A. Riepl, “Improvements of passenger car-trailer behaviour by a trailer based control system,” *Veh. Syst. Dyn.*, vol. 29, no. S1, pp. 438–450, 1998.

[7]T. Sun, Y. He and J. Ren, “Dynamics Analysis of Car-Trailer Systems with Active Trailer Differential Braking Strategies,” *SAE Int. J. Passeng. Cars - Mech. Syst.*, vol. 7, no. 1, pp. 73–85, 2014.

[8]R. Shamim, M. Islam and Y. He, “A Comparative Study of Active Control Strategies for Improving Lateral Stability of Car-Trailer Systems ,” *SAE Technical Paper*, 2011-01-0959, 2011.

[9]C. MacAdam and M. Hagan, “A Simple Differential Brake Control Algorithm for Attenuating Rearward Amplification in Doubles and Triples Combination Vehicles,” *Veh. Syst. Dyn.*, vol. 37, no. 1, pp. 234–245, 2002.

[10]S. Milani, Y. S. Ünlüsoy, H. Marzbani and R.N. Jazar, “Semitrailer Steering Control for Improved Articulated Vehicle Manoeuvrability and Stability,” *Nonlin. Eng.*, vol. 8, no. 1, pp. 568-581, 2019.

[11]S. H. Tabatabaei Oreh, R. Kazemi, S. and Azadi, “A new desired articulation angle for directional control of articulated vehicles,” *Proc. Inst. Mech. Eng., Part D: J. Autom. Eng.*, 226(4):298–314, 2012.

[12]M. Islam, X. Ding and Y. He, “A closed-loop dynamic simulation-based design method for articulated heavy vehicles with active trailer steering systems,” *Veh. Syst. Dyn.*, vol. 50, no. 5, pp. 675–697, 2012.

[13] Y. He, M. Islam and T. Webster, “An Integrated Design Method for Articulated Heavy Vehicles with Active Trailer Steering Systems,” *SAE Int. J. Passeng. Cars – Mech. Syst*, vol. 3, no. 1, pp. 158–174, 2010.

[14]M. Keldani and Y. He, “Design of an Improved Robust Active Trailer Steering Controller for Multi-trailer Articulated Heavy Vehicles Using Software/Hardware-in-the-Loop Real-Time Simulations,” *IAVSD*, 2019.

[15] M. Islam and Y. He, “A parallel design optimisation method for articulated heavy vehicles with active safety systems,” *Int. J. of Heavy Veh. Syst.*, vol. 20, pp. 327–341, 2013.

[16] S. Vempaty, Y. He and L. Zhao, “An overview of control schemes for improving the lateral stability of car-trailer combinations,” *Int. J. Veh. Perf.,* vol. 6, no. 2, pp. 151–199, 2020.

[17] M. Abroshan, R. Hajiloo, E. Hashemi and A. Khajepour, “Model predictive-based tractor-trailer stabilisation using differential braking with experimental verification,” *Veh. Syst. Dyn.*, vol. 59, no. 8, pp. 1–24, 2021.

[18] Y. Zhang, A. Khajepour, E. Hashemi, Y. Qin and Y. Huang, “Reconfigurable model predictive control for articulated vehicle stability with experimental validation,” *IEEE Trans. Transp. Elect.*, vol. 6, no. 1, pp. 308–317, 2020.

[19] W. Wang, J. Fan, R. Xiong and F. Sung, “Lateral stability control of four wheels independently drive articulated electric vehicle,” IEEE Transportation Electrification Conference and Expo, 2016.

[20] https://media.daimler.com/marsMediaSite/en/instance/ko/The-technology-How-Trailer-Stability-Assist-works.xhtml?oid=9904516, last accessed on 21 June 2021.

[21] H. Wu, F. Nardi, J. Chen and E. Hartman, “Closed-loop control for trailer sway mitigation,” US 008,740,317, 2014.

[22] H. Wu, “Trailer sway mitigation using torque vectoring,” US 009,061,663, 2015.

[23] AL-KO “Comprehensive catalogue trailer components,” Part No. 499 699 B, Edition 06/2021.

[24] M. Zanchetta, D. Tavernini, A. Sorniotti, P. Gruber, B. Lenzo, A. Ferrara, K. Sannen, J. De Smet and W. De Nijs, “Trailer control through vehicle yaw moment control: Theoretical analysis and experimental assessment,” *Mechatronics*, vol. 64, 2019.

[25] Y. Lee and A. Kade, “Trailer articulation angle estimation,” US 007,904,222, 2008.

[26] J. Vejlupek, “Trailer Backing-up Assistant using ultrasound sensors based control units to safely back-up the car with trailer,” 17th International Conference on Mechatronics – Mechatronika, 2016.

[27] J. H. Ahmad and A. Ghaffari, “Nonlinear estimator design based on extended Kalman filter approach for state estimation of articulated heavy vehicle.” *Proc. Inst. Mech. Eng., Part K: J. Multi-body Dyn.*, vol. 233, no. 2, pp. 254–265, 2018.

[28] L. Xu, E. Tseng, T. Pilutti and S. Schondorf “Yaw rate based trailer hitch angle estimation for trailer backup assist,” *SAE Technical Paper* 2017-01-0027, 2017.

[29] A. Habibnejad Korayem, “State and Parameter Estimation of Vehicle-Trailer Systems,” PhD thesis, University of Waterloo, 2021.

[30] C. Fuchs, F. Neuhaus and D. Paulus, “3d pose estimation for articulated vehicles using Kalman-filter based tracking,” *Pattern Rec. Image An.*, vol. 26, no. 1, pp. 109–113, 2016.

[31] L. Caup, J. Salmen, I. Muharemovic and H. Sebastian, “Video-Based Trailer Detection and Articulation Estimation,” IEEE Intelligent Vehicles Symposium, 2013.

[32] E. Kayacan, E. Kayacan, H. Ramon and W. Saeys, “Learning in centralised nonlinear model predictive control: application to an autonomous tractor-trailer system,” *IEEE Trans. Contr. Syst. Technol.*, vol. 23, no.1, pp. 197–205, 2015.

[33] Y. Zhang, A. Khajepour and A. Ataei, “A universal and reconfigurable stability control methodology for articulated vehicles with any configurations,” *IEEE Trans. Veh. Technol.*, vol. 69, no. 4, pp. 3748–3759, 2020.

[34] M. Metzler, D. Tavernini. P. Gruber and A. Sorniotti, “On prediction model fidelity in explicit nonlinear model predictive vehicle stability control,” *IEEE Trans. Contr. Syst. Technol.*, vol. 29, no. 5, 2020.

[35] A. Parra, D. Tavernini, P. Gruber, A. Sorniotti, A. Zubizarreta and J. Perez, “On pre-emptive vehicle stability control,” *Veh. Syst. Dyn.*, vol. 60, no. 6, pp. 2098–2123, 2021.

[36]E. Siampis, E. Velenis, S. Gariuolo and S. Longo "A real-time nonlinear model predictive control strategy for stabilization of an electric vehicle at the limits of handling," *IEEE Trans. Contr. Syst. Technol.*, vol. 26, no. 6, pp. 1982–1994, 2019.

[37]A. Parra, D. Tavernini, P. Gruber, A. Sorniotti, A. Zubizarreta and J. Perez, "On Nonlinear Model Predictive Control for Energy-Efficient Torque-Vectoring," *IEEE Trans. Veh. Technol.*, vol. 70, no. 1, pp. 173–188, 2021.

[38]M. Dalboni, D. Tavernini, U. Montanaro, A. Soldati, C. Concari, M. Dhaens and A. Sorniotti, "Nonlinear Model Predictive Control for Integrated Energy-Efficient Torque-Vectoring and Anti-Roll Moment Distribution," *IEEE/ASME Trans. Mechatr.*, vol. 26, no. 3, 2021.

[39]B. Houska, H. J. Ferreau and M. Diehl, "ACADO Toolkit – An Open Source Framework for Automatic Control and Dynamic Optimisation," *Opt. Contr. Appl. Meth.*, vol. 32, no. 3, pp. 298–312, 2011.

[40]L. De Novellis, A. Sorniotti, P. Gruber, J. Orus, J. M. Rodriguez Fortun, J. Theunissen and J. De Smet, "Direct yaw moment control actuated through electric drivetrains and friction brakes: Theoretical design and experimental assessment," *Mechatronics*, vol. 26, pp. 1–15, 2015.

[41]A. T. van Zanten, R. Erhardt and G. Pfaff, "VDC, the vehicle dynamics control system of Bosch," *SAE Technical Paper* 950759, 1995.

[42]G. Genta and L. Morello, The Automotive Chassis, Volume 2: System Design, Cham Switzerland, 2020.

[43]E. Bakker, L. Nyborg and H. B. Pacejka, "Tyre modelling for use in vehicle dynamics studies," *SAE Technical Paper* 870421, 1987.

[44]J. Maciejowski, Predictive control with constraints, Harlow: Prentice Hall, 2001.

[45]A. Linder, R. Kanchan, R. Kennel and P. Stolze P, Model-Based Predictive Control of Electric Drives, Cuvilier-Verlag, Gottingen, 2012.

[46]International Organization for Standardization (ISO), "Road Vehicles – Heavy Commercial Vehicle Combinations and Articulated Buses – Lateral Stability Test Methods," *ISO-14791*, 2000.

4.4 TORQUE-VECTORING AND ACTIVE SUSPENSIONS

4.4.1 STATE-OF-THE-ART

Trailers offer practical and versatile transportation solutions. In the past years, the use of trailers and semitrailers experienced steady growth mainly due to the rising demand by the logistics industry, the e-commerce business, and personal recreational activities. Although the market was strongly affected by the pandemic as reported by the US National Association of Trailer Manufacturers (NATM) in 2022 [1], the recovery within the last two years and the forecasts for this decade create an expectation for a constant increase in the market size [1]–[4].

An important limitation of car-semitrailer systems, which are the object of this study, is that they may suffer from major oscillations and stability issues, leading to safety-critical scenarios with partial or total loss of vehicle control by the driver. The occurrence of critical hitch angle dynamics mainly depends on the car and semitrailer parameters, driver inputs, and payload position. Typical challenging scenarios are represented by jack-knifing, in which the trailer makes the car spin, and snaking, during which the trailer periodically oscillates to the left and right sides of the longitudinal axis of the car. In the literature, the yaw mass moment of inertia of the semitrailer, the longitudinal position of its centre of gravity, the location of the hitch joint, and the position of the trailer axle/s are identified as crucial factors affecting lateral stability [5].

To mitigate trailer oscillations and limit the insurgence of safety-critical scenarios, several chassis control methods have been proposed. Direct yaw moment control (DYC) is evaluated in [6], where the former generates braking torque levels on the rear axle of the towing vehicle to stabilise the trailer, and the latter formulates two sliding mode controllers based on the sideslip angle and yaw rate of the car. While in traditional cars DYC for trailer stability is implemented through the friction brakes in emergency conditions, next-generation electric cars could be equipped with multiple motors capable of continuous wheel torque distribution control, i.e., torque-vectoring (TV) [7]. In [9], rear-wheel-steering control is implemented on the car (RWSC), based on measured signals from both car and trailer. In [10] and [11], active steering angle control is actuated on the trailer (SCT).

In this context, the development of computationally efficient solvers [12] and progressive improvement of automotive control hardware have made model predictive control (MPC), including nonlinear MPC (NMPC), real-time implementable for vehicle dynamics applications, see [13]–[15]. Examples of linear time-varying MPC implementations for car-trailer control are discussed in [16] and [17], which focus on differential braking on the towing vehicle and/or trailer. For the specific test cases, the control strategy acting on the towing vehicle is superior to the one acting on the trailer. Both [16] and [17] assume the inertial, geometric as well as tire parameters of the trailer to be known by the controller.

Reference [18] presents four real-time implementable NMPCs for the TV control of a car-semitrailer combination.

All the previous MPC implementations embed the model of the trailer in their prediction, and imply the knowledge, through measurement or estimation, of the hitch angle. Although this assumption might be restrictive, the literature proposes several methods for hitch angle estimation or measurement, e.g., through model-based techniques, ultrasonic sensors, or vision systems located on the rear end of the towing vehicle [19]–[25]. Moreover, the majority of trailer control studies require dedicated sensing devices and algorithms for the estimation of trailer characteristics. For instance, the algorithms in [26] and [27] derive the trailer mass from the longitudinal force balance of the articulated vehicle. Reference [28] applies Kalman filtering techniques to the longitudinal force balance of an articulated truck, by using the engine torque and longitudinal acceleration of the towing vehicle. Recursive techniques are applied to the estimation of the trailer yaw mass moment of inertia and centre of gravity height in [29], and trailer mass and yaw moment of inertia in [30], through observers based on the longitudinal, lateral, and/or yaw dynamics of the car-trailer system. Current industrial solutions for trailer sway mitigation are described in [31]–[33]. For ease of implementation, these algorithms lack any dedicated system to estimate or measure the hitch angle or hitch rate. They mitigate trailer oscillations by applying a braking torque and/or direct yaw moment to the towing vehicle when the band-pass filtered yaw rate error of the latter exceeds typical thresholds related to trailer sway. However, as shown in [7], their benefit is rather limited.

The previous literature review highlights that DYC, RWSC and SCT are the most widely assessed actuations for car-semitrailer control, either in isolation, or concurrently through integrated chassis control (ICC). The significance of ICC is growing, due to its capability of better exploiting the potential of the available actuators, see the ICC architecture classification in [34], based on the position and role of the actuator coordination layer.

Although active suspension (AS) systems can provide effective yaw rate control in proximity of the limit of handling through the variation of the front-to-total anti-roll moment distribution, see [15], [35] and [36], they have not been applied to the trailer sway mitigation problem yet. Moreover: i) while the effect of the anti-roll moment distribution is predictable on the cornering response of a car in isolation [37], it is much less intuitive when dealing with the oscillations of a car-semitrailer system; ii) ASs are likely to become more widely spread with the advent of driving automation, with the purpose of enhancing comfort and reducing motion sickness [38]; and iii) ASs are going to be implemented in vehicles already equipped with DYC capability based on the actuation of the friction brakes and/or electric powertrains. i)–iii) justify the design of advanced model-based architectures for the integrated control of anti-roll moment distribution and direct yaw moment for car-semitrailer systems.

In summary, the literature lacks investigations on:

The stability improvements brought by AS configurations capable of front-to-total anti-roll moment distribution on the towing car, in car-semitrailer combination vehicles.

MPC formulations for car-semitrailer control, embedding prediction models of the towing car only, while the trailer is considered through the estimated hitch joint force components. Such novel algorithms should facilitate the real-time implementation with respect to (w.r.t.) the more conventional formulations embedding the trailer dynamics.

This work aims to cover the identified gap through the following novel contributions:

- Hitch dynamics control of a car-semitrailer combination vehicle through active suspension control, complementing TV control is investigated due to its dynamic similarity to articulated buses, where ensuring safety is a prerequisite for integrating motion sickness metrics in automated vehicle systems.
- Prediction model formulations for the predictive control of car-semitrailer combination vehicles through AS and TV, considering the trailer either through: i) the estimated forces at the hitch joint at the current time instant; or ii) its hitch angle dynamics along the prediction horizon. The related controller configurations could operate without the requirement of any additional sensors on the trailer.
- Performance comparisons of the resulting NMPCs for AS and TV control, implemented through integrated or coexistence-based ICC architectures, with a benchmarking TV NMPC configuration targeting only the towing car.

The chapter is organised as follows: Section 4.4.2 describes the case study vehicle and simulation framework architecture; Section 4.4.3 presents the controller formulations; Section 4.4.4 discusses the controller implementation and tuning; Section 4.4.5 deals with the parameter estimation algorithms; Section 4.4.6 discusses the simulation results; finally, Section 4.4.7 outlines the main conclusions.

4.4.2 CASE STUDY VEHICLE AND CONTROL ARCHITECTURE

4.4.2.1 Target vehicle

Figure 4.4.1 is the top view schematic of the vehicle configuration, with indication of the sign conventions of the main variables. More specifically, $\dot{\psi}$ is the car yaw rate; β is the sideslip angle at the center of gravity of the car; V is the speed of the towing vehicle; θ is the hitch angle, between the longitudinal axes of the trailer and the car; the subscript i, with $i = F, R$, indicates the axle of the car (front or rear); the subscript j, with $j = L, R$, indicates the vehicle side (left or right); and the subscript 't' refers to the trailer-related variables and parameters.

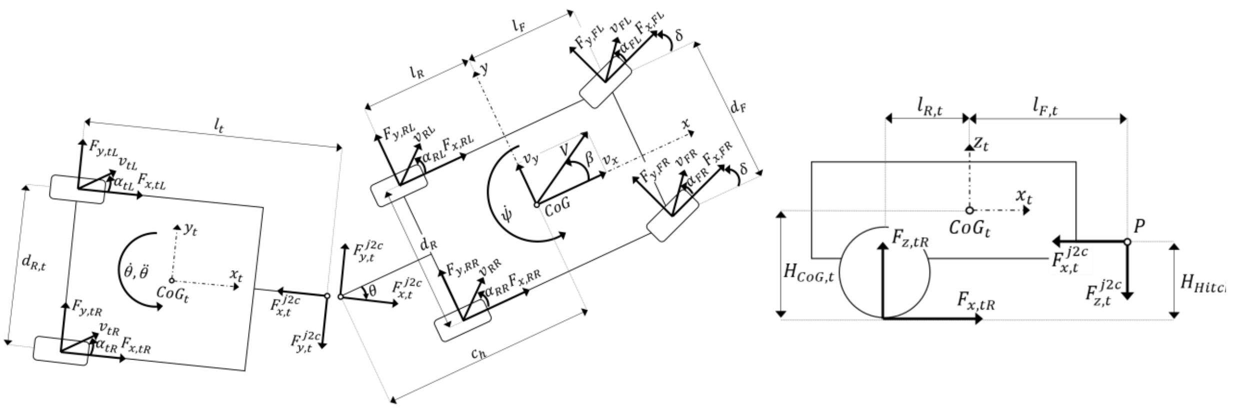

(a) *(b)*

Figure 4.4.1: (a) Top and (b) side views of the car-semitrailer system, with indication of the main parameters and variables, as well as their sign conventions

The car is equipped with: i) four in-wheel direct drive electric powertrains; and ii) an AS system based on the Kinetic^{TM} technology by Tenneco, including four double-acting hydraulic actuators, capable of providing variable front-to-total anti-roll moment distribution [39]. The semitrailer does not include any actuator nor sensor. Table 4.4.1 summarises the car parameters, while Table A 1 in the Appendix reports the main trailer data.

Table 4.4.1 – Main towing car parameters.

Symbol	Description and unit	Value
l	Wheelbase (m)	2.926
l_F	Front semi-wheelbase (m)	1.512
H_{CoG}	Center of gravity (CoG) height (m)	0.501
d_F	Front track width (m)	1.644
d_R	Rear track width (m)	1.638
m	Vehicle mass (kg)	2323
$\tau_{m,ij,max}$	Maximum individual IWM torque (Nm@rpm)	800@1000
P_{max}	Maximum individual IWM power (kW@rpm)	75@1000

With respect to (w.r.t.) the latter, the nominal configuration of the trailer is indicated as BMT (benchmarking trailer), while the notations $\left(m_t J_{z,t}\right)_{xt}$, $\left(l_{F,t}\right)_{xt}$ and $(l_t)_{xt}$, respectively indicate trailer configurations with modified mass and yaw mass moment of inertia, different distances between the trailer center of gravity and hitch joint, and modified distances between the trailer axle and hitch joint. The value of the subscript 'xt' permits to identify their parametrisation according to the table. In total, during the analysis, on top of BMT, 13 trailer configurations were considered, i.e., 3 with modified m_t and $J_{z,t}$, 5 with modified $l_{F,t}$, and 5 with modified l_t. The multiple trailer configurations will be used to assess the robustness of the controllers.

The vehicle is simulated with an experimentally validated high-fidelity model implemented in IPG CarMaker, within a Matlab-based co-simulation environment. The model includes the degrees of freedom of the sprung and unsprung masses and their dynamic couplings, the suspension kinematic and compliance effects, as well as tire nonlinearities, considered through version 5.2 of the Pacejka magic formula with relaxation effects. Realistic actuator dynamics are embedded in the plant model, emulating the response of the in-wheel motors (IWMs) and AS system, based on data provided by the respective manufacturers. For realism of controller evaluation, the high-fidelity model formulation is completely independent from those of the prediction models in Section III. In quasi-steady-state cornering conditions, the car on its own and also the considered combination vehicle are characterised by a stable understeering behaviour. However, as it will be shown in the simulations of critical manoeuvres in Section 4.4.6, during extreme transients the passive vehicle can become unstable in terms of the trailer roll and hitch angle dynamics. This kind of critical transient behaviour of the combination vehicle is quite typical and has been the subject of deep analyses in the relevant literature, e.g., see [40].

4.4.2.2 Simulation framework and controller architectures

Figure 4.4.2 is the schematic of the simulation framework, including:

- The virtual driver model, generating the accelerator pedal position, APP, brake pedal force, F_p, and steering wheel angle, δ_{sw}. The controller assessment is based on both open-loop tests, in which the driver commands are pre-defined and imposed to the vehicle system, and closed-loop tests, in which the CarMaker driver model is used to track a reference trajectory.

- The braking system model, which outputs the tandem master cylinder pressure, p_{TMC}, and individual braking torque levels, $T_{b,ij}$.

- The reference generation and parameter estimation layer, which outputs: a) the reference signals, such as the total powertrain torque demand, $\tau_{m.tot,d}$, the reference yaw rate for the car, $\dot{\psi}_{ref}$, and the reference hitch angle, θ_{ref}; and b) the estimated parameters and variables, such as the trailer mass and geometry, and the actuation limits.

- The control layer, which includes a set of alternative configurations that will be compared in the remainder, each of them covering the entire set of operating conditions of the vehicle:

i) The passive case, with fixed anti-roll moment distribution to provide an acceptable trade-off in terms of cornering response, although the controlled suspension system still provides an active anti-roll moment proportional to the measured lateral acceleration, to reduce the roll motion of the vehicle body. The powertrain torque is evenly distributed among the corners of the towing car.

ii) The single actuation cases, in which only the AS or TV systems are active. Such configurations are indicated as AS^{c} or TV^{c}, with $c = 1, 2$, depending on the embedded prediction model. In the remainder, the notation AS specifically refers to the activation of the variable anti-roll moment distribution capability of the suspension actuators, which – according to i) – are working for reducing roll in all the vehicle configurations of this study. Hence, the control input of the AS system is the reference front-to-total active anti-roll moment distribution variation, Δf_{ref}, w.r.t. a fixed nominal value, f_0, used in absence of such functionality. The TV control inputs are the reference motor torque values on each corner, $\tau_{m,ij,ref}$.

iii) The cases with the concurrent activation of AS and TV, through separate and parallel implementations of the respective nonlinear optimal control problems. If the two controllers do not share information of the respective control inputs, they are referred to as $(\text{AS}^{\text{c}}//\text{TV}^{\text{c}})_{\text{W/oComm}}$, with $c = 1, 2$. On the contrary, if the algorithms share the respective control inputs, which are accounted for by the internal models according to a peaceful coexistence [34] ICC approach, they are referred to as $(\text{AS}^{\text{c}}//\text{TV}^{\text{c}})_{\text{W/Comm}}$.

iv) The integrated AS and TV controllers, indicated as $(\text{AS-TV})^{\text{c}}$, which concurrently generate all control inputs for both the AS and TV actuations through a single optimisation.

As highlighted in the figure, each NMPC algorithm in ii)–iv) consists of: a) an internal (or prediction) model, which predicts the behaviour of the system along a finite horizon, see also the sensitivity analyses on the effect of the model complexity level in [41]; b) a cost function to be minimised; and c) a set of constraints to be met. Two prediction models are evaluated for each NMPC configuration in ii)–iv), namely a rigid vehicle model of the towing car, corresponding to $c = 1$ (Section 4.4.3.2), and an articulated vehicle model, corresponding to $c = 2$ (Section 4.4.3.3).

The high-fidelity vehicle model of Section 4.4.2.1, which generates the set of vehicle variables, Θ, required for the operation of the implemented algorithms.

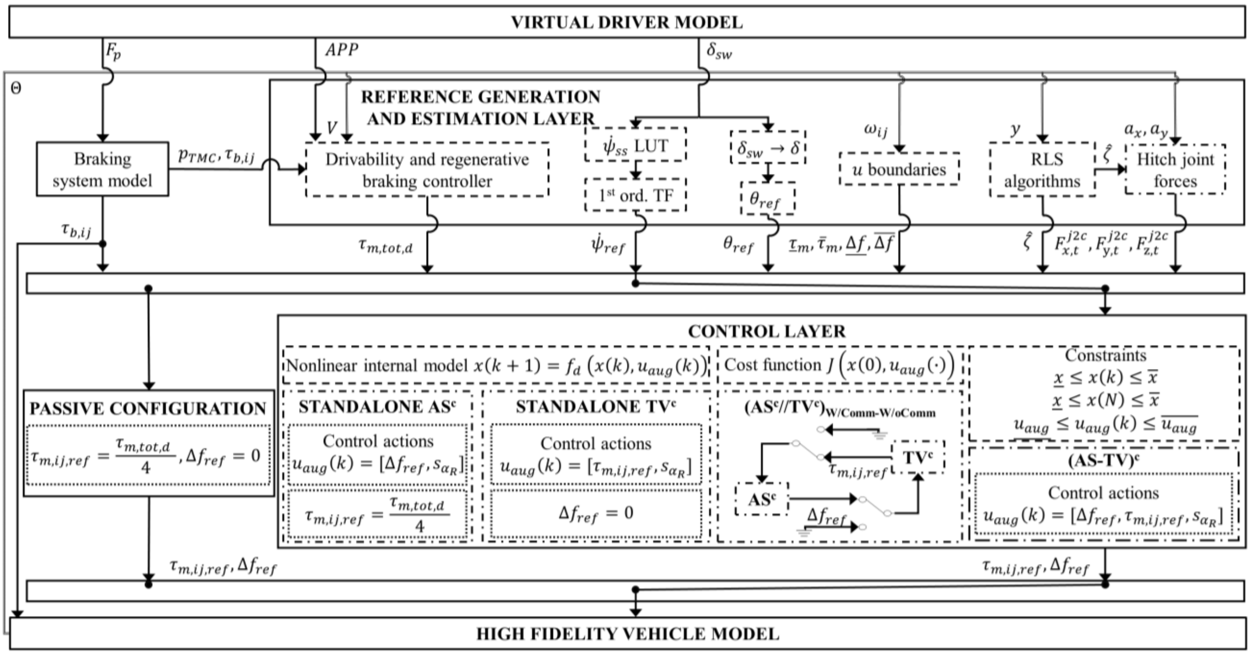

Figure 4.4.2: Simplified schematic of the simulation framework, where the dashed lines indicate the functional items that are common to all controller configurations, whilst the dash-dotted lines represent the subsystems that can be activated based on the selected controller configuration.

4.4.3 CONTROLLER FORMULATIONS

4.4.3.1 Reference definition

Based on the technical requirements from the involved industrial partner, during quasi-steady-state operation the controller is used only to limit the variations of the cornering response w.r.t. to nominal conditions, rather than for modifying the level of vehicle understeer such as in [42]–[44]. Hence, the steady-state reference yaw rate of the car-semitrailer system, $\dot{\psi}_{ss}$, is designed to match the steady-state cornering response of the passive rigid vehicle, according to the typical practice for vehicle stability control. $\dot{\psi}_{ss}$ is stored as a nonlinear map, as a function of steering angle δ (computed from δ_{sw} through the steering ratio) and vehicle speed V, see Figure 4.4.3. The map was generated by simulating the cornering response of the vehicle during ramp steer manoeuvres at different speeds, i.e., from 10 km/h to 180 km/h. In the online algorithm, the output of the map is saturated based on the estimated tire-road friction factor μ, i.e., the saturation level corresponds to a yaw rate magnitude $k\frac{\mu g}{V}$, where k is a tuning parameter. To provide realistic and desirable dynamics, the saturated output of the map is filtered by a first-order transfer function, to obtain $\dot{\psi}_{ref}$.

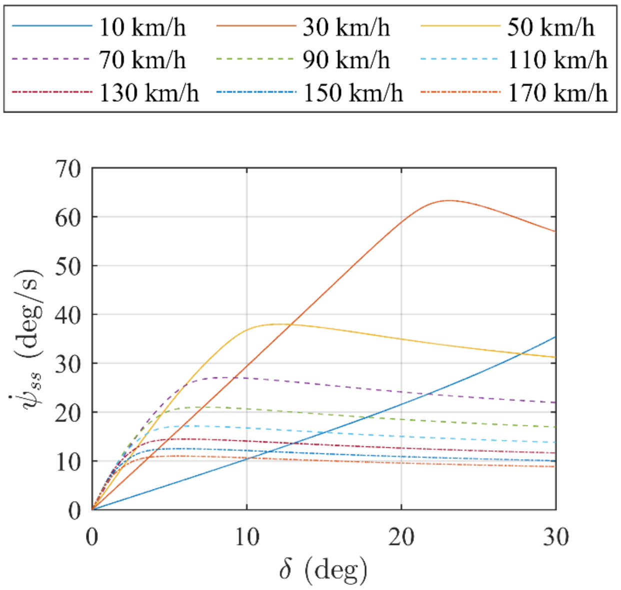

Figure 4.4.3: Map of the steady-state reference yaw rate $\dot{\psi}_{ss}$ of the car-semitrailer system, as a function of the steering angle δ and the vehicle speed V.

In the formulations that enable such functionality, the hitch angle dynamics are controlled by tracking the reference hitch angle, θ_{ref}, which – for simplicity – is computed as the kinematic hitch angle, i.e., the hitch angle in absence of slip angles, according to [45] and the geometric parameters defined in Figure 4.4.1:

$$\theta_{ref} = \tan^{-1}\left(\frac{\tan(\delta)\left[l^2 l_t + [c_h - l_R]\sqrt{\tan^2(\delta)\, l^2 [c_h - l_R]^2 - \tan^2(\delta) l^2 l_t^2 + l^4}\right]}{l\left[-\tan^2(\delta) l_t [c_h - l_R] + \sqrt{\tan^2(\delta) l^2 [c_h - l_R]^2 - \tan^2(\delta) l^2 l_t^2 + l^4}\right]}\right) \tag{4.4.1}$$

4.4.3.2 Rigid vehicle prediction model formulation ($c = 1$)

The proposed prediction model, i.e., the model used by the NMPC for predicting the system response [46], is based on the following assumptions:

- The motion is planar, with negligible road bank and inclination angles.
- The heave, roll and pitch dynamics are disregarded.
- For computational efficiency, the effect of the semitrailer is included by considering the forces – estimated at the beginning of the prediction – that are applied to the towing car through the hitch joint, see $F_{x,t}^{j2c}$, $F_{y,t}^{j2c}$, and $F_{z,t}^{j2c}$ in Figure 4.4.1, expressed in the trailer reference system.

In the remainder, the notations '$(\dot{\ })$' and '$(\ddot{\ })$' respectively refer to first and second order time derivatives. The model has 7 degrees of freedom, described by the following equations:

- Longitudinal force balance

$$m[\dot{v}_x - \dot{\psi} v_y] == \sum_{j=L,R} [F_{x,Fj}\cos(\delta) - F_{y,Fj}\sin(\delta)] + \sum_{j=L,R} F_{x,Rj} - F_{drag} + F_x^{j2c} \tag{4.4.2}$$

- Lateral force balance

$$\begin{aligned} &[\dot{v}_y + \dot{\psi} v_x] = \\ &= \sum_{j=L,R} \left[F_{x,Fj}\sin(\delta) + F_{y,Fj}\cos(\delta)\right] + \sum_{j=L,R} F_{y,Rj} + F_y^{j2c} \end{aligned} \tag{4.4.3}$$

- Yaw moment balance

$$\begin{aligned} J_z\ddot{\psi} = {} & l_F\left[F_{x,FL}\sin(\delta) + F_{y,FL}\cos(\delta) + F_{x,FR}\sin(\delta) + F_{y,FR}\cos(\delta)\right] - l_R\left[F_{y,RL} + F_{y,RR}\right] \\ & -\frac{d_R}{2}\left[F_{x,RL} + F_{x,RR}\right] - \frac{d_F}{2}\left[F_{x,FL}\cos(\delta) - F_{x,FR}\cos(\delta)\right] \\ & +\frac{d_F}{2}\left[F_{y,FL}\sin(\delta) - F_{y,FR}\sin(\delta)\right] + c_h F_y^{j2c} \end{aligned} \tag{4.4}$$

- Wheel moment balances

$$J_{w,i}^{eq}\dot{\omega}_{ij} = \tau_{m,ij,ref} - \tau_{b,ij} - R_{l,ij}F_{x,ij} - M_{y,ij} \tag{4.4.5}$$

where v_x and v_y are the longitudinal and lateral components of the velocity at the center of gravity of the car; $F_{x,ij}$ and $F_{y,ij}$ are the longitudinal and lateral tire forces in the wheel reference frame; F_{drag} is the aerodynamic drag force; J_z is the yaw mass moment of inertia; l_F and l_R are the front and rear semiwheelbases; c_h is the distance of the hitch joint to the car's center of gravity; $J_{w,i}^{eq}$ is the equivalent mass moment of inertia of the wheels; $\dot{\omega}_{ij}$ are the angular wheel accelerations; $\tau_{m,ij,ref}$ is the individual reference IWM torque (the prediction model neglects the actuation delays); and F_x^{j2c} and F_y^{j2c} are the longitudinal and lateral forces applied by the trailer to the car through the hitch joint, in the car reference system.

Based on the experimental tire data provided by the industrial partners involved in this research work, the Pacejka magic formula (vers. 2002, [47]) – appropriately tuned to fit the experimental tire data – calculates the rolling radius, laden radius, rolling resistance, longitudinal force, lateral force, and self-aligning moment of the tires, namely $R_{e,ij}$, $R_{l,ij}$, $M_{y,ij}$, $F_{x,ij}$, $F_{y,ij}$, and $M_{z,ij}$, as functions of the tire slip angle, α_{ij}, longitudinal slip ratio, $\sigma_{x,ij}$, and vertical load, $F_{z,ij}$. $\sigma_{x,ij}$ and α_{ij} are defined as:

$$\begin{gathered} \alpha_{ij} = \tan^{-1}\left(\frac{v_y + k_1 l_i\dot{\psi}}{v_x + k_2\frac{d_i}{2}\dot{\psi}}\right) - k_3\delta \\ \begin{cases} k_1 = \ \ 1, & k_3 = 1 \quad \text{if} \quad i = F \\ k_1 = -1, & k_3 = 0 \quad \text{if} \quad i = R \\ \ \ k_2 = -1 & \qquad\quad \text{if} \quad j = L \\ \ \ k_2 = \ \ 1 & \qquad\quad \text{if} \quad J = R \end{cases} \end{gathered} \tag{4.4.6}$$

$$\sigma_{x,ij} = \frac{\omega_{ij}R_{e,ij} - v_{x,ij}}{v_{x,ij}} \tag{4.4.7}$$

where $v_{x,ij}$ is the longitudinal component of the wheel velocity in the tire reference frame. $F_{z,ij}$ is expressed as a function of F_x^{j2c}, F_y^{j2c}, and F_z^{j2c}; the longitudinal and lateral load transfers caused by the longitudinal and lateral accelerations, a_x and a_y, where the lateral load transfer includes the anti-roll moment contribution due to the active suspension actuation; and the longitudinal load transfer due to the aerodynamic drag force, ΔF_z^{drag}:

$$\begin{aligned} F_{z,Fj} &= \frac{1}{2}\frac{mgl_R}{l} + \frac{1}{2}\left[-ma_x\frac{H_{CoG}}{l} + F_x^{j2c}\frac{H_{Hitch}}{l}\right] + F_{z,t}^{j2c}\frac{c_h - l_R}{2l} + k_1\Delta F_{z,F}^{y} - \Delta F_z^{drag} \\ F_{z,Rj} &= \frac{1}{2}\frac{mgl_F}{l} + \frac{1}{2}\left[ma_x\frac{H_{CoG}}{l} - F_x^{j2c}\frac{H_{Hitch}}{l}\right] - F_{z,t}^{j2c}\frac{c_h + l_F}{2l} + k_1\Delta F_{z,R}^{y} + \Delta F_z^{drag} \\ k_1 &= \begin{cases} -1 & \text{if } j = L \\ 1 & \text{if } j = R \end{cases} \end{aligned} \tag{4.4.8}$$

The lateral load transfer on the i-th axle, $\Delta F_{z,i}^{y}$, is computed as

$$\Delta F_{z,F}^{y} = \left[ma_y\frac{l_R}{l} + F_y^{j2c}\frac{c_h - l_R}{l}\right]\frac{H_{RC}}{d_F} + \frac{M_{AR,F}^{tot}}{d_F} \tag{4.4.9}$$

$$\Delta F_{z,R}^{y} = \left[ma_y\frac{l_F}{l} - F_y^{j2c}\frac{c_h + l_F}{l}\right]\frac{H_{RC}}{d_R} + \frac{M_{AR,R}^{tot}}{d_R} \tag{4.4.10}$$

where the total suspension anti-roll moments, $M_{AR,F}^{tot}$ and $M_{AR,R}^{tot}$, are given by:

$$\begin{aligned} M_{AR,F}^{tot} &= M_{AR,F}^{passive} + M_{AR,F}^{AS} \\ M_{AR,R}^{tot} &= M_{AR,R}^{passive} + M_{AR,R}^{AS} \end{aligned} \tag{4.4.11}$$

Since – for computational efficiency – the model neglects the roll dynamics, in *(4.4.12)* the passive anti-roll moment contributions, $M_{AR,i}^{passive}$, consider only the effect of the springs:

$$\begin{aligned} M_{AR,F}^{passive} &= \frac{K_{\varphi,F}}{K_{\varphi,F} + K_{\varphi,R}}\left\{\left[1 - K_{comp}\right]ma_y\left[H_{CoG} - H_{RC}\right] - F_y^{j2c}\left[H_{Hitch} - H_{RC}\right]\right\} \\ M_{AR,R}^{passive} &= \frac{K_{\varphi,R}}{K_{\varphi,F} + K_{\varphi,R}}\left\{\left[1 - K_{comp}\right]ma_y\left[H_{CoG} - H_{RC}\right] - F_y^{j2c}\left[H_{Hitch} - H_{RC}\right]\right\} \end{aligned} \tag{4.4.12}$$

where $K_{\phi,i}$ is the roll stiffness of the passive suspension components; H_{RC} is the roll axis height at the longitudinal coordinate of CoG; and H_{Hitch} is the height of the hitch joint. The active suspension anti-roll moments, $M_{AR,i}^{AS}$, are linear functions of the lateral acceleration, a_y, according to the suspension control design practice of the involved industrial company:

$$\begin{aligned} M_{AR,F}^{AS} &= K_{comp}fma_y\left[H_{CoG} - H_{RC}\right] \\ M_{AR,R}^{AS} &= K_{comp}\left[1 - f\right]ma_y\left[H_{CoG} - H_{RC}\right] \end{aligned} \tag{4.4.13}$$

where $0 \le K_{comp} \le 1$ is the roll motion compensation factor, i.e., $K_{comp} = 1$ implies that the whole roll moment is compensated by the suspension actuators rather than by the passive suspension components, with virtually zero roll angle in cornering; and $f = f_0 + \Delta f$ is the variable front-to-total anti-roll moment distribution factor, with f_0 being its nominal value.

4.4.3.3 Articulated vehicle prediction model formulation ($c = 2$)

The internal model equations of the car-semitrailer dynamics of the alternative NMPC configurations were obtained through the Lagrange method [48], [49]. The articulated vehicle dynamics are described by (see also Figure 4.4.1):

- Longitudinal dynamics equation

$$
\begin{aligned}
M\left[\dot{v}_x - \dot{\psi} v_y\right] &- m_t l_{F,t}\left[\ddot{\psi} - \ddot{\theta}\right]\sin(\theta) - 2 m_t l_{F,t}\dot{\psi}\dot{\theta}\cos(\theta) + m_t l_{F,t}\dot{\theta}^2\cos(\theta) \\
&+ m_t\dot{\psi}^2\left[c_h + l_{F,t}\cos(\theta)\right] \\
&= \left[F_{x,FL} + F_{x,FR}\right]\cos(\delta) - \left[F_{y,FL} + F_{y,FR}\right]\sin(\delta) + F_{x,RL} + F_{x,RR} \\
&+ \sum_{j=L,R}\left[F_{x,tj}\cos(\theta) + F_{y,tj}\sin(\theta)\right] - F_{drag}
\end{aligned}
\tag{4.4.14}
$$

- Lateral dynamics equation

$$
\begin{aligned}
M\left[\dot{v}_y + \dot{\psi} v_x\right] &- m_t\ddot{\psi}\left[c_h + l_{F,t}\cos(\theta)\right] + m_t l_{F,t}\ddot{\theta}\cos(\theta) - m_t l_{F,t}\sin(\theta)\left[\dot{\psi} - \dot{\theta}\right]^2 \\
&= \left[F_{x,FL} + F_{x,FR}\right]\sin(\delta) + \left[F_{y,FL} + F_{y,FR}\right]\cos(\delta) + \left[F_{y,RL} + F_{y,RR}\right] \\
&+ \sum_{j=L,R}\left[-F_{x,tj}\sin(\theta) + F_{y,tj}\cos(\theta)\right]
\end{aligned}
\tag{4.4.15}
$$

- Yaw dynamics equation

$$
\begin{aligned}
J_{1,\theta}\ddot{\psi} - J_{2,\theta}\ddot{\theta} &+ m_t l_{F,t} c_h\sin(\theta)\left[\dot{\theta}^2 - 2\dot{\theta}\dot{\psi}\right] - m_t l_{F,t}\sin(\theta)\left[\dot{v}_x - v_y\dot{\psi}\right] \\
&- m_t\left[\dot{v}_y + v_x\dot{\psi}\right]\left[c_h + l_{F,t}\cos(\theta)\right] \\
&= l_F\left\{\left[F_{y,FL} + F_{y,FR}\right]\cos(\delta) + \left[F_{x,FL} + F_{x,FR}\right]\sin(\delta)\right\} \\
&- l_R\left[F_{y,RL} + F_{y,RR}\right] \\
&+ \frac{d_F}{2}\left\{\left[F_{y,FL} - F_{y,FR}\right]\sin(\delta) + \left[F_{x,FR} - F_{x,FL}\right]\cos(\delta)\right\} \\
&+ \frac{d_R}{2}\left[F_{x,RR} - F_{x,RL}\right] \\
&+ \sum_{j=L,R}\left\{F_{x,tj}\left[c_h\sin(\theta) - \frac{d_{R,t}}{2}\right] + F_{y,tj}\left[-c_h\cos(\theta) - l_t\right]\right\}
\end{aligned}
\tag{4.4.16}
$$

- Hitch dynamic equation

$$
\begin{aligned}
J_{3,\theta}\ddot{\theta} - J_{2,\theta}\ddot{\psi} &+ m_t l_{F,t}\cos(\theta)\left[\dot{v}_y + v_x\dot{\psi}\right] + m_t l_{F,t}\sin(\theta)\left\{\dot{v}_x - \dot{\psi}\left[v_y - c_h\dot{\psi}\right]\right\} \\
&= \sum_{j=L,R}\left[F_{x,tj}\frac{d_{R,t}}{2} + F_{y,Tj} l_t\right] - \Gamma\dot{\theta}
\end{aligned}
\tag{4.4.17}
$$

- Wheel moment balances, i.e., the same as in (4.4.5) this time also including those for the trailer wheels.

In the previous formulations, M is the mass of the car-semitrailer system; m_t is the mass of the trailer; $F_{x,tj}$ and $F_{y,tj}$ are the longitudinal and lateral tire forces for the trailer; l_t is distance from the hitch joint to the trailer axle; $l_{F,t}$ is the distance from the hitch joint to the center of gravity of the trailer, CoG_t; $l_{R,t}$ is the distance from CoG_t to the trailer axle; $d_{R,t}$ is the trailer track width; Γ is the coefficient of the Rayleigh dissipation term, accounting for the damping level within the hitch joint; and $J_{1,\theta}$, $J_{2,\theta}$, and $J_{3,\theta}$ are equivalent mass moments of inertia, defined as:

$$J_{1,\theta} = J_z + J_{z,t} + m_t\left[l_{F,t}^2 + c^2 + 2l_{F,t}c_h\cos(\theta)\right] \tag{4.4.18}$$

$$J_{2,\theta} = J_{z,t} + m_t\left[l_{F,t}^2 + l_{F,t}c_h\cos(\theta)\right] \tag{4.4.19}$$

$$J_{3,\theta} = J_{z,t} + m_t l_{F,t}^2 \tag{4.4.20}$$

where $J_{z,t}$ is the trailer yaw mass moment of inertia. The longitudinal and lateral tire forces are calculated with the same magic formula version as for c =1. The tire slip angles and slip ratios of the car are given by (4.4.6) and (4.4.7). For the semitrailer, the tire slip ratios, $\sigma_{x,tj}$, are calculated as in (4.4.7), while the slip angles, α_{tj}, are defined as:

$$\alpha_{tj}= \tan^{-1}\left(\frac{v_x\sin(\theta)+v_y\cos(\theta)-c_h\dot{\psi}\cos(\theta)-l_t[\dot{\psi}-\dot{\theta}]}{v_x\cos-v_y\sin(\theta)+c_h\dot{\psi}\sin(\theta)-\frac{d_{R,t}}{2}[\dot{\psi}-\dot{\theta}]}\right) \tag{4.4.21}$$

For the car, the vertical tire loads $F_{z,ij}$ are obtained as in (8), whereas the lateral load transfer on the trailer, $\Delta F_{z,t}^{y}$, is given by:

$$\Delta F_{z,t}^{y} = \frac{m_t a_{y,t} l_{R,t}}{d_{R,t} l_t} H_{Hitch} - \frac{m_t a_{y,t} H_{CoG,t}}{d_{R,t}} \tag{4.4.22}$$

where $H_{CoG,t}$ is the height of CoG_t. (4.4.14)–(4.4.22) are re-arranged through a symbolic computation software (MAPLE) into a nonlinear state-space formulation.

4.4.3.4 Nonlinear optimal control problem formulation

The NMPC prediction models are expressed through the following continuous nonlinear state-space formulation:

$$\dot{x}(t) = f\big(x(t), u(t)\big) \tag{4.4.23}$$

where the state vectors for the rigid and articulated vehicle models, i.e., x_1 and x_2, are:

$$x_1 = \begin{bmatrix} v_x & v_y & \dot{\psi} & \omega_{FL} & \omega_{FR} & \omega_{RL} & \omega_{RR} \end{bmatrix} \tag{4.4.24}$$

$$x_2 = \begin{bmatrix} v_x & v_y & \dot{\psi} & \dot{\theta} & \theta & \omega_{FL} & \omega_{FR} & \omega_{RL} & \omega_{RR} & \omega_{tL} & \omega_{tR} \end{bmatrix} \tag{4.4.25}$$

while the control input vector, u, of the integrated AS-TV system, which is the most advanced control option, is:

$$u = [\Delta f \quad \tau_{m,FL} \quad \tau_{m,FR} \quad \tau_{m,RL} \quad \tau_{m,RR}] \tag{4.4.26}$$

For the NMPC algorithms involving only AS or TV control, u respectively includes either the Δf or $\tau_{m,ij}$ terms.

The NMPC control law minimises the cost function J, subject to a set of equality and inequality constraints. According to the receding horizon approach [50], the optimal control problem is defined in discrete time as:

$$\begin{gathered}
\min_u J(x(0), u_{aug}(\cdot)) \coloneqq \ell_N\big(x(N)\big) + \sum_{k=0}^{N-1} \ell_c(x(k), u_{aug}(k)) \\
\text{s.t.} \\
x(0) = x_{in} \\
x(k+1) = f_d\left(x(k), u_{aug}(k)\right) \\
\underline{x} \leq x(k) \leq \overline{x} \\
\underline{x} \leq x(N) \leq \overline{x} \\
\underline{u_{aug}} \leq u_{aug}(k) \leq \overline{u_{aug}} \\
u_{aug}(\cdot)\colon [0, N-1]
\end{gathered} \tag{4.4.27}$$

where $\ell_N\big(x(N)\big)$ is the terminal cost, facilitating convergence and stability; N is the number of steps of the prediction horizon H_p, in the considered implementation equal to the control horizon H_c, i.e., $H_p = H_c = Nt_s$, with t_s being the sampling time; k indicates the discretisation step along H_p; $\underline{x}$ and $\overline{x}$ are the lower and upper limits for x; $\underline{u_{aug}}$ and $\overline{u_{aug}}$ include the lower and upper limits for the components of the augmented control input vector u_{aug}, which, according to Figure 4.4.2, on top of the components of u in (4.4.26) (referring to the most advanced control case), includes the slack variable s_{α_R}, defining the soft constraint on the average rear slip angle of the car, α_R; the notation $u_{aug}(\cdot)\colon [0, N-1]$ defines the control horizon for u_{aug}, from the first step, corresponding to $k = 0$, up to the last step, with $k = N-1$; and $x(k+1) = f_d\left(x(k), u_{aug}(k)\right)$ is the discretised version of the model in (4.4.23).

The stage costs ℓ_c, with $c = 1$ or 2, are defined by the following least-squares functions, depending on the selected prediction model:

$$\begin{aligned}
l_1\big(x(k), u(k)\big) = {} & W_{Q,\Delta\dot{\psi}}\Delta\dot{\psi}^2 + W_{Q,\Delta\tau_{m,tot}}\Delta\tau_{m,tot}^2 + W_{R,\tau_{m,ij}} \sum_{\substack{i=F,R \\ j=L,R}} \tau_{m,ij}^2 + W_{R,\Delta f}\Delta f^2 \\
& + W_{R,s_{\alpha_R}} s_{\alpha_R}^2
\end{aligned} \tag{4.4.28}$$

$$\begin{aligned}
& l_2\big(x(k), u(k)\big) \\
& \quad = W_{Q,\Delta\dot{\psi}}\Delta\dot{\psi}^2 + W_{Q,\Delta\tau_{m,tot}}\Delta\tau_{m,tot}^2 + W_{Q,\Delta\theta}\Delta\theta^2 + W_{R,\tau_{m,ij}} \sum_{\substack{i=F,R \\ j=L,R}} \tau_{m,ij}^2 \\
& \quad + W_{R,\Delta f}\Delta f^2 + W_{R,s_{\alpha_R}} s_{\alpha_R}^2
\end{aligned} \tag{4.4.29}$$

where $\Delta\dot{\psi} = \dot{\psi}_{ref} - \dot{\psi}$ is the yaw rate tracking error; $\Delta\tau_{m,tot}$ is the wheel torque tracking error at the vehicle level, i.e., the difference between the driver torque request and the total reference wheel torque from the controller; $\Delta\theta = \theta_{ref} - \theta$ is the hitch angle tracking error, which is included only in the cost function of the controllers with the articulated vehicle prediction model; $W_{Q,\Delta\dot{\psi}}$, $W_{Q,\Delta\tau_{m,tot}}$ and $W_{Q,\Delta\theta}$ are weights, respectively prioritising the tracking of the reference yaw rate of the car, the driver torque demand, and the reference hitch angle; $W_{R,s_{\alpha_R}}$ is the weight for the rear slip angle slack variable; and $W_{R,\tau_{m,ij}}$ and $W_{R,\Delta f}$

are the weights that penalise the actuation effort. $\ell_N\big(x(N)\big)$ has the same formulation as the stage cost, apart from the control input contributions, which are absent by definition.

In (4.4.27), inequality constraints are implemented on:

- The IWM torque, i.e., $\underline{\tau}_m \leq \tau_{m,ij} \leq \bar{\tau}_m$, where $\underline{\tau}_m$ and $\bar{\tau}_m$ are the minimum and maximum torque values according to the powertrain limitations.
- The deviation of the front-to-total anti-roll moment distribution from f_0, i.e., $\underline{\Delta f} \leq \Delta f \leq \overline{\Delta f}$, where $\underline{\Delta f}$ and $\overline{\Delta f}$ are the minimum and maximum admissible front-to-total anti-roll moment distribution deviations.
- α_R, such that $|\alpha_R| \leq \alpha_R^{max}\left[1 + s_{\alpha_R}\right]$, which, coupled with $s_{\alpha_R} \geq 0$, imposes a soft constraint on the rear slip angle, to facilitate lateral stability, where α_R^{max} is set to 3 deg in all the simulations of this study.

According to the typical NMPC implementations for vehicle dynamics control, the driver inputs, i.e., δ_{sw}, APP, and F_p, are kept constant along H_p. The same applies to the longitudinal and lateral accelerations that are used for the computation of the load transfers; the vehicle speed V used for computing F_{drag} and ΔF_z^{drag}; and the longitudinal, lateral and vertical components of the hitch joint force, F_x^{j2c}, F_y^{j2c}, and F_z^{j2c}, for the controller configurations with the rigid vehicle internal model including the trailer contributions.

4.4.4 CONTROLLERS IMPLEMENTATION AND TUNING

4.4.4.1 Controller implementation

The NMPC algorithms are implemented in their implicit form via the ACADO toolkit [12], with the following settings: i) Gauss Newton Hessian approximation; ii) multiple shooting discretisation; iii) qpOASES solver; iv) two iterations in the optimisation; v) $N = 2$; and vi) 5 ms discretisation time (t_d) of the internal models, which ensures numerical stability.

Table 4.4.2: Controller Settings for Real-Time Implementation

Controller	Prediction model	States	Integrator	t_d (ms)	t_s (ms)
AS^1	RV+F_i^{j2c}	$v_x, v_y, \dot{\psi}$	IRK-GL4	5	15
AS^2	AV	$v_x, v_y, \dot{\psi}, \dot{\theta}, \theta$	IRK-GL2	5	35
TV^1	RV+F^{j2c}	$v_x, v_y, \dot{\psi}, \omega_{ij}$	IRK-GL4	5	15
TV^2	AV	$v_x, v_y, \dot{\psi}, \dot{\theta}, \theta, \omega_{ij}$	IRK-GL2	5	35
(AS-TV)^1	RV+F^{j2c}	$v_x, v_y, \dot{\psi}, \omega_{ij}$	IRK-GL4	5	15
(AS-TV)^2	AV	$v_x, v_y, \dot{\psi}, \dot{\theta}, \theta, \omega_{ij}$	IRK-GL2	5	35
AS^1	RV+F_i^{j2c}	$v_x, v_y, \dot{\psi}$	IRK-GL4	5	15

RV+F_i^{j2c}: rigid vehicle prediction model with consideration of the hitch joint forces
AV: articulated vehicle prediction model

Table 4.4.2 summarises the integrator type and order, i.e., 2nd and 4th order Implicit Runge

Kutta integrators, referred to as IRK-GL2 and IRK-GL4, and the sampling time, t_s, for each controller configuration. Extensive simulations showed that the adopted parametrisations are a good compromise between performance and computational efficiency, and enable all controllers to run in real-time on a dSPACE MicroAutoBox II system (900 MHz, 16 Mb flash memory), as shown in Figure 4.4.4 reporting the turnaround time (t_{ta}) profiles for (AS-TV)^1 and (AS-TV)^2. Given the reduced number of prediction steps to achieve real-time capability, the specific dynamic system cannot be considered to be operating in steady-state conditions at the end of the prediction horizon [51], and therefore the controllers are set to have the same number of steps for the prediction and control horizons.

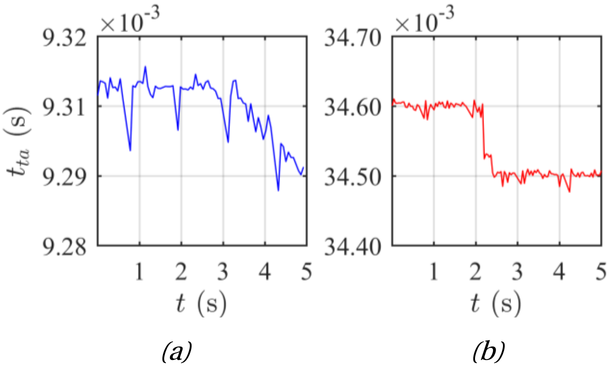

Figure 4.4.4: Profiles of the turnaround time for a) (AS-TV)^1 and b) (AS-TV)^2 during an extreme step steer test.

4.4.4.2 Controller tuning routine

On the one hand, the cost function weights on the control effort terms are selected to be the same across all the considered controllers, to provide good performance and comfortable behaviour in normal driving conditions for both rigid and articulated vehicle operation. On the other hand, for fairness of assessment, the cost function weights that are relevant to the vehicle cornering response (see Table 4.4.3) are optimised via an automated routine.

The routine runs the simulation model for control system assessment, including the controllers, along a typical critical test for trailer dynamics evaluation, namely the lane change manoeuvre defined in [52], from an initial speed of 88 km/h, at a constant 200 Nm wheel torque demand, carried out with the BMT. The optimisation based tuning parameters of each controller, see Table 4.4.3, are: i) $W_{Q,\Delta\dot{\psi}}$, the yaw rate tracking weight; ii) $W_{R,s_{\alpha_R}}$, the weight of the slack variable providing the soft constraint on the rear slip angle of the towing car; and iii) $W_{Q,\Delta\theta}$, the hitch angle tracking weight, which is present only in the controllers embedding the articulated vehicle model.

Table 4.4.3: Tuning Parameters Resulting from Optimisation.

Controller	Description	Tuning parameters
AS^1	Standalone AS controller	$0 \leq W_{Q,\Delta\dot{\psi}} \leq \overline{W}_{Q,\Delta\dot{\psi}}$ $0 \leq W_{R,s_{\alpha_R}} \leq \overline{W}_{R,s_{\alpha_R}}$
TV^1	Standalone TV controller	
(AS-TV)^1	Integrated AS-TV controller	
AS^2	Standalone AS controller	$0 \leq W_{Q,\Delta\dot{\psi}} \leq \overline{W}_{Q,\Delta\dot{\psi}}$
TV^2	Standalone TV controller	$0 \leq W_{Q,\Delta\theta} \leq \overline{W}_{Q,\Delta\theta}$
(AS-TV)^2	Integrated AS-TV controller	$0 \leq W_{R,s_{\alpha_R}} \leq \overline{W}_{R,s_{\alpha_R}}$

Given the rather limited number of tuning parameters, a brute force algorithm is used to solve the following optimisation problem:

$$\begin{gathered} J_{KPI}^{*} = \min_{W_{opt}} J_{KPI}\big|_{t_i}^{t_f} \\ \text{s.t.}\ \underline{W} \leq W_{opt} \leq \overline{W} \end{gathered} \tag{4.4.30}$$

where $\overline{W}$ is the vector of the upper bounds of the tuning weights, whose parameter space is discretised with a fine granularity within the defined interval; W_{opt} is the optimal value of the weight vector; t_i and t_f are the initial and final times of the relevant portion of the test; and J_{KPI}^{*} is the optimal value of the cost function J_{KPI}, given by the weighted sum of multiple non-dimensional key performance indicators (KPIs):

$$\begin{aligned} J_{KPI} = {} & W_{RMSE_{\Delta\dot{\psi}}} K_{RMSE_{\Delta\dot{\psi}}} RMSE_{\Delta\dot{\psi}} + W_{RMSE_{\Delta\theta}} K_{RMSE_{\Delta\theta}} RMSE_{\Delta\theta} \\ & + W_{\Delta F_z^{meas}} K_{\Delta F_z^{meas}} RMS_{\Delta F_z^{meas}} + W_{|\theta|^{max}} K_{|\theta|^{max}} |\theta|^{max} \\ & + W_{|\alpha_R|^{max}} K_{|\alpha_R|^{max}} |\alpha_R|^{max} + W_{RWA} K_{RWA} RWA \end{aligned} \tag{4.4.31}$$

where the terms W_{KPI} (with the subscript $KPI = RMSE_{\Delta\dot{\psi}}$, $RMSE_{\Delta\theta}$, $RMS_{\Delta F_z^{meas}}$, $|\theta|^{max}$, $|\alpha_R|^{max}$, and RWA) are the weights for the individual indicators, i.e., $W_{RMSE_{\Delta\dot{\psi}}} = 0.25$, $W_{RMSE_{\Delta\theta}} = 0.25$, $W_{\Delta F_z^{meas}} = 0.10$, $W_{|\theta|^{max}} = 0.20$, $W_{|\alpha_R|^{max}} = 0.10$, and $W_{RWA} = 0.10$ in the specific implementation; and K_{KPI} are normalisation factors, expressed as the maximum expected value of the KPI. The selected KPIs in (4.4.31) are:

- The root-mean-square value of the yaw rate error of the towing car:

$$RMSE_{\Delta\dot{\psi}} = \sqrt{\frac{1}{t_f - t_i} \int_{t_i}^{t_f} \left[\dot{\psi}_{ref}(t) - \dot{\psi}(t)\right]^2 dt} \tag{4.4.32}$$

- The root-mean-square value of the hitch angle error, to assess the level of trailer sway:

$$RMSE_{\Delta\theta^*} = \sqrt{\frac{1}{t_f - t_i} \int_{t_i}^{t_f} [\Delta\theta^*]^2 dt} \tag{4.4.33}$$

with:

$$\Delta\theta^* = \begin{cases} \left|\theta_{ref}(t) - \theta(t)\right| - \Delta\theta_{bound} & if \quad \left|\theta_{ref}(t) - \theta(t)\right| > \Delta\theta_{bound} \\ 0 & if \quad \left|\theta_{ref}(t) - \theta(t)\right| \leq \Delta\theta_{bound} \end{cases} \tag{4.4.34}$$

where $\Delta\theta_{bound} = 7$ deg is the hitch angle error bound of the dead-band function in (4.4.34), i.e., the hitch angle error is accounted for only when it exceeds the defined threshold.

- The root-mean-square value of the lateral load transfer computed from the tire loads generated by the high-fidelity model:

$$RMS_{\Delta F_z^{meas}} = \sqrt{\frac{1}{t_f - t_i}\int_{t_i}^{t_f}\left[F_{z,FL} + F_{z,RL} - F_{z,FR} - F_{z,RR}\right]^2 dt} \tag{4.4.35}$$

- The maximum hitch angle magnitude, which shows the most critical condition of the combination vehicle:

$$\theta^{max} = max|\theta| \tag{4.4.36}$$

- The maximum rear axle slip angle magnitude, to assess the stability of the towing car:

$$\alpha_R^{max} = max|\alpha_R| \tag{4.4.37}$$

- The rearward amplification factor, to assess trailer stability:

$$RWA = \frac{max|a_{y,t}|}{max|a_y|} \tag{4.4.38}$$

  where $a_{y,t}$ is the lateral acceleration of the trailer.

In addition to being used for optimised control tuning with the BMT, in the remainder J_{KPI} and the respective individual indicators are also calculated for different trailers and manoeuvres, to support the controller assessment phase.

4.4.5 ESTIMATION OF RELEVANT VARIABLES AND PARAMETERS.

4.4.5.1 Hitch joint forces

In real-world conditions, the hitch joint force components are not available, because of the lack of dedicated sensors on typical car-semitrailer combination vehicles. Hence, for the NMPCs embedding the rigid vehicle model ($c = 1$), F_x^{j2c}, F_y^{j2c} and F_z^{j2c} are computed outside the internal model, under reasonable assumptions, and are kept constant along the prediction horizon. More specifically, the three forces are calculated from the hitch joint force components in the trailer reference system, $F_{x,t}^{j2c}$, $F_{y,t}^{j2c}$, and $F_{z,t}^{j2c}$, see Figure 4.4.1a)–b):

$$F_x^{j2c} = F_{x,t}^{j2c}\cos(\theta) + F_{y,t}^{j2c}\sin(\theta) \tag{4.4.39}$$

$$F_y^{j2c} = F_{x,t}^{j2c}\sin(\theta) + F_{y,t}^{j2c}\cos(\theta) \tag{4.4.40}$$

$$F_z^{j2c} = F_{z,t}^{j2c} \tag{4.4.41}$$

where θ can be obtained from ultra-sonic sensors located on the rear bumper of the towing car, see Section 4.4.1. By neglecting the yaw and pitch accelerations of the trailer, and assuming that the longitudinal and lateral trailer accelerations, i.e., $a_{x,t}$ and $a_{y,t}$, are equal to the acceleration components of the towing car, $F_{x,t}^{j2c}$, $F_{y,t}^{j2c}$ and $F_{z,t}^{j2c}$ are derived from the longitudinal force balance (4.4.42), the yaw moment balance (4.4.43), and the pitch moment balance of the trailer (4.4.44):

$$F_{x,t}^{j2c} = -m_t a_{x,t} \cong -m_t a_x \tag{4.4.42}$$

$$F_{y,t}^{j2c} = -\frac{m_t a_{y,t} l_{R,t}}{l_t} \cong -\frac{m_t a_y l_{R,t}}{l_t} \tag{4.4.43}$$

$$\begin{aligned} F_{z,t}^{j2c} &= \frac{m_t g l_{R,t}}{l_t} + \frac{m_t a_{x,t}\left[H_{CoG,t} - H_{Hitch}\right]}{l_t} \cong -\frac{m_t g l_{R,t}}{l_t} + \frac{m_t a_x\left[H_{CoG,t} - H_{Hitch}\right]}{l_t} \\ &= F_z^{j2c,stat} + \Delta F_{z,t}^x \end{aligned} \tag{4.4.44}$$

The control system performance analyses, see the following Section 4.4.6, highlighted that, in the considered extreme cornering conditions, F_x^{j2c} and F_z^{j2c} tend to bring negligible effects w.r.t. F_y^{j2c}, and therefore the focus must be on the accurate estimation of the lateral force component. Figure 4.4.5 shows validation examples of F_y^{j2c} profiles computed through (4.4.40) and (4.4.43) against the CarMaker model output.

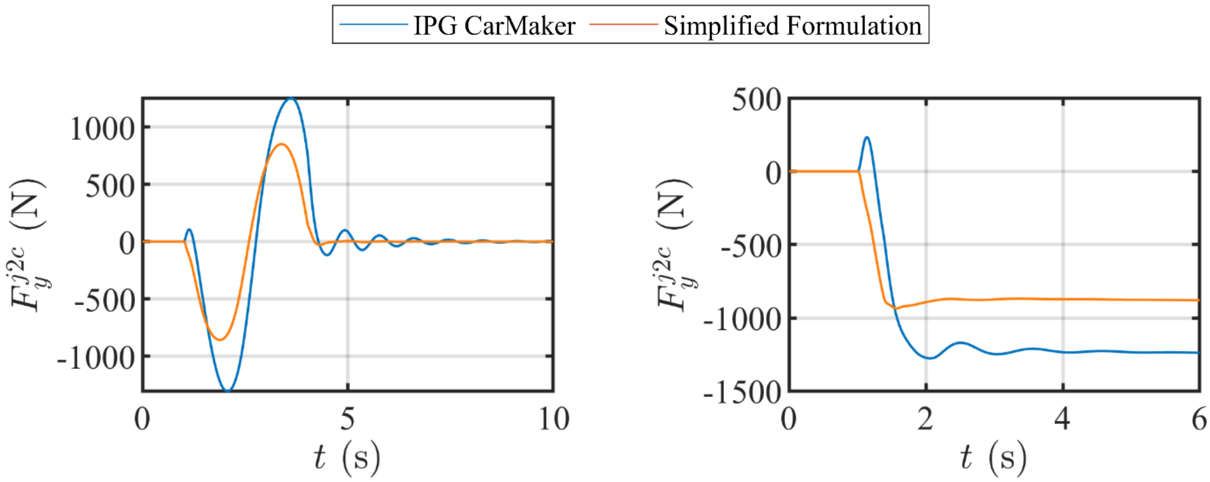

(a) (b)

Figure 4.4.5: Validation – against the high-fidelity model results – of the proposed simplified method for computing the lateral component of the hitch joint force, along: a) a sinusoidal steering manoeuvre at 60 km/h, with 50 deg of steering wheel angle amplitude; and b) a step steer at 40 km/h, with 150 deg of steering wheel angle magnitude.

4.4.5.2 Trailer parameters estimation

As shown in Section 4.4.5.1, the estimation of the hitch joint force inputs, required by the NMPC implementations based on the rigid vehicle model (NMPC^1 in the remainder), requires the knowledge of: i) the trailer mass, m_t; and ii) the ratio $l_{R,t}/l_t$. Additionally, the NMPCs based on the articulated vehicle prediction model in Section 4.4.3.3 (referred to as NMPC^2) need the knowledge of a more complete set of inertial, geometric and component parameters of the trailer, including the track width and tire parameters.

Since the load-independent trailer parameters, such as l_t, remain constant along the trailer lifetime, their values can be assumed to be stored in the trailer, and accurately provided to the controller on the towing car, without significant additional cost or complexity. To some extent, this can be considered valid also for the trailer tire parameters. On the contrary, the mass and longitudinal position of the center of gravity of the trailer must be estimated in real-time. The following paragraphs provide an overview of the estimation algorithms adopted in the implementations of this study.

As per the trailer mass estimation, m_t is estimated through a recursive least square (RLS) algorithm based on the longitudinal force balance of the car-semitrailer configuration, starting from the measured longitudinal acceleration, and the estimated wheel torque levels. The RLS formulation is:

$$\hat{\zeta}_k = \hat{\zeta}_{k-1} + K_k\left[y_k - \varphi_k^T \hat{\zeta}_{k-1}\right] \tag{4.4.45}$$

where $\hat{\zeta}$ is the vector of the parameters to be estimated, i.e., in this case m_t; the subscript k defines the time step; the measurement vector y_k includes the total estimated longitudinal tire forces of the towing car, $F_{x,tot}$; the coefficient φ_k derives from the longitudinal force balance, see [53]; and K_k is the correction gain, which depends on a forgetting factor λ [54].

Similarly to the studies in [53], [55] and [56], the RLS estimates are reliable when the vehicle is in pure longitudinal motion. In particular, the RLS algorithm is activated when the following conditions are concurrently met: i) the measured lateral acceleration magnitude is very low, i.e., $|a_y| < 0.3$ m/s^2; ii) the measured longitudinal acceleration is higher than a positive threshold ($a_x > 0.3$ m/s^2), i.e., braking conditions are discarded [56]; iii) the estimated slip ratios magnitudes on the car tires are relatively small ($|\sigma_{x,ij}| < 0.05$) [56]; and iv) the vehicle is not operating at very low speed ($v_x > 15$ km/h) [55], [56].

A buffer of the latest valid 50 RLS estimates is generated to compute the average trailer mass, $m_{t,avg,buffer}$, which is the output of the trailer mass estimation algorithm. The estimation is considered to be abnormal if:

$$\left|m_{t,RLS} - m_{t,avg,buffer}\right| > 0.1\, m_{t,avg,buffer} \tag{4.4.46}$$

When the previous condition is met, the estimate is neglected in the buffer definition. The RLS algorithm is stopped once the estimation is deemed to be complete, based on the following conditions: a) the RLS algorithm has run for at least 150 s; b) the estimation in the last 150 s stays in a pre-defined range [53], [55]; and c) the vehicle operation time during the trip exceeds a defined threshold (600 s) [55].

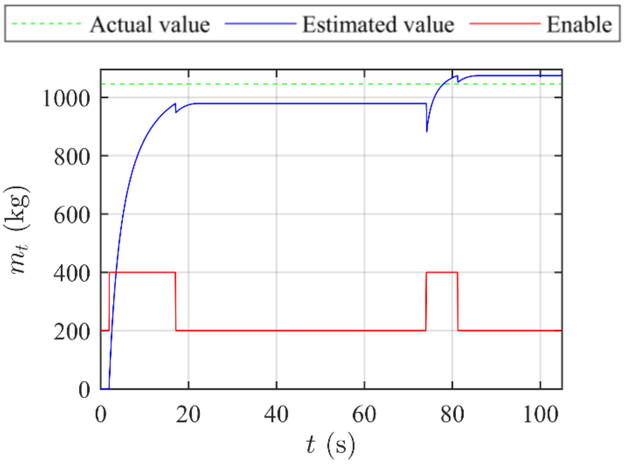

Figure 4.4.6: Example of trailer mass estimation during a manoeuvre with variable steering wheel, accelerator and brake pedal inputs, with vehicle speeds ranging from 40 km/h to 120 km/h. The enable signal is equal to 200 when the estimation algorithm is inactive, and to 400 when the estimation algorithm is active.

Figure 4.4.6 reports an example of mass estimation test, along a normal driving manoeuvre consisting of concurrent steering, accelerator and brake pedal inputs.

As per the trailer geometric ratio, i.e. $l_{R,t}/l_t$, it is estimated in real-time through a second RLS algorithm. The information required by the RLS includes the estimated trailer mass, the measured lateral acceleration of the towing car, the estimated wheel torque levels, and the lateral tire forces of the car, which can be estimated through a UKF [57]. The RLS formulation is the same as in (4.4.45), with $\hat{\zeta} = l_{R,t}/l_t$; y_k includes the estimated longitudinal tire forces on the front axle of the car, $F_{x,Fj}$; and φ_k derives from the re-arranged lateral force balance of the car-semitrailer system. The estimates are deemed reliable when the vehicle is in steady-state cornering, hence the RLS is activated when the following conditions are concurrently met: i) $|a_y| > 0.3$ m/s^2; ii) $|a_x| < 0.3$ m/s^2; iii) $v_x >$ 15 km/h; and iv) the mass estimation routine has already been successfully completed in the previous part of the trip

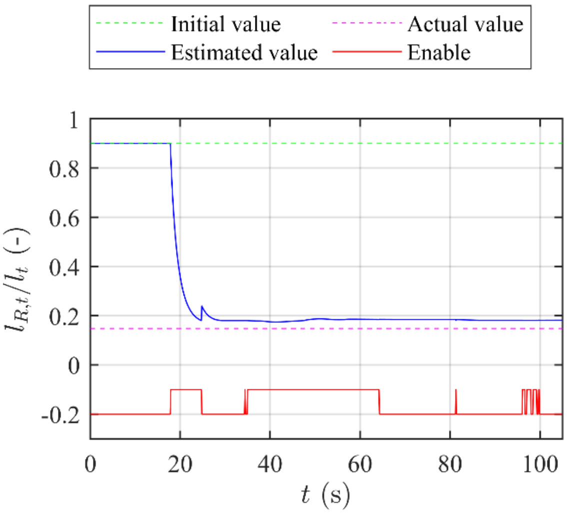

Figure 4.4.7: Example of trailer ratio estimation during the same test as in Figure 4.4.6.

Also in this case, a buffer of the latest valid 50 RLS estimates is generated to compute the average value of the ratio, i.e., $\left(\frac{l_{R,t}}{l_t}\right)_{avg,buffer}$. Similarly to the trailer mass estimation routine, the abnormal data are identified and eliminated from the buffer and replaced by the latest valid values. The RLS algorithm is stopped once the same conditions a)–c) defined for the mass estimation are met [53], [55]. Figure 4.4.7 shows an example of geometric trailer ratio estimation during the same manoeuvre as in Figure 4.4.6, under the assumption that the estimation of m_t has already been completed.

4.4.6 RESULTS AND DISCUSSION

This section assesses:

- The proposed integrated AS and TV controllers, referred to as $(\text{AS-TV})^{\text{c}}$.
- The standalone TV control strategies (TV^{c}).
- The standalone AS control strategies (AS^{c}).
- The parallel AS and TV configurations, $(\text{AS}^{\text{c}}//\text{TV}^{\text{c}})_{\text{W/oComm}}$, which do not share any information on the respective control inputs.
- The parallel AS and TV controllers, $(\text{AS}^{\text{c}}//\text{TV}^{\text{c}})_{\text{W/Comm}}$, which share the control input information.
- The baseline versions of the controllers, which embed the rigid vehicle prediction model in Section III.B and neglect the presence of the trailer. Such algorithms can be implemented as standalone torque-vectoring or active suspension controllers, referred to as TV^{Bas} and AS^{Bas} in the remainder, or in an integrated setup, referred to as $(\text{AS-TV})^{\text{Bas}}$.
- The passive vehicle configuration, with an even motor torque distribution among the corners of the towing car, and absence of variable anti-roll moment distribution.

All cases include active suspension actuation to reduce the roll motions of the towing car. The AS notation indicates that the suspension controller also varies the front-to-total anti-roll moment distribution to achieve a vehicle dynamics benefit. The cost function weights of the baseline controllers are optimised for the rigid vehicle, while all the other controllers are tuned for the combination vehicle with BMT. In fact, it is supposed that the car controllers are aware of whether the vehicle is towing a trailer, and thus a dedicated setting can be implemented for this occurrence. Nevertheless, it was verified that all controllers tuned for the combination vehicle provide safe performance also for rigid vehicle operation. The parallel control configurations have the same tuning as the corresponding standalone cases.

4.4.6.1 Comparison of the control configurations applied to the benchmarking trailer

Figure 4.4.8 compares the behaviour of the NMPC^1 algorithms with the one of their respective baseline versions, i.e., those neglecting the hitch joint forces. Figure 4.4.8(a) refers to a series of step steers and focuses on the active suspension actuation. The passive vehicle becomes unstable following the first steering input, while AS^{Bas} handles the first counter-steering action, before losing control after ~4 s, which results in trailer rollover. On the contrary, AS^1 is able to complete the manoeuvre by limiting the magnitude of the trailer hitch and roll angles ($|\theta_{max}| \cong 5$ deg and $|\varphi_{t,max}| \cong 15$ deg). Figure 4.4.8(b) reports the performance of the torque-vectoring setups during a single sinusoidal steering test at high speed. Also in this case, the passive vehicle cannot complete the manoeuvre, and the TV^{Bas} configuration becomes unstable once the driver steering command goes back to zero. Instead, the hitch joint force contributions allow to overcome the flaws of the baseline setups. The benefits of the NMPC^1 configurations are confirmed in Figure 4.4.8(c), referring to a sweep steering test with the integrated AS and TV controllers. The general conclusion is that the baseline AS and TV controllers, or their combination, are unable to limit the trailer hitch and roll dynamics. Vice versa, the inclusion of the estimated hitch joint forces is sufficient to account for the trailer presence in the rigid vehicle prediction model, and to provide stability without significantly increasing complexity.

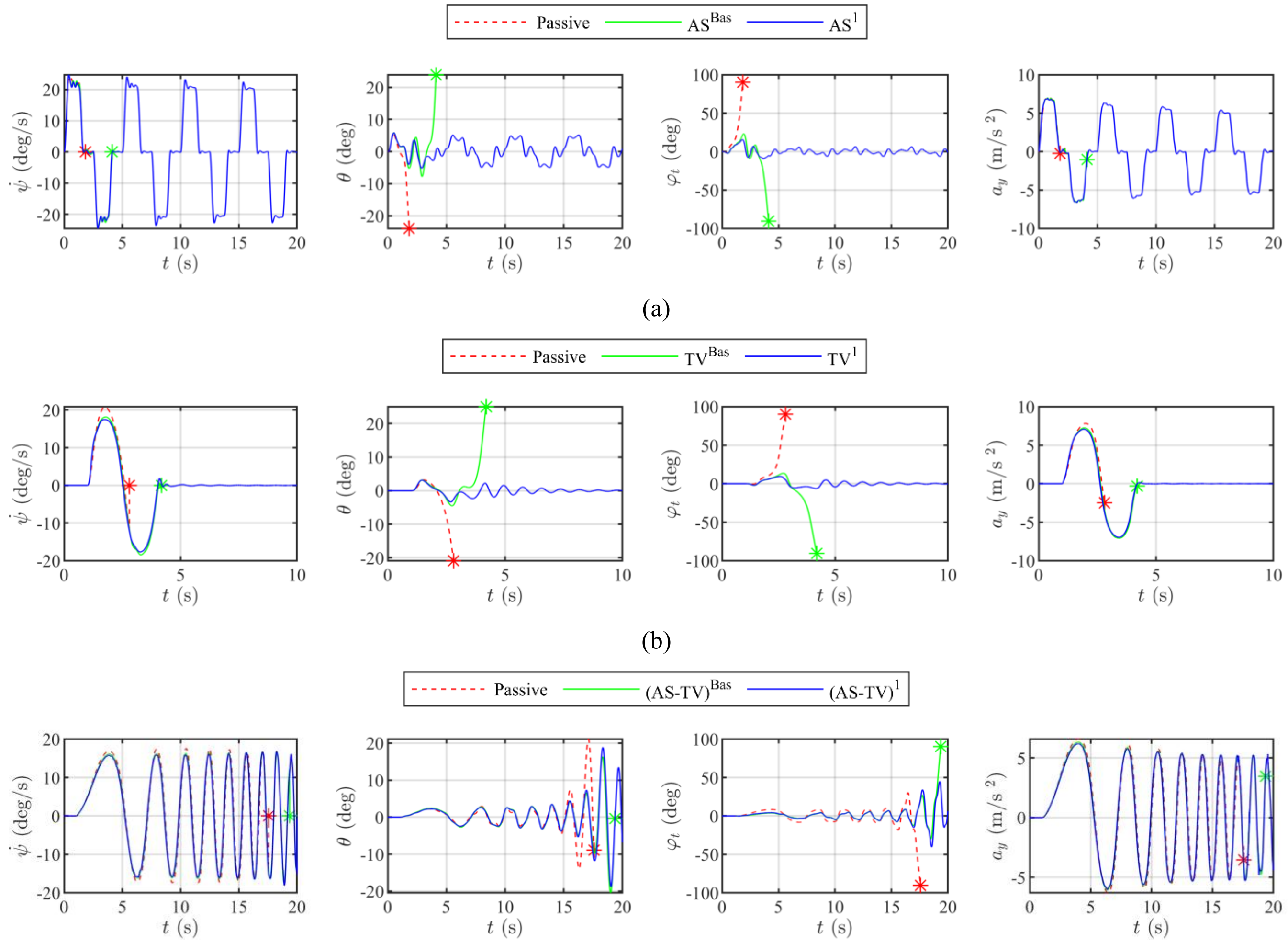

(a)

(b)

(c)

Figure 4.4.8: Results for the combination vehicle with the BMT in high-μ conditions. Comparison of the passive vehicle with: a) AS^{Bas} and AS^1 during a multiple step steer test with 60 deg of steering wheel angle amplitude, 1000 Nm of wheel torque demand, from an initial speed of 65 km/h; b) TV^{Bas} and TV^1 during a single sinusoidal steering test with 50 deg of steering wheel angle amplitude, 1000 Nm of torque demand, from 90 km/h; and c) (AS-TV)^{Bas} and (AS-TV)^1 during a sine sweep steering manoeuvre with 40 deg amplitude, 1000 Nm torque demand, from 85 km/h.

Figure 4.4.9 reports the response of the NMPC^1 and NMPC^2 algorithms along an ISO lane change [52], in which the passive car-semitrailer is unstable. Figure 4.4.9(a) and (b) highlight that the AS actuation on its own leads to higher trailer roll angle w.r.t. the integrated (AS-TV)^1 solution, for both internal model formulations. Nevertheless, the standalone AS configurations provide comparable performance to (AS-TV)^1 in limiting the hitch angle peak (4.28 deg for AS^1, 4.34 deg for AS^2, and 4.37 deg for (AS-TV)^1), although their results are inferior to those of $(\text{AS-TV})^2$ (with a 3.61 deg peak). Figure 4.4.9(c) and (d) highlight that the parallel configurations need to undergo a new calibration process w.r.t. their individual optimal settings, otherwise – with the original tuning for the separate actuations – they may generate chattering in the yaw rate response. This issue is more evident for the peaceful coexistence $(\text{AS}^1//\text{TV}^1)_{\text{W/Comm}}$ configuration, while the parallel configurations $\text{AS}^2//\text{TV}^2$ with and without communication show better overall performance than the respective $(\text{AS}^1//\text{TV}^1)$.

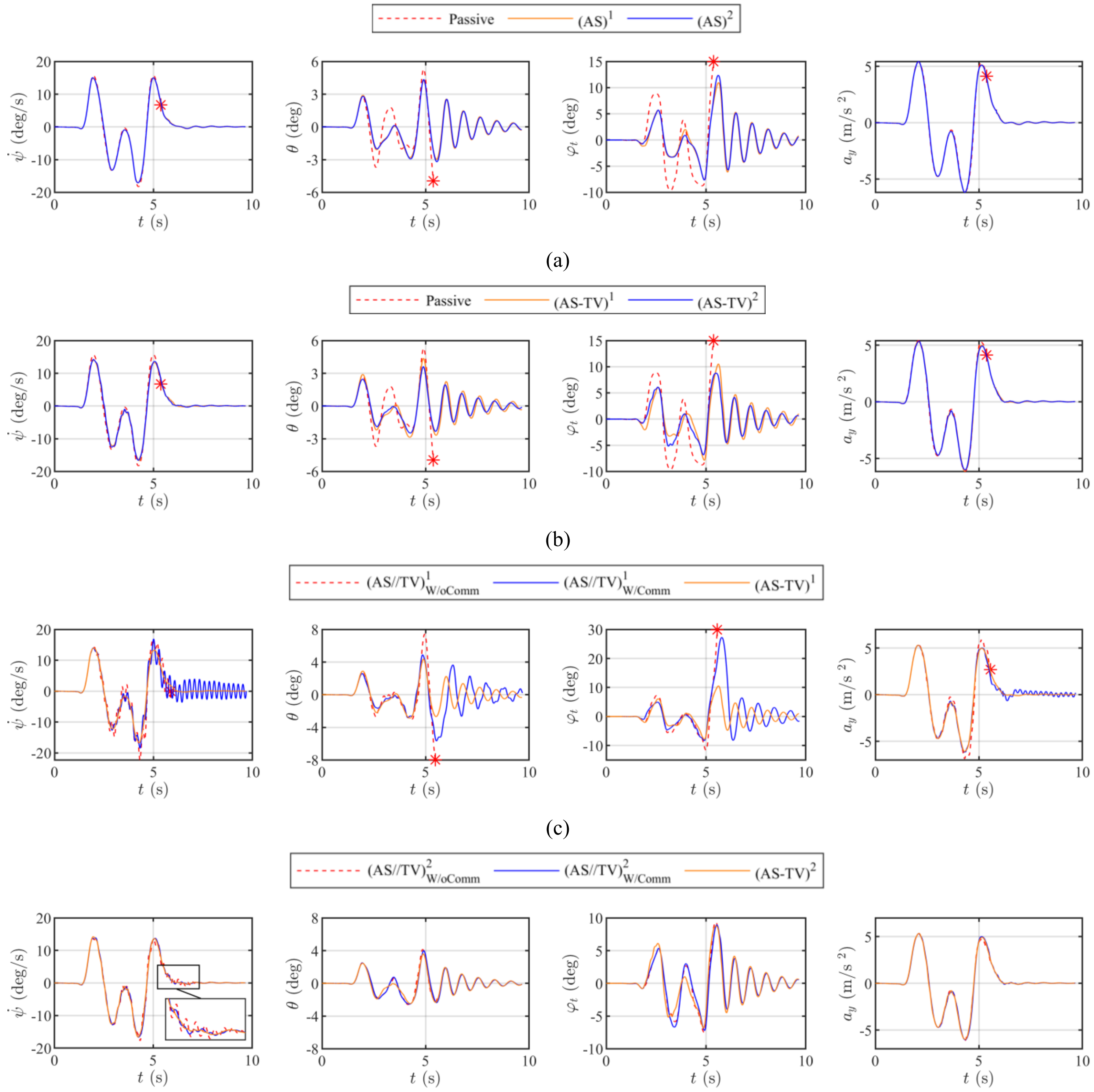

(a)

(b)

(c)

(d)

Figure 4.4.9: Results for the combination vehicle with the BMT, during an ISO lane change manoeuvre from 88 km/h, with 200 Nm wheel torque demand, in high-μ conditions. Comparison of the passive vehicle with: a) the

standalone AS configurations; b) the integrated AS-TV configurations, c) the (AS-TV)^1 and AS^1//TV^1 configurations; and d) the (AS-TV)^2 and AS^2//TV^2 configurations.

The resulting KPIs are reported in Figure 4.4.10. Figure 4.4.10(a) compares the individual actuation cases with the integrated (AS-TV)^1 and (AS-TV)^2, while Figure 4.4.10(b) contrasts the parallel control architectures with the integrated ones. To penalise the J_{KPI} values obtained when the car-trailer configuration is unstable, each KPI is multiplied by a factor 2 whenever the trailer roll angle exceeds an extreme value (70 deg, corresponding to rollover) during the test, condition in which the simulation is also automatically interrupted. Figure 4.4.10 does not include $RMSE_{\Delta\theta}$, as for the controlled cases $\Delta\theta$ exceeds the error bound of 7 deg defined in Section 4.4.4.2 only in the (AS^1//TV^1)$_{\mathrm{W/oComm}}$ case.

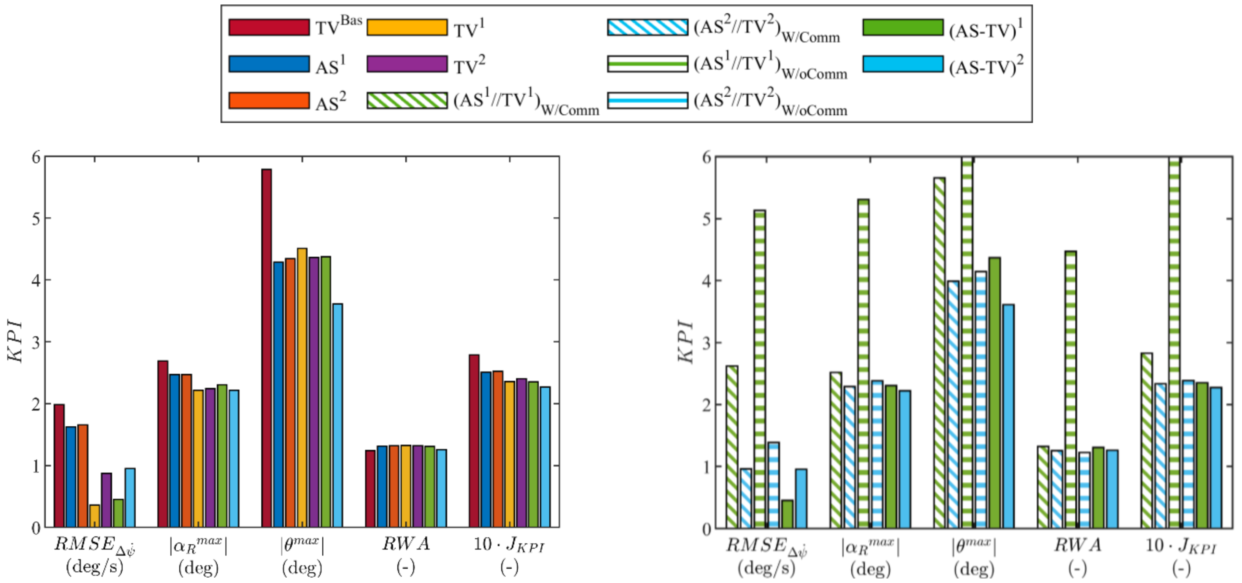

(a) (b)

Figure 4.4.10: KPI summary for the selected ISO lane change manoeuvre of the combination vehicle with BMT. Comparison of the integrated strategies with: a) TV$^{\mathrm{Bas}}$ and the standalone AS$^{\mathrm{c}}$ and TV$^{\mathrm{c}}$ controllers; and b) the parallel and the peaceful coexistence configurations, (AS$^{\mathrm{c}}$//TV$^{\mathrm{c}}$)$_{\mathrm{W/oComm}}$ and (AS$^{\mathrm{c}}$//TV$^{\mathrm{c}}$)$_{\mathrm{W/Comm}}$.

The analysis of the plots leads to the following observations:

- TV$^{\mathrm{bas}}$, i.e., the torque-vectoring controller calibrated for isolated vehicle control purposes, keeps the car-semitrailer stable, but the performance is degraded w.r.t. all the proposed control configurations for articulated vehicles, with the exception of (AS^1//TV^1)$_{\mathrm{W/oComm}}$.
- As expected, the AS performance on its own is always slightly worse than the one of the corresponding standalone TV control configurations, i.e., J_{KPI} is ~6.5% higher for AS^1 w.r.t. TV^1, and ~5.1% higher for AS^2 w.r.t. TV^2.
- Despite being less effective than the corresponding TV control configurations, the standalone AS settings perform better than TV$^{\mathrm{Bas}}$, because of the inclusion of some form of trailer consideration. For example, w.r.t. TV$^{\mathrm{Bas}}$, AS^1 and AS^2 reduce the cost function respectively by ~10% and ~9.5%.

- When integrated with the torque-vectoring system, the active suspension provides only a marginal performance improvement for the NMPC^1 case, i.e., the J_{KPI} reduction amounts to less than 0.5% for (AS-TV)^1 w.r.t. TV^1. Instead, the AS benefit is much more evident for the NMPC^2 implementations, for which (AS-TV)^2 reduces J_{KPI} and $|\theta^{max}|$ by ~5% and ~17% w.r.t. TV^2, thanks to the inclusion of the continuous hitch angle tracking term in (4.4.29).
- Because of their formulation, the standalone and integrated NMPC^1 implementations tend to provide better car yaw rate tracking and worse hitch angle tracking performance than the corresponding NMPC^2 algorithms. For example, TV^1 reduces $RMSE_{\Delta\dot{\psi}}$ by ~20% w.r.t. (AS-TV)^1, and by ~62% w.r.t. (AS-TV)^2. However, among the controllers that are able to complete the test, TV^1 also shows the third highest hitch angle peak after (AS^1//TV^1)$_{\text{W/Comm}}$ and TV$^{\text{Bas}}$, corresponding to a ~3% $|\theta^{max}|$ increase w.r.t. (AS-TV)^1, and to a ~25% increment w.r.t. (AS-TV)^2. Given the focus of the controllers on stable car-trailer operation, J_{KPI} more heavily penalises the hitch angle error than the yaw rate error, and thus, for example, J_{KPI} is ~3% lower for (AS-TV)^2 w.r.t. TV^1.
- When associated to a single actuation system, the considered real-time NMPC^1 algorithms always provide marginally better performance than the corresponding NMPC configurations including the trailer dynamics in the prediction model, i.e., J_{KPI} amounts to 0.251 and 0.253 for AS^1 and AS^2, and to 0.236 and 0.240 for TV^1 and TV^2.
- When associated with both chassis actuation methods, the NMPC^2 configurations provide better performance than the respective NMPC^1 versions, i.e., J_{KPI} amounts to 0.283 and 0.233 for (AS^1//TV^1)$_{\text{W/Comm}}$ and (AS^2//TV^2)$_{\text{W/Comm}}$, 0.995 and 0.239 for (AS^1//TV^1)$_{\text{W/oComm}}$ and (AS^2//TV^2)$_{\text{W/oComm}}$, and 0.235 and0.227 for (AS-TV)^1 and (AS-TV)^2, where the latter provides the best overall performance for the BMT case and reduces J_{KPI} by ~3.4% w.r.t. (AS-TV)^1.
- The parallel configurations without communication of the control inputs provide worse KPIs than the peaceful coexistence layouts, which, on their end, are already less performant than the integrated control solutions. The variation of the KPIs is especially evident for the NMPC^1 configurations. In fact, while (AS^1//TV^1)$_{\text{W/Comm}}$ implies limited performance degradation, amounting to ~17% w.r.t. (AS-TV)^1, (AS^1//TV^1)$_{\text{W/oComm}}$ brings a ~76% J_{KPI} increase, corresponding – very importantly – to an unstable vehicle response with trailer rollover. Indeed, (AS^1//TV^1)$_{\text{W/oComm}}$ performs by far worse than the individual controllers, including TV$^{\text{bas}}$, and thus such configuration is not recommended for further development. On the contrary, the parallel NMPC^2 architectures are not significantly affected by the absence of control action information exchange. In fact, w.r.t. (AS-TV)^2, J_{KPI} increases by ~4.9% and ~2.7%, respectively for (AS^2//TV^2)$_{\text{W/oComm}}$ and (AS^2//TV^2)$_{\text{W/Comm}}$.

As a summary, the configuration ranking w.r.t. J_{KPI} for BMT operation, from the worst to the best controller, is $(AS^1//TV^1)_{W/oComm}$; TV^{bas}; $(AS^1//TV^1)_{W/Comm}$; AS^2; AS^1; TV^2; $(AS^2//TV^2)_{W/oComm}$; $(AS^2//TV^2)_{W/Comm}$; TV^1; $(AS\text{-}TV)^1$; and $(AS\text{-}TV)^2$.

Corresponding simulations were run also for the sinusoidal steering test, involving less critical roll dynamics and more extreme hitch angle dynamics. The results show similar trends, apart from the fact that in these conditions also $(AS^2//TV^2)_{W/oComm}$ becomes unstable.

The overall recommendation from the previous analyses on the nominal trailer setup is to opt for an integrated controller based on the more advanced prediction model. Moreover, in Section 4.4.4.1, the real-time implementability of the parallel control solutions was verified in terms of the individual controllers running in real-time on the dSpace MicroAutoBox II unit. This means that the real-time implementation of the parallel architectures would require two control hardware devices, while the proposed integrated controllers, i.e., $(AS\text{-}TV)^1$ and $(AS\text{-}TV)^2$, are able to run in real-time on a single rapid control prototyping device, because of their longer sampling time. Hence, a comparison among the real-time controller configurations running on the same single device would highlight an even more evident advantage of the integrated solutions.

4.4.6.2 Sensitivity analysis on trailer parameters

This section analyses the control system robustness w.r.t. the variation of the geometric and inertial trailer parameters, according to the configurations in Table A 1, during the considered ISO lane change manoeuvre. In the tests of this section, the parameters are modified in the high-fidelity CarMaker model at the beginning of each simulation, but are kept unaltered in the prediction models, which always use the BMT parameters. In these simulations, the trailer parameter estimation algorithms are purposely deactivated, to prevent any adaptation to the different trailers, which corresponds to the worst-case scenario. The cost function weights are also the same as for the case with nominal trailer.

For each trailer configuration, Table A 2 in the Appendix highlights the controllers and trailer parameters that lead the car-semitrailer to unstable conditions. Table 4.4.4 and Figure 4.4.11 report the average (hence the symbol ‘ ¯ ’ in the notations) KPIs obtained across the simulated trailer setups. The table also shows the average percentage variation, $\Delta\bar{J}_{KPI}$, of J_{KPI} for the different control configurations w.r.t. the value (J_{KPI,TV^2}) for the TV^2 controller, which represents the current state-of-the-art in hitch angle control, see [18]:

$$\Delta\bar{J}_{KPI} = \frac{1}{n_t}\sum_{j_t=1}^{n_t} 100\frac{J_{KPI,Ctrl,j_t} - J_{KPI,TV^2,j_t}}{J_{KPI,TV^2,j_t}} \tag{4.4.47}$$

where n_t is the number of considered trailer configurations; j_t is an index referring to the trailer parametrisation; and $J_{KPI,Ctrl,j_t}$ is the objective function value across the trailers for the specific controller, identified through the subscript $Ctrl$. Negative $\Delta\bar{J}_{KPI}$ values indicate an improvement w.r.t. TV^2.

Table 4.4.4 – Average KPIs with all the trailers (all the discussed configurations).

KPI (units)	$\overline{RMSE}_{\Delta\dot{\psi}}$ (deg/s)	$\overline{RMSE}_{\Delta\theta}$ (deg)	$\overline{\|\alpha_R^{max}\|}$ (deg)	$\overline{\|\theta^{\ max}\|}$ (deg)	$\overline{RWA}$ (-)	$\bar{J}_{KPI}$ (-)	$\Delta\bar{J}_{KPI}$ (%)
TV^{Bas}	2.44	1.33	3.19	15.18	1.81	0.49	81.48
AS^1	1.64	0	2.45	4.38	1.28	0.25	**-7.41**
AS^2	2.09	0.48	2.85	7.38	1.51	0.33	22.22
TV^1	0.54	0.2	2.64	5.65	1.38	0.27	**0**
TV^2	**0.98**	**0.18**	**2.38**	**5.73**	**1.38**	**0.27**	**-**
(AS^1//TV^1)$_{\text{W/Comm}}$	2.65	0.67	2.92	8.85	1.56	0.38	40.74
(AS^2//TV^2)$_{\text{W/Comm}}$	1.2	0.31	2.61	7.11	1.46	0.31	14.81
(AS^1//TV^1)$_{\text{W/oComm}}$	4.92	3.16	5.32	32.2	2.91	0.94	248.15
(AS^2//TV^2)$_{\text{W/oComm}}$	1.49	0.32	2.68	7.06	1.44	0.31	14.81
(AS-TV)^1	0.8	0.25	2.45	5.93	1.39	0.28	3.7
(AS-TV)^2	0.99	0.23	2.22	5.22	1.28	0.25	**-7.41**

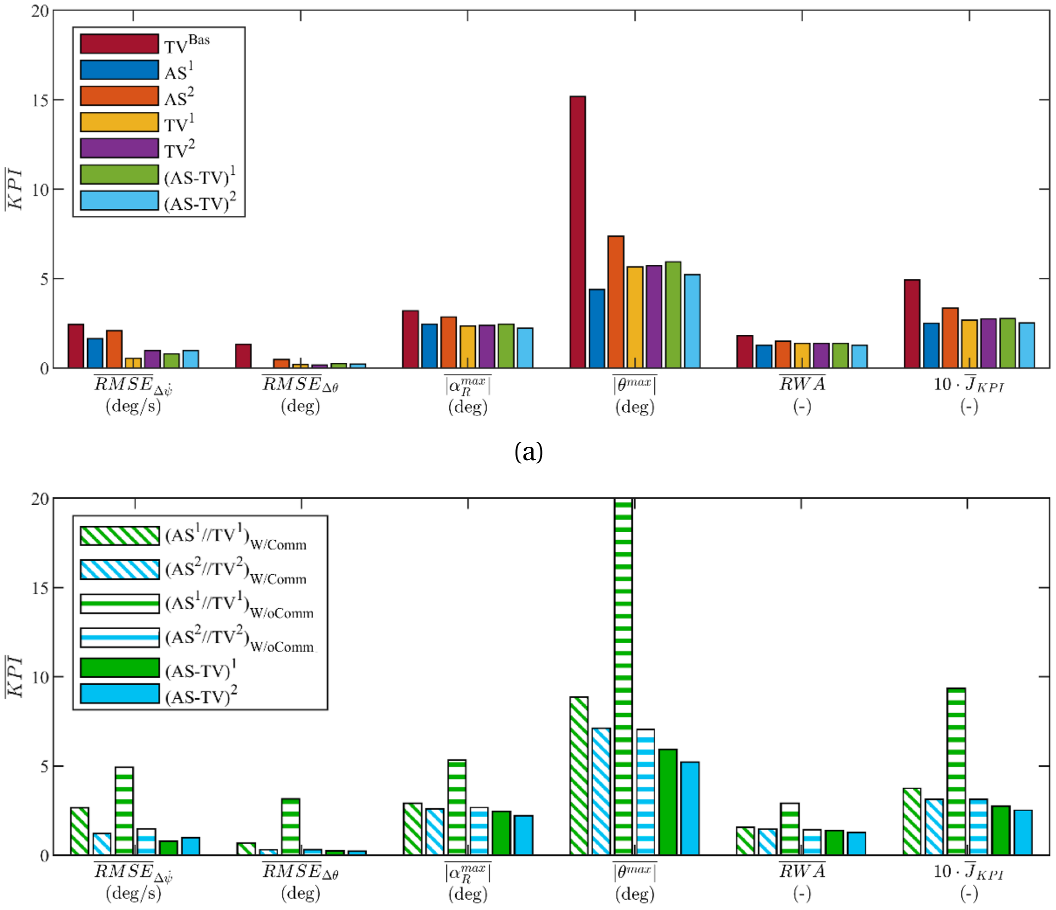

(a)

(b)

Figure 4.4.11: Average KPIs for the trailer configurations in Table A 1.

The controller configuration ranking is the same in terms of stability (Table A 2) and $\Delta\bar{J}_{KPI}$, and sees, from the worst to the best case: (AS^1//TV^1)$_{\text{W/oComm}}$ (13 unstable cases out of 14, including the BMT); TV^{bas} (4 unstable cases); (AS^1//TV^1)$_{\text{W/Comm}}$ (3 unstable cases); AS^2,

$(AS^2//TV^2)_{\mathrm{W/oComm}}$, and $(AS^2//TV^2)_{\mathrm{W/Comm}}$ (2 unstable cases); TV^1, TV^2, and $(AS\text{-}TV)^1$ (1 unstable instance); and AS^1 and $(AS\text{-}TV)^2$, which are always stable.

Interestingly, w.r.t. the nominal case, in the robustness analysis the standalone controller configurations provide better performance than the parallel configurations based on the articulated vehicle prediction model, excluding and including information exchange on the control inputs.

4.4.6.3 Sensitivity analysis of the AS^1 performance as a function of the considered force contributions

Since the hitch joint forces that are necessary for the operation of the NMPC^1 configurations are extremely difficult to be accurately estimated, a specific sensitivity analysis is carried out to assess the deterioration of the AS^1 performance when the estimation of some of the hitch joint force components is not available. To this purpose, for the ISO lane change test of the previous sections, Figure 4.4.12(a) reports the force related deterioration index, DI_F, of the AS^1 KPIs, expressed in terms of $RMSE_{\Delta\dot{\psi}}$, $|\theta^{max}|$, and RWA when only some of the three force components are provided to the controller, w.r.t. the case where all the forces are available:

$$DI_F = 100\frac{KPI_{F_h^{j2c}} - KPI_{F_x^{j2c},F_y^{j2c},F_z^{j2c}}}{KPI_{F_x^{j2c},F_y^{j2c},F_z^{j2c}}} \tag{4.4.48}$$

where $KPI_{F_x^{j2c},F_y^{j2c},F_z^{j2c}}$ refers to the nominal controller benefitting from the estimation of all the trailer force components; and $KPI_{F_h^{j2c}}$ refers to the same controller receiving a limited combination of estimated hitch joint forces, whose direction is indicated by the subscript $h = x, y, z$. The main conclusions are: i) the lateral hitch joint force is of the essence for the correct operation of the controller, which, when provided only with F_y^{j2c}, shows very limited DI_F – bounded to a peak value of ~3% – w.r.t. to AS^1 fed with all the joint forces; ii) the AS^1 configuration receiving only F_x^{j2c} and F_y^{j2c} has a maximum DI_F of ~2%, with a deterioration trend across the trailers that is similarly shaped to the case in i). This observation highlights the low influence of the addition of F_x^{j2c} as input signal in the specific test conditions; and iii) the AS^1 version receiving F_y^{j2c} and F_z^{j2c} shows negligible performance deterioration, i.e., F_z^{j2c} is more beneficial than F_x^{j2c}. To analyze the impact of the force estimation algorithms on controller performance, Figure 4.4.12(b) compares the AS^1 KPIs when the hitch joint forces used by the controller are those generated by the high-fidelity CarMaker model, which corresponds to the notation $KPI_{F_{h,CM}^{j2c}}$, with the KPIs, referred to as $KPI_{F_{h,est}^{j2c}}$, for the same controller when the input force values are those estimated through (4.4.42)–(4.4.44). In this case, the deterioration index, DI_E, is defined as:

$$DI_E = 100\frac{KPI_{F_{h,est}^{j2c}} - KPI_{F_{h,CM}^{j2c}}}{KPI_{F_{h,CM}^{j2c}}} \tag{4.4.49}$$

For generality, in the figure DI_E is computed for each of the considered combinations of input forces provided to the controller. The AS^1 configuration with the estimated forces shows limited KPI deterioration w.r.t. its counterpart fed with the correct values of the joint forces from the plant model, e.g., DI_E never exceeds 6%. Moreover, the selected combinations of hitch joint forces does not have any significant impact on the estimation-related performance deterioration level, i.e., the subplots in Figure 4.4.12(b) are approximately the same regardless of the assessed combination.

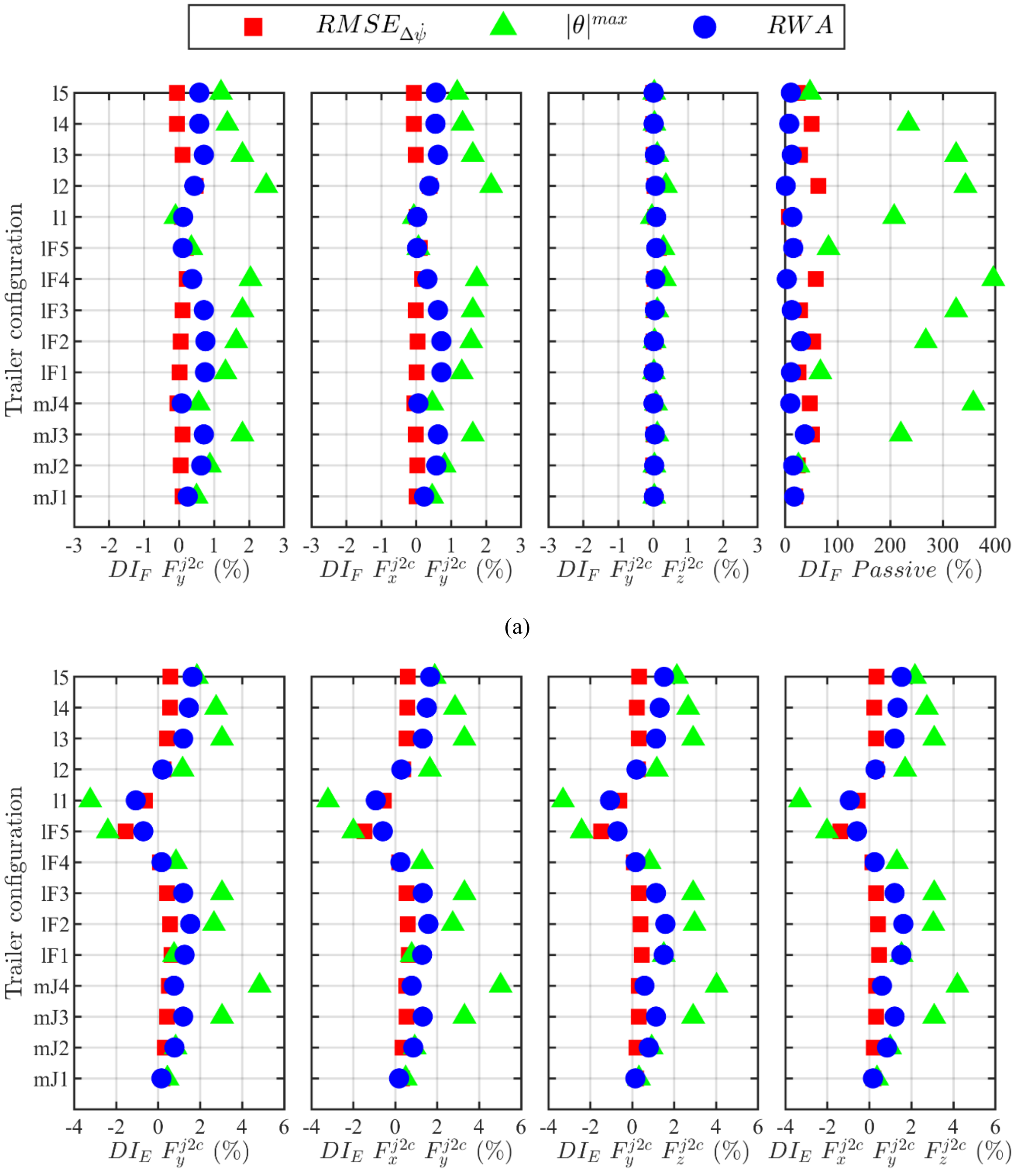

(a)

(b)

Figure 4.4.12: Degradation indices of the average AS^1 performance associated with: a) different combinations of estimated hitch joint forces provided to the controller; and b) the proposed estimation method of the hitch joint forces w.r.t. their true value, for controller versions using different input force combinations.

4.4.7 CONCLUDING REMARKS

This study explored the potential of controlling the hitch dynamics of a car-semitrailer combination through an active suspension (AS) system installed on the towing car, capable of varying the anti-roll moment distribution, and operating in isolation or concurrently with a torque-vectoring (TV) controller based on the actuation of the electric powertrains and friction brakes, to stabilise the semitrailer during limit cornering manoeuvres. The proposed algorithms are based on nonlinear model predictive control. Two alternative prediction model formulations were embedded in the controllers: i) the model of the isolated car, supported in its prediction by the consideration – which represents a novelty point – of the estimated forces currently applied by the trailer at the hitch joint. The related controller formulations are referred to with the superscript '1'; and ii) the model of the articulated vehicle, i.e., considering the hitch angle dynamics. The related controllers are indicated with the superscript '2'.

By using a high-fidelity simulation model for control system assessment and optimised controller parameters for operation with a nominal trailer, the comparison considered the real-time versions of: a) controllers for the actuators operating in a standalone setup (AS^1, AS^2, TV^1, and TV^2 configurations); b) individual controllers for each actuation method operating in parallel without ($(AS^1//TV^1)_{W/oComm}$ and $(AS^2//TV^2)_{W/oComm}$) or with ($(AS^1//TV^1)_{W/Comm}$ and $(AS^2//TV^2)_{W/Comm}$) communication exchange of the respective control inputs; and c) integrated controllers, i.e., $(AS\text{-}TV)^1$ and $(AS\text{-}TV)^2$, concurrently generating the control inputs for the two actuations. The algorithms in a)–c) were compared with a conventional NMPC-based TV controller (TV^{Bas}) neglecting the presence of the trailer. The study involved consideration of controller robustness w.r.t. significant variations of the main geometric and inertial trailer parameters, where these were not communicated to the algorithms.

The main conclusions are:

- TV^{Bas} cannot guarantee safe vehicle behaviour during the assessed extreme cornering manoeuvres, i.e., the trailer tends to be subject to rollover or hitch angle instability.
- The consideration of the lateral force at the hitch joint is sufficient for effective operation of the $NMPC^1$ formulations. Also, it was verified that the level of approximation associated with the proposed hitch joint force estimation routines does not significantly affect the results across the variety of investigated conditions.
- The $NMPC^1$ configurations are characterised by lower computational burden due to the simpler internal model formulation, and can be implemented at more than halved sample times w.r.t. the $NMPC^2$ algorithms, on the considered control hardware.
- With the nominal trailer, AS^1 and AS^2 provide equivalent performance, with an evident improvement w.r.t. TV^{Bas}. Nevertheless, the proposed standalone TV algorithms are more effective than the AS counterparts. However, in the robustness analysis on the trailer parameters, although remaining beneficial w.r.t. TV^{Bas}, AS^2, which shows two instances of instability, becomes significantly less effective than AS^1, which is never associated with instability in the considered test cases, and thus proves to be the most robust controller together with $(AS\text{-}TV)^2$.

- The integrated or parallel control configurations based on the articulated vehicle prediction model always correspond to better performance indicators than the counterparts using the rigid vehicle prediction setup and the estimated hitch joint forces.
- Among the considered algorithms, $(\text{AS-TV})^2$ consistently guarantees the best performance, and therefore is the control version that will be characterised by further analyses at higher technology readiness levels.

BIBLIOGRAPHY

[1] "Trailer output report: 2022," Trailer Body Builders, https://www.trailer-bodybuilders.com/trailer-output/article/21262072/trailer-output-report-2022, (accessed Mar. 7, 2024).

[2] "Semi-trailer market size, share and Trends report, 2030," Semi-trailer Market Size, Share and Trends Report, 2030, https://www.grandviewresearch.com/industry-analysis/semi-trailer-market, (accessed Mar. 7, 2024).

[3] "Automotive Trailer Market Size Global Report, 2022 - 2030," Polaris Market Research, https://www.polarismarketresearch.com/industry-analysis/automotive-trailer-market, (accessed Mar. 7, 2024).

[4] Research and Markets, "Trailer global market report 2023: Sector to reach $85.65 billion by 2027 at a 10.1% CAGR," GlobeNewswire Newsroom, https://www.globenewswire.com/news-release/2023/05/02/2658939/28124/en/Trailer-Global-Market-Report-2023-Sector-to-Reach-85-65-Billion-by-2027-at-a-10-1-CAGR.html (accessed Mar. 7, 2024).

[5] J. Darling, D. Tilley, and B. Gao, "An experimental investigation of car-trailer high-speed stability," *Proc. Inst. Mech. Eng. Part D J. Automob. Eng.*, 2009.

[6] E. Gerum, P. Laszlo, A. Semsey, and G. Barta, "Method for drive stability enhancement of multi-unit vehicles," US 005,747,683, 1998.

[7] O. Mokhiamar and M. Abe, "Examination of different models following types of yaw moment control strategy for improving handling safety of a car-caravan combination," *Proc. Inst. Mech. Eng. Part D J. Automob. Eng.*, vol. 217, no. 7, pp. 561–572, 2003.

[8] M. Zanchetta, D. Tavernini, A. Sorniotti, P. Gruber, B. Lenzo, A. Ferrara, K. Sannen, J. De Smet, and W. De Nijs, "Trailer control through vehicle yaw moment control: Theoretical analysis and experimental assessment," *Mechatronics*, vol. 64, no. 102282, 2019.

[9] W. K. Deng and X. Kang, "Parametric study on vehicle-trailer dynamics for stability control," *SAE Trans.*, pp. 1411–1419, 2003.

[10] Y. He, M. M. Islam, and T. D. Webster, "An integrated design method for articulated heavy vehicles with active trailer steering systems," *SAE Int. J. Passeng. Cars - Mech. Syst.*, vol. 119, no. 6, pp. 158–174, 2010.

[11] M. M. Islam, X. Ding, and Y. He, "A closed-loop dynamic simulation-based design method for articulated heavy vehicles with active trailer steering systems," *Veh. Syst. Dyn.*, vol. 50, no. 5, pp. 675–697, 2012.

[12] B. Houska, H. J. Ferreau, and M. Diehl, "An auto-generated real-time iteration algorithm for nonlinear MPC in the microsecond range," *Automatica*, vol. 47, no. 10, pp. 2279–2285, 2011.

[13] E. Siampis, E. Velenis, S. Gariuolo, and S. Longo, "A real-time nonlinear model predictive control strategy for stabilization of an electric vehicle at the limits of handling," *IEEE Trans. Control Syst. Technol.*, vol. 26, no. 6, pp. 1982–1994, 2017.

[14] A. Parra, D. Tavernini, P. Gruber, A. Sorniotti, A. Zubizarreta, and J. Perez, "On nonlinear model predictive control for energy-efficient torque-vectoring," *IEEE Trans. Veh. Technol.*, vol. 70, no. 1, pp. 173–188, 2020.

[15] M. Dalboni, D. Tavernini, U. Montanaro, A. Soldati, C. Concari, M. Dhaens, and A. Sorniotti, "Nonlinear model predictive control for and anti-roll moment distribution," *IEEE/ASME Trans. Mechatronics*, vol. 26, no. 3, pp. 1212–1224, 2021.

[16]Y. Zhang, A. Khajepour, E. Hashemi, Y. Qin, and Y. Huang, "Reconfigurable model predictive control for articulated vehicle stability with experimental validation," *IEEE Trans. Transp. Electrif.*, vol. 6, no. 1, pp. 308–317, 2020.

[17]M. Abroshan, R. Hajiloo, E. Hashemi, and A. Khajepour, "Model predictive-based tractor-trailer stabilisation using differential braking with experimental verification," *Veh. Syst. Dyn.*, vol. 59, no. 8, pp. 1190–1213, 2021.

[18]M. De Bernardis, G. Rini, F. Bottiglione, A.E. Hartavi and A. Sorniotti, "On nonlinear model predictive direct yaw moment control for trailer sway mitigation," *Veh. Syst. Dyn,* vol. 61, no. 2, pp. 445–471, 2023.

[19]Y. H. Lee and A. Kade, "Trailer articulation angle estimation," US 7,904.222 B2, 2011.

[20]J. Vejlupek, "Trailer backing-up assistant using ultrasound sensors based control units to safely back-up the car with trailer," in *17th International Conference on Mechatronics-Mechatronika (ME)*, 2016, pp. 1–6.

[21]H. Ahmadi Jeyed and A. Ghaffari, "Nonlinear estimator design based on extended Kalman filter approach for state estimation of articulated heavy vehicle," *Proc. Inst. Mech. Eng. Part K J. Multi-body Dyn.*, vol. 233, no. 2, pp. 254–265, 2019.

[22]L. Xu, E. Tseng, T. Pilutti, and S. Schondorf, "Yaw rate based trailer hitch angle estimation for trailer backup assist," *SAE Tech. Pap.*, no. 2017-01–0027, pp. 1–7, 2017.

[23]A. H. Korayem, "State and Parameter Estimation of Vehicle-Trailer Systems," University of Waterloo, 2021.

[24]C. Fuchs, F. Neuhaus, and D. Paulus, "3D pose estimation for articulated vehicles using Kalman-filter based tracking," *Pattern Recognit. Image Anal.*, vol. 26, no. 1, pp. 109–113, 2016.

[25]L. Caup, J. Salmen, I. Muharemovic, and S. Houben, "Video-based trailer detection and articulation estimation," in *IEEE Intelligent Vehicles Symposium, Proceedings*, 2013, no. IV, pp. 1179–1184.

[26]S. Hao, P. Luo, and J. Xi, "Estimation of vehicle mass and road slope based on steady-state Kalman filter," in *2017 IEEE International Conference on Unmanned Systems (ICUS)*, 2017, pp. 582–587.

[27]Z. Liu, H. Zheng, and W. Xu, "A model-based mass estimation and optimal braking force distribution algorithm of tractor and semi-trailer combination," *SAE Tech. Pap.*, no. 2013-01–0418, 2013.

[28]D. Y. Jung and G. Choi, "A new adaptive mass estimation approach of heavy truck based on engine torque local convex minimum characteristic at low speeds," *Energies*, vol. 13, no. 7, pp. 1–19, 2020.

[29]C. Cheng and D. Cebon, "Parameter and state estimation for articulated heavy vehicles," *Veh. Syst. Dyn.*, vol. 49, no. 1–2, pp. 399–418, 2011.

[30]N. Esmaeili, R. Kazemi, and S. H. Tabatabaei Oreh, "An adaptive sliding mode controller for the lateral control of articulated long vehicles," *Proc. Inst. Mech. Eng. Part K J. Multi-body Dyn.*, vol. 233, no. 3, pp. 487–515, 2019.

[31]"The technology: How trailer stability assist works," 2005. [Online]. Available: https://media.daimler.com/marsMediaSite/en/instance/ko/The-technology-How-Trailer-Stability-Assist-works.xhtml?oid=9904516, [Accessed: 16-Feb-2022].

[32]H. Wu, Nardi, J.J. Chen, and Hartman, "Closed-loop control for trailer sway mitigation," US 008,740,317 B2, 2014.

[33]H. Wu, "Trailer sway mitigation using torque vectoring," US 9,061,663 B2, 2015.

[34] V. Mazzilli S. De Pinto, L. Pascali, M. Contrino, F. Bottiglione, G. Mantriota, P. Gruber, and A. Sorniotti, “Integrated chassis control: Classification, analysis and future trends,” *Annu. Rev. Control*, vol. 51, pp. 172–205, 2021.

[35] M. Ricco, A. Percolla, G. Cardolini Rizzo, M. Zanchetta, D. Tavernini, M. Dhaens, M. Geraerts, A. Vigliani, A. Tota, and A. Sorniotti, “On the model-based design of front-to-total anti-roll moment distribution controllers for yaw rate tracking,” *Veh. Syst. Dyn.*, vol. 60, no. 2, pp. 569–596, 2020.

[36] M. Ricco, M. Dalboni, P. Gruber, M. Dhaens, and A. Sorniotti, “On the Design of Front-To-Total Anti-roll Moment Distribution Controllers for Enhancing the Cornering Response”, *12th International Munich Chassis Symposium 2021*, pp. 241–260, 2022.

[37] M. Schiebahn. P. Zegelaar, M. Lakehal-Ayat and O. Hofmann, “The yaw torque influence of active systems and smart actuators for coordinate vehicle dynamics controls,” *Veh. Syst. Dyn.*, vol. 48, no. 11, pp. 1269–1284, 2010.

[38] Y. Zheng., B. Shyrokau, and T. Keviczky, “3DOP: Comfort-oriented Motion Planning for Automated Vehicle with Active Suspensions,” *IEEE Intelligent Vehicle Symposium (IV)*, pp. 390–395, 2022.

[39] M. Ricco, A. Alshawi, P. Gruber, M. Dhaens, and A. Sorniotti, “Nonlinear model predictive control for yaw rate and body motion control through semi-active and active suspensions,” *Veh. Syst. Dyn.*, pp. 1–34, 2023.

[40] A.H. Korayem, A. Khajepour, and B. Fidan, “A Review on Vehicle-Trailer State and Parameter Estimation,” *IEEE Trans. Intell. Transp. Systems*, vol. 23, no. 7, pp. 5993–6010, 2022.

[41] M. Metzler, D. Tavernini, P. Gruber, and A. Sorniotti, “On prediction model fidelity in explicit nonlinear model predictive vehicle stability control,” *IEEE Trans. Control Syst. Technol.*, vol. 29, no. 5, pp. 1964–1980, 2020.

[42] L. De Novellis, A. Sorniotti, and P. Gruber, “Optimal wheel torque distribution for a four-wheel-drive fully electric vehicle,” *SAE Int. J. Passeng. Cars - Mech. Syst.*, no. 2013-01–0673, 2013.

[43] L. De Novellis, A. Sorniotti, and P. Gruber, “Wheel torque distribution criteria for electric vehicles with torque-vectoring differentials,” *IEEE Trans. Veh. Technol.*, vol. 63, no. 4, pp. 1593–1602, 2014.

[44] L. De Novellis, A. Sorniotti, P. Gruber, J. Orus, J.M. Rodriguez Fortun, J. Theunissen, and J. De Smet, “Direct yaw moment control actuated through electric drivetrains and friction brakes : Theoretical design and experimental assessment,” *Mechatronics*, vol. 26, pp. 1–15, 2015.

[45] G. Rill, Road vehicle dynamics: fundamentals and modelling. 1st ed. Boca Raton, USA: CRC Press, 2011.

[46] L. Grune and J. Pannek, *Nonlinear model predictive control: Theory and algorithms*. London: Springer, 2010.

[47] H. B. Pacejka, *Tyre and vehicle dynamics*. Oxford: Elsevier, 2006.

[48] G. Genta, *Motor vehicle dynamics: modeling and simulation*. Singapore: World Scientific Publishing Co. Pte. Ltd., 2006.

[49] G. Genta and L. Morello, *The automotive chassis - Volume 2: system design*. London, United Kingdom: Springer Nature, 2019.

[50] J. M. Maciejowski, P.J. Goulart, and E.C. Kerrigan, *Predictive control with constraints*. London, United Kingdom: Pearson education, 2002.

[51] A. Linder, R. Kanchan, and P. Stolze, *Model-based predictive control of electrice drives*. Gottingen, Germany: Cuvillier Verlag Gottingen, 2010.

[52] International Organization for Standardization, "Road vehicles - Heavy commercial vehicle combinations and articulated buses - Lateral stability test methods," no. ISO14791:2000(E), 2002.

[53] K. J. Han, I.K. Kim, H.Y. Jo, and K.S. Huh, "Development and experimental evaluation of an online estimation system for vehicle mass," *Proc. Inst. Mech. Eng., Part D: J. Autom. Eng.*, 2009, vol. 223, no. 2, pp. 167–177.

[54] P. C. Young, *Recursive estimation and time-series analysis - An introduction for student and practitioner*. Lancaster: Springer Science & Business Media, 2012.

[55] N. Lin, C. Zong, and S. Shi, "The method of mass estimation considering system error in vehicle longitudinal dynamics," *Energies*, vol. 12, no. 1, pp. 52–67, 2019.

[56] J. Ghosh, S. Foulard, and R. Fietzek, "Vehicle mass estimation from CAN data and drivetrain torque observer," *SAE Tech. Pap.*, no. 2017-01-1590, pp. 1–8, 2017.

[57] V. Mazzilli, D. Ivone, S. De Pinto, L. Pascali, M. Contrino, G. Tarquinio, P. Gruber, and A. Sorniotti, "On the benefit of smart tyre technology on vehicle state estimation," *Veh. Syst. Dyn.,*vol. 60, no. 11, pp. 3694–3719, 2022.

.

APPENDIX

Table A 1 – Trailer Inertial and Geometric Parameters.

Tr. conf.	m_t [kg]	$J_{z,t}$ [kg m^2]	$l_{F,t}$ [m]	l_t [m]
BMT	1000	646	1.961	2.300
$\left(m_t J_{z,t}\right)_1$	600	333	1.961	2.300
$\left(m_t J_{z,t}\right)_2$	800	445	1.961	2.300
$\left(m_t J_{z,t}\right)_3$	1200	778	1.961	2.300
$\left(l_{F,t}\right)_1$	1000	646	1.631	2.300
$\left(l_{F,t}\right)_2$	1000	646	1.796	2.300
$\left(l_{F,t}\right)_3$	1000	646	1.961	2.300
$\left(l_{F,t}\right)_4$	1000	646	2.126	2.300
$\left(l_{F,t}\right)_5$	1000	646	2.291	2.300
$\left(l_t\right)_1$	1000	646	1.961	1.970
$\left(l_t\right)_2$	1000	646	1.961	2.135
$\left(l_t\right)_3$	1000	646	1.961	2.300
$\left(l_t\right)_4$	1000	646	1.961	2.465
$\left(l_t\right)_5$	1000	646	1.961	2630

Table A 2 – Trailer Instability Occurrences.

Tr. conf.	$\mathrm{TV}^{\mathrm{Bas}}$	AS^1	AS^2	TV^1	TV^2	$(\mathrm{AS}^1//\mathrm{TV}^1)_{\mathrm{W/Comm}}$	$(\mathrm{AS}^2//\mathrm{TV}^2)_{\mathrm{W/Comm}}$	$(\mathrm{AS}^1//\mathrm{TV}^1)_{\mathrm{W/oComm}}$	$(\mathrm{AS}^2//\mathrm{TV}^2)_{\mathrm{W/oComm}}$	$(\mathrm{AS}\text{-}\mathrm{TV})^1$	$(\mathrm{AS}\text{-}\mathrm{TV})^2$
BMT	√	√	√	√	√	√	√	×	√	√	√
$(m_t J_{z,t})_1$	√	√	√	√	√	√	√	√	√	√	√
$(m_t J_{z,t})_2$	√	√	√	√	√	√	√	×	√	√	√
$(m_t J_{z,t})_3$	×	√	√	√	√	√	×	×	×	√	√
$(l_{F,t})_1$	√	√	√	√	√	√	√	×	√	√	√
$(l_{F,t})_2$	√	√	√	√	√	√	√	×	√	√	√
$(l_{F,t})_3$	√	√	√	√	√	√	√	×	√	√	√
$(l_{F,t})_4$	×	√	√	√	√	×	√	×	√	√	√
$(l_{F,t})_5$	×	√	×	×	×	√	×	×	×	×	√
$(l_t)_1$	×	√	×	√	√	×	√	×	√	√	√
$(l_t)_2$	√	√	√	√	√	×	√	×	√	√	√
$(l_t)_3$	√	√	√	√	√	√	√	×	√	√	√
$(l_t)_4$	√	√	√	√	√	√	√	×	√	√	√
$(l_t)_5$	√	√	√	√	√	√	√	×	√	√	√

5

CONCLUSIONS

You've got to constantly keep challenging yourself and keep raising the bar.

Lewis Hamilton

This chapter summarises all the findings, limitations open questions and guidelines for future developments from Chapters 2–4.

5.1 RESEARCH FINDINGS

This dissertation aimed to explore the fundamentals of motion sickness (MS) in automated vehicles, focusing on understanding its underlying mechanisms. It also sought to design and evaluate a motion planning algorithm that can optimise either journey time or minimise motion sickness. Additionally, multi-actuation control strategy for various vehicle types to ensure stability in safety-critical situations are designed and presented, aiming to integrate them within the motion planner to assess their effectiveness in mitigating motion sickness.

In Chapter 2, a systematic review of motion sickness (MS) is presented. This review begins with an in-depth analysis of MS theories developed over centuries, detailing the fundamentals of each theory and their key differences. A central aspect of understanding MS is the interaction between the vestibular and visual systems. While theories such as sensory conflict, postural instability, and subjective vertical mismatch provide valuable insights, future advances in MS research may require a more integrative approach that synthesises these perspectives. The chapter then examines MS assessment methods, covering questionnaires, scales, indexes, and models. These models are discussed extensively, with key information summarised in Table 2.1. Finally, the chapter explores MS mitigation strategies, highlighting a diverse array of approaches—behavioural, medical, and technological—each with its unique advantages and limitations. Although behavioural methods, like habituation, and pharmacological solutions can provide relief, they often face limitations in effectiveness or side effects. Notably, technological innovations, particularly in motion planning, hold significant promise for mitigating MS. By influencing vehicle dynamics to keep translational accelerations within comfort limits and reducing the most provocative frequencies associated with MS onset, motion planning offers a powerful strategy to counteract MS effectively.

Chapter 3 focuses on designing a motion planning algorithm specifically for MS mitigation. It begins with a review of the state-of-the-art, identifying gaps in the literature. Key issues highlighted include the need to incorporate a precise seat-to-head transfer function within the optimal control problem to avoid underestimating MS, applying frequency weightings that emphasise frequencies most likely to trigger MS, and developing motion planning algorithms through nonlinear model predictive control (NMPC) to improve both MS mitigation and postural stability. The chapter details the comfort assessment process, emphasising the importance of carefully designing sets of filters for integration within the optimal control problem, even though this increases complexity and computational demand. Four distinct motion planners are developed, each differing in how the MS metric is calculated: the first uses vehicle-based accelerations, the second applies seat-to-head transfer functions, the third incorporates frequency-weighting filters, and the fourth combines both seat-to-head transfer functions and frequency-weighting filters. Additionally, given the diverse terms in the cost function, normalisation factors are applied to ensure fair representation of each term. The results reveal that the motion planner without normalised terms in the cost function can effectively mitigate MS and minimise journey time. However, it also introduces greater complexity in defining the weights of the cost terms and shows inconsistent weight magnitudes in extreme cases (i.e., minimum time and minimum MS), complicating the interpretation of control priorities. In contrast, the motion planner with a normalised cost function offers simpler weight definitions and produces more consistent control actions. Overall, the algorithm proves effective in mitigating MS, and the relationship between journey time and cumulative MS is clearly illustrated by the generated Pareto front.

Chapter 4 devles into the design of several NMPC approaches for torque-vectoring and traction controller, solely torque-vectoring for mitigation of trailer sway and integrated torque-vectoring and active suspension system. For the first control agorithm, in this work five NMPC strategies for torque-vectoring and tracion control, focusing on both centralised and multi-layer architectures are compared. The key findings include: i) peformance, All proposed strategies significantly enhance vehicle response over baseline, even with parameter variations; ii) efficiency, the multi-layer architecture with torque feedback, despite its reduced complexity and fewer control inputs, achieve comparable vehicle dynamics results to the centralised setup but with significantly lower computational time; iii) optimisation, reducing controller's time steps is more effective for enhancing performance than extending the prediction horizon; iv) slip control, the centralised architecture excels in lateral control, but induces slip oscillations, which are avoided with the multil-layer designs; robustness, the multi-layer setups exhibit more stable control performance than the centralised setup, especially under parameter variations. The second set of NMPCs focues on torque-vectoring control in car-trailer system, incorporating hitch angle data for more stable and safe operation. The main conclusions are: i) in terms of controller comparison, the controllers based on the rigid vehicle model, struggles with heavier trailers, underscoring the need for advanced control strategies in vehicle combinations; ii) the top-performing controllers, i.e. $YR + HAE_{fun}$ and $YR + SC_{HAE}$, include the car-trailer dynamics in the prediction model and use hitch angle error in control objectives, providing stable trailer sway management across varied trailer conditions; iii) the controllers with car-trailer models perform well across a range of trailer parameters, demonstrating adaptability and safety, even with short prediction horizons, thus proving their robustness. Finally the last set of NMPCs investigates the control of hitch dynamics in car-semitrailer setup, using an active suspension system, both alone and combined with a torque-vectoring controller. The conclusions highlight that: i) the standard NMPC for torque-vectoring alone is inadequate for safety in extreme cornering; ii) the NMPC formulations using the estimated hitch joint forces, maintain effectiveness reducing the computational demands and allowing for shorter sampling times; iii) the solely active-suspension performs better than torque-vectoring for safety but is less effective than torque-vectoring; however the active suspension shows more robust performance across varied trailer parameters; and iv) integrated controllers, especially those based on articulated vehicle model, outperform others in terms of safety and robusness, indicating strong potential for turther testing at higher techinology readiness levels.

5.2 STUDY LIMITATIONS

The study limitations in this dissertation stem from the inherent challenges of modeling complex vehicle dynamics, the controlled experimental settings, and the assumptions made during the design and implementation of motion planning and control algorithms. While the proposed solutions show promising results in mitigating motion sickness and enhancing vehicle stability, certain factors such as the simplification of models, the reliance on simulation-based assessments, and the specific conditions under which the experiments were conducted may limit the generalisability of the findings to broader real-world scenarios. Furthermore, the computational demands of the advanced control strategies and the need for optimisation routines present additional constraints that could impact practical application. These limitations are important to address for future research, as they will contribute to refining and validating the proposed methodologies. More in detail, while this dissertation focuses on motion planning and mitigation strategies for motion sickness in automated vehicles, the vehicle models used may not encompass the full complexity of all potential vehicle configurations. For instance, certain vehicle-specific dynamics or non-linearities might not be fully represented, which could limit the generalisation of the results to a broader range of vehicles. Furthermore, given the advances in future vehicle designs, the results may not be diretly applicable to all vehicle types or configurations. Regarding the evaluation of motion sickness, despite the different methods explored in this dissertation, i.e. questionnaires, indexes, scales and modes, it still remains an highly subjective phenomenon, influenced by many factors such as personal sensitivity, environment and context, thus the results might not fully reflect real-world variability. The test cases showed in Chapter 3, evaluate motion sickness cumulation under controlled conditions, i.e. maximum speed of 50 km/h, which may not completely replicate real-world driving situations. Factors such as road surface variation, weather conditions, or real-world driving styles might not be fully accounted for. Moreover, as mentioned before, the test environment may not capture the full spectrum of factors that influence MS in real-world driving conditions. As for the NMPC strategies implemented in simulations, the real-time application of these algorithms might face computational challenges, especially when accounting for complex vehicle dynamics and environmental factors. The computational burden of these strategies, though optimised, could still be a limitation for practical implementation in autonomous vehicles. Furthermore, the real-time implementation of advanced motion planning algorithms may still be computationally expensive and may require further optimisation or hardware advancemetns to work effectively in commercial systems. In this dissertation is highly stressed that motion planning holds the potential to represent a technological solution for mitigating motion sickness, potentially downplaying other complementary strategies, however, focussing on the solely motion planning as primary mitigation strategy might overlook the potential for integrated, multi-modal approaches that combine motion planning with other solutions, which could improve overall efficacy in mitigating motion sickness. The designed motion planning and related findings regarding motion sickness mitigation, are strictly linked to the use of automated vehicles, however, the same results might not be directly transferable to non-automated vehicles or partially atuomated vehicles, where human control is involved, thus a re-designing of the strategies might be necessary in driving scenarios where the driver control and feedback could play a significant role in motion sickness development. Given the uncertainty in the understading of motion sickness, and the way metrics used to measure its cumulation are developed, a full coverage of individual passenger sensitivities might not be ensured, therefore the variations in passengers' tolerance to motion sickness could not be fully captured.

5.3 OPEN QUESTIONS TO BE ADDRESSED

While this dissertation provides valuable insights into theories that try to describe the phenomenon of motion sickness, mitigation strategies and optimisation of vehicle control strategies for trasnlational motion, several open questions remain that could further enhance the understanding of motion sickness and application of these solutions in real-world scenarios:

- Will there ever be a comprehensive unified theory that can fully explain all the complexities of motion sickness? Despite the significant advances made over the years in terms of theoretical frameworks, including sensory conflict theory, postural instability, and subjective vertical mismatch, a complete and universally accepted explanation of motion sickness remains elusive. The interactions between the vestibular system, visual input, and other sensory modalities are incredibly complex, and individual differences (such as genetic predispositions, psychological factors, and previous experiences) add layers of unpredictability to the phenomenon. These nuances challenge the creation of a singular theory that can encompass all possible causes and effects of motion sickness in every scenario.
- A comprehensive theory that fully captures all aspects of motion sickness would be great, but what about the effectiveness of mitigation strategies? While understanding the underlying mechanisms may lead to more targeted interventions, control strategies will still play a vital role in managing and mitigating motion sickness in practice. For instance, technological solutions, such as motion planning algorithms, real-time control systems, and vehicle design considerations, can adapt the driving environment to minimise the effects of

motion sickness. These solutions are crucial, as they allow for real-time adjustments that can alleviate symptoms for passengers, even when theoretical understanding continues to evolve. Ultimately, motion sickness mitigation will require a combination of well-founded theoretical knowledge and practical, real-time implementation of control strategies that can address the individual needs and preferences of passengers.

- Can the advanced control systems be fine-tuned to not only enhance vehicle performance but also significantly improve the comfort and well-being of passengers, reducing motion sickness to a level where it no longer poses a major issue for passengers? While these actuation methods are known to improve vehicle dynamics, their direct impact on mitigating motion sickness remains an area that requires further investigation. Specifically, how will these control strategies influence passengers' perceived comfort in different driving conditions, and will they be sufficient to effectively reduce or prevent motion sickness? Traction control and torque vectoring systems work by adjusting the distribution of forces between the wheels to optimise vehicle handling, while active suspension control can adapt the vehicle's ride characteristics in real-time to manage excessive accelerations. While these systems can improve vehicle stability and reduce uncomfortable motion, the extent to which they can specifically target the factors that contribute to motion sickness – such as unwanted accelerations, oscillations, or high-frequency motions – remains unclear. Moreover, the interaction between these actuation methods and human physiological responses to motion is not yet fully understood. While reducing harsh or unpredictable vehicle movements can reduce motion sickness, it is uncertain whether these technologies can address the broader spectrum of factors that contribute to motion sickness, such as sensory conflict or postural instability.
- A provocative question to consider is whether motion sickness will remain a "major issue" for future generations, particularly as we transition into an era where autonomous vehicles are the norm. For our generation, who has experienced the shift from human-driven to automated vehicles, motion sickness represents a significant challenge – especially as it stems from the sensory mismatches between how we perceive movement and how the vehicle actually moves. But will this issue persist for future generations who may never know the traditional human-driven vehicle experience? Or perhaps, over time, human physiology will adapt through evolution to the new modes of transportation, rendering motion sickness obsolete in the context of automated vehicles? In other words, as we move further into a world where control is increasingly taken over by machines, could we eventually become more attuned to the motions of self-driving cars, reducing or even eliminating the phenomenon of motion sickness? Will our bodies learn to interpret the vehicle's movement differently, no longer causing the discomfort we currently experience? It's a thought-provoking question that challenges us to consider

whether motion sickness is truly an insurmountable issue, or whether it is simply a temporary discomfort that will fade as we adjust – both technologically and biologically – to the new realities of autonomous transportation.

ACKNOWLEDGEMENTS

Aknowledgements are intentionally left blank.